Dissertation

submitted to the
Combined Faculty for Natural Sciences and Mathematics
of the Ruperto Carola University of Heidelberg, Germany
for the degree of
Doctor of Natural Sciences

presented by
M. Sc. Linda Liedgens
born in Tuttlingen, Germany

Oral examination: September 17th, 2018

Investigation of oxidative protein folding in protist mitochondria and elucidation of the catalytic mechanism of glutaredoxins

Referees: Prof. Dr. Michael Lanzer
Prof. Dr. Marcel Deponte

Table of contents

ACKNOWLEDGEMENT / DANKSAGUNG

Als erstes möchte ich dem Betreuer meiner Doktorarbeit, Prof. Dr. Marcel Deponte, dafür danken, dass ich in seiner Arbeitsgruppe promovieren konnte. Vielen Dank Marcel für deine Betreuung, Unterstützung und die stete Diskussionsbereitschaft.

Bei Prof. Dr. Lanzer möchte ich mich für die Aufnahme in seine Abteilung der Parasitologie und für die Betreuung meiner "TAC-Meetings" bedanken. Vielen Dank für die hilfreichen Anregungen und Diskussionen zum Projekt.

Thank you, PhD Faith Osier, for helping me out so spontaneously and being examiner in my defense. Thank you also very much, PhD Silvia Portugal, for being my examiner.

Vielen Dank Frau Prof. Dr. Luise Krauth-Siegel für die Teilnahme an meinen "TAC-Meetings" und Ihre hilfreichen Ratschläge und Anregungen.

Vielen Dank Marcel Deponte, Verena Staudacher, Sandra Kohlbecher, Sandra Specht, Gino Turra und Robin Schumann für das Korrekturlesen dieser Arbeit.

Ich möchte auch meinen Arbeitskollegen für Ihre Unterstützung und die großartige Zeit auch außerhalb des Labors danken. Danke Verena Staudacher, Sandra Specht, Gino Turra, Cletus Wezena, Johannes Krafczyk, Kristina Feld, Patricia Begas, Robin Schumann und Fabian Geissel. Vielen Dank auch der AG Frischknecht, vor allem Jessica Kehrer und Katharina Quadt für die Unterstützung am Mikroskop.

Ich danke meinen Eltern, meinem Bruder und meinem Großvater dafür, dass sie mich während meines gesamten Studiums und während der Promotion unterstützt haben. Danke für alles!

Vielen Dank auch an alle meine Freunde für den Ausgleich zur Wissenschaft!

Zuletzt möchte ich meinem Partner Philipp dafür danken, dass er mit mir auch die Höhen und Tiefen des Studiums und der Promotion durchgestanden hat und stets ein verlässlicher Partner war.

SUMMARY

Protein import into the mitochondrial intermembrane space (IMS) of parasitic protists differs from other eukaryotes despite a general conservation of mitochondrial protein import signals. Imported proteins typically carry conserved cysteine-motifs that are oxidized in the IMS. In opisthokonta such as yeast and mammals, these motifs are recognized and oxidized by the oxidoreductase Mia40 leading to the formation of intramolecular disulfide bonds. Reduced Mia40 is subsequently re-oxidized by the sulfhydryl electron transferase Erv1. In kinetoplastida, such as *Leishmania tarentolae*, and in apicomplexan parasites, such as *Plasmodium falciparum*, no Mia40 homolog could be identified so far. However, conserved substrates and an Erv homolog in these parasites suggest the existence of a Mia40 replacement. Indeed, preliminary results revealed two disulfide-bonded interaction partners of *Pf*Erv as demonstrated by western blot analyses.

The major objective of this thesis was the identification of a potential Mia40 replacement in the parasite *L. tarentolae*. Numerous experiments were performed in order to trap mixed disulfide intermediates between the model substrate *Lt*sTim1 or *Lt*Erv and a potential interaction partner. A variety of protocols with alkylating, oxidizing or reducing agents did not reveal mixed disulfides between *Lt*Erv and the adapter replacement in western blot analyses. In addition, even with highly enriched *Lt*Erv protein levels after denaturing or native pull-down, no mixed disulfide intermediate could be identified. In contrast, staining against *Lt*sTim1 in western blot analyses showed disulfide-bridged intermediates indicating potential heterodimers of *Lt*sTim1 and Mia40 replacement candidates. However, an enrichment of these intermediates by affinity chromatography and further analysis failed because of systematic problems with the hydrophobicity of the substrate and the *Lt*sTim1-antibody.

To summarize, a potential replacement for Mia40 in parasitic protists remains to be identified and the oxidative folding machinery in the IMS of kinetoplastida and apicomplexa could not be unraveled during this PhD project. Four alternative cysteine-containing substrates of the oxidative protein folding pathway in the IMS were already designed during this project and might lead to a rather fast breakthrough in further experiments.

Glutaredoxins (Grx) are highly conserved enzymes that play important roles in redox catalysis and iron metabolism and are found in almost all organisms. The traditional monothiol mechanism of Grx catalysis is divided into an oxidative half-reaction with the first glutathionylated substrate and a reductive half reaction with the reduced tripeptide glutathione (GSH) as the second substrate. However, this traditional model cannot explain how exactly the two different substrates of Grx are bound. Hence, two refined models of Grx catalysis namely the “glutathione scaffold model” and the “glutathione activator model” were previously proposed and experimentally confirmed for two residues of *Sc*Grx7. This model can help to distinguish protein areas that either interact with the disulfide substrate (a scaffold site, including Glu170 in *Sc*Grx7) or with the reducing agent (an activator site, including Lys105 in *Sc*Grx7).

The second objective of this PhD project was to test the general applicability of this model using the non-related enzyme *Pf*Grx. Moreover, four additional residues that were previously suggested to contribute to the glutathione activator site in *Sc*Grx7 were characterized in this thesis.

Taken together, I confirmed the existence of two distinct glutathione interaction sites with the non-related model enzyme *Pf*Grx. Moreover, I could identify Arg153 of *Sc*Grx7 as another potential scaffold site residue. In addition, I could show that the two charge inversion mutants with a positively charged amino acid of the helix 3 residues Asp144 and Glu147 in *Sc*Grx7 enhanced the interaction with the second substrate GSH. Hence, the helix 3 of these “gain-of-function” mutants indeed seems to affect the glutathione activator site. Furthermore, I could show that the introduced mutations influenced the pK_a value of the active site cysteine of *Sc*Grx7 only to a minor degree, except for *Sc*Grx7^{K105E}. Modeling of the transition states and analyses of the different mutants by roGFP assays may help to elucidate the structure-function relationships of Grx in further analyses.

ZUSAMMENFASSUNG

Der Proteinimport in den mitochondrialen Intermembranraum von parasitären Protisten unterscheidet sich trotz einer allgemeinen Konservierung der mitochondrialen Proteinimport-Signalen von anderen Eukaryoten. Importierte Proteine weisen typischerweise konservierte Cysteinmotive auf und werden im Intermembranraum oxidiert. In Opisthokonta, wie z.B. Hefe oder Säugetieren, werden diese Motive durch die Oxidoreduktase Mia40 erkannt und oxidiert, was zu der Bildung von intramolekularen Disulfidbrücken führt. Reduziertes Mia40 wird anschließend durch die Sulfhydryl-Elektronentransferase Erv1 wieder oxidiert. In Kinetoplastida, wie *Leishmania tarentolae* und Apicomplexa wie *Plasmodium falciparum*, konnte bislang kein Mia40-Homolog identifiziert werden. Jedoch deuten konservierte Substrate und ein Erv-Homolog auf die Existenz eines Mia40-Ersatzes in diesen Parasiten hin. In der Tat zeigten vorläufige Ergebnisse zwei disulfidverbrückte Interaktionspartner von *Pf*Erv in Western-Blot-Analysen.

Das Hauptziel dieser Arbeit war die Identifizierung eines potentiellen Mia40-Ersatzes in dem Parasiten *L. tarentolae*. Zahlreiche Experimente wurden durchgeführt, um ein gemischtes Disulfid zwischen dem Modellsubstrat *Lt*sTim1 oder *Lt*Erv und einem potentiellen Interaktionspartner zu stabilisieren. Eine Vielzahl an Protokollen mit Alkylierungs-, Oxidations- oder Reduktionsmitteln ließ keine gemischten Disulfide zwischen *Lt*Erv und einem Mia40-Ersatz in Western-Blot-Analysen erkennen. Darüber hinaus konnte selbst nach starker Proteinanreicherung durch denaturierende oder native Affinitätschromatographie kein gemischtes Disulfid nachgewiesen werden. Im Gegensatz dazu zeigte die Markierung von *Lt*sTim1 in Western-Blot-Analysen disulfidverbrückte Zwischenprodukte, welche möglicherweise Heterodimere zwischen *Lt*sTim1 und Mia40-Ersatzkandidaten darstellen. Allerdings war eine Anreicherung dieser Intermediate durch Affinitätschromatographie und eine weitere Untersuchung aufgrund systematischer Probleme mit der Hydrophobizität des Substrates und dem Antikörper gegen *Lt*sTim1 nicht möglich.

Zusammenfassend konnte in diesem Projekt weder ein Mia40-Ersatz in parasitären Protisten identifiziert, noch die oxidative Faltungs-Maschinerie im Intermembranraum von Kinetoplastida und Apicomplexa weiter aufgeklärt werden. Vier alternative, cysteinhaltige Substrate des oxidativen Proteinfaltungswegs im Intermembranraum wurden bereits während dieser Arbeit geplant und könnten zu einem eher schnellen Durchbruch in zukünftigen Experimenten führen.

Glutaredoxine (Grx) sind hochkonservierte Enzyme, die eine wichtige Rolle in der Redoxkatalyse und im Eisen-Stoffwechsel spielen und in fast allen Organismen vorkommen. Der traditionelle Monothiol-Mechanismus der Grx-Katalyse wird in eine oxidative Halbreaktion mit dem ersten glutahionylierten Substrat und eine reduktive Halbreaktion mit dem reduzierten Tripeptid Glutathion (GSH), welches als zweites Substrat agiert, unterteilt. Jedoch kann das traditionelle Modell nicht erklären, wie genau die zwei verschiedenen Substrate von Grx gebunden werden. Daher wurde zuvor ein verfeinertes Modell der Grx-Katalyse, bestehend aus dem „Glutathiongerüst-Modell“ und dem „Glutathionaktivierungs-Modell“, vorgeschlagen und experimentell für zwei Aminosäure-Reste von *Sc*Grx7 bestätigt. Dieses Modell kann helfen, Proteinbereiche zu unterscheiden, die entweder mit dem Disulfid-Substrat (eine „Glutathiongerüst“-Stelle, die Glu170 von *Sc*Grx7 beinhaltet) oder mit dem Reduktionsmittel interagieren (eine „Glutathionaktivierungs“-Stelle, die Lys105 von *Sc*Grx7 beinhaltet).

Ein weiteres Ziel dieser Arbeit war es, durch die Analyse des nichtverwandten Enzyms *Pf*Grx herauszufinden, ob dieses Modell eine allgemeine Anwendbarkeit findet. Außerdem wurden vier weitere Aminosäurereste von *Sc*Grx7, die zuvor als mögliche Elemente der „Glutathionaktivierungs“-Stelle vorgeschlagen wurden, in dieser Arbeit untersucht.

Zusammengefasst konnte ich die Existenz zweier unterschiedlicher Glutathion-Interaktionsstellen durch die Analyse des nichtverwandten Modell-Enzyms *Pf*Grx bestätigen. Zudem konnte ich Arg153 von *Sc*Grx7 als eine weitere mögliche „Glutationgerüst“-Stelle nachweisen. Darüber hinaus konnte ich zeigen, dass die beiden Ladungsinversionsmutanten der Aminosäurereste Asp144 und Glu147 in der Helix 3 von *Sc*Grx7 die Interaktion mit dem zweiten Substrat GSH verbesserten. Demzufolge scheint die Helix 3 dieser „Funktionsgewinn”-Mutanten tatsächlich die “Glutathionaktivierungs”-Stelle zu beeinflussen. Außerdem konnte ich zeigen, dass die eingefügten Punktmutationen nur einen geringen Einfluss auf den pK_S-Wert des Cysteins im aktiven Zentrum von *Sc*Grx7 haben. Eine Modellierung der Übergangszustände und weitere Analysen der verschiedenen Mutanten durch Untersuchungen mit roGFP könnten zukünftig helfen, die Struktur-Funktions-Beziehungen von Grx weiter aufzuklären.

LIST OF FIGURES

LIST OF TABLES

ABBREVIATIONS

α	anti
Δ	delta
°C	degree Celsius
µl	microliter
µm	micrometer
µM	micromolar
Amp	ampicillin
Amp^R	ampicillin resistant
AMP	adenosine monophosphate
APEX	ascorbate peroxidase
app	apparent
APS	ammonium persulfate
as	antisense
ATP	adenosine triphosphate
BHI	brain heart infusion
BioID	proximity-dependent biotin identification
β-ME	β-mercaptoethanol
bp	base pairs
BSA	bovine serum albumin
CBP	calmodulin binding peptide
CL	cutaneous leishmaniasis
CRISPR	clustered regularly interspaced short palindromic repeats
C-terminal	carboxy-terminal
ddH_2O	double deionized water
DMSO	dimethyl sulfoxide
DNA	deoxyribonucleic acid
dNTP	deoxyribonucleoside triphosphate
DTT	dithiothreitol
ECL	enhanced chemiluminescence
E. coli	*Escherichia coli*
EDTA	ethylenediaminetetraacetic acid
Erv	essential for respiration and viability
et al.	*et alii* (and others)
FCS	fetal calf serum
Glp	glutaredoxin-like protein
GR	glutathione reductase
Grx	glutaredoxin
GSH	reduced glutathione
GSSCys	L-cysteine-glutathione disulfide
GSSG	glutathione disulfide
h	hours
HEDS	bis(2-hydroxyethyl)disulfide
HEPES	4-(2-hydroxyethyl)-1-piperazineethanesulfonic acid
HRP	horseradish peroxidase
IAM	iodoacetamide
IM	inner mitochondrial membrane
IMS	intermembrane space
IPTG	isopropyl β-D-1-thiogalactopyranoside

kb	kilo bases
k_{cat}	turnover number
kDa	kilo Dalton
KISS	kinetoplastida-specific second
K_m	Michaelis-Menten constant
LB	Luria-Bertani
L. braziliensis	*Leishmania braziliensis*
L. donovani	*Leishmania donovani*
Li	*Leishmania infantum*
L. infantum	*Leishmania infantum*
Lt	*Leishmania tarentolae*
L. tarentolae	*Leishmania tarentolae*
mA	milliampere
MCS	multiple cloning site
MES	2-(*N*-morpholino)ethanesulfonic acid
mg	milligram
MIA	mitochondrial IMS import and assembly
MIM	mitochondrial import
min	minute
ml	milliliter
MMTS	*S*-methyl-methanethiosulfonate
MOPS	3-(*N*-morpholino)propanesulfonic acid
MPI	mitochondrial protein import
MPP	mitochondrial processing peptidase
NADPH	nicotinamide adenine dinucleotide phosphate
NEM	*N*-ethylmaleimide
Ni-NTA	nickel-nitrilotriacetic acid
nm	nanometer
N-terminal	amino-terminal
OD	optical density
OD_{600nm}	optical density at 600 nm
OM	outer mitochondrial membrane
PAGE	polyacrylamide gel electrophoresis
PAM	presequence translocase-associated motor
PBS	phosphate-buffered saline
PCR	polymerase chain reaction
PDI	protein disulfide isomerase
Pf	*Plasmodium falciparum*
PFA	paraformaldehyde
P. falciparum	*Plasmodium falciparum*
*Pf*GR	*P. falciparum* glutathione reductase
RNA	ribonucleic acid
RNAi	RNA interference
rpm	rounds per minute
RR	ribonucleotide reductase
RST	rapid serodiagnostic test
RT	room temperature
s	sense
SAM	sorting and assembly machinery
Sc	*Saccharomyces cerevisiae*
S. cerevisiae	*Saccharomyces cerevisiae*

*Sc*GR	*S. cerevisiae* glutathione reductase
SDS	Sodium dodecyl sulfate
SILAC	stable isotope labeling of amino acids in cell culture
TAE	Tris-acetate-EDTA-buffer
Tb	*Trypanosoma brucei*
TBS	Tris buffered saline
TCA	Trichloroacetic acid
TCEP	tris(2-carboxyethyl)phosphine
TEMED	tetramethylethylenediamine
TFB	transformation buffer
TIM	translocase of the inner mitochondrial membrane
TM	transmembrane domain
TOM	translocase of the outer mitochondrial membrane
Tris	tris(hydroxymethyl)aminomethane
Trx	thioredoxin
Trxl	thioredoxin-like domain
T. brucei	*Trypanosoma brucei*
T. cruzi	*Trypanosoma cruzi*
U	units
V	Volt
VL	visceral leishmaniasis
v/v	volume per volume
w/v	weight per volume
wt	wild-type

For the amino acids, the standard one letter or three letter codes were used.

1 Introduction

1.1 Mitochondrial protein import

1.1.1 Mitochondria

Mitochondria are ubiquitous organelles that can be found in all eukaryotes. They are crucial for different cellular processes including energy metabolism, apoptotic cell death and essential metabolic pathways such as iron-sulfur cluster biosynthesis [1, 2]. The organelle evolved from endosymbiosis of an anaerobe progenitor cell that had engulfed an aerobe α-proteobacterium [3]. Thus, the organelle contains its own genome encoding mitochondrial proteins that are synthesized at ribosomes in the mitochondrial matrix and are crucial for oxidative phosphorylation [1]. However, these mitochondrial-encoded proteins represent less than 1% of the around 1000 (yeast) [4-6] to 1500 (human) [7, 8] overall mitochondrial proteins. The majority of mitochondrial proteins (more than 99%) are synthesized at ribosomes in the cytosol and consequently have to be transported to one of the four mitochondrial compartments (Figure 1) [1]. For trafficking proteins to the outer membrane (OM), the intermembrane space (IMS), the inner membrane (IM) or the matrix, different mitochondrial protein import (MPI) pathways evolved that are described in the following section.

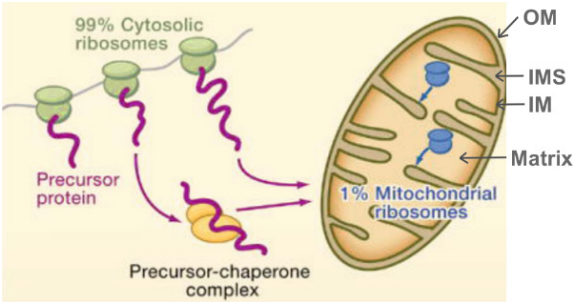

Figure 1 | Biogenesis of mitochondrial proteins. More than 99% of all mitochondrial proteins are synthesized at cytosolic ribosomes and are subsequently imported into one of the four mitochondrial compartments (OM, IMS, IM or matrix). Less than 1% of the mitochondrial proteins are a relict of endosymbiosis and are synthesized at mitochondrial ribosomes. OM: outer mitochondrial membrane; IMS: intermembrane space; IM: inner mitochondrial membrane. Adapted from Chacinska *et al.* 2009 [1].

1.1.2 Mitochondrial protein import machineries

Most of the knowledge of MPI derives from studies on *Saccharomyces cerevisiae*, *Neurospora crassa* or mammals, which are part of the same group of the evolutionary tree – the opisthokonts. The five principles of MPI pathways described in this section are mainly based on these studies (Figure 2) [9, 10]. The classical and first discovered pathway for MPI is called the presequence pathway. Precursor proteins carrying a presequence are imported through the translocase of the OM (TOM) complex as well as the translocase of the IM (TIM) complex. Hydrophilic proteins are transported to the matrix with the help of the presequence translocase-associated motor (PAM), whereas proteins with a hydrophobic sorting signal are inserted into the IM [11, 12]. The mitochondrial processing peptidase (MPP) in the matrix subsequently removes the presequence and releases mature proteins [13]. Another pathway for the insertion of proteins into the IM is the carrier protein pathway. Here, proteins enter the mitochondria through the TOM complex and are guided by the help of small TIM chaperones of the IMS to the carrier translocase TIM22, which subsequently inserts the proteins into the IM [14-16]. Proteins of the matrix and IM represent around 80% of all mitochondrial proteins [17-19]. All proteins of the IMS are synthesized in the cytosol and subsequently have to be transported to the mitochondria [20]. Cysteine-rich proteins of the IMS usually carry conserved motifs (twin Cx_3C or Cx_9C) and are imported by TOM and the redox-regulated MIA (mitochondrial IMS import and assembly) pathway. This pathway acts as a folding trap by inserting intramolecular disulfide bonds into the substrates, preventing them from diffusing back to the cytosol [21]. β-barrel proteins of the OM are inserted via the β-barrel pathway through TOM and the sorting and assembly machinery (SAM) by the help of small TIM chaperones in the IMS [22]. The insertion of α-helical proteins into the OM is achieved via the mitochondrial import (MIM) complex [9, 22, 23].

Despite significant compositional differences of the MPI machineries in several eukaryotic groups, the general protein import pathways seem to be conserved among eukaryotes. This was previously shown using the model organism *Leishmania tarentolae* (non-opisthokont) and *S. cerevisiae* (opisthokont). In that study, different marker proteins could be successfully imported into mitochondria of the respective other species [24]. For this work, the compositional differences of the oxidative protein folding pathway of the IMS are of major interest and are therefore described in detail below.

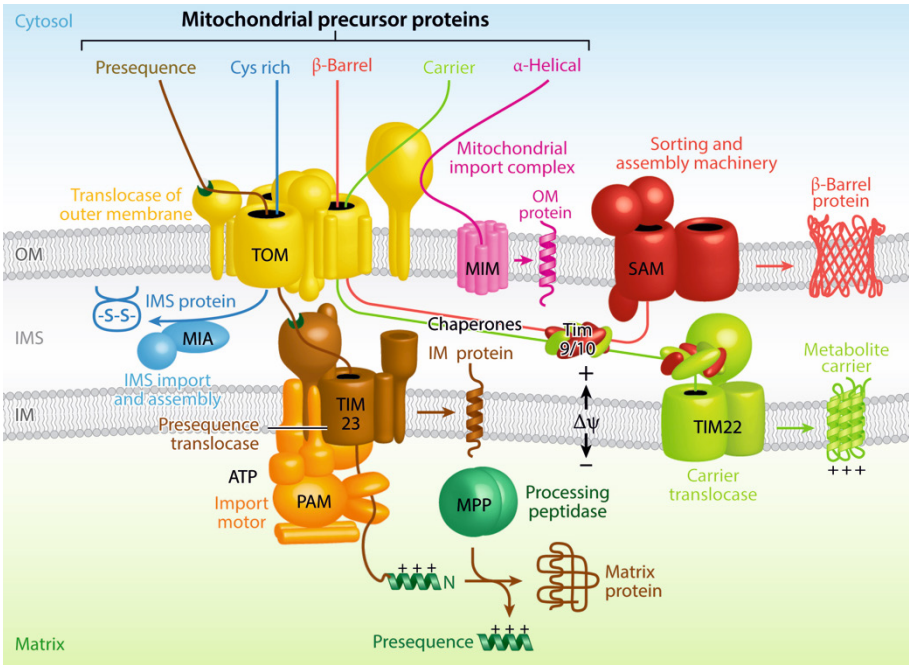

Figure 2 | Overview of the five mitochondrial protein import pathways. Nuclear encoded mitochondrial proteins are transported into the organelle via different import machineries. Precursor proteins carrying a presequence are imported through the TOM- and TIM-complex into the matrix with the help of PAM (hydrophilic proteins) or the IM (proteins with a hydrophobic sorting signal). The MPP subsequently removes the presequences. Proteins of the IMS are mainly cysteine-rich and are imported by TOM and the MIA system, which acts as a folding trap by inserting intramolecular disulfide bonds into the substrates. β-barrel proteins that are inserted into the OM are translocated through TOM and SAM by the help of small TIM chaperones in the IMS. Proteins of the IM are imported via TOM by the help of small TIM chaperones of the IMS and the carrier translocase TIM22. The MIM complex imports α-helical proteins of the OM. TOM: translocase of the outer mitochondrial membrane, TIM: translocase of the inner mitochondrial membrane, PAM: presequence translocase-associated motor, IM: inner mitochondrial membrane, MPP: mitochondrial processing peptidase, IMS: intermembrane space, MIA: mitochondrial IMS import and assembly, OM: outer mitochondrial membrane, SAM: sorting and assembly machinery, MIM: mitochondrial import. The figure was taken from Wiedemann *et al.* 2017 [9].

1.1.3 The Mia40-Erv1 disulfide relay system in opisthokonta

The majority of proteins in the IMS of yeast and other opisthokonts are targeted and trapped by oxidative protein folding by the help of the oxidoreductase Mia40 in cooperation with the flavoprotein Erv1 (essential for respiration and viability; Figure 3 A) [1, 25, 26]. This MPI pathway was first discovered in *S. cerevisiae* independently by several groups in 2004 [21, 27, 28]. Substrates of the oxidative folding pathway enter the IMS in a reduced and unfolded state via the TOM complex. Mia40 exerts two functions. First, it serves as an adapter and recognizes the mainly conserved twin Cx_3C- or Cx_9C-motif of its substrates. Second, it acts as an oxidoreductase and oxidizes the cysteine residues of the unfolded protein, yielding mature proteins that are trapped in the IMS because of the formation of intramolecular disulfide bonds. An intermediate of this import mechanism is a mixed disulfide between Mia40 and the

incoming substrate. Once the substrate is released, Erv1 re-oxidizes Mia40. An intermediate of this reaction is a mixed disulfide between Mia40 and Erv1 [29, 30]. Reduced Erv1 subsequently transfers electrons to the respiratory chain via cytochrome *c* [31]. It was suggested, that Erv1 can also use fumarate and/or molecular oxygen as alternative electron acceptors [32, 33].

1.1.4 Mitochondrial protein import in kinetoplastida and apicomplexa

The pathway for mitochondrial protein import into the IMS via the MIA pathway was analyzed extensively in yeast (Figure 3 A) and was long considered to be highly conserved in eukaryotes. But yeast together with all mammals represent just one out of six or eight supergroups of eukaryotes (Figure 4) [34-36]. *In silico* analyses failed to reveal a Mia40 homolog in kinetoplastida and apicomplexa, which belong to different branches of the evolutionary tree. Hence, the pathway for MPI into the IMS differs among various eukaryotes [24, 25, 37, 38]. However, conserved substrates with distinct cysteine-motifs and Erv homologs can be found in these parasites. The lack of Mia40 suggests the existence of a novel, so far unidentified component in kinetoplastida and apicomplexa that could act as a Mia40 replacement (Figure 3 B and C) [24, 38]. A Mia40 adapter replacement in parasitic protists might be an interesting target for future intervention strategies and drug development because this novel component is parasite-specific and most likely essential.

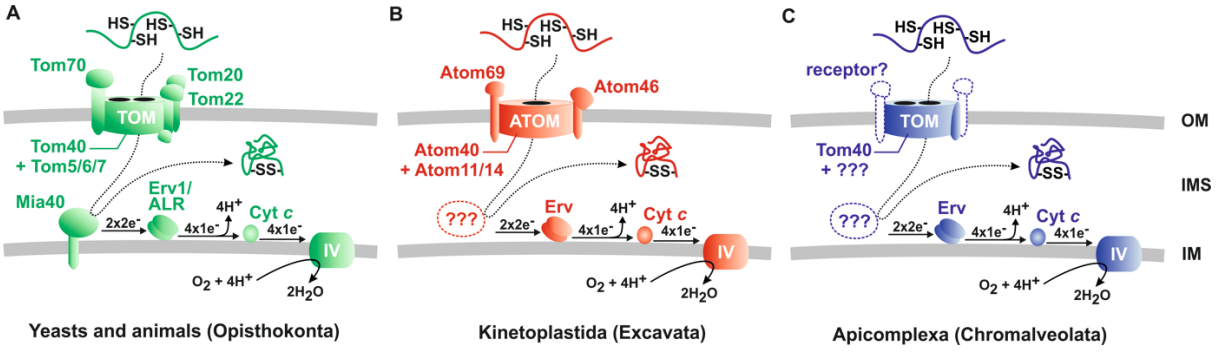

Figure 3 | Comparison of oxidative protein folding in the intermembrane space of mitochondria. Current models of the pathway for oxidative protein folding in the mitochondrial IMS of yeast and other opisthokonta (A), the kinetoplastid parasite *L. tarentolae* (B) and the apicomplexan parasite *P. falciparum* (C) are shown. Absent or unknown components are highlighted with dashed lines or question marks. In kinetoplastida and apicomplexa a Mia40 homolog is missing and a replacement candidate is not known so far. OM: outer mitochondrial membrane; IMS: intermembrane space; IM: inner mitochondrial membrane. Adapted from Eckers *et al.* 2012 [24].

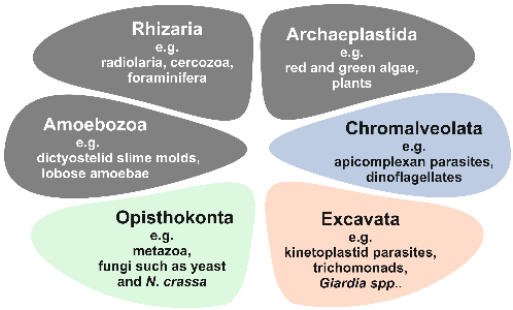

Figure 4 | Opisthokonts represent just one of several eukaryotic supergroups. The parasitic protists *L. tarentolae* (Excavata) and *P. falciparum* (Chromalveolata) belong to different branches of the evolutionary tree. The figure was adapted from Eckers *et al.* 2012 [24] and is based on the publication of Adl *et al.* 2005 [34].

1.2 Parasitic protists

Parasitic protists can be found in different branches of the evolutionary tree (Figure 4), for instance apicomplexan parasites in the branch of Chromalveolata or kinetoplastid parasites in the branch of Excavata. Parasitic protists can cause severe human diseases and are responsible for more than a million deaths per year worldwide [39, 40]. Among these diseases, malaria is the major cause of morbidity and mortality with 0.4-1.1 million deaths per year between 1990 and 2015 [40-42]. The disease is caused by an apicomplexan parasite of the genus *Plasmodium*. Only five species out of around 200 are known to infect humans. *Plasmodium falciparum* is the most virulent species and responsible for most of the severe cases of malaria infections [43, 44]. The parasite is transmitted by infected female *Anopheles* mosquitos and has a complex life cycle alternating between the insect vector and the vertebrate host. Other major human parasitic diseases are caused by kinetoplastida as outlined below.

1.2.1 Kinetoplastida

Kinetoplastida belong to the phylum Euglenazoa and comprise several eukaryotic, unicellular and flagellated parasites. This class is named after the kinetoplast, a unique network of DNA inside the single mitochondrion [45]. The kinetoplast is placed at the flagellar basal body of the organism and represents the structurally most complex mitochondrial DNA, which is organized in interlocked maxi- and minicircles that are 20-40 kb and 0.7-2.5 kb in size, respectively [46]. The kinetoplastida *Trypanosoma brucei*, *T. cruzi* and different *Leishmania* species, which all belong to the order Trypanosomatida, can cause severe human diseases and are one of the oldest eukaryotic groups [47]. *Trypanosoma brucei* is transmitted by the tsetse fly vector, is the causative agent of African Trypanosomiasis (also called sleeping sickness) and caused devastating epidemics in the past century. However, the reported cases have

decreased every year from around 9000 deaths in 2010 [40] to less than 3000 cases in 2015 [48] and the disease is targeted to elimination by the World Health Organization (WHO). Chagas disease is caused by infection with *T. cruzi* and threatens the lives of about 6-7 million people worldwide, mainly in Latin America [49]. The parasite is transmitted by contact with faeces or urine of an infected triatomine bug. The second most deadly parasitic disease after malaria, and the most deadly kinetoplastid disease with estimated 0.7 to 1 million new cases and 20 000 to 30 000 deaths per year, is Leishmaniasis caused by different *Leishmania* species [50, 51]. There are 20 different species of *Leishmania* that cause three different types of leishmaniasis: cutaneous leishmaniasis (CL, see Figure 5 for epidemiological situation), which represents the most common type, muccocutaneous leishmaniasis, which leads to deformation of the mouth, throat or nose and visceral leishmaniasis (VL, also called kala-azar), which represents the most severe type [51]. The most dangerous species for humans are *L. braziliensis*, which cause muccocutaneous leishmaniasis and *L. donovani* together with *L. infantum,* which cause visceral leishmaniasis and lead to death in 95% of the cases when left untreated [51]. The protozoan parasite is transmitted to its mammalian host by the bite of an infected female phlebotomine sandfly. In the vertebrate host, the exflagellated, extracellular promastigotic insect stage develops into intracellular amastigotes [39].

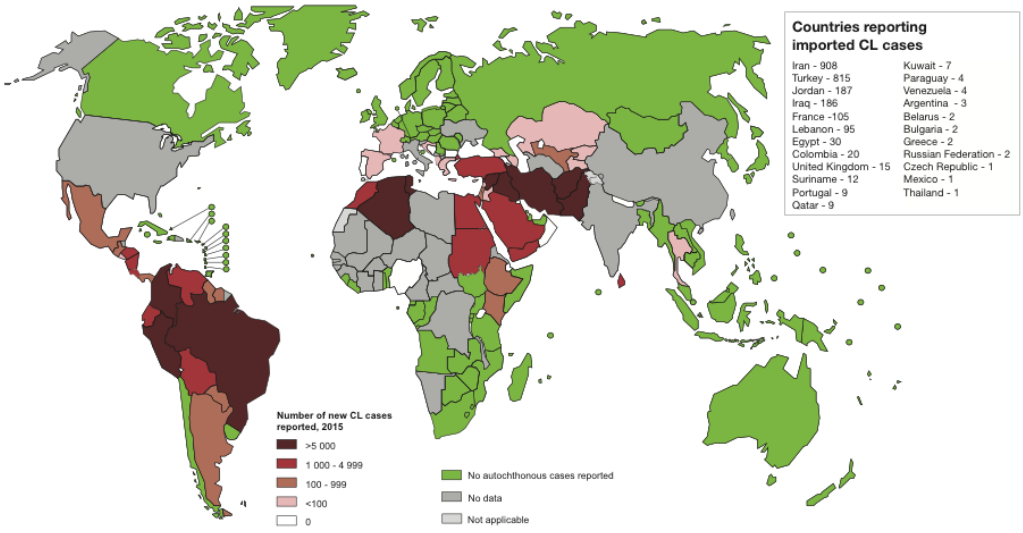

Figure 5 | Epidemiological situation of cutaneous leishmaniasis. The map shows the worldwide epidemiological situation of cutaneous leishmaniasis in 2015. The majority of reported cases occurred in Afghanistan, Algeria, Brazil, Colombia, Iran, Pakistan, Peru, Saudi Arabia and the Syrian Arab Republic. Source: Word Health Organization [51].

1.2.2 *Leishmania tarentolae* as a model organism

Leishmania tarentolae is closely related to the virulent *Leishmania* species described in the previous section. It was isolated from the gecko *Tarentola mauritanica*, is non-infectious for humans and can therefore be handled under S1 security level [52]. Non-infectious parasite species can be useful to gain further insights into the biology of their pathogenic relatives. *Leishmania tarentolae,* for instance, can be used as a model organism for drug development against the infective agents of visceral and cutaneous leishmaniasis [53].

Moreover, the parasite is a commonly used model organism for the investigation of principle mechanisms such as RNA editing [54-57]. As a unicellular eukaryote, it can also help to understand fundamental processes in more complex eukaryotic cells. For instance, it was the first parasitic protist used for the analysis of non-opisthokont mitochondrial protein import into all compartments revealing a functional conservation among eukaryotes [24]. Furthermore, studies on kinetoplastid parasites were crucial for the research field of glycosylphosphatidylinositol (GPI) anchors [58]. The model organism is particularly suited for mitochondrial analyses as it has only one big mitochondrion showing autofluorescence [59]. As a consequence, staining of the mitochondria for microscopy is not necessary. Results obtained from analyses of kinetoplastida could often be transferred to other eukaryotes. Consequently, analyses of the mitochondrial protein import in *L. tarentolae* might be helpful to gain more insights about general mechanisms of the mitochondrial protein import in eukaryotes.

Furthermore, *L. tarentolae* became an important tool for the production of recombinant proteins in recent years. These recombinant proteins are well suited for structural studies owing to their homogenous structure [52]. There are a lot of examples in literature showing that biologically active and natively processed proteins could be produced in *L. tarentolae* [60-64]. High yields of recombinant protein can be obtained because *L. tarentolae* has fast growth rates and reaches high cell densities in culture. Moreover, the parasites grow in comparatively cheap medium without serum [52] and under normal atmosphere [61]. Another advantage of this expression system is that the parasite cells can easily be disrupted compared to yeast cells [60]. In conclusion, sufficient amounts of mitochondria can be generated for analyses of mitochondrial protein import [56] on the basis of previously established protocols from our lab [24].

1.3 Methods for the identification of potential interaction partners

In general, there are two major strategies for the identification of potential interaction partners of a known protein: (i) Screening of protein libraries with the known bait protein (a classical approach of this strategy is the yeast-two hybrid method) or (ii) the *de novo* purification of protein complexes with the known protein and subsequent analyses by mass spectrometry [65]. Stable isotope labeling of amino acids in cell culture (SILAC) leads to a higher specificity of the later strategy. A relatively new method for the identification of unknown interaction partners of a protein of interest is the proximity-dependent biotin identification (BioID) or proximity labeling by ascorbate peroxidase (APEX).

1.3.1 Stable isotope labeling of amino acids in cell culture (SILAC)

SILAC in combination with semi-quantitative mass spectrometry is a popular method for proteome-wide quantification or comparison of tagged and untagged bait protein samples from a pull-down experiment (Figure 6). SILAC was first described in 2002 [66-68] and is based on the metabolic incorporation of essential, isotopically enriched amino acids into the proteome of living cells [69, 70]. One subpopulation of cells, expressing the tagged bait protein, is grown in “light” medium (containing normal isotope abundance amino acids with ^{1}H, ^{12}C, ^{14}N), whereas the control cells are grown in “heavy” medium (containing the heavy isotope amino acids arginine and lysine with ^{2}H, ^{13}C, ^{15}N) for at least five generations to ensure efficient labeling of the proteome [69]. Afterwards, the cells can be combined for further processing to ensure reproducibility of the experimental workflow. The samples are subsequently fractionated, purified by affinity chromatography and analyzed by mass spectrometry. Isotopically labeled proteins can be distinguished from their normal isoforms because of a mass shift. Protein-protein interactions can therefore be identified and quantified with the advantage to discriminate between unspecific binding and actual interaction partners. This method is already established for a wide range of organisms including the protist *L. infantum* [71, 72]. Label-free mass spectrometry is a cheaper alternative for SILAC [73].

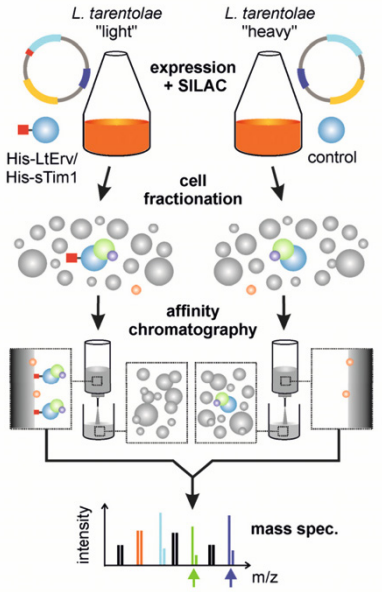

Figure 6 | Workflow of a SILAC experiment. *Leishmania tarentolae* cells containing the tagged bait protein or the respective control without a tag are cultured in "light" medium (containing normal isotope abundance amino acids) or "heavy" medium (containing the heavy isotope amino acids arginine and lysine). After at least five generations, the cells are fractionated and purified by affinity chromatography. Subsequently, the samples are analyzed by mass spectrometry.

1.3.2 Proximity-dependent biotin identification (BioID)

In 2012, Roux *et al.* published a new method called proximity-dependent biotin identification (BioID) for the identification of potential interaction partners of a protein of interest [74]. The approach is based on an optimized prokaryotic biotin ligase from *E. coli* called BirA* that is fused to the protein of interest. The fusion construct is expressed in living cells and was already successfully used in a variety of different cell types including the protistic parasites *T. brucei* [75, 76], *Toxoplasma gondii* [77] and different *Plasmodium* species [78-80]. The method was also successfully used in various subcellular compartments including mitochondria [81-83]. BirA* generates reactive biotinyl-AMP from biotin and ATP. Subsequently the biotinyl-AMP covalently reacts with primary amines [84]. Proteins in the close proximity of the fusion protein in a labeling radius of around 10-15 nm are biotinylated [83, 85, 86] and can subsequently be affinity-purified by streptavidin beads for further analyses (Figure 7). There are several advantages of BioID over classical approaches. First, the biotinylated proteins can be purified under denaturing conditions because of the strong interaction of streptavidin and biotin [85]. Second, also weak and/or transient interactions can be potentially detected that could be missed with classical approaches because the biotinylated interacting proteins accumulate over time [84]. Third, protein interactions in their natural cellular context can be identified with BioID. A disadvantage of this approach is that it does not distinguish actual

interacting proteins from proteins that are only in close proximity of the fusion protein [84]. Furthermore, the labeling is rather slow compared to APEX that might be used as an alternative for BioID [87].

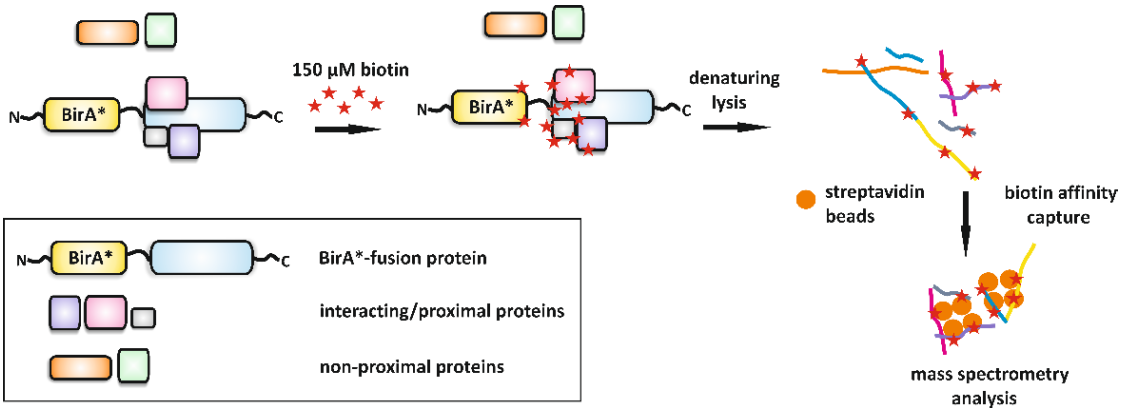

Figure 7 | Proximity-dependent biotin identification (BioID). A fusion construct between the protein of interest and the optimized *E. coli* biotin ligase BirA* is expressed in living cells. After incubation of the cells for 24 h with 150 µM biotin, proteins that are proximate to the BirA*-fusion protein are biotinylated and are subsequently affinity-purified under denaturing conditions by streptavidin beads. The potential interacting proteins can be analyzed by western blotting and mass spectrometry. Adapted from Roux *et al.* 2012 [74].

1.4 Glutaredoxins

1.4.1 Functions of glutaredoxins

Glutaredoxins (Grx) are highly conserved enzymes that play important roles in redox catalysis and iron metabolism and can be found in almost all organisms ranging from prokaryotes to yeast, plants and animals [88-91]. The small redox enzymes catalyze thiol-disulfide exchange reactions with the reduced tripeptide glutathione (GHS; Glu-Cys-Gly) as electron donor with the major function of reducing glutathionylated proteins [91, 92]. Glutaredoxins are part of the glutathione system consisting of NADPH, the flavoenzyme glutathione reductase, glutathione and Grx [92]. Glutaredoxins play a crucial role for DNA synthesis because oxidized ribonucleotide reductase (RR), an enzyme catalyzing the production of deoxyribonucleotides from ribonucleotides [93], is a physiological substrate of Grx [94-97]. Moreover, several studies showed that Grx plays a role in the regulation of apoptosis [98-101]. Altered Grx contents and activities in the cell may also have medical implications as reviewed by Mieyal *et al*. or Lillig *et al.* for diabetes, Parkinson's disease, cancer and many other diseases [102-104].

1.4.2 Structure and classification

Glutaredoxins structurally belong to the superfamily of thioredoxins (Trx), which are defined by a characteristic Trx fold consisting of about 80 residues that are arranged in four β-strands and three flanking α-helices [105]. The Grx-family is highly diverse and isoforms are therefore often classified according to their subcellular localization, enzymatic activity or structural property. Traditionally, the different Grx isoforms are grouped into two subfamilies, the so-called monothiol and dithiol Grx. The classification depends on the motif at the active site: enzymes with a CxxC- and CxxS-motif are assigned as dithiol or monothiol Grx, respectively [106]. The latter ones are usually, except for *Sc*Grx6/7 from yeast, inactive in standard enzymatic *in vitro* assays [107-115]. Due to moderately conserved polar and charged residues around its active site, enzymatically active Grx show a preference for GSH and are reduced non-enzymatically in contrast to Trx, which is reduced enzymatically by a specific reductase [106, 113, 116-118].

1.4.3 Mechanism of catalysis

The traditional model of Grx catalysis is based on analyses of dithiol Grx [119-122] and can be separated into a monothiol and dithiol mechanism (Figure 8). This model illustrates the reduction of disulfide bonds in either glutathionylated substrates (monothiol mechanism) or protein disulfide substrates (dithiol mechanism).

The monothiol mechanism requires only the more N-terminal active site cysteine residue [104] and is used by classical dithiol Grx as well as monothiol Grx. It occurs via a ping-pong mechanism that can be separated into an oxidative and reductive half-reaction [106]. The glutathionylated substrate is reduced by Grx during the oxidative half-reaction, releasing a deglutathionylated product and a disulfide intermediate between Grx and glutathione (Grx-SSG). During the rate-limiting reductive half-reaction, Grx is regenerated by GSH, producing glutathione disulfide (GSSG) and deglutathionylated Grx.

In the dithiol mechanism, protein disulfide substrates are reduced by a disulfide bond exchange reaction that requires both cysteines of the active site motif. A mixed disulfide bond between the substrate and Grx is formed as an intermediate before the C-terminal cysteine residue of the active site motif generates an intramolecular disulfide bond with the N-terminal cysteine residue of the CxxC-motif. Two molecules of GSH recycle Grx in two steps yielding

GSSG [106]. The glutathione disulfide is in both mechanisms subsequently regenerated by glutathione reductase using NADPH as an electron donor [104].

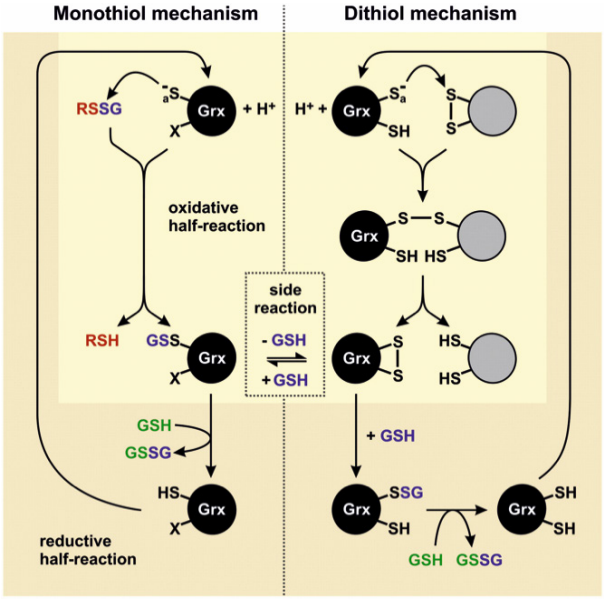

Figure 8 | The traditional monothiol and dithiol mechanism of glutaredoxin catalysis. On the left side, the monothiol mechanism of Grx catalysis for glutathionylated substrates is shown. On the right side, the dithiol mechanism for the reduction of substrates with protein disulfides is shown. For the monothiol mechanism, the second cysteine in the active site is not needed. The figure was taken from Deponte, 2013 [106].

However, the traditional model does not answer the question how exactly the two different substrates of Grx (the glutathionyl moiety of protein-bound RSSG during the oxidative half-reaction and GSH during the reductive half-reaction) are bound. Hence, two refined models of Grx catalysis namely the “glutathione scaffold model” and the “glutathione activator model” were previously proposed based on the reaction geometry of S_N2 reactions. The refined model could help to distinguish protein areas that either interact with the disulfide substrate (a scaffold site) or the reducing agent (an activator site) (Figure 9) [106, 113]. Modifications of the two distinct substrate interaction sites could also help to explain the differences between active and inactive monothiol Grx in standard enzymatic assays. Previous kinetic experiments with the model enzyme *Sc*Grx7 could confirm two different glutathione interaction sites. The glutathione scaffold site includes Glu170 and interacts with the glutathionylated disulfide substrate and the glutathione activator site includes Lys105 and interacts with GSH [116].

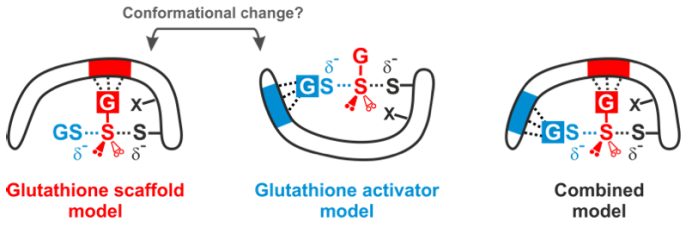

Figure 9 | The two refined models of glutaredoxin catalysis. Those models could help to distinguish protein areas that either interact with the glutathione moieties of GSSR (a scaffold site, marked in red) or the reducing agent GSH (an activator site, marked in blue). The two models are nonexclusive and might also be combined to one mechanistic model. The figure was taken from Begas *et al.* 2017 [116].

1.4.4 Glutaredoxin assays

Different enzymatic assays exist to study the exact structure-function relationships and differences among enzymatically active and inactive Grx that have so far remained elusive. These assays use either physiological substrates such as RR or artificial low molecular weight disulfide substrates. A set of GSH-dependent coupled spectrophotometric assays with bis(2-hydroxyethyl)disulfide (HEDS) as a non-glutathione substrate or L-cysteine-glutathione disulfide (GSSCys) as a glutathionylated substrate were established for *Sc*Grx7 from yeast as a model enzyme in previous studies from our group (Figure 10) [112, 116, 123]. Glutathione disulfide (GSSG) is a product of this reaction and is subsequently recycled by glutathione reductase. The enzyme activity is monitored spectrophotometrically by the consumption of NADPH [123]. The HEDS assay was already established in 1968 by Nagai and Black [124] and since then the assay was used to determine the activity of various Grx isoforms from different organisms such as Grx from *P. falciparum* [125], Grx1 and Grx2 from *T. brucei* [126], the dithiol *Sc*Grx1, *Sc*Grx2 [127, 128] and *Sc*Grx8 [113] from *S. cerevisiae* as well as the unusual monothiols *Sc*Grx6 and *Sc*Grx7 [112].

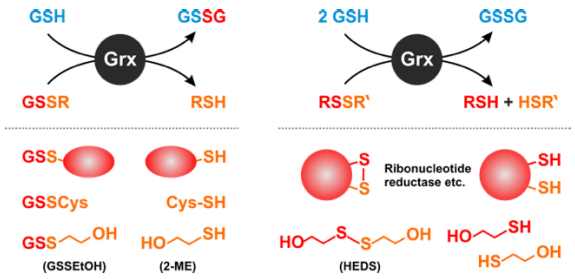

Figure 10 | Substrates of glutaredoxins. Several coupled enzymatic assays exist to measure the activity of Grx. Besides physiological substrates such as ribonucleotide reductase, artificial low molecular weight substrates are often used. On the left side, the reduction of high- and low-molecular weight glutathione disulfide substrates such as GSSCys is shown. On the right side, the reduction of non-glutathione disulfide substrates such as HEDS is displayed. GSH is used as an electron donor for the reduction and glutathione disulfide (GSSG) is produced. The figure was taken from Begas *et al.* 2017 [116].

1.4.5 Glutaredoxins in yeast

Saccharomyces cerevisiae has eight Grx, from which five belong to the group of monothiol Grx (*Sc*Grx3-7) and three are dithiol Grx (*Sc*Grx1/2/8) [104, 112, 113, 129]. The different Grx vary in their active site and subcellular localization (Figure 11). The two dithiol *Sc*Grx1 and *Sc*Grx2 share a typical CPYC-motif in their active site and a high identity of 64% with respect to their amino acid residues [127]. *Sc*Grx8 was discovered much later and has an unusual CPDC-motif in its active site [113]. All three dithiol Grx from yeast were shown to be active in the classical HEDS assay, although *Sc*Grx8 has very little activity [113, 130]. *Sc*Grx2 is dually targeted to the cytosol and mitochondria, in contrast to *Sc*Grx1 and *Sc*Grx8 that do not contain a targeting signal [113, 131]. The two monothiol enzymes *Sc*Grx3 and *Sc*Grx4 are both dually localized to the cytosol and nucleus and play an important role in iron trafficking and iron sensing [132]. The monothiol *Sc*Grx5 possesses a mitochondrial targeting sequence and is therefore localized in the mitochondrial matrix. It was the first Grx-isoform shown to play a role in iron metabolism [133] and is important for the protection against oxidative damage [134]. The two monothiol isoforms *Sc*Grx6 and *Sc*Grx7 are remarkable due to their subcellular localization and their activity in the HEDS assay. They were the first Grx that were found in the secretory pathway of eukaryotes and are anchored in the Golgi with a suggested role in redox homeostasis [114, 115]. Furthermore, they were the first and only monothiol Grx that were shown to be active in the HEDS assay [112, 135]. *Sc*Grx7 is an excellent model enzyme owing to its high activity in kinetic assay. Moreover, the reaction is neither further complicated by an additional cysteine in the active site nor by iron-sulfur cluster binding [123]. Not much is known about the physiological substrates and the exact catalytic mechanisms of the different Grx in yeast, which is surprising since Grx were already described four decades ago [94].

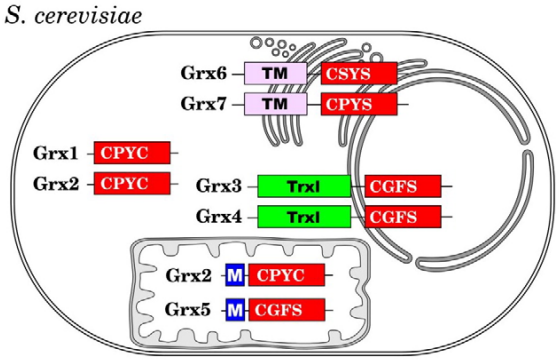

Figure 11 | Intracellular distribution of the glutaredoxins in yeast. The intracellular distribution of the two dithiol Grx (*Sc*Grx1/2) and the five monothiol Grx (*Sc*Grx3-7) is shown. The active site is marked in red. Please note, that dithiol *Sc*Grx8 is not shown in this overview. TM: transmembrane domain, M: mitochondrial signal peptide, Trxl: thioredoxin-like domain. The figure was taken from Lillig *et al.* 2008 [104].

1.4.6 Glutaredoxins in *Plasmodium falciparum*

Plasmodium falciparum only possesses one known classical dithiol Grx that is located in the cytosol [125, 136, 137]. *Pf*Grx has three cysteines in total, of which two are in a classical CPYC-motif (residue 29 and 32) and one additional cysteine is in a GGC-motif at positon 88 [123, 138]. The fully functional monothiol mutant *Pf*Grx$^{C32S/C88S}$, that was recently established in our lab, does not have complicated side reactions and allows a direct comparison with other monothiol glutaredoxins [138]. The crystal structure of *Pf*Grx was resolved in 2014 revealing structural conservation of the glutathione-binding motifs with other Grx [139]. A proteomic approach identifying 17 hypothetically interacting partners of *Pf*Grx could show that the functions of *Pf*Trx and *Pf*Grx seem to partially overlap [140]. The identified candidate target proteins point to a function of *Pf*Grx in different processes such as anti-oxidative defense, transcription/translation, protein folding and signal transduction [140]. In addition to the classical dithiol Grx, *P. falciparum* has three monocysteinic Grx-like proteins (*Pf*Glp1-3) of unknown physiological function with the second cysteine replaced by a serine in the active site [108, 136]. Due to solubility reasons it was not yet possible to investigate the mitochondrial *Pf*Glp3 with a CKYS-motif in the active site [108, 137]. The two other cytosolically located Grx-like proteins of *P. falciparum* were not active in a classical Grx assay, which is in accordance with typical monothiol Grx [108, 137].

1.5 Aim of this work

The main objective of this PhD was the identification of a Mia40 adapter replacement in the non-pathogenic parasite *L. tarentolae*, which is a close relative to human pathogenic kinetoplastida. As the mitochondrial protein import into the IMS is redox-regulated, different approaches were tested for potential trapping of mixed disulfide intermediates. For this purpose, *L. tarentolae* small Tim1 (*Lt*sTim1) could serve as a reference substrate with a twin Cx_3C-motif that should interact with the oxidized Mia40 adapter replacement. The reduced adapter should subsequently interact with *Lt*Erv. Methods such as chemical trapping for stabilization of the mixed disulfide intermediates, SILAC or BioID could be helpful to identify the so far unknown protein in the oxidative folding pathway of the IMS. The already published genome sequence of *L. tarentolae* will be helpful for a potential SILAC experiment followed by mass spectrometry [141].

The second objective of this PhD was to analyze the general applicability of the results obtained from prior analysis of *Sc*Grx7, which revealed a distinct glutathione scaffold and activator site during the MD thesis of Patricia Begas. Thus, *Pf*Grx should be analyzed as a non-related model system. Additional residues of *Sc*Grx7 that were previously suggested to be part of the glutathione activator site should be analyzed to gain more insights into the exact structure-function relationships of Grx and to define the substrate interaction sites in more detail.

2 Materials and Methods

2.1 Materials and equipment

2.1.1 Technical equipment

Table 1 | List of technical equipment.

Technical equipment	Description and Manufacturer
Autoclave	VX-95; Systec GmbH
Balance	TE124S-OCE; Sartorius
	Kern EW; Kern & Sohn GmbH
Blotting device (semi-dry)	PerfectBlue SEDEC M; Peqlab
Centrifuges	5417R; Eppendorf
	J-6B, J2-21M/E with JA-10/17 rotor; Beckman Coulter GmbH
Counting chamber	Neubauer counting chamber improved; Carl Roth GmbH
Developing machine	Curix 60; AGFA
DNA electrophoresis apparatus	Bio-Rad
Electroporator for *L. tarentolae*	Nucleofector™ 2b Device; Lonza
Gel chambers for SDS-PAGE	Mini-PROTEAN™ Tetra Cell; BioRad
Gel documentation device	E.A.S.Y 440 K, UV transilluminator (UVT-28L); Herolab
Heating block	MBT 250; Kleinfeld Labortechnik
	Thermomixer comfort; Eppendorf
Incubator for *E. coli*	Heraeus; Thermo Fisher Scientific
Incubator for *L. tarentolae*	Memmert
Magnetic stirrer	MR Hei-Standard; Heidolph Instruments
Microscope	AE30; Motic
	Zeiss LSM780
Microwave	AEG
Peristaltic pump	Pump P-1; GE Healthcare
pH electrode	pH electrode PY-P10; Sartorius
pH-meter	Basic Meter PB-11; Sartorius
Pipettes	PIPETMAN™; Gilson
Pipetus	Accu-jet™ pro; Brand
Portable photometer	Ultrospec 10; Amersham Biosciences
Power supply	PowerPac™ Basic; Bio-Rad
	EPS 601; Amersham Biosciences
Red-light lamp	Electric Petra
Rotating wheel	Grant-bio PTR30
Shaking device for *L. tarentolae*	Rotamax 120; Heidolph Instruments
Shaking device for western blotting	Duomax 1030; Heidolph Instruments
Shaking incubator for *E. coli*	Innova 4000 shaker; Infors AG
Spectrophotometer	NanoDrop™; Thermo Fisher Scientific
Sterile hood for *E. coli*	Gelaire™ BSB 3A
Sterile hood for *L. tarentolae*	SAFE 2020; Thermo Fisher Scientific
Thermocycler	Mastercycler gradient; Eppendorf

Ultrasonic device	Sonoplus HD 2070; BANDELIN electronic
UV/Vis spectrophotometer	V-650 spectrophotometer; JASCO
Vortex-mixer	Heidolph Instruments
Water bath	F12-ED; JULABO

2.1.2 Disposables

Table 2 | List of disposables.

Disposable	Supplier
0.2 µm sterile filters	Merck KGaA
125 ml Erlenmeyer flasks	Corning
1.5 and 2 ml reaction tubes	Sarstedt AG & Co
15 and 50 ml reaction tubes	Sarstedt AG & Co
Cell culture flasks (25 cm^2 T-flasks)	Corning
Cryotubes	Greiner Bio-One
Cuvettes (single-use)	Sarstedt AG & Co
Microscope slides	Buddeberg
Needles	BD Microlance 3 needle, 0.4 x 19 mm
Nitrocellulose membrane	GE Healthcare
Parafilm	Sigma-Aldrich
PCR reaction tubes	Kisker Biotech
Petri dishes	Sarstedt AG & Co
Pipette tips	Steinbrenner
Poly-Prep chromatography columns	Bio-Rad
Quartz cuvettes 104B-OS	Hellma
Scalpel	B. Braun Melsungen AG
Serological pipettes	Sarstedt AG & Co
Super RX western blot films	Fuji
Syringes	BD
Whatman™ paper	GE Healthcare

2.1.3 Chemicals

Table 3 | List of chemicals.

Chemical	Supplier
Acetic acid	Merck KGaA
Acetone	Honeywell
Acrylamide/bisacrylamide solution 37.5:1	Serva Electrophoresis GmbH
Agar	Sigma-Aldrich
Agarose	Serva
AlbuMax™ II Lipid-Rich BSA	Thermo Fisher Scientific
Amersham™ ECL™ Western Blotting Reagent	GE Healthcare
Ammonium persulfate (APS)	Sigma-Aldrich
Ampicillin	AppliChem GmbH
Atto 594-Streptavidin	Sigma-Aldrich

Biotin	Sigma-Aldrich
β-mercaptoethanol	Sigma-Aldrich
Bradford reagent	Bio-Rad Laboratories GmbH
BSA	Serva Electrophoresis GmbH
Bromophenol blue	Waldeck GmbH & Co. KG
Calcium chloride	Merck KGaA
cOmplete™ EDTA-free protease-inhibitor cocktail	Roche
Coomassie Brilliant Blue G-250	AppliChem GmbH
D-glucose monohydrate	Merck KGaA
Diamide	Sigma-Aldrich
Digitonin	AppliChem
DMSO	Sigma-Aldrich
DNA ladder (100 bp, 1 kb)	New England Biolabs
dNTPs	Thermo Scientific
DTT	Sigma-Aldrich
EDTA	Sigma-Aldrich
Ethanol	Zentralbereich Neuenheimer Feld
Ethanol absolute	VWR Chemicals
FCS, dialyzed	Silantes
FCS, heat-inactivated	Life Technologies GmbH
Folic acid	Sigma-Aldrich
G418-disulfate solution	AppliChem GmbH
Gel loading dye, Purple 6×	New England Biolabs
Glycerol	AppliChem GmbH
Glycine	Merck KGaA
GSH	Sigma-Aldrich
GSSCys	Toronto Research Chemicals
GSSG	Sigma-Aldrich
Hydrochloric acid	VWR
HEDS	Alfa Aesar
Hemin chloride	Calbiochem
HEPES	Merck KGaA
Imidazole	AppliChem GmbH
Iodoacetamide	Sigma-Aldrich
IPTG	Serva
Luria Bertani (LB) medium	Carl Roth GmbH + Co. KG
Luria Bertani (LB) agar	Carl Roth GmbH + Co. KG
Manganese(II) chloride	Merck KGaA
Methanol	Honeywell Research Chemicals
Midori Green Advance	Nippon Genetics
Milk powder	Carl Roth GmbH + Co. KG
MMTS	Thermo Fisher Scientific
MOPS	GERBU Biotechnik GmbH
NADPH	GERBU Biotechnik GmbH
NEM (N-ethylmaleimide)	Sigma-Aldrich
Ni-NTA agarose	Qiagen
Paraformaldehyde	Sigma-Aldrich
PonceauS	Serva Electrophoresis GmbH
Potassium acetate	Sigma-Aldrich
Potassium chloride	AppliChem GmbH

Potassium dihydrogenphosphate	Merck KGaA
Prestained protein ladder	Thermo Scientific
2-propanol	Sigma-Aldrich
Protease inhibitor cocktail tablets cOmplete, EDTA-free	Roche
Rubidium chloride	AppliChem GmbH
Saponin	Sigma-Aldrich
Sodium acetate	Sigma-Aldrich
Sodium borohydride	AppliChem GmbH
Sodium chloride	Sigma-Aldrich
Sodium dihydrogen phosphate	Merck KGaA
Sodium dodecyl sulfate	Serva Electrophoresis GmbH
Sodium hydroxide	Sigma-Aldrich
Sodium phosphate dibasic	Merck KGaA
Streptavidin-HRP	Abcam
Sucrose (D-sucrose)	AppliChem
TEMED	Serva Electrophoresis GmbH
Trichloroacetic acid	Merck KGaA
Tri-sodium citrate dihydrate	Merck KGaA
Tris	Carl Roth GmbH + Co. KG
Triton™ X-100	Merck KGaA
Tween™ 20	Sigma-Aldrich
Unstained protein ladder	Thermo Scientific
Urea	Serva Electrophoresis GmbH

2.1.4 Enzymes

Table 4 | List of enzymes.

Enzyme	Supplier
DNaseI	Sigma-Aldrich
Lysozyme	Serva Electrophoresis GmbH
Pfu Polymerase	Promega
Restriction enzymes	New England Biolabs
RNAse A	Sigma-Aldrich
*Sc*GR	Sigma-Aldrich
T4-ligase	Fermentas

2.1.5 Cell culture media

Table 5 | List of cell culture media.

Cell culture medium	Supplier
BHI	BD
DMEM (#42430025)	Thermo Fisher Scientific
DMEM/F-12 (#11330032)	Thermo Fisher Scientific
IMDM (#12440053)	Thermo Fisher Scientific
McCoy's 5A (#26600023)	Thermo Fisher Scientific

MEM (#31095029)	Thermo Fisher Scientific
RPMI-1640 (#52400-041)	Thermo Fisher Scientific

2.1.6 Kits

Table 6 | List of kits.

Kit	Supplier
Basic Parasite Nucleofector™ Kit 2	Lonza
Qiagen Plasmid Midi Kit	Qiagen
Qiaprep™ Spin Miniprep Kit	Qiagen
Wizard™ SV Gel and PCR Clean-Up System	Promega

2.1.7 Plasmids and constructs

Table 7 | List of plasmids/constructs.

Plasmid	Details	Reference
pQE30	Amp^R, N-terminal MRGSH_6GS-tag, T5-Promoter	Qiagen
pQE30 *SCGR*	*SC*GR (*Bam*HI/*Hin*dIII), N-terminal His_6-tag	Urscher *et al.* 2012 [142]
pQE30 *SCGRX7*	*SCGRX*7 (*Bam*HI/*Sal*I) starting from amino acid V34, N-terminal His_6-tag	Mesecke *et al.* 2008 [112]
pQE30 *SCGRX7*^{K105A}	*SC*GRX7 (*Bam*HI/*Sal*I) starting from amino acid V34, N-terminal His_6-tag, point mutation K105A	Begas *et al.* 2017 [116]
pQE30 *SCGRX7*^{K105E}	*SC*GRX7 (*Bam*HI/*Sal*I) starting from amino acid V34, N-terminal His_6-tag, point mutation K105E	Begas *et al.* 2017 [116]
pQE30 *SCGRX7*^{Y110A}	*SC*GRX7 (*Bam*HI/*Sal*I) starting from amino acid V34, N-terminal His_6-tag, point mutation Y110A	this work
pQE30 *SCGRX7*^{Y110F}	*SC*GRX7 (*Bam*HI/*Sal*I) starting from amino acid V34, N-terminal His_6-tag, point mutation Y110F	this work
pQE30 *SCGRX7*^{Y110H}	*SC*GRX7 (*Bam*HI/*Sal*I) starting from amino acid V34, N-terminal His_6-tag, point mutation Y110H	this work
pQE30 *SCGRX7*^{D144A}	*SC*GRX7 (*Bam*HI/*Sal*I) starting from amino acid V34, N-terminal His_6-tag, point mutation D144A	this work
pQE30 *SCGRX7*^{D144K}	*SC*GRX7 (*Bam*HI/*Sal*I) starting from amino acid V34, N-terminal His_6-tag, point mutation D144K	this work
pQE30 *SCGRX7*^{E147A}	*SC*GRX7 (*Bam*HI/*Sal*I) starting from amino acid V34, N-terminal His_6-tag, point mutation E147A	this work
pQE30 *SCGRX7*^{E147K}	*SC*GRX7 (*Bam*HI/*Sal*I) starting from amino acid V34, N-terminal His_6-tag, point mutation E147K	this work
pQE30 *SCGRX7*^{R153A}	*SC*GRX7 (*Bam*HI/*Sal*I) starting from amino acid V34, N-terminal His_6-tag, point mutation R153A	this work
pQE30 *SCGRX7*^{R153E}	*SC*GRX7 (*Bam*HI/*Sal*I) starting from amino acid V34, N-terminal His_6-tag, point mutation R153E	this work
pQE30 *SCGRX7*^{E170A}	*SC*GRX7 (*Bam*HI/*Sal*I) starting from amino acid V34, N-terminal His_6-tag, point mutation E170A	Begas *et al.* 2017 [116]

pQE30 *PFGRX*$^{C32S/C88S}$	*PFGRX* (*Bam*HI/*Hin*dIII), N-terminal His_6-tag, point mutation C32S and C88S	Djuika *et al.* 2013 [138]
pQE30 *PFGRX*$^{C32S/C88S/K26A}$	*PFGRX* (*Bam*HI/*Hin*dIII), N-terminal His_6-tag, point mutation C32S, C88S and K26A	this work [116]
pQE30 *PFGRX*$^{C32S/C88S/D90A}$	*PFGRX* (*Bam*HI/*Hin*dIII), N-terminal His_6-tag, point mutation C32S, C88S and D90A	this work [116]
pX	Amp^R, Neo^R, C-terminal TAP-tag	LeBowitz *et al.* 1990 [143]
pX-backbone	removal of TAP-tag (CBP, TEV-site, ProtA) and Flag-tag, introduction of N-terminal His_8-tag and MCS	this work
pX *LTERV*	*LTERV* (*Bam*HI/*Hin*dIII) in pX-backbone	this work
pX His_8-*LTERV*	*LTERV* (*Xba*I/*Hin*dIII) in pX-backbone, N-terminal His_8-tag	this work
pX *LTERV*^{C63S}	*LTERV* (*Bam*HI/*Hin*dIII) in pX-backbone, point mutation C63S	this work
pX His_8-*LTERV*^{C63S}	*LTERV* (*Xba*I/*Hin*dIII) in pX-backbone, N-terminal His_8-tag, point mutation C63S	this work
pX *LTsTIM1*	*LTsTIM1* (*Bam*HI/*Hin*dIII) in pX-backbone	this work
pX His_8-*LTsTIM1*	*LTsTIM1* (*Xba*I/*Hin*dIII) in pX-backbone, N-terminal His_8-tag	this work
pX *LTsTIM1*$^{C1-3S}$	*LTsTIM1* (*Bam*HI/*Hin*dIII) in pX-backbone, point mutations C36S, C40S and C58S	this work
pX His_8-*LTsTIM1*$^{C1-3S}$	*LTsTIM1* (*Xba*I/*Hin*dIII) in pX-backbone, N-terminal His_8-tag, point mutations C36S, C40S and C58S	this work
pX *LTsTIM1*$^{C2-4S}$	*LTsTIM1* (*Bam*HI/*Hin*dIII) in pX-backbone, point mutations C40S, C58S and C62S	this work
pX His_8-*LTsTIM1*$^{C2-4S}$	*LTsTIM1* (*Xba*I/*Hin*dIII) in pX-backbone, N-terminal His_8-tag, point mutations C40S, C58S and C62S	this work
pX *PFERV*	*PFERV* (*Bam*HI/*Hin*dIII)	this work
pX His_8-*PFERV*	*PFERV* (*Xba*I/*Hin*dIII), N-terminal His_8-tag	this work

2.1.8 Oligonucleotides (primers)

Table 8 | List of primers. Name and sequence of the primers used for side-directed mutagenesis, cloning and sequencing are listed. The mutation introduced by the mutagenesis-primers is highlighted. All primers were purchased from Metabion or were selected from the GATC repertoire for sequencing.

Mutagenesis primer	Sequence
*SCGRX*7/Y110A/s	5'-GCAAGACTGGCTGCCCA*GCT*AGCAAAAAACTGAAAGC-3'
*SCGRX*7/Y110A/as	5'-GCTTTCAGTTTTTTGCT*AGC*TGGGCAGCCAGTCTTGC-3'
*SCGRX*7/Y110F/s	5'-GCAAGACTGGCTGCCCA*TTT*AGCAAAAAACTGAAAGC-3'
*SCGRX*7/Y110F/as	5'-GCTTTCAGTTTTTTGCT*AAA*TGGGCAGCCAGTCTTGC-3'
*SCGRX*7/Y110H/s	5'-GCAAGACTGGCTGCCCA*CAT*AGCAAAAAACTGAAAGC-3'
*SCGRX*7/Y110H/as	5'-GCTTTCAGTTTTTTGCT*ATG*TGGGCAGCCAGTCTTGC-3'
*SCGRX*7/D144A/s	5'-CACACAAAAGAACTACAA*GCC*CAGATTGAAAAAGTCACTGG-3'
*SCGRX*7/D144A/as	5'-CCAGTGACTTTTTCAATCTG*GGC*TTGTAGTTCTTTTGTGTG-3'
*SCGRX*7/D144K/s	5'-CACACAAAAGAACTACAA*AAA*CAGATTGAAAAAGTCACTGG-3'
*SCGRX*7/D144K/as	5'-CCAGTGACTTTTTCAATCTG*TTT*TTGTAGTTCTTTTGTGTG-3'
*SCGRX*7/E147A/s	5'-GAACTACAAGACCAGATT*GCA*AAAGTCACTGGTAGGAGAAC-3'
*SCGRX*7/E147A/as	5'-GTTCTCCTACCAGTGACTTT*TGC*AATCTGGTCTTGTAGTTC-3'

*SCGRX*7/E147K/s	5’-GAACTACAAGACCAGATT*AAA*AAAGTCACTGGTAGGAGAAC-3’
*SCGRX*7/E147K/as	5’-GTTCTCCTACCAGTGACTTT*TTT*AATCTGGTCTTGTAGTTC-3’
*SCGRX*7/R153A/s	5’-GAAAAAGTCACTGGTAGG*GCA*ACAGTCCCAAACGTTATCATC-3’
*SCGRX*7/R153A/as	5’-GATGATAACGTTTGGGACTGT*TGC*CCTACCAGTGACTTTTTC-3’
*SCGRX*7/R153E/s	5’-GAAAAAGTCACTGGTAGG*GAA*ACAGTCCCAAACGTTATCATC-3’
*SCGRX*7/R153E/as	5’-GATGATAACGTTTGGGACTGT*TTC*CCTACCAGTGACTTTTTC-3’
PFGRX/32S/88S/K26A/s	5’-GAACATCATTGCTGTATTTGCA*GCA*ACGGAATGCCCATATAG-3’
PFGRX/32S/88S/K26A/as	5’-CTATATGGGCATTCCGT*TGC*TGCAAATACAGCAATGATGTTC-3’
PFGRX/32S/88S/D90A/s	5’-CGTTGTCGGCGGAAGTGAT*GCT*TTAGTTAAAGAAAATGATG-3’
PFGRX/32S/88S/D90A/as	5’-CATCATTTTCTTTAACTAA*AGC*ATCACTTCCGCCGACAACG-3’
Cloning primer	**Sequence**
p/*LTERV*/BamHI/s	5’-GATCGGATCATGTCGGACGACGACGTACACG-3’
p/*LTERV*/SpeI/as	5’-GATCACTAGTGAGCTTGAGTTCTTCGTCCTCTG-3’
p/pX/backbone/s	5’-GATCCATGCATCATCACCATCATCACCATCACTCTAGAAAGCTTGC-3’
p/pX/backbone/as	5’-GGCCGCAAGCTTTCTAGAGTGATGGTGATGATGGTGATGATGCATG-3’
p/pX/BirA/XmaI/s	5’-GATCCCCGGGATGGAACAAAAACTCATCTCAGAAGAG-3’
p/pX/BirA/BamHI/as	5’-GATCGGATCCGCGGTTTAAGCTTAAGCTTGG-3’
p/pX/*PFERV*/BamH1/s	5’-GATCGGATCCATGATATTTATTGAAAAGTGCTATGAAC-3’
p/pX/*PFERV*/HindIII/as	5’-GATCAAGCTTTTAATCAACTGTTTTGTACTTGTCAATT-3’
p/pX/*PFERV*/XbaI/s	5’-GATCTCTAGAATATTTATTGAAAAGTGCTATGAAC-3’
Sequencing primer	**Sequence**
pQE/s	5’-CGGATAACAATTTCACACAG-3’
pQE/as	5’-GTTCTGAGGTCATTACTGG-3’
p/pX/LS/s	5’-CACCCTCAACCACCCCTCA-3’
p/pX/far/as	5’-CACCCCAGGCTTTACACTT-3’

2.1.9 Antibodies

Table 9 | List of antibodies. Name and origin of the antibodies used for western blot analyses and immunofluorescence microscopy are listed. All antibodies used for western blot analyses were diluted in 5% milk in TBS as indicated.

Primary antibody	**Dilution**	**Origin**
Mouse αEF1α	1:10000	Merck Millipore
Mouse αMyc	1:1000	abcam
Rabbit α*Lt*Erv	1:500	Eckers *et al.* 2012 [24]
Rabbit α*Lt*sTim1	1:500	Eckers *et al.* 2012 [24]
Rabbit α*Pf*Erv	1:200	Eckers *et al.* 2013 [38]
Secondary antibody		
Goat αMouse IgG (H+L)-HRP conjugate	1:5000 – 1:10000	BioRad
Goat αMouse Alexa Fluor 488	1:500	Invitrogen
Goat αRabbit IgG (H+L)-HRP conjugate	1:5000 – 1:10000	BioRad

2.1.10 Software and Databases

Table 10 | List of software, databases and online tools.

Software	Copyright, Webpage
BioEdit 7.2.5	Tom Hall
Clustal Omega	www.ebi.ac.uk/Tools/msa/clustalo/
Corel Draw X7	Corel Corporation
EndNote X6	Thomson Reuters
Excel 2010	Microsoft
JustBio	www.justbio.com
Power Point	Microsoft
SigmaPlot 12.5 and SigmaPlot 13	Systat Software Inc.
Spectra Manager	JASCO
TriTrypDB	www.tritrypdb.org
Word 2010	Microsoft
ZEN2010	Zeiss

2.2 Molecular biological methods

2.2.1 Generation of chemically competent *E. coli* XL1-Blue cells

Chemically competent *E. coli* XL1-Blue cells were used for the production of recombinant proteins and for cloning of plasmids. All buffers were sterilized using a 0.2 µm filter before use and aliquots were stored at - 20°C. A 50 µl aliquot of an old batch of competent XL1-Blue cells was transferred to a 4 ml pre-culture. This culture was inoculated in 500 ml LB medium in two 1 l flasks the next morning. The cultures were incubated overnight at 20°C and 160 rpm in the Innova 4000 shaker. Aliquots of 150 ml TFB1 and 10 ml TFB2 were thawed and transferred to an ice-water bath before use. After reaching an OD_{600nm} of 0.5, the cells were pre-cooled in an ice-water bath for 10 min and centrifuged at 2600 × *g* for 15 min at 4°C. Afterwards, the supernatant was discarded and the pellet was resuspended in 75 ml ice-cold TFB1 buffer per 250 ml culture. The suspensions were incubated for 15 min in the ice-water bath and centrifuged at 2600 × *g* for 15 min at 4°C. After discarding the supernatant, the cells were resuspended in 5 ml ice-cold TFB2 buffer per 250 ml starting culture. Aliquots containing 100 µl each were frozen in liquid nitrogen and subsequently transferred to -80°C.

Transformation buffer TFB 1

30 mM potassium acetate
10 mM $CaCl_2$
50 mM $MnCl_2$
100 mM RbCl
15% glycerol
pH 5.8 at RT (adjusted with acetic acid)

Transformation buffer TFB 2	10 mM MOPS 75 mM $CaCl_2$ 10 mM RbCl 15% glycerol pH 6.5 at RT (adjusted with 1 M KOH)

2.2.2 Transformation of chemically competent *E. coli* cells

For all transformations done in this work, self-made chemically competent *E. coli* XL1-Blue cells (section 2.2.1) were used. An aliquot of these cells was thawed on ice prior to the addition of 0.5-10 µl plasmid DNA. The suspension was incubated on ice for 30 min after mixing the tube 1-3 times by flicking. A heat shock was performed in a 42°C heating block for exactly 90 s without shaking the cells. Afterwards, the cells were cooled on ice for 5 min before ten volumes of pre-warmed LB medium were added. After shaking the cells at 500 rpm in the thermomixer comfort (Eppendorf) for up to 1 h at 37°C, 20-200 µl of the cell suspension were spread on agar plates containing 100 µg/ml ampicillin. The plates were incubated overnight at 37°C, afterwards sealed with parafilm and stored at 4°C for up to one week.

2.2.3 Isolation of plasmid DNA from *E. coli* – Miniprep

The following protocol is based on the publication of Birnboim and Doly [144]. A colony of transformed *E. coli* cells from a fresh LB agar plate was inoculated in 3 ml LB medium and incubated overnight at 37°C with 130 rpm in the Innova 4000 shaker (Infors AG). The next day, 1-2 ml of the culture were transferred to a 2 ml reaction tube and centrifuged at 13000 × *g* for 30 s at 4°C. The supernatant was discarded and the pellet was completely dried by tapping the inverted tube onto a paper towel. The following steps of the protocol were performed on ice. The bacterial pellet was resuspended in 100 µl ice-cold buffer P1 by using a plastic rack as a ratchet. Afterwards 200 µl of lysis buffer P2 were added to the suspension and the alkaline cell lysis was performed by inverting the tube five times without shearing the genomic DNA. The pH was neutralized and the genomic DNA was precipitated by the addition of 150 µl ice-cold buffer P3. The suspension was centrifuged again at 13000 × *g* for 10 min at 4°C. The clear supernatant was transferred to a fresh reaction tube and the plasmid DNA was precipitated by adding 600 µl of isopropanol at RT. The suspension was centrifuged at 13000 × *g* for 5 min at 4°C. The supernatant was completely removed by aspiration. The DNA was subsequently washed by adding 600 µl ice-cold 70% ethanol stored at -20°C. The sample was centrifuged at 13000 × *g* for 5 min at 4°C and the supernatant was completely removed by aspiration. The DNA pellet was dried under a red-light lamp and subsequently resuspended in 30 µl sterile

ddH_2O. Alternatively, the QIAprep™ Spin Miniprep Kit from Qiagen was used when higher purities were needed.

Miniprep buffer P1	50 mM Tris 10 mM EDTA 0.1 mg/ml RNAse A pH 8.0 (adjusted before the addition of RNAse A) stored at 4°C
Miniprep buffer P2	0.2 M NaOH 1% (w/v) SDS stored at RT
Miniprep buffer P3	60 ml 3 M potassium acetate 11.5 ml glacial acid 28.5 ml ddH_2O stored at 4°C

2.2.4 Isolation of plasmid DNA from *E. coli* – Midiprep

Plasmid preparations were done with the Qiagen Plasmid Midi Kit when higher DNA yields and purities were needed for transfection of *L. tarentolae*. The preparation was performed according to the manufacturer's protocol.

2.2.5 Polymerase chain reaction

Polymerase chain reactions (PCR) were performed for the amplification of DNA or for the introduction of point mutations via side-directed mutagenesis. The pipetting scheme for a standard cloning PCR is shown in Table 11. The reaction was prepared in a total volume of 50 µl. *Pfu* polymerase was used for DNA-fragments bigger than 500 bp taking advantage of the proofreading-activity of this polymerase to prevent mutations.

Table 11 | Pipetting scheme for a standard cloning PCR.

Component	Volume
ddH_2O	40.5 µl
Pfu buffer containing $MgSO_4$	5 µl
Template DNA	0.5 µl (minipreps 1:100 diluted)
Sense primer	0.5 µl (after 1:10 dilution of a 100 µM stock)
Antisense primer	0.5 µl (after 1:10 dilution of a 100 µM stock)
dNTPs	2 µl
Pfu polymerase	1 µl

The DNA was initially denatured at 94°C for 120 s in the thermocycler. After this initial denaturation, 30 cycles of denaturation (45 s at 94°C), annealing (30 s, temperature dependent on the T_m of the primer) and elongation (72°C, duration dependent on length of amplificate; 2 min/kb) were performed. After a final elongation step (twice as long as the prior

elongation steps), the reaction was cooled down to 4°C. The annealing temperature of the primers was determined according to the following formula:

$$T_m = 4 \times N (G + C) + 2 \times N (A + T) – 5°C.$$

2.2.6 Side-directed mutagenesis

Point mutations were introduced by PCR using the double stop-codon construct of pQE30/*SCGRX7* (Mesecke *et al.* [112]) or the double mutant construct pQE30/*PFGRX*$^{C32S/C88S}$ (Djuika *et al.* 2013 [138]) as a template. *Pfu* polymerase was used for side-directed mutagenesis. The used mutagenesis primers are listed in Table 8 (section 2.1.8) and were designed according to the following criteria: the length of the complementary primers should be between 25 and 45 bases, primers should end with a G or C for stability reasons, primers should have a T_m > 78°C and the point mutation should be introduced in the middle of the primer. Template DNA, forward and reverse primers, dNTPs, buffer and *Pfu* polymerase were mixed in a total reaction volume of 50 µl according to Table 12 and the reactions were placed in a pre-heated thermocycler. After an initial denaturation step at 94°C for 90 s, 16 cycles each comprising 30 s denaturation, 60 s annealing and 2 min/kb elongation at 72°C for the *SCGRX* mutants or 68°C for the *PFGRX* mutants were performed. The samples were cooled down to 4°C after a final elongation step that was twice as long as the prior elongation steps. Following digestion of the methylated template DNA with 2 µl *Dpn*I overnight at 37°C, plasmids were transformed into chemically competent *E. coli* XL1-Blue cells. After isolation of plasmid DNA, the correct mutations were confirmed by sequencing the protein coding sequence by GATC.

Table 12 | Pipetting scheme for a standard mutagenesis PCR.

Component	Volume
ddH_2O	37 µl
DMSO	2 µl
Pfu buffer containing $MgSO_4$	5 µl
Template DNA	2 µl
Sense primer	0.5 µl (after 1:10 dilution of a 100 µM stock)
Antisense primer	0.5 µl (after 1:10 dilution of a 100 µM stock)
dNTPs	2 µl
Pfu polymerase	1 µl

2.2.7 Agarose gel electrophoresis

Horizontal agarose gel electrophoresis was used to separate DNA-fragments according to their size and to check for the quality of DNA preparations. DNA-samples were supplemented with 6 × loading dye containing 1% midori green. The samples were loaded on an agarose gel (1-2% agarose in 1 × TAE) together with a DNA-ladder (100 bp- or 1 kb-ladder) and separated in 1 × TAE-buffer at 100 V for around 30 min. Afterwards, the DNA was visualized on a trans-illuminator and documented with the attached camera.

1 × TAE	40 mM Tris/HAc 1 mM EDTA pH 7.6

2.2.8 Restriction digest of DNA

Restriction digests were either performed to analyze different constructs or for subcloning. Enzymes and corresponding buffers were purchased from New England Biolabs. Analytical digests were performed in a reaction volume of 20 µl containing 15 µl ddH_2O, 2 µl appropriate buffer, 2 µl plasmid DNA and 0.5 µl of each restriction enzyme. The reaction was incubated for 1-3 h at 37°C. For preparative restriction digests the reaction volume was scaled up to 50 µl and the digested fragment was cut from a preparative agarose gel followed by purification with the Promega Wizard and PCR Clean-up system according to the manufacturer's instructions.

2.2.9 Ligation of DNA fragments

For ligation of two DNA-fragments the T4-DNA ligase was used. A typical reaction was performed in a 20 µl total reaction volume containing 14 µl ddH_2O, 2 µl buffer, 1 µl plasmid, 1 µl insert and 1 µl T4 ligase. The ligation reaction was performed at 16°C overnight followed by transformation of *E. coli* XL1-Blue cells with 1-5 µl of the ligation reaction.

2.2.10 Sequencing

The introduction of correct mutations after mutagenesis PCR and the results of cloning were analyzed by sequencing. Therefore, the DNA derived from the miniprep protocol (section 2.2.3) was diluted 1:10 in ddH_2O and sent to GATC for sequencing of both strands either with standard primers from GATC or with primers indicated in Table 8 (section 2.1.8). The results were analyzed with help of the software BioEdit, JustBio and Clustal Omega.

2.2.11 Determination of DNA concentration

The concentration of plasmid DNA was determined for transfection of *L. tarentolae* (section 2.3.5). The absorption at 280 nm and 260 nm was measured with a NanoDrop™ spectrophotometer. Nucleic acids show a specific absorption at 260 nm and the concentration can be calculated with help of the Lambert-Beer law. The purity of the preparation was determined with the quotient A_{260nm}/A_{280nm} and a value between 1.8 and 2.0 was considered as DNA of sufficient quality without major protein contamination.

2.2.12 Sterilization of DNA

The DNA derived from plasmid midipreps was sterilized before transfection of *L. tarentolae*. The concentration of the DNA was calculated and 10 µl of 3 M sodium acetate, pH 5 were added to 20 µg of DNA and filled up to 100 µl with ddH_2O. The DNA was precipitated by the addition of 250 µl 100% ethanol and incubation for at least 30 min at -20°C. The sample was centrifuged at 20800 × *g* for 30 min at 4°C and the supernatant was discarded. The resulting pellet was rinsed with 500 µl 70% ethanol and centrifuged again at 20800 × *g* for 15 min at 4°C. The supernatant was removed and the pellet was dried under sterile conditions for 5-10 min. The DNA was subsequently resuspended in 10 µl sterile ddH_2O and stored at -20°C or directly used for the transfection of *L. tarentolae*.

2.3 Methods of *Leishmania tarentolae* cultivation and manipulation

In this work, the *L. tarentolae* UCLA wild-type strain obtained from André Schneider and different transfectants derived from this strain were used. The parasites were cultured in the promastigote stage.

2.3.1 Standard cultivation of *Leishmania tarentolae*

The standard cultivation of *L. tarentolae* promastigotes was performed in brain heart infusion (BHI) liquid medium at 27°C shaking at 50 rpm (Rotamax 120 shaker; Heidolph Instruments). Usually the parasites were cultivated in 25 cm^2 culture flasks containing 10 ml cell suspension. If higher amounts of cells were needed, they were transferred to 50 ml pre-cultures in 125 ml Erlenmeyer plastic flasks. The cells were maintained in the mid-log phase at approximately 5×10^7 cells/ml. For transfected parasites, the BHI medium was supplemented with 0.1 mg/ml G418 selection marker.

hemin solution (2 mg/ml)	2 mg/ml hemin chloride in 0.05 M NaOH sterilized with a 0.2 µm filter
BHI medium	37 g BHI powder *ad* 1 l ddH_2O autoclaved for 20 min at 120°C 10 µg/ml hemin solution
G418 solution	diluted 1:500 in BHI (final concentration of 0.1 mg/ml)

2.3.2 Cryoconservation of *Leishmania tarentolae*

L. tarentolae strains were cryoconserved in liquid nitrogen. Therefore, parasites in the logarithmic phase (5-9 × 10^7 cells/ml) were mixed with the same volume of sterile BHI freezing medium and transferred to labeled cryotubes. The tubes were wrapped in paper towels, incubated at -80°C for 24 h and finally transferred to liquid nitrogen.

BHI freezing medium	37 g/l BHI 30% (v/v) glycerol 10 µg/ml hemin solution sterilized with a 0.2 µm filter

2.3.3 Thawing of *Leishmania tarentolae* cryocultures

For starting a *L. tarentolae* culture, the parasites were removed from the liquid nitrogen and thawed in a water bath at 27°C. After completely thawing the cells, they were transferred to 10 ml pre-warmed BHI medium, properly mixed and centrifuged at 1500 × *g* at RT for 10 min to get rid of the glycerol included in the freezing medium. The cell pellet was resuspended in 1 ml fresh BHI medium and incubated for 24 h without shaking and without antibiotics. Afterwards, the parasites were cultivated under standard cultivation conditions (section 2.3.1).

2.3.4 Determination of the cell density of *Leishmania tarentolae* cultures

L. tarentolae cells were counted before splitting or for experiments that needed a defined cell number. An aliquot of the parasite culture was mixed with 1 × SSC fixation solution and incubated for 5 min at RT. Afterwards the cells were resuspended, transferred to a Neubauer counting chamber and counted under the microscope after complete settling.

1 × SSC fixation solution	10% (w/v) paraformaldehyde in 1 × SSC
20 × SSC	3 M NaCl 0.3 M Na_3citrate pH 7.4 at RT

2.3.5 Transfection of *Leishmania tarentolae*

For transfection of the parasites, *L. tarentolae* cells in the mid-logarithmic phase were used. The protocol is based on the manufacturer's protocol of the utilized kit (Basic Parasite Nucleofector™ Kit, Lonza). After counting the cells, 5×10^7 cells were centrifuged for 3 min at 1500 × *g* at RT. The supernatant was discarded and the pellet was resuspended in 1 ml transfection buffer. The suspension was centrifuged again for 3 min at 1500 × *g* at RT and the pellet was resuspended in 100 µl Nucleofector Solution that was pre-warmed to RT. The cell suspension was combined with 20 µg sterile DNA (section 2.2.12) that was dissolved in 10 µl ddH_2O. The mixture was transferred into an electroporation cuvette and the cells were electroporated with the program U-033 in the Nucleofector™ 2b Device (Lonza). Once the program was finished, 500 µl of pre-warmed BHI medium were added to the cells. Then, the cells were transferred to a culture flask containing 9.5 ml BHI medium. The culture was subsequently incubated overnight at 27°C without antibiotics and without selection marker and the next day centrifuged at 1500 × *g* for 10 min at RT. The resulting pellet was resuspended and spread on BHI agar plates that were sealed properly with parafilm to avoid moisture loss. Growth of parasites was observed after around 2-3 weeks after incubating the plates at 27°C.

BHI agar	3.7% BHI 0.08% (w/v) folic acid 0.8% (w/v) agar 10% (v/v) heat-inactivated FCS 20 µg/ml hemin 40 µg/ml G418
transfection buffer	21 mM HEPES 137 mM NaCl 5 mM KCl 0.7 mM NaH_2PO_4 6 mM Glucose pH 7.4

2.3.6 Preparation of *Leishmania tarentolae* cell lysates

L. tarentolae whole cell lysates for western blot analyses contained 5×10^7 cells per sample. The cell number was determined by counting the cells in a Neubauer chamber. The parasites were centrifuged at 1500 × *g* for 10 min and directly lysed in 5 × Laemmli-buffer either containing 10-15% β-ME for reducing conditions or without β-ME for non-reducing conditions. The samples were sheared 10 times over a centrifugation tube rack to disrupt the genomic DNA and to improve the running behavior of the samples on the SDS-gel. Afterwards, the

samples were boiled at 95°C for 10 min. If an additional treatment of the cells was needed, the protocol was modified as follows.

2.3.6.1 Preparation of NEM- or MMTS-treated *Leishmania tarentolae* cell lysates

L. tarentolae cells were treated with the alkylating substances NEM or MMTS to trap mixed disulfide intermediates by blocking free thiols. Different concentrations of NEM or MMTS were tested in a first experiment and in following experiments incubation with 100 mM NEM for 5 min was used as the standard condition. The NEM-solution was always prepared freshly due to stability reasons. After determination of the cell density, the cell suspension was centrifuged at RT at 1500 × *g* for 10 min. The cells were resuspended in PBS containing 100 mM NEM for 5 min. Afterwards, the cells were centrifuged at 4°C for 1 min at 10000 × *g*. The resulting pellet was resuspended in 5 × Laemmli buffer containing 10% of the initial NEM or MMTS concentration. Subsequently, samples for western blot analyses were prepared according to the standard protocol in the previous section.

2.3.6.2 Preparation of diamide- or DTT-treated *Leishmania tarentolae* cell lysates

L. tarentolae parasites were treated either with the thiol oxidizing agent diamide or the reducing agent dithiothreitol (DTT) prior to NEM-blocking of free thiols to stabilize potential mixed disulfide intermediates. After determination of the cell number, 5×10^7 cells/sample were centrifuged at 1500 × *g* for 10 min at RT. Parasites were treated with either 2 mM diamide or 2 mM DTT in PBS for 1-120 min. After another centrifugation step, the cells were incubated with 100 mM NEM in PBS for 5 min at RT. Parasites treated only with PBS or 100 mM NEM served as control samples. The samples for western blot analyses were prepared as described above.

2.3.7 Differential fractionation of *Leishmania tarentolae* whole cell lysates

To analyze the localization of proteins, *L. tarentolae* whole cell lysates were differentially fractionated by hypotonic swelling followed by digitonin treatment. A control sample was removed from the cell culture with 5×10^7 cells (=input sample). This sample was centrifuged at 1500 × *g* for 10 min at 4°C and resuspended in 20 µl 5 × Laemmli buffer containing 15% (v/v) β-ME. All buffers and solutions were pre-cooled on ice and 10^9 cells were harvested by centrifugation at 1500 × *g* for 10 min at 4°C. The resulting cell pellet was washed once with

10 ml ice-cold PBS. For hypotonic swelling, the cell pellet was resuspended in 1.66 ml freshly prepared, ice-cold DT buffer per 10^9 cells. The cells were lysed by manually shearing them ten times through a needle (BD Microlance 3 needle, 0.4 × 19 mm). Before shearing, an aliquot of cells was removed for SDS-PAGE analysis (=control without shearing). The hypotonic swelling was stopped by the addition of sucrose in a final concentration of 7.5% (w/v) followed by mixing the lysate. Aliquots of the cell lysate containing 10^8 cells/tube were prepared and subsequently treated with 0, 50, 100, 150, 200, 250 or 2000 µg digitonin or 2% (v/v) Triton™ X-100 (=positive control). The samples were mixed, incubated on ice for 1 h interrupted by several mixing steps. The lysates were centrifuged at 20000 × *g* for 30 min at 4°C and the resulting pellets were resuspended in 50 µl 5 × Laemmli buffer containing 15% (v/v) β-ME. The supernatants obtained from the centrifugation were transferred to fresh reaction tubes and precipitated with acetone according to Fic *et al.* 2010 [145]. The supernatants were supplemented with 5-6 volumes of ice-cold acetone and thoroughly mixed. The samples were incubated for at least 1 h at -20°C and afterwards centrifuged at 15000 × *g* for 15 min at 4°C. The supernatant was removed and the resulting pellets were completely dried at RT for about 15 min. The pellets were dissolved in 50 µl 5 × Laemmli buffer containing 15% β-ME and vortexed twice for 30 s until the pellets were completely dissolved. All samples were incubated for 5 min at 95°C and subsequently loaded on a SDS-PAGE gel. The different fractions were analyzed by western blot analysis. EF1α served as a cytosolic marker and *Lt*Erv and *Lt*sTim1 served as markers for the IMS.

DT buffer	1 mM Tris/HCl pH 7.9 (at 4°C) 1 × cOmplete EDTA free protease inhibitor

2.3.8 Affinity chromatography of *Leishmania tarentolae* proteins

Different protocols for affinity chromatography of up-regulated *L. tarentolae* proteins produced in *L. tarentolae* were tested for the enrichment of these proteins and their potential interaction partners. All protocols were based on Ni-NTA affinity chromatography interacting with the N-terminal His_8-tag of the respective proteins.

2.3.8.1 Native affinity chromatography of *Lt*Erv^{wt}

A native affinity chromatography experiment was performed with recombinant N-terminally His_8-tagged *Lt*Erv^{wt} from *L. tarentolae*. The untagged version of the protein served as a control.

Cells lysis was performed by shearing hypotonically swelled cells. Membrane proteins were further solubilized with digitonin. All buffers and solutions were pre-cooled on ice and kept cool during the whole experiment. An input sample of the culture containing 5×10^7 cells per SDS-sample was prepared for western blot analysis ("input") after determination of the cell number. 1 L of parasites in the mid-log phase were centrifuged at 1500 × *g* for 10 min at RT. The cells were resuspended in 10 ml PBS containing 100 mM NEM and incubated for 5 min at RT in the dark. Afterwards, the cells were centrifuged at 4000 × *g* for 15 min at 4°C and the resulting pellet was resuspended in 0.83 ml fresh, ice-cold DT buffer per 10^9 cells for hypotonic swelling. The swollen cells were sheared twice through a needle (BD Microlance 3 0.4 × 19 mm) with 6 bar. The cell lysate was collected on ice and the success of lysis was controlled under the microscope. The lysis was stopped by adding 7.5% (w/v) sucrose. From this step, a sample "lysate" was taken for western blot analysis. The lysate was centrifuged at 16000 × *g* for 20 min at 4°C and the supernatant (except for an aliquot for western blot analysis "supernatant") was discarded. The remaining pellet was resuspended in 1 ml ST20 buffer per 2.5×10^{10} cells. The protein concentration of the lysate was determined with a Bradford assay and adjusted to 5 mg/ml with ST20 buffer. A sample "pellet 1" was prepared for western blot analysis. Digitonin (1% (w/v) final concentration) was added to the sample and the buffer concentration was adjusted with 5 × ST20 buffer to obtain a 1 × ST20 buffer concentration. This resulted in a further dilution of the protein concentration to 3.3 mg/ml. The sample was inverted several times and manually sheared through a needle twice for mixing followed by incubation for 1 h on ice. In the meantime, 20 µl Ni-NTA beads were equilibrated with ST20-buffer. Therefore, the Ni-NTA beads were washed three times with 1 ml buffer followed by centrifugation at 1000 × *g* for 1 min at 4°C. The Ni-NTA beads were incubated with the digitonin-treated cell lysate for 1 h at 4°C on a rotating wheel. Afterwards, the protein-agarose mixture was centrifuged for 1 min at 1000 × *g* at 4°C and a sample "depleted supernatant" was removed for western blot analysis. The beads were washed once with 1 ml ST20-buffer ("W1") and three times with 2 ml of ST20-buffer ("W2-W4") and samples of each washing step were removed for western blot analysis. The protein was eluted by the addition of 100 µl elution buffer (ST20-buffer + 500 mM imidazole + 10 mM NEM) to the pellet and incubation for 5 min on ice. The sample was centrifuged for 3 min at 1000 × *g* and an aliquot of the elution fraction was prepared together with the other samples for western blot analysis on a 15% SDS-PAGE gel.

PBS	1.84 mM KH_2PO_4 10 mM Na_2HPO_4 137 mM NaCl 2.7 mM KCl pH 7.4 (at 24°C)
DT buffer	1 mM Tris/HCl 10 mM NEM pH 7.9 (at 4°C) 1 × cOmplete EDTA free protease inhibitor
ST20 buffer	250 mM sucrose 25 mM Tris/HCl 20 mM imidazole 10 mM NEM pH 7.9 (at 4°C) 1 × cOmplete EDTA free protease inhibitor

2.3.8.2 Denaturing affinity chromatography of *Lt*Erv^{C63S} and *Lt*sTim1 mutants

A denaturing affinity chromatography experiment was performed with recombinant N-terminally His_8-tagged *Lt*Erv^{C63S} or His_8-tagged *Lt*sTim1^{mut} from *L. tarentolae*. The untagged version of the mutants served as a control. All buffers and solutions were precooled on ice and kept cool during the whole experiment. A sample of the input containing 5×10^7 cells was removed after determination of the cell number. 1 L of the parasites in the mid-log phase were centrifuged at 1500 × *g* for 10 min at RT. The supernatant was discarded, the resulting pellet resuspended in 10 ml PBS containing 100 mM NEM and incubated for 5 min on ice. After centrifugation of the parasites at 1500 × *g* for 15 min at 4°C, the pellet was resuspended on ice with 10 ml lysis buffer and incubated for 1 h on ice. The cell suspension was centrifuged at 10000 × *g* for 30 min at 4°C. For affinity chromatography, an empty reaction tube with 100 µl Ni-NTA (200 µl of 50% slurry) was equilibrated with 1.5 ml of lysis buffer. The supernatant was mixed with the Ni-NTA agarose beads and incubated for 1 h on ice. Afterwards, the Ni-NTA agarose beads were washed with 1.5 ml of washing buffer in three steps of centrifugation at 1000 × *g* at 4°C for 3 min. The Ni-NTA beads were incubated with 100 µl of elution buffer for protein elution. After 3 min of incubation, the sample was centrifuged at 1000 × *g* for 3 min at 4°C. The supernatant was transferred to a fresh reaction tube and one sample for reducing conditions (containing 15% β-ME) and one sample for non-reducing conditions (without β-ME) was prepared for further analysis. The Ni-NTA beads were resuspended in Laemmli-buffer and analyzed as “beads fraction”. Samples of all steps were taken for SDS-PAGE and western blot analyses and supplemented with 2 × Laemmli-buffer containing 15% (v/v) β-ME.

PBS	1.84 mM KH_2PO_4 10 mM Na_2HPO_4 137 mM NaCl 2.7 mM KCl pH 7.4 at RT
lysis buffer	20 mM sodium phosphate 8 M urea 20 mM imidazole 500 mM NaCl 2% (v/v) Triton™ X-100 1 × Protease Inhibitor pH 8.0 at 4°C
washing buffer	20 mM sodium phosphate 8 M urea 20 mM imidazole 500 mM NaCl 1 × Protease Inhibitor pH 8.0 at 4°C
elution buffer	20 mM sodium phosphate 8 M urea 400 mM imidazole 500 mM NaCl 1 × Protease Inhibitor pH 8.0 at 4°C

2.3.9 Screen of different media for the cultivation of *Leishmania tarentolae*

The following media with a defined composition were tested as potential replacements for the undefined standard BHI medium: DMEM, RPMI-1640, DMEM/F-12, IMDM, McCoy's 5A (Modified) Medium and MEM. McCoy's 5A (Modified) Medium and MEM were supplemented with 25 mM HEPES and sterile filtered through a 0.2 µM filter prior to use. Heat inactivated fetal bovine serum was added to the media in different concentrations (0%, 5% or 10% (v/v)). As a serum free alternative 0.5% AlbuMax™ II Lipid-Rich BSA was tested. The different media were also supplemented with folic acid (0 µg/ml, 10 µg/ml or 50 µg/ml) and hemin chloride solution (5 µg/ml, 10 µg/ml or 20 µg/ml). *L. tarentolae* cells in the mid-logarithmic phase were centrifuged at 1500 × *g* for 10 min at RT and washed once with the appropriate medium (without any supplements). After another centrifugation step, the pellet was resuspended in the appropriate medium obtaining a concentration of 5×10^6 cells/ml. A volume of 500 µl cell suspension was seeded per well in a 48-well plate. The different supplements were directly added resulting in 216 different test-conditions. The parasites were cultivated at 27°C and their morphology was checked under a microscope every 24 h to visually evaluate the best growth conditions. Growth kinetics of *L. tarentolae* cells cultivated in the following media were determined in 25 cm^2 culture flasks: IMDM supplemented with 5% FCS, 10% FCS or 0.5%

AlbuMax™, McCoy's 5A (Modified) Medium supplemented with 5% or 10% FCS, MEM supplemented with 25 mM HEPES and 5% or 10% FCS. Cells cultivated with BHI liquid medium served as a positive control. All media were supplemented with 10 µg/ml hemin chloride. *L. tarentolae* cells in the mid-log phase were centrifuged at 1500 × *g* for 10 min at RT and washed once with the appropriate medium containing the supplements named above. After another centrifugation step, the pellet was resuspended in the appropriate medium obtaining a concentration of 5×10^6 parasites/ml in a total volume of 10 ml. The parasites were cultivated under normal cultivation conditions (27°C shaking at 50 rpm on the Rotamax 120 shaker) and the cells were counted every 24 h. After counting, the cells were centrifuged at 1500 × *g* for 10 min at RT and the pellet was resuspended in 10 ml fresh medium to avoid nutrient depletion. The data was analyzed with SigmaPlot using a sigmoidal curve fit with the equation $f = y_0 + a / (1 + \exp(- (x - x_0) / b))$. The maximum growth rate (L) was determined using the equation $L = b + y_0$. The doubling time (tD) was determined in the exponential phase using the following equation: $tD = \log_2 \times (t - t_0) / (\log N - \log N_0)$. *L. tarentolae* promastigotes in the respective medium were used for determination of the morphology. A thin layer of parasites in the mid-logarithmic phase was dropped on a microscope slide and sealed with paraffin. The living cells were directly analyzed using a Zeiss LSM780 microscope and the software ZEN2010.

2.3.10 BioID for identification of proximal and interacting proteins

Leishmania tarentolae cells transfected with pX/BirA*-*LTERV* or pX/BirA*-*LTsTIM1* were cultivated in the logarithmic phase according to the standard protocol. The cell number was determined and 10 ml cell suspension diluted to 8×10^6 cells/ml (8×10^7 cells in total) were centrifuged for 10 min at RT with 1500 × *g*. The parasites were resuspended in 10 ml BHI containing 150 µM biotin and incubated for 24 h according to Chen *et al.* [77] before harvesting. In parallel, untreated (without biotin) control samples were prepared. After biotin treatment, the cells were harvested for western blot analysis. Several independent clones were analyzed by western blotting with an αMyc antibody, streptavidin-HRP (1:10000) and an antibody against *Lt*Erv or *Lt*sTim1. The parasites were also analyzed by immunofluorescence microscopy with the help of Jessica Kehrer. Therefore, 5×10^7 cells were centrifuged at 1500 × *g* for 10 min at RT and washed once with 1 ml PBS. The cells were fixed with 4% (w/v) PFA in PBS overnight at 4°C. Then, the cells were washed three times with 100 µl PBS before the membrane was permeabilized with 100 µl 0.5% Triton X-100 in PBS for 10 min. The parasites were washed three times with 100 µl PBS and resuspended in 100 µl PBS containing

the αMyc-antibody (1:500). After one hour of incubation at RT the cells were washed again three times with 100 µl PBS and resuspended in 100 µl PBS containing the secondary antibody against αMyc (Alexa Fluor 488, goat anti-mouse, 2 mg/ml, Invitrogen, 1:500), Hoechst (1:500) and labeled Streptavidin (1:500). After another hour of incubation at RT, the cells were washed three times with 100 µl PBS, resuspended in 50 µl PBS and analyzed under the Zeiss LSM780 microscope.

2.4 Preparation of *Plasmodium falciparum* cell lysates

P. falciparum trophozoites of the strain 3D7 were used for the identification of potential interaction partners of *Pf*Erv. The parasites were cultured by Verena Staudacher according to a standard protocol [146] at 37°C in fresh human erythrocytes (A^+) with a hematocrit of 3% in RPMI-1640 medium. The medium was supplemented with 0.45% (w/v) AlbuMax™ II, 0.2 mM hypoxanthine and 2.7 µg/ml gentamicin. After reaching a parasitemia of about 4%, the cultures were centrifuged at 300 × *g* for 5 min. The pellet was resuspended in 100 mM NEM in PBS and incubated for 5 min at RT. The culture was centrifuged 5 min at 755 × *g* and the pellet was resuspended in ice-cold PBS containing 10 mM NEM and 0.05% saponin. Cell lysis was performed for 60 s on ice and the culture was subsequently centrifuged at 1800 × *g* for 10 min at 4°C. The parasite pellet was washed once with 10 mM NEM in PBS and once with PBS containing a protease inhibitor (cOmplete EDTA-free protease-inhibitor cocktail, Roche). A control sample was prepared in parallel without NEM in all steps. The cell density of the parasite samples was determined in a Neubauer chamber. The pellet was resuspended in PBS, frozen in liquid nitrogen and stored at -80°C until western blot analyses were performed. For each sample 10^7 parasites were lysed in 5 × Laemmli buffer (± 30% β-ME), boiled for 10 min at 95°C and analyzed on a 15%-SDS gel under reducing and non-reducing conditions.

2.5 Protein biochemical methods

2.5.1 Expression and purification of recombinant proteins

Recombinant N-terminally MRGS$(H)_6$-tagged *S. cerevisiae* or *P. falciparum* Grx (*Sc*Grx7 or *Pf*Grx), different Grx mutants of both species and *Pf*GR were produced in *E. coli* XL1-Blue cells. Therefore, 1 µl of pQE30-plasmid containing the coding sequence for the respective protein was transformed into chemically competent XL1-Blue cells according to the standard protocol

(section 2.2.2). A starter culture was prepared with 20 ml ampicillin-containing medium inoculated with one colony of the transfectant. The pre-culture was incubated at 37°C shaking at 130 rpm in the Innova 4000 shaker overnight. The next morning, the OD_{600nm} of the starter culture was determined. The starter culture was diluted into a main culture resulting in a starting OD_{600nm} of 0.04. The main culture was incubated at 37°C shaking at 130 rpm in the Innova 4000 shaker until an OD_{600nm} of 0.5-0.6 was reached. For expression of *Pf*GR the culture was incubated at 37°C at 130 rpm in the Innova 4000 shaker until an OD_{600nm} of 0.15 was reached and then shifted to 28°C. At an OD_{600nm} of 0.4 the culture was shifted to 16°C until an OD_{600nm} of 0.6 was reached. Protein production was induced by adding 0.5 mM IPTG for expression of GRX or 0.3 mM IPTG for expression of *PFGR* to the culture, which subsequently was incubated for another 4 h for GRX expression or 14 h for *PFGR* expression. Afterwards, the culture was transferred to precooled 1 L buckets and the cells were harvested by centrifugation at 4000 × *g* for 15 min at 4°C. The pellet obtained from a 1 L of culture was resuspended on ice with 10 ml buffer I, divided into two aliquots and stored at -20°C. For kinetic analyses the protein was freshly purified. For cell lysis, the pellet was therefore thawed on ice, 10 mg lysozyme and a spatula tip of DNaseI were added to the cell suspension (derived from a 500 ml culture) and the mixture was incubated for 1 h on ice whilst stirring. The suspension was sonicated on ice with 60-70% power for 5 cycles with 10 s for each cycle (including a 10 s pause on ice between the steps). Afterwards, the lysates were centrifuged for 30 min at 4°C at 10000 × *g*. Meanwhile, a column with 750 µl Ni-NTA was prepared and equilibrated with 10 ml buffer I. The supernatant derived from centrifugation of the cell lysate was loaded with a peristaltic pump (flow rate set to 10 ×) and the column was washed with 10 ml buffer I prior to elution with one column volume of buffer II. To recycle the column, it was washed with 10 ml buffer I and stored at 4°C. The eluate was analyzed on a SDS-gel and the concentration was determined by Bradford assay.

Buffer I Grx	10 mM imidazole 300 mM NaCl 50 mM $Na_xH_yPO_4$ pH 8.0 at 4°C
Buffer II Grx	125 mM imidazole 300 mM NaCl 50 mM $Na_xH_yPO_4$ pH 8.0 at 4°C

Buffer I GR	20 mM imidazole 300 mM NaCl 50 mM $Na_xH_yPO_4$ pH 8.0 at 4°C
Buffer II GR	200 mM imidazole 300 mM NaCl 50 mM $Na_xH_yPO_4$ pH 8.0 at 4°C

2.5.2 Bradford assay for determination of protein concentrations

The determination of the protein concentrations was based on the protocol of Bradford [147]. A calibration curve with 0-14 µg/ml BSA was prepared freshly for every measurement. The protein solutions (appropriate dilutions determined before) were pipetted into cuvettes containing 800 µl ddH_2O minus the volume of the protein solution. All samples were prepared in triplicates and two different dilutions of the protein sample were measured. The reaction was started by the addition of 200 µl Bradford reagent followed by thorough mixing. After exactly 15 min incubation of the solution at RT, the absorbance at 595 nm was followed with the software "spectra manager". The calibration curve was fitted hyperbolically in Sigma Plot and the protein concentration was calculated from the following formula using the absorption values: $y = a*x / (b + x)$.

2.5.3 SDS-Polyacrylamide gel electrophoresis (SDS-PAGE)

SDS-Polyacrylamide gel electrophoresis was used to separate protein solutions in an electrical field according to the molecular weight of the proteins [148]. The pore size of the gel was varied using different acrylamide-concentrations for the separating gel according to the expected size of the proteins. The acrylamide polymerizes after the addition of ammonium persulfate (APS) and tetramethylethylenediamine (TEMED). The proteins were denatured in 5 × Laemmli buffer by boiling the samples for 10 min at 95°C directly before loading onto the gel. For reducing conditions, the samples contained 10-20% β-ME to reduce disulfide bonds. The negative charge of the SDS covers the intrinsic charge of the proteins and therefore, the separation is only based on the molecular weight of the proteins. The proteins were first focused in the stacking gel and then separated in a 12-18% gel. The gels were run in SDS running buffer with maximum 30 mA for each small SDS-gel for about 1 h. Afterwards the gels were either stained with Coomassie Brilliant Blue for visualization of the protein bands or the proteins were transferred to a nitrocellulose membrane by western blotting.

stacking gel	5% (w/v) acrylamide 0.03% (w/v) bisacrylamide 60 mM Tris-HCl, pH 6.8 0.1% (w/v) SDS 0.05% (w/v) APS 0.1% (v/v) TEMED
separating gel	12-18% (w/v) acrylamide 0.1% (w/v) bisacrylamide 375 mM Tris-HCl, pH 8.8 0.1% (w/v) SDS 0.05% (w/v) APS 0.15% (v/v) TEMED
SDS running buffer	25 mM Tris 250 mM glycine 0.1% (w/v) SDS pH 8.3
5 × Laemmli buffer	50 mM Tris-HCl, pH 6.8 25% glycerol 10% (w/v) SDS 0.1% bromophenol blue 0-20% β-ME

2.5.4 Coomassie Brilliant Blue staining of SDS-gels

To visualize protein bands after separation by SDS-PAGE, the gels were stained with Coomassie Brilliant Blue. Therefore, the gels were transferred to the staining solution and incubated on a vertical shaker at RT for at least one hour. For destaining, the gels were transferred to a destaining solution, which was replaced several times. To increase the contrast of the protein bands, the background was completely destained by incubating the gel overnight in ddH_2O without shaking.

Staining solution	65% (v/v) ddH_2O 25% (v/v) isopropanol 10% (v/v) acetic acid 0.05% (w/v) Coomassie Brilliant Blue G-250
Destaining solution	65% (v/v) ddH_2O 25% (v/v) isopropanol 10% (v/v) acetic acid

2.5.5 Western blotting

Proteins that were separated according to their molecular weight by SDS-PAGE were subsequently transferred to a nitrocellulose membrane by semi-dry blotting for immunodetection. Hence, the stacking gel of the SDS-gel was removed and the separating gel was incubated in transfer buffer. For each gel, one membrane and 10 Whatman papers were prepared and incubated in transfer buffer. The blotting sandwich was assembled without air

bubbles as follows: i) anode, ii) 5 Whatman papers, iii) nitrocellulose membrane, iv) SDS separating gel, v) 5 Whatman papers and vi) cathode. The semi-dry blotting was performed with a constant electric current at 100 mA per small gel or 250 mA per big gel for 1 h. The successful transfer of the proteins was checked by PonceauS staining of the membrane. Therefore, the membrane was shortly incubated in PonceauS solution followed by destaining of the background with ddH_2O. After documentation, the membrane was completely destained with TBS for several minutes on the shaker.

transfer buffer	150 mM glycine 20 mM Tris 0.02% (w/v) SDS 20% (v/v) methanol pH 8.3
PonceauS solution	0.2% (w/v) PonceauS 3% (w/v) trichloroacetic acid

2.5.6 Immunodetection of proteins

Proteins that were immobilized on nitrocellulose membranes by western blotting were subsequently detected by immunostaining with protein specific antibodies. Unspecific binding sites of the membrane were blocked by incubation for 1 h at RT in blocking buffer. Afterwards, the membrane was incubated in TBS with 5% (w/v) milk powder containing the primary antibody (dilutions see Table 9) overnight at 4°C on a horizontal shaker. Subsequently, the membrane was washed three times for 10 min with TBS and incubated with the secondary HRP-conjugated antibody diluted 1:5000-1:10000 in blocking buffer for 1 h at RT. Then, the membrane was washed again three times for 10 min with TBS or TBST. For detection of the proteins, the membrane was incubated with an ECL-Mix (Amersham™ ECL™ Western Blotting Reagent, GE Healthcare) and covered with a film in the dark for a few seconds until overnight depending on the intensity of the luminescence signal. The film was developed and afterwards documented by scanning.

blocking buffer	5% milk (w/v) in TBS
TBS	10 mM Tris 0.9% (w/v) NaCl pH 7.4 (adjusted with HCl)
TBST	10 mM Tris 0.9% (w/v) NaCl pH 7.4 (adjusted with HCl) 0.05% (v/v) Tween™ 20

2.5.7 Stripping of membranes

A mild stripping buffer according to a protocol from Abcam was used to remove primary and secondary antibodies from a western blot membrane for redecoration with further primary antibodies. The membrane was washed twice for 10 min with TBS and three times for 10 min with mild stripping buffer. Afterwards, the membrane was washed twice for 10 min with TBS and twice for 5 min with TBST (0.1% Tween™ 20). The membrane was subsequently incubated in blocking buffer and further processed according to the standard protocol.

mild stripping buffer	15 g glycine 1 g SDS 10 ml Tween™ 20 *ad* 1 l ddH_2O pH 2.2

2.5.8 Glutathione reductase assay

Glutathione reductase was needed for the coupled spectrophotometric GSSCys and HEDS oxidoreductase assays and therefore its activity was measured prior to these assays. Pure *Sc*GR or *Pf*GR was diluted 1:100 with elution buffer. A 4 mM stock solution of NADPH and a 20 mM stock solution of GSSG were prepared in assay buffer. The assay buffer was pre-warmed to 25°C and the whole assay was performed at 25°C. The total reaction volume in the cuvette (green quartz cuvette) was 1000 µl and contained assay buffer with a final concentration of 100 µM NADPH and 5 µl of diluted GR. A baseline was recorded for 30 s before the reaction was started by the addition of GSSG in a final concentration of 1 mM. The decrease of absorbance of NADPH at 340 nm was determined spectrophotometrically with the software JASCO Spectra Manager. The reaction was repeated five times and the baseline was subtracted from the decrease of absorption for each value. The mean of the five values was calculated as ΔAbs.korr/min. With the extinction factor of NADPH (ε340nm = 6.22 $mM^{-1}cm^{-1}$) the decrease of NADPH was calculated with the following formula: Δ[NADPH] / min = (ΔAbs.korr × 1 cm) / (6.22 $mM^{-1}cm^{-1}$). The units contained in the assay were calculated as follows: Units in assay = (Δ[NADPH] × $V_{total)}$ / min. To obtain the volume activity (Units) of GR in the stock solution the following formula was used: Units in stock solution = (units in assay × dilution factor) / volume. The GR was diluted to 200 U/ml prior to its use in the GSSCys or HEDS assay.

GR assay buffer	0.1 M Tris 1 mM EDTA pH 8.0 at 25°C

2.5.9 GSSCys and HEDS oxidoreductase assays

Steady-state kinetics of wild-type and mutant *Sc*Grx7 or *Pf*Grx were determined in a coupled spectrophotometric GSSCys and HEDS assay. The assays are based on the oxidation of GSH by Grx yielding GSSG, which is subsequently reduced by glutathione reductase (GR) using NADPH as an electron donor. The consumption of NADPH can be followed spectrophotometrically at 340 nm. Stock solutions of NADPH, GSH and GSSCys or HEDS were prepared freshly in Grx assay buffer, whereas the enzymes *Sc*Grx7 or *Pf*Grx and *Sc*GR or *Pf*GR were diluted in buffer II (section 2.5.1) to keep the imidazole-concentration in the assay constant. The protocols were based on the publication of Mesecke *et al.* [112]. All measurements were performed with freshly purified Grx in a reaction volume of 1 ml in Grx assay buffer at 25°C. The obtained data were analyzed using the software JASCO Spectra Manager. For both assays 0.1 mM NADPH and 1 U/ml *Sc*GR or *Pf*GR was used. Final concentrations of the *Sc*Grx^{Y110X} mutants were 5 nM to 150 nM, for the Asp144 and Glu147 mutants 10 nM and for the Arg153 mutants 25 to 50 nM. A final concentration of 5-10 nM, 50-100 nM and 5-12.5 nM was used for *Pf*Grx$^{C32S/C88S}$, *Pf*Grx$^{C32S/C88S/K26A}$ and *Pf*Grx$^{C32S/C88S/D90A}$, respectively. The GSH concentration was varied in the GSSCys assay of the *Sc*Grx mutants between 50 µM and 1.5 mM at fixed GSSCys concentrations (25, 50, 100 and 150 µM GSSCys). For the GSSCys assay with the *Pf*Grx mutants, either GSH was varied between 50 µM and 2.0 mM at fixed GSSCys concentrations (25, 50, 100 and 150 µM GSSCys) or GSSCys was varied between 25 and 200 µM with fixed GSH concentrations (0.3, 0.5, 1.0 and 2.0 mM GSH). A baseline for the background activity of NADPH, GSH, GR and Grx was recorded for 30 s before the assay was started by the addition of GSSCys. For the HEDS assay of the *Sc*Grx mutants, fixed concentrations of HEDS were used (0.18, 0.37, 0.55 and 0.74 mM) and GSH was varied between 100 µM and 2.0 mM. For the *Pf*Grx mutants either GSH was varied between 250 µM and 3.0 mM at fixed concentrations of HEDS (0.18, 0.37, 0.55 and 0.74 mM) or HEDS was varied between 90 and 920 µM at fixed concentrations of GSH (0.25, 0.5, 1 and 2 mM). NADPH, GSH and HEDS were mixed and pre-incubated for exactly 120 s before a baseline was recorded for 30 s after the addition of GR. During the pre-incubation step, the formation of mixed disulfides between HEDS and GSH takes place [123]. The HEDS assay was started by the addition of *Sc*Grx or *Pf*Grx. The decrease

in absorbance was normalized against a reference cuvette measured in parallel including all components except the investigated enzyme. The kinetic parameters k_{cat}^{app} and K_m^{app} were determined by non-linear regression according to the Michaelis-Menten theory and linear regression based on Lineweaver-Burk, Eadie-Hofstee and Hanes theory with SigmaPlot 12.5 or 13 based on established protocols [112, 113, 123].

Grx assay buffer	0.1 M Tris 1 mM EDTA pH 8.0 at 25°C

2.5.10 Determination of the thiol pK_a values

The thiol pK_a values of *Sc*Grx7 wild-type enzyme and selected mutants were determined to gain further insights into the function of different amino acid residues. The protocol used for the determination of the thiol pK_a values of the enzymes was modified from Mieyal *et al.* [149] and Gallogly *et al.* [150]. It is based on the pH-dependent alkylation of the cysteine thiolate of *Sc*Grx7 by iodoacetamide (IAM), followed by determination of the residual enzyme activity in a standard kinetic assay. Only freshly purified protein was used for determination of the thiol pK_a values. The enzyme was reduced with $NaBH_4$ for 2 h on ice according to a previously established protocol resulting in 304 µM protein solution with a 20-fold molar excess of BH_4^- over protein [138]. Subsequently, 6 µM *Sc*Grx7 or mutant enzyme was incubated for exactly 180 s with 150 µM IAM at 23°C in a three-buffer system (Ellis *et al.* [151]) containing 100 mM KCl, 50 mM potassium acetate, 50 mM MES and 100 mM Tris with pH values varying over a range from 3.5 to 8.5. Each assay was also performed with a mock control containing ddH_2O instead of IAM and the activity of the enzyme at each pH was normalized against the corresponding mock control. A standard HEDS assay was started in parallel to the IAM pre-incubation step and was subsequently carried out as described in the previous section to determine the residual enzyme activity. The remaining enzyme activity after alkylation calculated in per cent for every pH value was plotted as a sigmoidal curve (Hill, 4 parameter) in SigmaPlot 13. From this curve, the pK_a values for *Sc*Grx7 and the different mutants were determined.

3 Results

3.1 Mitochondrial protein import

3.1.1 Endogenous chemical trapping of mixed disulfide intermediates

Different approaches were tested for the chemical trapping of a mixed disulfide intermediate between endogenous *Lt*Erv and a potential Mia40 adapter replacement in wild-type *L. tarentolae* parasites. Analogous experiments were performed for the other site of the reaction. In this reaction, a mixed disulfide intermediate between the model substrate *Lt*sTim1 and a potential Mia40 adapter replacement candidate should be trapped. For stabilizing the mixed disulfide bonds between the model substrate *Lt*sTim1, the potential adapter and *Lt*Erv *in vivo*, free cysteine residues in intact cells were blocked by alkylation with *N*-ethylmaleimide (NEM) or *S*-methyl-methanethiosulfonate (MMTS). Another approach was to alter the redox state and therefore possibly shift the redox equilibrium by adding the oxidizing agent diamide or the reducing agent DTT in combination with alkylation by NEM. A schematical overview for the potential outcome of the different trapping experiments is shown in Figure 12.

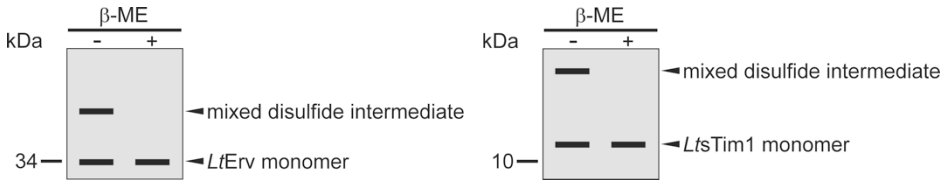

Figure 12 | Schematic overview for the potential outcome of the trapping experiments. Under non-reducing conditions (-β-ME) a mixed disulfide intermediate between *Lt*Erv and a potential interaction partner (left side) or *Lt*sTim1 and a potential interaction partner (right side) is detected in addition to the lower band reflecting monomeric *Lt*Erv or *Lt*sTim1. After reduction of the sample (+β-ME) only the monomeric band should be detectable. Only one potential higher band indicating one specific interaction is shown for the sake of convenience but also several bands or a smear of bands that reflect several potential interactions are possible. β-ME: β-mercaptoethanol.

Endogenous *Lt*Erv

None of the approaches performed with *L. tarentolae* wild-type cells showed specific bands with a higher molecular weight that might reflect a trapped mixed disulfide intermediate between *Lt*Erv and a potential Mia40 adapter replacement under non-reducing conditions in western blot analyses. The NEM-concentration was varied between 10 µM and 100 mM and each sample was incubated for 5 min (Figure 13 A). As an alternative alkylating agent MMTS

was used and the result of this experiment is shown in Figure 13 B. A specific *Lt*Erv antibody was used for the detection. In another experiment the parasites were treated with 2 mM diamide or DTT for 1 min to 120 min followed by alkylation with 100 mM NEM for 5 min (Figure 13, C and D; data from 120 min diamide- or DTT-treatment are not shown). Only one specific band corresponding to the calculated molecular mass of monomeric *Lt*Erv with 34.8 kDa was detectable for all the conditions that were tested and no disulfide intermediate could be enriched.

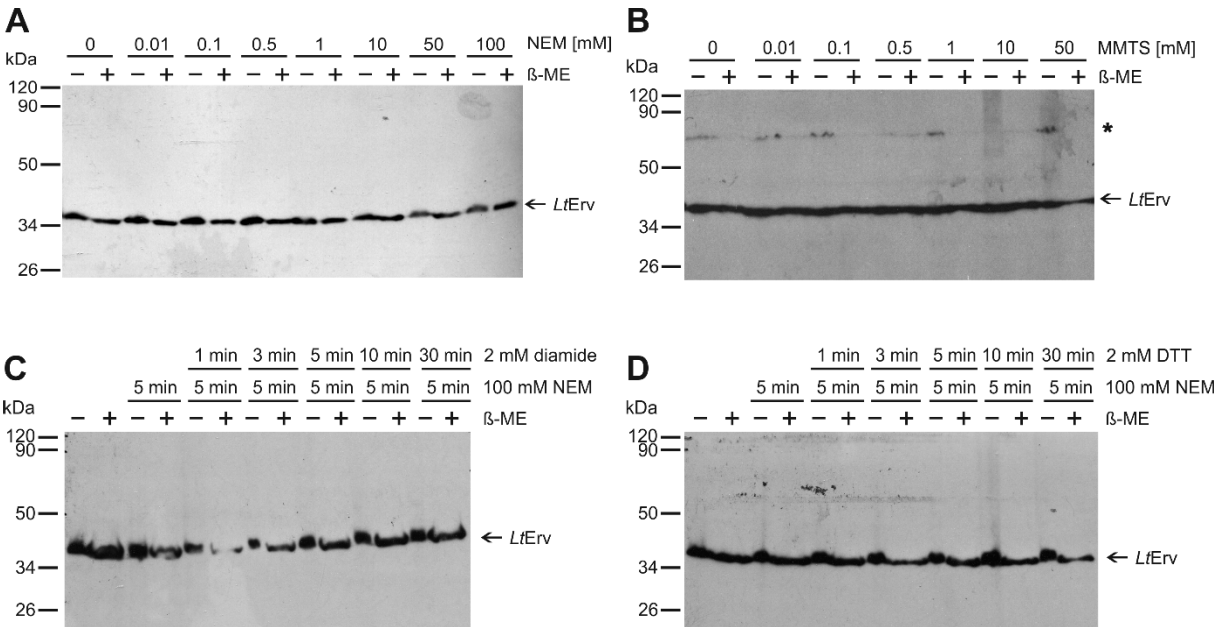

Figure 13 | Chemical trapping of *Lt*Erv. Representative SDS-PAGE and western blot analysis with 5 × 10^7 parasites/lane under reducing and non-reducing conditions (±β-ME). The primary antibody α*Lt*Erv was diluted 1:500, the secondary antibody αRabbit (BioRad) was used 1:5000. The calculated molecular mass of monomeric *Lt*Erv is 34.8 kDa. A: NEM-trapping of *Lt*Erv. *L. tarentolae* treated for 5 min with different concentrations (10 µM up to 100 mM) of NEM. B: MMTS-trapping of *Lt*Erv. *L. tarentolae* treated for 5 min with different concentrations (10 µM up to 50 mM) of MMTS. The asterisk indicates unspecific bands that were also observed in the control. C: Diamide-trapping of *Lt*Erv. *L. tarentolae* treated for 1-30 min with 2 mM diamide followed by 5 min treatment with 100 mM NEM. D: DTT-trapping of *Lt*Erv. *L. tarentolae* treated for 1-30 min with 2 mM DTT followed by 5 min treatment with 100 mM NEM. For all conditions, the cells were lysed in 5 × Laemmli-buffer (±β-ME) after the treatment. NEM: *N*-ethylmaleimide; DTT: dithiothreitol; MMTS: *S*-methyl-methanethiosulfonate; β-ME: β-mercaptoethanol.

In another experiment the treatment conditions shown above were combined with precipitation of the samples with 5% trichloroacetic acid (TCA) leading to an immediate pH drop that quenches redox reactions and unspecific thiol exchange reactions [152, 153]. The cells were treated with diamide or DTT in combination with NEM before centrifugation and resuspension of the cells in ice-cold PBS containing 5% TCA. The solution was incubated for 30 min on ice (longer incubations led to insolubility of the resulting pellet). After centrifugation

of the solution at 10000 × *g* for 10 min, the pellet was washed three times with ice-cold acetone. In all TCA-precipitation experiments only one band reflecting monomeric *Lt*Erv was detectable in western blot analyses with the *Lt*Erv-specific antibody (Figure 14).

Hence, endogenous *Lt*Erv could not be enriched as a trapped mixed disulfide intermediate under the chosen conditions including varying treatment durations and concentrations of the alkylating substances NEM or MMTS or the redox-active chemicals diamide or DTT.

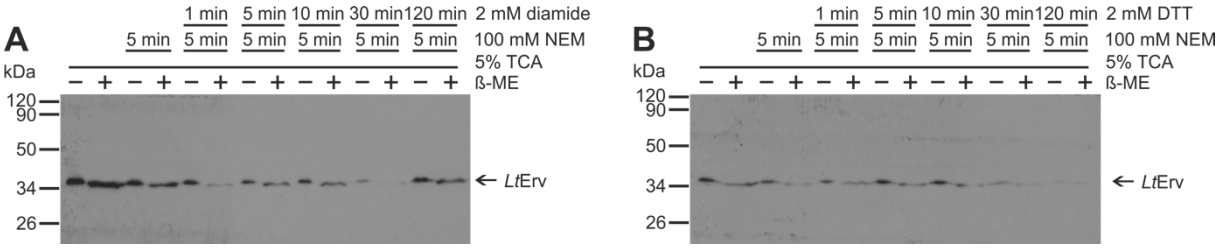

Figure 14 | Chemical trapping of *Lt*Erv combined with TCA precipitation. SDS-PAGE and western blot analysis with 5 × 10^7 parasites/lane. The primary antibody α*Lt*Erv was diluted 1:500, the secondary antibody αRabbit (BioRad) was used 1:5000. The calculated molecular mass of monomeric *Lt*Erv is 34.8 kDa. A: Diamide-trapping of *Lt*Erv combined with TCA precipitation. *L. tarentolae* treated for 1-30 min with 2 mM diamide followed by 5 min treatment with 100 mM NEM. B: DTT-trapping of *Lt*Erv combined with TCA precipitation. *L. tarentolae* treated for 1-30 min with 2 mM DTT followed by 5 min treatment with 100 mM NEM. The samples were afterwards precipitated with 5% TCA and analyzed under reducing and non-reducing conditions (±β-ME). NEM: *N*-ethylmaleimide; DTT: dithiothreitol; TCA: trichloroacetic acid; β-ME: β-mercaptoethanol.

Endogenous *Lt*sTim1

L. tarentolae wild-type lysates were also used for western blot analysis with a specific antibody against the model substrate *Lt*sTim1. Endogenous *Lt*sTim1 and strains with upregulated *Lt*sTim1 protein levels were in general difficult to analyze because the small Tim proteins are highly hydrophobic and tend to form higher molecular oligomers. There was a strong signal in the upper part between the stacking and separating SDS-gel in all western blot analyses performed with the *Lt*sTim1-antibody that could reflect these oligomers. First, different types of gels recommended for small and hydrophobic proteins were tested to improve the migration pattern of *Lt*sTim1. Urea gels containing 8 M urea, a precast gel (BioRad, 16.5% Mini-PROTEAN™ Tris-Tricine) and a Tris-Tricine buffer system according to a published protocol by Schägger *et al.* [154] did not help to decrease the strong signal. Second, various protocols for the preparation of SDS-samples were tested. Different temperatures ranging from RT to 95°C, incubation times from 10-30 min, urea in concentrations up to 8 M in the sample and shearing of the DNA did not alter the migration pattern. The influence of the incubation temperature and the addition of urea to the SDS-samples is shown in Figure 15 as

a representative result. However, the *Lts*Tim1 monomeric-specific signal was variable and often not detectable with standardized or alternative experimental procedures.

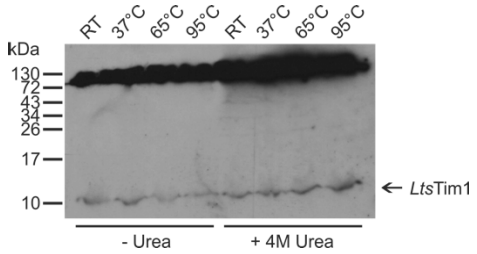

Figure 15 | Migration pattern of *Lts*Tim1. SDS-PAGE and western blot analysis with 5 × 10^7 parasites/lane under reducing conditions. The SDS-samples were incubated at the indicated temperatures for 10 min and one portion of the samples was supplemented with 4 M urea. The primary antibody α*Lts*Tim1 was diluted 1:250, the secondary antibody αRabbit (BioRad) was used 1:5000. The calculated molecular mass of monomeric *Lts*Tim1 is 11.5 kDa. The figure is representative also for the other conditions that were tested. RT: room temperature.

Nevertheless, experiments analogous to the ones with *L. tarentolae* wild-type cells detecting endogenous *Lt*Erv in western blot analyses were performed with the *Lts*Tim1-specific antibody to test for disulfide bridged intermediates after chemical trapping (Figure 16). In this approach faint bands with a higher molecular weight were observed under non-reducing conditions that were not detectable after reduction of the samples. Hence, these bands could reflect mixed disulfide intermediates between endogenous *Lts*Tim1 and potential Mia40 adapter replacement candidates. Again, a strong signal was detectable in the upper part of the gel and could not be reduced. In order to enrich the potential mixed disulfide intermediates by affinity chromatography, different *LT*sTIM1 overexpressing strains were generated.

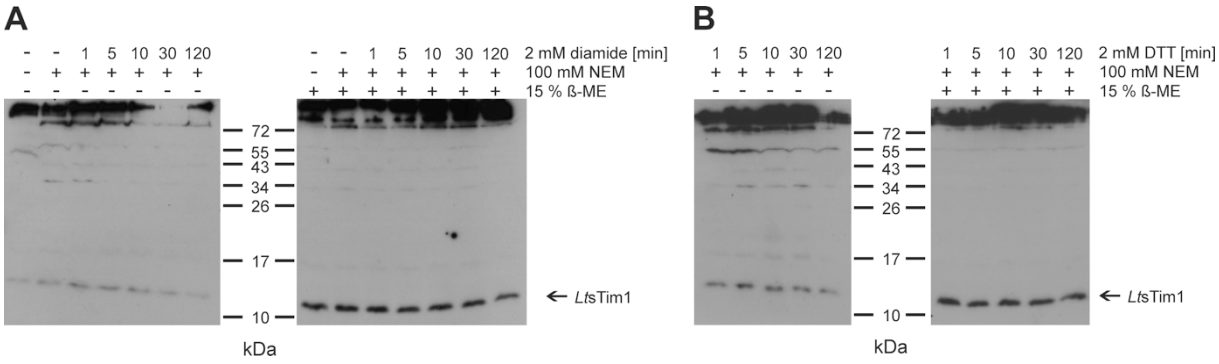

Figure 16 | Chemical trapping of *Lts*Tim1. SDS-PAGE and western blot analysis with 5 × 10^7 parasites/lane under reducing and non-reducing conditions (±β-ME). The primary antibody α*Lts*Tim1 was diluted 1:250, the secondary antibody αRabbit (BioRad) was used 1:5000. The calculated molecular mass of monomeric *Lts*Tim1 is 11.5 kDa. A: Diamide-trapping of *Lts*Tim1. *L. tarentolae* treated for 1-120 min with 2 mM diamide followed by 5 min treatment with 100 mM NEM. B: DTT-trapping of *Lts*Tim1. *L. tarentolae* treated for 1-120 min with 2 mM DTT followed by 5 min treatment with 100 mM NEM. NEM: *N*-ethylmaleimide; DTT: dithiothreitol; β-ME: β-mercaptoethanol.

In another experiment, it was tested if the higher molecular band at around 55 kDa (Figure 16) could reflect a heterodimer between *Lt*Erv and *Lts*Tim1. This would suggest that Erv acts alone as recently proposed [155]. The membranes showing higher molecular bands with the *Lts*Tim1 antibody in western blot analyses were stripped and subsequently redecorated with the *Lt*Erv antibody. However, only the monomeric band for *Lt*Erv and no bands with a higher molecular weight were detected (data not shown).

3.1.2 Expression of bait protein-encoding genes

Since the identification of potential interaction partners with endogenous *Lt*Erv levels was not possible and the bands observed with endogenous *Lts*Tim1 were very faint, the bait proteins should be upregulated in *L. tarentolae* parasites in order to perform pull-down studies. First, constructs encoding the two bait proteins and cysteine mutants that could lead to an enrichment of the disulfide complexes between the bait protein and potential interacting proteins were generated and are shown in Figure 17. All constructs were cloned in the newly designed vector termed "pX-backbone" for the expression in *L. tarentolae*. This vector encodes an N-terminal His_8-tag and no further tags. Constructs without His_8-tag were generated in parallel and served as negative controls for pull-down studies.

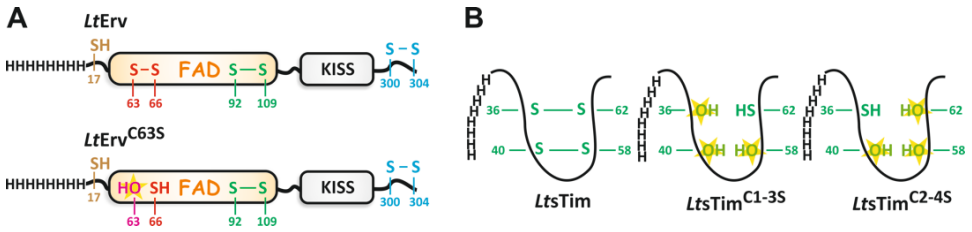

Figure 17 | Constructs for pull-down experiments. All the constructs were cloned into the newly designed vector termed "pX-backbone" for expression in *L. tarentolae*. A: Constructs for production of wild-type *Lt*Erv and *Lt*Erv^{C63S} for enrichment of disulfide complexes between *Lt*Erv and the unknown adapter replacement candidate. B: Constructs for production of wild-type *Lts*Tim1 and the mutants *Lts*Tim1^{C1-3S} or *Lts*Tim1^{C2-4S} for enrichment of disulfide complexes between *Lts*Tim1 and the unknown adapter replacement candidate. Constructs without His_8-tag serve as a negative control for pull-down studies.

L. tarentolae was transfected with each of the constructs shown in Figure 17 and clonal lines were generated. At least three independent clones for each construct were analyzed regarding their protein levels by western blot analyses with specific *Lt*Erv and *Lts*Tim1 antibodies. The lysates of *L. tarentolae* transfected with pX/His_8*LTERV* were also analyzed under non-reducing conditions by western blotting to investigate if disulfide-bridged intermediates could be enriched. The protein level of *Lt*Erv was increased compared to the

wild-type control in all of the four analyzed clones (Figure 18). Only one band corresponding to monomeric His_8-tagged *Lt*Erv was detectable and no bands with a higher molecular weight were visible with the chosen conditions. Thus, even with highly enriched protein levels of *Lt*Erv resulting in strong signals in western blot analysis, no band with a higher molecular weight potentially reflecting an interaction between *Lt*Erv and potential interaction partners could be detected. The upregulation of the *Lt*Erv^{C63S} mutant is shown in Figure 20.

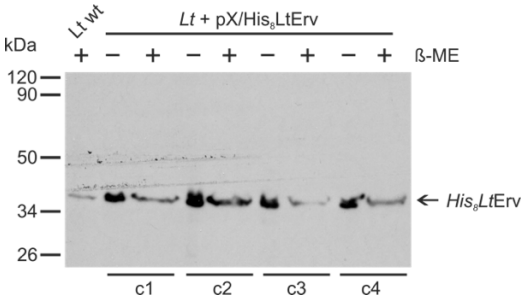

Figure 18 | *L. tarentolae* with upregulated His_8*Lt*Erv levels. Representative SDS-PAGE and western blot analysis with 5 × 10^7 parasites/lane under reducing and non-reducing conditions (±β-ME). Four clones of *L. tarentolae* transfected with pX/His_8*LTERV* were analyzed. The cells were treated with 100 mM NEM for 5 min before harvesting. The primary antibody α*Lt*Erv was diluted 1:500, the secondary antibody αRabbit (BioRad) was used 1:5000. The calculated molecular mass of monomeric *Lt*Erv is 34.8 kDa. wt: wild-type; β-ME: β-mercaptoethanol.

Protein levels of *Lts*Tim1 and the two mutants *Lts*Tim1^{C1-3} and *Lts*Tim1^{C2-4S} were also increased compared to the wild-type control in most of the analyzed clones (Figure 19). The samples were analyzed on different gels but were exposed in parallel to ensure comparability. Only the clones with strongest upregulation were used for the following experiments (see Figure 21).

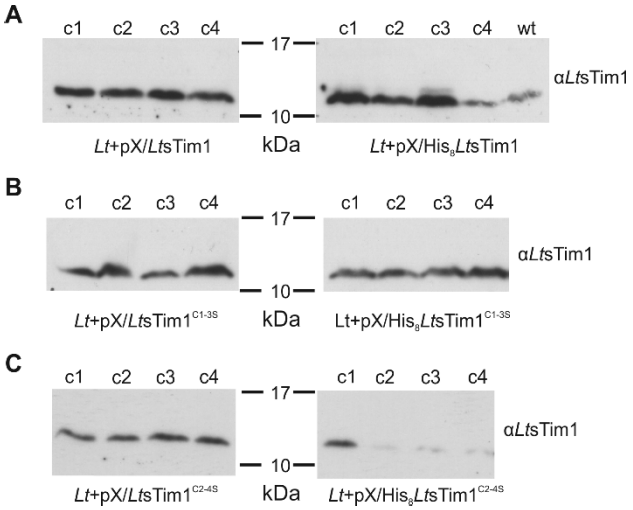

Figure 19 | Expression of *Lts*Tim1-bait protein-encoding genes. SDS-PAGE and western blot analysis with 5 × 10^7 parasites/lane under reducing conditions. Four clones of each *L. tarentolae* strain were analyzed regarding their protein levels. The primary antibody α*Lts*Tim1 was diluted 1:250, the secondary antibody αRabbit (BioRad) was used 1:5000. The calculated molecular mass of monomeric *Lts*Tim1 and the N-terminally His_8-tagged version is 11.5 kDa and 13 kDa, respectively. wt: wild-type.

3.1.3 Trapping of mixed disulfide intermediates with mutated *Lt*Erv and *Lt*sTim1

The two cysteine mutants of *LT*sTIM1 with all but one cysteines mutated to a serine (*LT*sTIM1$^{C1\text{-}3S}$ and *LT*sTIM1$^{C2\text{-}4S}$) were previously generated by Oren Shatz during an internship in our lab. The *Lt*sTim1 mutants and the single cysteine mutant *Lt*Erv^{C63S} should mechanistically trap the mixed disulfide intermediate with a potential Mia40 replacement candidate. Western blot analyses under reducing and non-reducing conditions were performed with cell lysates of the transfected *L. tarentolae* strains after alkylation with 100 mM NEM.

Mutated *Lt*Erv

Three to five clones of *L. tarentolae* transfected with pX/*LTERV*^{C63S} or pX/His$_8$*LTERV*^{C63S} were analyzed regarding their protein levels and investigated under non-reducing conditions by western blot analysis. Two clones of the *L. tarentolae* strain transfected with pX/*LTERV*^{C63S} only showed a minor upregulation of *Lt*Erv compared to the endogenous protein level observed in the wild-type sample (Figure 20, clone 2 and clone 3). These clones were not used for further experiments. All other clones of *L. tarentolae* transfected with pX/*LTERV*^{C63S} or the N-terminally His$_8$-tagged version of the protein showed a strong upregulation of the protein. For all analyzed clones of the *Lt*Erv^{C63S} mutant no additional bands that potentially reflect mixed disulfide intermediates could be observed under non-reducing conditions.

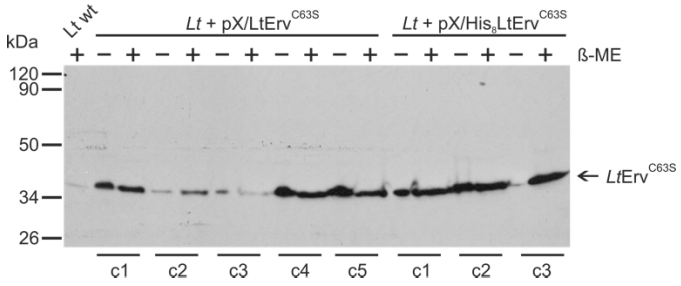

Figure 20 | *L. tarentolae* with upregulated *Lt*Erv^{C63S} levels. Representative SDS-PAGE and western blot analysis with 5 × 10^7 parasites/lane under reducing and non-reducing conditions (±β-ME). Five clones of *L. tarentolae* transfected with pX/*LTERV*^{C63S} and three clones of *L. tarentolae* transfected with pX/His$_8$*LTERV*^{C63S} were analyzed regarding their protein levels. The cells were treated with 100 mM NEM for 5 min before harvesting. The primary antibody α*Lt*Erv was diluted 1:500, the secondary antibody αRabbit (BioRad) was used 1:5000. The calculated molecular mass of monomeric *Lt*Erv and *Lt*Erv^{C63S} is 34.8 kDa and 35.9 kDa for the tagged version, respectively. wt: wild-type; β-ME: β-mercaptoethanol.

Mutated *Lt*sTim1

The western blot analysis of lysates from *L. tarentolae* transfected with the different *LT*sTIM1 mutants showed several bands with a higher molecular weight under non-reducing conditions. These bands could be reduced by the addition of β-ME (Figure 21). The pattern

was identical to the one observed for wild-type *Lt*sTim1 treated with different alkylating and redox active chemicals (see Figure 16). Hence, the trapping of mixed disulfide intermediates of *Lt*sTim1 and a potential Mia40 adapter replacement could not be further enhanced by mutating all but one cysteines of *Lt*sTim1 in the two different mutants. For the C2-4S mutant only faint bands with a higher molecular weight were detectable. Hence, upregulated wild-type *Lt*sTim1 and the C1-3S mutant were selected for further experiments.

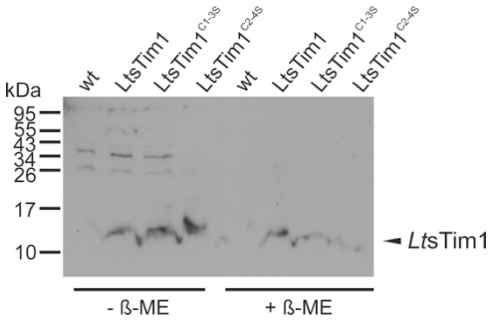

Figure 21 | Potential interaction partners of *Lt*sTim1^{wt} and *Lt*sTim1 mutants. Representative SDS-PAGE and western blot analysis with 5 × 10^7 parasites/lane under reducing and non-reducing conditions (±β-ME). One of each clones of *L. tarentolae* transfected with pX/His$_8$*LT*sTIM1 (*Lt*sTim1), pX/His$_8$*LT*sTIM1^{C1-3S} (*Lt*sTim1^{C1-3S}) and pX/His$_8$*LT*sTIM1^{C2-4S} (*Lt*sTim1^{C2-4S}) together with wild-type *L. tarentolae* lysates were analyzed by western blotting. The cells were treated with 100 mM NEM for 5 min before harvesting. The primary antibody α*Lt*sTim1 was diluted 1:250, the secondary antibody αRabbit (BioRad) was used 1:5000. The calculated molecular mass of monomeric *Lt*sTim1 and the N-terminally His$_8$-tagged version is 11.5 kDa and 13 kDa, respectively. wt: wild-type; β-ME: β-mercaptoethanol.

3.1.4 The up-regulated bait proteins are correctly localized

The localization of the different up-regulated bait proteins in *L. tarentolae* was analyzed by digitonin fractionation to test if the proteins were correctly imported into the IMS of the mitochondria. EF1α served as a cytosolic marker and was released to the supernatant already at low concentrations of digitonin. Even in the fractions without digitonin but after hypotonous swelling or without digitonin and without hypotonous swelling EF1α was partially released to the supernatant. Wild-type *Lt*Erv and *Lt*sTim1 (Figure 22, panel A) were released to the supernatant at higher concentrations of digitonin compared to the cytosolic marker. In several independent experiments the same pattern for *Lt*Erv and *Lt*sTim1 was obtained and therefore this was used as a control pattern for the mitochondrial localization of mutant *Lt*Erv and *Lt*sTim1. *Lt*Erv was always released to the supernatant at around 100-150 µg digitonin/10^8 cells whereas *Lt*sTim1 was only solubilized with the highest concentration of 2 mg digitonin/10^8 parasites or in the control with 2% Triton™ X-100. The *L. tarentolae* mutant strains were also analyzed regarding their specific solubilization pattern by western blot

analysis. In contrast to cytosolic EF1α, the proteins appeared to be correctly localized to the mitochondria of *L. tarentolae* and showed a similar pattern as endogenous *Lt*Erv. No protein was observed in the supernatant fractions without or with low concentrations of digitonin. The upregulated proteins of the *Lt*sTim1 mutants containing only one cysteine were also correctly localized to the IMS. This behavior is not self-explanatory because the mutant *Lt*sTim1 cannot form internal disulfide bonds anymore, which are usually a prerequisite for trapping the substrates in the IMS. Potential reasons for this behavior are discussed in section 4. Answering the question, to which membrane *Lt*Erv is associated would be also interesting but will require the use of additional marker antibodies and was not part of this work.

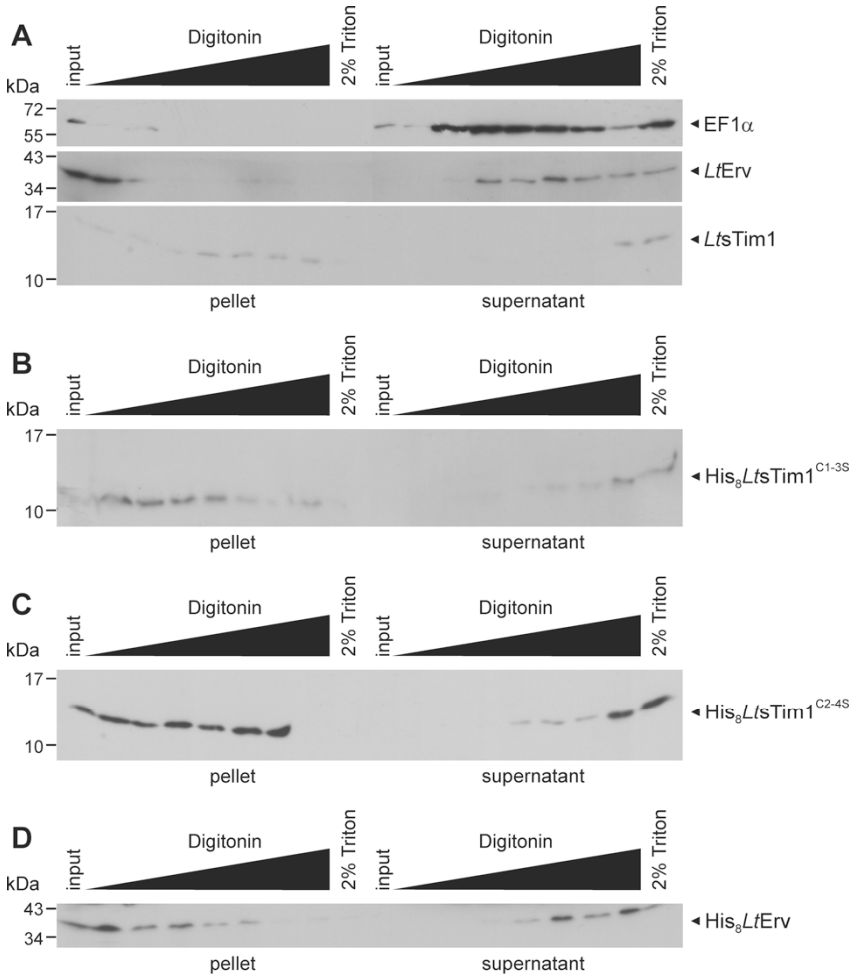

Figure 22 | Differential fractionation of whole cell lysates of *L. tarentolae*. Hypotonous swelling in combination with increasing digitonin concentrations ranging from 0-2 mg/10^8 cells were used for differential fractionation of the cells. Parasites treated with 2% Triton™ X-100 served as a positive control for complete solubilization. A: *L. tarentolae* wild-type lysates showing the localization of endogenous *Lt*Erv and *Lt*sTim1 protein. EF1α served as a marker for cytosolic localization whereas *Lt*Erv and *Lt*sTim1 served as marker proteins for the IMS of the mitochondria. B-D: Differential fractionation of *L. tarentolae* strains expressing the indicated His_8-tagged *Lt*sTim1- or *Lt*Erv-proteins.

3.1.5 Enrichment of mixed disulfide intermediates by affinity chromatography

Only a small proportion of the bait protein is probably bound as a mixed disulfide intermediate with its potential interaction partner and is therefore difficult to detect in western blot analyses without prior protein enrichment. Thus, affinity chromatography by Ni-NTA agarose with His_8-tagged bait proteins was performed under native and denaturing conditions. A native affinity chromatography with *Lt*Erv as the bait protein led to a slight enrichment of the *Lt*Erv fraction, although no bands with a higher molecular weight were visible under non-reducing conditions (Figure 23).

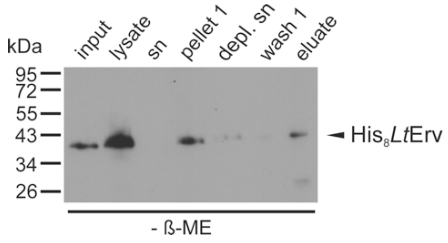

Figure 23 | Native pull-down with N-terminally His_8-tagged *Lt*Erv. Cell lysis was done by hypotonous swelling and shearing. The cells were treated with 100 mM NEM for 5 min prior to harvesting. All fractions were investigated under non-reducing conditions (-β-ME) in order to identify mixed disulfide intermediates between *Lt*Erv and a potential Mia40 adapter replacement. β-ME: β-mercaptoethanol; sn: supernatant; depl.: depleted.

A denaturing pull-down with *Lt*Erv^{C63S} using 8 M urea and 2% Triton™ X-100 as the denaturing agents led to a stronger enrichment of the bait protein than under native conditions, but also in this experiment no bands with a higher molecular weight were visible under non-reducing conditions by western blot analysis (Figure 24). The chance to identify potential interaction partners of *Lt*Erv in mass spectrometry analysis was therefore very little and a pull-down protocol for *Lt*sTim1 should be established as the next step because for this bait protein faint bands with a higher molecular weight were already detectable endogenously.

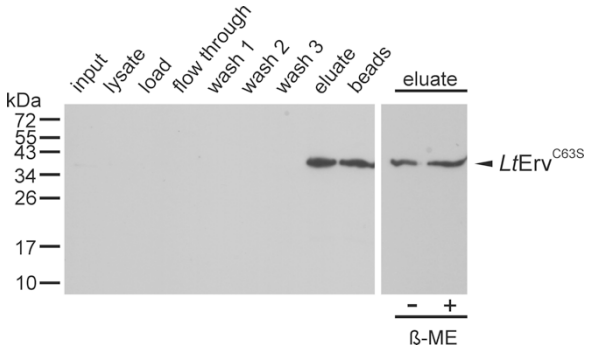

Figure 24 | Denaturing pull-down with N-terminally His_8-tagged *Lt*Erv^{C63S}. Cell lysis and denaturation were done with a lysis buffer containing 8 M urea and 2% Triton™ X-100. The eluate fraction was also investigated under non-reducing conditions (-β-ME) in order to identify mixed disulfide intermediates between *Lt*Erv and a potential Mia40 adapter replacement. β-ME: β-mercaptoethanol.

The protocol for denaturing affinity chromatography was also used for the *L. tarentolae* strains with upregulated *Lt*sTim1$^{C1\text{-}3S}$ and *Lt*sTim1$^{C2\text{-}4S}$ but did not lead to an enrichment of the mutated bait protein even with altered buffer compositions or the use of guanidine-HCl as the denaturing agent, thus raising the question of stability and expression levels. For all protocols that were tested with all different *Lt*sTim1-strains, no enrichment of the bait protein was possible in the eluate fraction (data not shown). Thus, no samples of these trials were further analyzed by mass spectrometry.

3.1.6 Screening for a defined *Leishmania tarentolae* culture medium

For the identification of potential interaction partners of *Lt*Erv and *Lt*sTim1, a SILAC (=stable isotope labeling of amino acids in cell culture) approach followed by mass spectrometry was initially planned to discriminate between unspecific bindings and actual interaction partners. Such experiments require a defined culture medium to ensure a labeling efficiency of at least 95%. With a defined medium, the incorporation of heavy amino acids is not diluted by unlabeled amino acids.

A medium screen was performed with six different media that are also available as SILAC-media with heavy isoforms of arginine and lysine with different supplements. To exclude a pH-dependent effect on the cell survival, the pH of the different media was determined and revealed comparable values between 7.0 and 7.39 and a pH of 6.92 for the BHI control. The concentrations of folic acid, hemin solution and FCS were titrated resulting in a total number of 216 different media that were screened for their suitability as BHI-replacement for following SILAC experiments. The cells were visually analyzed under the microscope and RPMI-1640, DMEM and DMEM/F12 with all different variants of supplements could be excluded for further analyses because the cells completely died after one to three days, which is not long enough for sufficient labeling with heavy amino acids in a SILAC experiment.

Subsequently, selected compositions of IMDM, McCoy's 5A and MEM were further investigated in comparison to BHI as a positive control in a growth curve analysis (Figure 25). The cells showed medium specific maximum growth rates and doubling times that were calculated from the growth curves and are listed in Table 13. The highest maximum cell density and shortest doubling time were observed in McCoy's media containing 10% FCS. The cells in this culture grew even better than in the BHI control. For all media, the growth of cells was better with 10% FCS compared to 5% FCS, which shows that addition of serum is necessary

when using a defined medium. IMDM supplemented with 0.5% AlbuMax™ as a serum-free alternative confirmed this result because the cells did not grow at all.

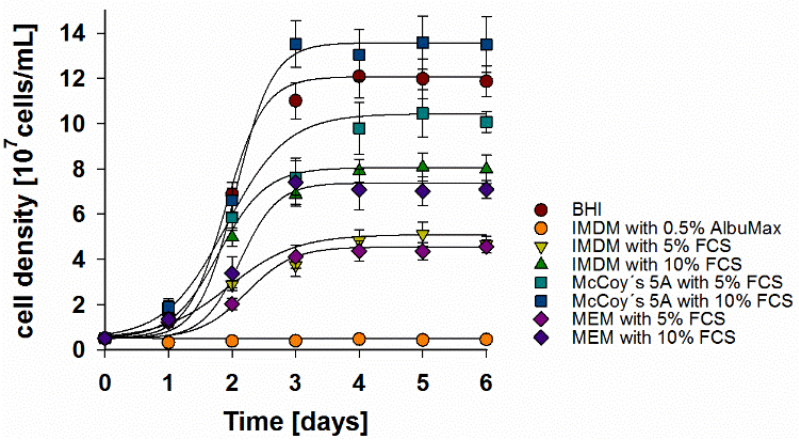

Figure 25 | Growth rates of *L. tarentolae* in different media. *L. tarentolae* cells were cultivated under normal conditions in different media. The cell density was determined every 24 h by counting. The data was analyzed with SigmaPlot 13 using a sigmoidal curve fit. All data points represent the mean ± standard deviation from two independent experiments. FCS: fetal calf serum.

The parasites were also analyzed regarding their cell morphology (Figure 26). Cells cultivated in IMDM supplemented with 0.5% AlbuMax™ as a serum-free alternative served as a negative control and showed aggregates of cells with reduced motility. Parasites cultivated in IMDM, MEM or McCoy's 5A supplemented with 10% FCS all showed a normal cell morphology and a motility comparable to the positive control with *L. tarentolae* cultivated in BHI.

Table 13 | Growth parameters for *L. tarentolae* from Figure 25. Comparison of growth parameters for *L. tarentolae* in different defined culture media in comparison to BHI.

Medium	Maximum cell density [10^7 cells/mL]	Doubling time [h]
BHI	12.08	12.41
IMDM + 0.5% AlbuMax™	0.66	N/A
IMDM + 5% FCS	5.09	22.02
IMDM + 10% FCS	8.05	17.85
McCoy's + 5% FCS	10.44	18.85
McCoy's + 10% FCS	13.57	9.42
MEM + 5% FCS	4.55	13.02
MEM + 10% FCS	7.37	9.80

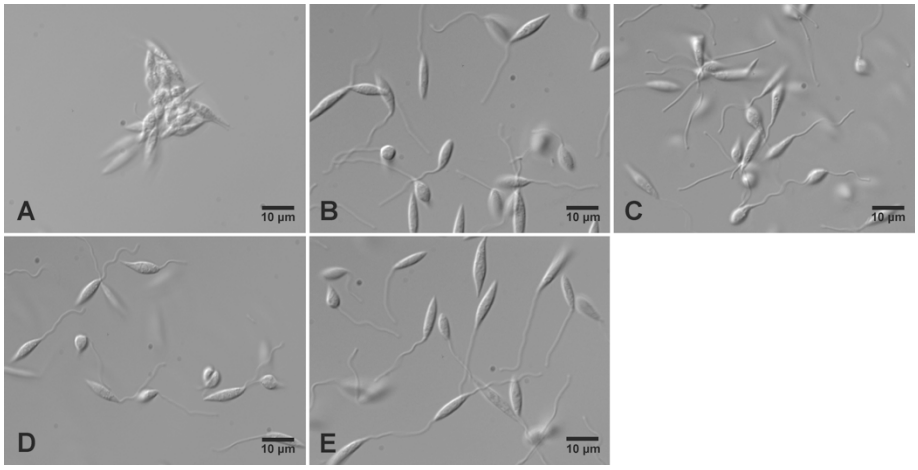

Figure 26 | Morphology of *L. tarentolae* in different media. Light microscopy of mid-log phase *L. tarentolae* promastigotes in A) IMDM + 0.5% AlbuMax™, B) BHI, C) IMDM + 10% FCS, D) MEM + 10% FCS or E) McCoy's 5A + 10% FCS.

The FCS used for the experiments shown above also contains amino acids and therefore needs to be changed to dialyzed FCS to avoid dilution of the labeling efficiency in a SILAC experiment. Hence, the influence of dialyzed FCS on the parasite growth was determined and cells were cultivated in IMDM supplemented with 10% dialyzed FCS. Cells cultivated with BHI and cells cultivated with IMDM supplemented with 10% non-dialyzed FCS served as positive controls. All media were supplemented with 10 µg/ml hemin chloride. Cells cultivated in IMDM with 10% dialyzed FCS died within 24 h whereas the positive controls showed normal growth rates and morphology. Hence, a SILAC experiment with *L. tarentolae* was not possible because no suited defined cultivation medium that might be used instead of undefined BHI could be identified in this work. Further testing of different supplements would be necessary to determine a defined medium for the use in a SILAC experiment.

3.1.7 Identification of interaction partners with BioID

As the different trials of trapping a mixed disulfide intermediate of *Lt*Erv or *Lt*sTim1 with a potential Mia40 adapter replacement were not successful, BioID should be tested as an independent approach for finding potential interaction partners of the two bait proteins. *L. tarentolae* was transfected with the constructs shown in Figure 27 containing a Myc-tagged BirA* fused to the N-terminus of the bait protein.

The parasites transfected with the BirA*-*LT*sTIM1 construct were first analyzed by immunofluorescence microscopy. No signal for Myc and Streptavidin could be detected after an unspecific binding of the secondary antibody was excluded by omitting the primary antibody. Therefore, the success of the transfection should first be confirmed by western blot

analysis. Only unspecific signals for the Myc-antibody could be detected and no streptavidin-signal was visible. The level of overexpression was difficult to elucidate because of the problems with the *Lt*sTim1-antibody described before. Owing to that difficulties, the strains transfected with the BirA*-*LTERV* construct should be analyzed instead. Western blot analysis revealed much higher levels of *Lt*Erv in the control sample (*L. tarentolae* transfected with pX/*LTERV*) compared to the strains with the BirA*-*Lt*Erv fusion protein. No signal was detectable for streptavidin, which showed that no biotinylation of proteins took place under the used experimental conditions. Therefore, prolonged incubation times with 150 µM biotin for 48 h or 72 prior to harvesting were also tested and showed the same results than a 24 h incubation (data not shown). In summary, the identification of a potential Mia40 adapter replacement was not possible in this work using BioID.

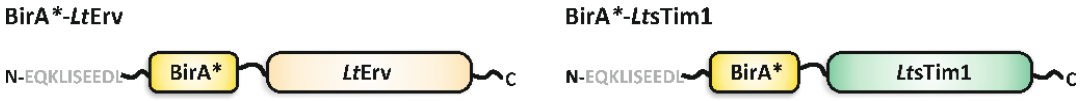

Figure 27 | Constructs for BioID experiments. The constructs were cloned into the pX-backbone vector for expression in *L. tarentolae*. The proteins contain a Myc-tagged BirA* fused to the N-terminus of *Lt*Erv or *Lt*sTim1. The strategy is based on the publication of Roux *et al.* 2014 [74].

3.1.8 Redox state of Erv in *Leishmania tarentolae*

To determine the redox state of endogenous *Lt*Erv, a mobility shift assay was performed. A redox mobility shift assay using alkylation by mm(PEG)$_{24}$, which leads to a mass shift of 1.2 kDa per accessible cysteine residue, was therefore established in this work. The first lane in Figure 28 showed reduced, unmodified *Lt*Erv with an expected molecular mass of around 35 kDa. Lanes 2-6 showed *Lt*Erv signals for differently treated *L. tarentolae* samples modified by mm(PEG)$_{24}$. In lane 2 the physiological redox state of *Lt*Erv was elucidated. There were mainly two bands detectable, of which the lower one corresponds to the size of unmodified *Lt*Erv as shown in lane 1. The band with the higher molecular weight indicated the modification of probably one cysteine residue of *Lt*Erv. The results suggest that in the predominant form all but one of the cysteine residues of *Lt*Erv are either oxidized or inaccessible to mm(PEG)$_{24}$ under physiological conditions. The next lanes showed the modification of mildly (lane 3) or strongly (lane 4) reduced *Lt*Erv by TCEP at either 27°C or 95°C. A shift towards higher molecular weight species of *Lt*Erv indicating the modification of reduced cysteines by mm(PEG)$_{24}$ was detectable. For the strong reduction of the sample only one band reflecting the modification

of all cysteines was expected in theory. In this experiment, mainly two bands with a higher molecular weight were observed indicating that either not all cysteines were accessible even after a theoretically complete reduction or that the concentration of mm(PEG)$_{24}$ was not sufficient for modification of all cysteines. The second possible explanation was excluded by titrating the concentration of the alkylating agent leading to the same result. With the samples analyzed in the two last lanes it should be tested if the concentration of NEM is sufficient to alkylate free cysteines in living *L. tarentolae* cells as it was done for several other experiments in order to freeze the redox state of the cell and potentially trap mixed disulfide intermediates between *Lt*Erv or *Lt*sTim1 and a potential Mia40 adapter replacement. A shift towards lower molecular species of *Lt*Erv compared to lane 2 and 3 was observed indicating that the concentration of NEM was at least partially sufficient to enter the cell and block free cysteines in living *L. tarentolae*. In summary, endogenous *Lt*Erv appears to be mainly oxidized *in vivo*.

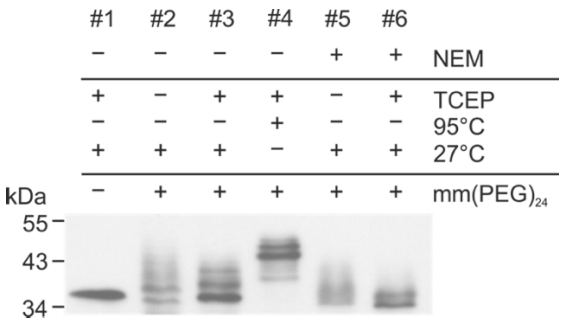

Figure 28 | Evaluation of the physiological redox state of *Lt*Erv using mm(PEG)$_{24}$-redox mobility shift assays. *Leishmania tarentolae* promastigotes were treated with or without 100 mM NEM in order to preserve the redox state and to block free thiol groups. The cells were lysed in SDS-sample buffer with or without the reducing agent TCEP at 27 or 95°C as indicated. Free thiols were subsequently alkylated with mm(PEG)$_{24}$, which leads to a theoretical mass shift of 1.2 kDa per accessible cysteine residue. Lysates containing 5 × 10^7 parasites per lane were analyzed by SDS-PAGE and western blotting against *Lt*Erv.

3.1.9 Overexpression of the gene encoding *Pf*Erv in *Leishmania tarentolae*

P. falciparum ERV1 was cloned with or without an N-terminal His$_8$-tag in the *L. tarentolae* vector pX-backbone. The protein-coding sequences of both plasmids were confirmed by sequencing before the transfection of *L. tarentolae*. The heterologous expression of recombinant *PFERV* was confirmed by western blot analysis of *L. tarentolae* lysates with a *Pf*Erv-specific antibody (Figure 29). *Leishmania tarentolae* and *P. falciparum* wild-type lysates served as a negative and positive controls, respectively. There was a band detectable with the expected mass for His$_8$-tagged *Pf*Erv at around 17 kDa (calculated molecular mass: 18.5 kDa) in addition to an unspecific band below that was also detected in the negative control. The

upregulation of His_8-tagged *Pf*Erv appeared to be strongest with 10 × G418 (1 mg/ml) at comparable allover protein levels shown by the PonceauS-staining of the membrane (data not shown). This G418-concentration was used for purification trials by affinity chromatography using Ni-NTA agarose columns. *Pf*Erv should be purified from *L. tarentolae* because different purification trials with *E. coli* were not successful before and resulted in the formation of inclusion bodies [38]. There are a lot of examples in literature with biologically active, natively processed proteins produced in *L. tarentolae* as reviewed by Breitling *et al.* 2002 [60]. The resulting eluate fraction was planned to be used for crystallization trials and kinetic analyses.

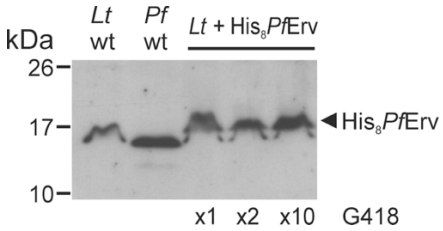

Figure 29 | Recombinant expression of *PFERV* in *L. tarentolae*. *Leishmania tarentolae* and *P. falciparum* wild-type lysates (*Lt* wt and *Pf* wt) served as negative and positive controls, respectively. The selection marker G418 was added in different concentrations to parasites producing His_8-tagged *Pf*Erv. The calculated molecular mass of His_8-tagged *Pf*Erv is 18.5 kDa.

Different protocols were tested for the purification of *Pf*Erv from *L. tarentolae*. The *L. tarentolae* strains producing N-terminally His_8-tagged *Pf*Erv were cultivated in 1 liter of mid-log phase cells. In a first trial a protocol similar to the one used for the purification of *Pf*GR from *E. coli* was used (see section 2.5.1; buffer I and II GR). The cell lysis was performed by sonication and the success of the lysis was checked under the microscope. A prolonged sonication (10 cycles with each 10 sec) was necessary to lyse the parasites and the column volume was reduced to 100 µl Ni-NTA (protocol a). A western blot analysis was performed with the *Pf*Erv-specific antibody and a signal at around 18 kDa corresponding to the molecular mass of *Pf*Erv was detected in the input and pellet fraction. Only a faint band for *Pf*Erv was visible in all the other fractions including the eluate fraction showing that under these conditions no enrichment of *Pf*Erv was possible.

To increase the solubility of the protein, different other protocols were tested with the same negative result. A disruption buffer containing 0.25% (v/v) Tween 20, 20 mM imidazole, 300 mM NaCl and 50 mM sodium phosphate with a pH of 8.5 at 4°C combined with sonication was tested with two rounds of lysis (protocol b). In another protocol, a hypotonic buffer containing 1 mM Tris/HCl with pH 7.9 at 4°C combined with sonication in two rounds of lysis was tested (protocol c). Furthermore, the pellet resulting from protocol b was solubilized with

250 µg digitonin per 10^8 cells. This approach also did not lead to an enrichment of *Pf*Erv in the eluate fraction. Taken together *Pf*Erv could be successfully produced in *L. tarentolae* but a native purification for further studies was not possible under the chosen conditions.

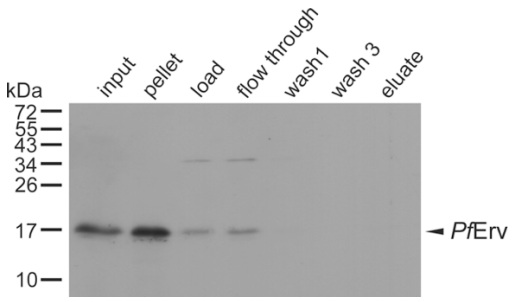

Figure 30 | Native pull-down with a *L. tarentolae* strain producing N-terminally His_8-tagged *Pf*Erv. Cell lysis was done according to protocol a) by sonication. The different fractions were analyzed by western blotting and the result is representative also for the other purification trials with altered conditions.

3.1.10 Detection of potential interaction partners of *Pf*Erv

Potential interaction partners of *Pf*Erv in *P. falciparum* 3D7 trophozoite lysates were analyzed by western blotting under reducing and non-reducing conditions with a *Pf*Erv-specific antibody [38]. The parasites were treated with or without 100 mM NEM for 5 min to stabilize potential disulfide-bridged interaction partners. Figure 31 shows a strong *Pf*Erv-specific signal with the expected mass for the monomeric isoform at around 17 kDa for all conditions. There are three additional bands visible in the sample treated with 100 mM NEM that was analyzed under non-reducing conditions. The protein detected with the highest molecular mass at around 34 kDa might indicate a dimeric isoform of *Pf*Erv. This band is not visible under reducing conditions as expected for disulfide-bridged protein interactions. Band 2 at around 26 kDa could indicate a potential interaction partner of *Pf*Erv might be also disulfide-bridged because it disappears under reducing conditions. Band 3 runs below the monomeric isoform of *Pf*Erv between 10 and 17 kDa and might indicate a monomeric isoform of *Pf*Erv with intramolecular disulfide-bridges that are stabilized by the alkylating agent NEM because this band is not visible in the sample that was analyzed under reducing conditions after NEM-treatment.

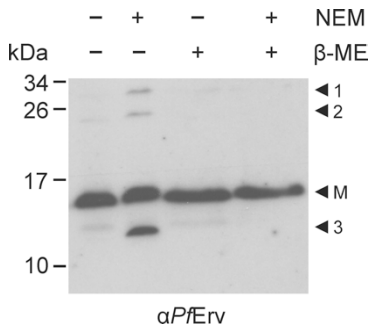

Figure 31 | Identification of potential interaction partners of *Pf*Erv. *P. falciparum* 3D7 trophozoites were treated with or without 100 mM NEM as indicated. Parasite lysates containing 10^7 parasites per lane were analyzed by (non-)reducing SDS-PAGE and western blotting. M, monomeric *Pf*Erv (with a calculated molecular mass of 17.2 kDa). Bands 1 and 2 might indicate either disulfide-bonded dimeric *Pf*Erv or potential interaction partners of *Pf*Erv.

3.2 Glutaredoxins

The second objective of this PhD was to analyze the general applicability of the results obtained from prior analysis of *Sc*Grx7, which revealed a distinct glutathione scaffold and activator site during the MD thesis of Patricia Begas. Thus, *Pf*Grx was analyzed as a non-related model system and the results were published in Nature Communications with the title "Glutaredoxin catalysis requires two distinct glutathione interaction sites" by Begas *et al.* 2017 [116]. Additional residues of *Sc*Grx7 that might be part of the glutathione activator site were analyzed to gain more insights into the exact structure-function relationships of Grx and to define the substrate binding sites in more detail.

3.2.1 Selection of residues of *Pf*Grx and *Sc*Grx7 mutants

First, homologous residues of the proposed glutathione activator and glutathione scaffold site in *S. cerevisiae* were selected in Grx from the non-related parasite *P. falciparum*. Lys26 from *Pf*Grx is corresponding to Lys105 of *Sc*Grx7 and is shown in Figure 32 as residue 1 in strand 1. This residue is conserved in many Grx [106, 112, 113, 156]. Furthermore, the positive charge of this amino acid could help to bind the substrate GSH as GS^-. The acidic residue Asp90 of *Pf*Grx was chosen as the homolog of residue Glu170 in *Sc*Grx7 and is shown as residue 6 in Figure 32. This residue could contribute to a strong ionic glutathione interaction due to its charge. Furthermore, residue 6 is conserved in enzymatically active in contrast to enzymatically inactive Grx. Alanine mutants of both residues of *Pf*Grx were generated by side-directed mutagenesis. The correct mutations were confirmed by sequencing.

For a potential further mapping of the glutathione activator site, several *Sc*Grx7 mutants were selected and subsequently analyzed in GSSCys or HEDS steady-state kinetic assays. First, Tyr110 in the CPYS-motif in helix 2 of *Sc*Grx7 was selected as a potential glutathione interaction residue. The hydroxyl group of the conserved residue Tyr110 could contribute to the glutathione activator site because it is replaced in enzymatically inactive Grx [112, 113] and sticks out on the protein surface. Phe, His and Ala mutants were generated of residue Tyr110 and subsequently analyzed in GSSCys and HEDS assays. The two acidic amino acids Asp144 and Glu147 in helix 3 (residue r_3* in Figure 32) were selected as potential glutathione activator residues because of geometric reasons and Glu147 is also conserved in many enzymatically active Grx. As another potential residue that could contribute to the glutathione activator site Arg153 in the loop was chosen (residue 3, Figure 32). Charge inversion and alanine mutants of Asp144, Glu147 and Arg153 were generated and subsequently analyzed in a GSSCys assay.

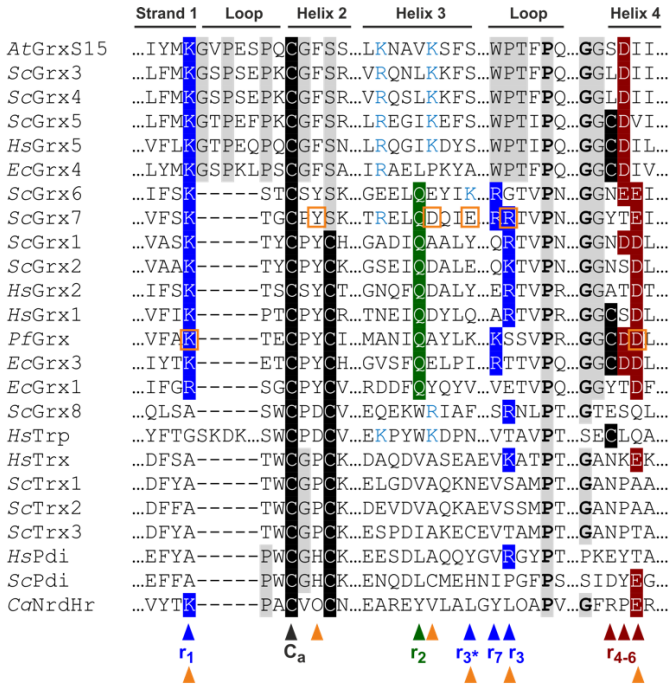

Figure 32 | Sequence alignment of different members of the thioredoxin superfamily. The sequences of different glutaredoxin isoforms were compared with other members of the thioredoxin superfamily from *A. thaliana* (*At*), *S. cerevisiae* (*Sc*), *Homo sapiens* (*Hs*), *P. falciparum* (*Pf*), *E. coli* (*Ec*) and *C. glutamicium* (*Cg*). The alignment was done manually based on structural overlays. The figure was adapted from Begas *et al*. [116]. The numbering of the residues $r_{1\text{-}7}$ as potential glutathione-interacting amino acids is based on previous publications [106, 112]. The residues marked with orange boxes and arrows were analyzed as potential glutathione-interacting amino acids in this work.

3.2.2 Purification of recombinant *Pf*Grx and *Sc*Grx mutants

The different mutants of *Sc*Grx7 and *Pf*Grx were purified by Ni-NTA affinity chromatography for kinetic characterization. The obtained eluate fractions were analyzed regarding their purity on a SDS-gel. Figure 33 shows gels with representative eluate fractions. The observed size for *Pf*Grx fits to the calculated molecular mass of 13.6 kDa. *Sc*Grx7 (calculated molecular mass of 20.2 kDa) runs above 25 kDa as observed before [112] and shows only a minor fraction of degradation product or contamination. The protein concentrations were determined by Bradford assays. Average yields from up to seven independent protein purifications of *Pf*Grx$^{C32S/C88S}$, *Pf*Grx$^{C32S/C88S/K26A}$ and *Pf*Grx$^{C32S/C88S/D90A}$ were 8.8±3.8, 31±10 and 5.1±1.9 mg of recombinant protein per liter of *E. coli* culture, respectively. Average yields from up to seven independent protein purification experiments for each *Sc*Grx7 mutant were highly reproducible and ranged from 12.6±4.1 to 16.4±7.7 mg of recombinant protein per liter of *E. coli* culture depending on the mutant.

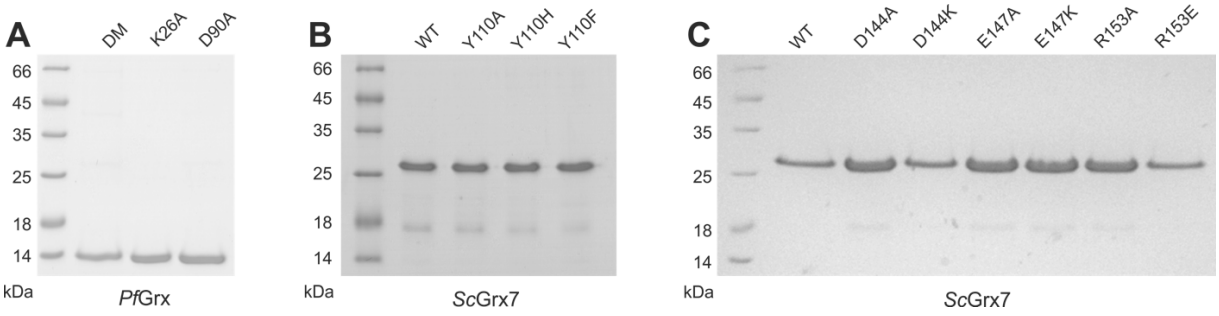

Figure 33 | Purification of recombinant wild-type and mutant *Sc*Grx7 and *Pf*Grx enzymes. The eluate fractions of representative Grx purifications by Ni-NTA affinity chromatography are shown on a 15% SDS-gel. A: Mutants of the double cysteine mutant *Pf*Grx$^{C32S/C88S}$ run according to the calculated molecular mass of 13.6 kDa. DM: *Pf*Grx$^{C32S/C88S}$, K26A: *Pf*Grx$^{C32S/C88S/K26A}$, D90A: *Pf*Grx$^{C32S/C88S/D90A}$. B: Tyr110-mutants of *Sc*Grx7. C: Asp144, Glu147 and Arg153 mutants of *Sc*Grx7. The calculated molecular mass of *Sc*Grx7 is 20.2 kDa. WT: *Sc*Grx7 wild-type, Y110A: *Sc*Grx7^{Y110A}, Y110H: *Sc*Grx7^{Y110H}, Y110F: *Sc*Grx7^{Y110F}, D144E: *Sc*Grx7^{D144E}, D144A: *Sc*Grx7^{D144A}, D144K: *Sc*Grx7^{D144K}, E147A: *Sc*Grx7^{E147A}, E147K: *Sc*Grx7^{E147K}, R153A: *Sc*Grx7^{R153A}, R153E: *Sc*Grx7^{R153E}. Panel A was adapted from Begas *et al.* 2017 [116].

3.2.3 Kinetics of *Pf*Grx mutants in the GSSCys assay confirm a conserved mechanism

It was tested if the results obtained from kinetic characterization of *Sc*Grx7 mutants indicate a general catalysis mechanism with two distinct glutathione interaction sites as previously suggested [106, 116]. Therefore, corresponding point mutants of the non-related *P. falciparum* enzyme *Pf*Grx were analyzed in Grx steady-state kinetic assays. The mutants *Pf*Grx$^{C32S/C88S/K26A}$ and *Pf*Grx$^{C32S/C88S/D90A}$ were generated in the monothiol double mutant

*Pf*Grx$^{C32S/C88S}$, which has only one cysteine to avoid side reactions that might complicate the interpretation of the kinetics [138].

Recombinant mutants obtained from affinity chromatography were subsequently analyzed in a GSSCys and HEDS assay with *Pf*Grx$^{C32S/C88S}$ as a control. In a first set of experiments, the effects of the mutations were analyzed in steady-state assays with variable GSH concentrations at fixed GSSCys concentrations or variable GSSCys concentrations with fixed GSH concentrations, respectively. Both mutants, as well as the control, revealed ping-pong kinetics shown by parallel lines for the different substrate concentrations in the Lineweaver-Burk blots (Supplementary figure 1, panel b, c, e and f). This indicates that a general mechanism with separated oxidative and reductive half-reaction as it was observed before for the *Sc*Grx7 mutants was not affected by the mutations [116]. The activity of *Pf*Grx$^{C32S/C88S/K26A}$ in the GSSCys assay was strongly reduced and the final concentration of that mutant had to be increased by factor 10, whereas the activity of *Pf*Grx$^{C32S/C88S/D90A}$ was similar to the control (Supplementary figure 1, panel a and d) and the final concentration of *Pf*Grx$^{C32S/C88S/D90A}$ in the assay was the same as used for the control. The enzyme-specific apparent parameters K_m^{app} and k_{cat}^{app} were derived from analysis according to Michaelis-Menten, Lineweaver Burk, Eadie Hofstee and Hanes theory and showed high similarities for all analyses. Supplementary table 1 lists selected kinetic constants from non-linear regression analysis of the Michaelis-Menten plots of Supplementary figure 1. In Figure 34 the apparent kinetic constants are visualized as bar charts (panel A, B and C). The replacement of Lys26 in *Pf*Grx by an alanine led to a decrease of the k_{cat}^{app} of 68-95% for both substrates indicating a role of this residue for the oxidative half-reaction with GSSCys as well as the reductive half-reaction with GSH (Figure 34, panel A). Furthermore, *Pf*Grx$^{C32S/C88S/K26A}$ showed increased K_m^{app} (GSSCys) values and decreased K_m^{app} (GSH) values compared to the control. The observed effects on the k_{cat}^{app} and K_m^{app} are mostly significant (statistical analyses are listed in Supplementary table 8 A). The catalytic efficiencies defined by the ratio k_{cat}^{app}/K_m^{app} were decreased by 62-67% for the reductive half-reaction with GSH and 95% for the oxidative half-reaction with GSSCys for *Pf*Grx$^{C32S/C88S/K26A}$ (Figure 34, panel C).

The replacement of Asp90 in *Pf*Grx by an alanine affected the kinetic parameters to a smaller extent than the Lys26 mutant. The *Pf*Grx$^{C32S/C88S/D90A}$ mutant showed slightly reduced k_{cat}^{app} and K_m^{app} values for GSH whereas the k_{cat}^{app} and K_m^{app} values for GSSCys were increased (Figure 34, panel A and B; Supplementary table 1). The catalytic efficiencies k_{cat}^{app}/K_m^{app} for

GSSCys were reduced by around 20% in contrast to the catalytic efficiencies for GSH that were increased to 125-144% (Figure 34, panel C; Supplementary table 1).

For further analyses of the kinetic properties of the two alanine mutants, secondary plots were generated (Supplementary figure 2). The values for K_m^{app} and k_{cat}^{app} were obtained from the Michaelis-Menten plots in Supplementary figure 1. These plots allow the estimation of the true k_{cat} value from the y-axis intercept ($1/k_{cat}$) and the true K_m value from the x-axis intercept ($-1/K_m$). The estimated true kinetic parameters are listed in Table 14. Both of the mutants as well as the control tended to have infinite true k_{cat} and K_m values as shown before for *Sc*Grx7 [116]. This means that the enzymes are not saturated by both of the substrates. The equation $[E]/V = \Phi_1/[GSSCys] + \Phi_2/[GSH]$ can be used to describe the velocity of such a ping-pong reaction. The Dalziel coefficient Φ_1 is the slope of the secondary plot for k_{cat}^{app} (GSH), whereas the Dalziel coefficient Φ_2 is the slope of the secondary plot for k_{cat}^{app} (GSSCys). The reciprocal Dalziel coefficient $1/\Phi_1$ can be interpreted as the apparent rate constant k_{ox}^{app} for the oxidative half-reaction with GSSCys, whereas $1/\Phi_2$ can be interpreted as the apparent rate constant k_{red}^{app} for the reductive half-reaction with GSH. These values for *Pf*Grx$^{C32S/C88S/K26A}$ and *Pf*Grx$^{C32S/C88S/D90A}$ as well as for the corresponding control are listed in Table 14. Both reciprocal Dalziel coefficients were highly similar to the corresponding apparent catalytic efficiencies as it was also observed before for the homologous *Sc*Grx7 mutants [116]. For *Pf*Grx$^{C32S/C88S/K26A}$, both values were decreased by up to one or two orders of magnitude, whereas for *Pf*Grx$^{C32S/C88S/D90A}$ only $1/\Phi_1$ was slightly reduced in contrast to the second reciprocal Dalziel coefficient $1/\Phi_2$ (Figure 34, panel D and Table 14).

Table 14 | Kinetic constants for *Pf*Grx mutants in the GSSCys assay. Estimated true kinetic constants k_{cat}, K_m and Dalziel coefficients of *Pf*Grx$^{C32S/C88S}$ and the mutants K26A and D90A in the GSSCys assay. The constants were obtained from Supplementary figure 2. DM: *Pf*Grx$^{C32S/C88S}$; K26A: *Pf*Grx$^{C32S/C88S/K26A}$; D90A: *Pf*Grx$^{C32S/C88S/D90A}$. The data was already published in Begas *et al.* 2017 [116].

***Pf*Grx**	**$1/\Phi_1$** ($M^{-1}s^{-1}$)	**$1/\Phi_2$** ($M^{-1}s^{-1}$)	**k_{cat}** (s-1)	**$K_{m\ (GSH)}$** (mM)	**$K_{m\ (GSSCys)}$** (mM)
DM	1.3×10^6	1.2×10^5	∞	∞	∞
K26A	6.9×10^4	5.0×10^4	34 - ∞	0.7 - ∞	1.2 - ∞
DM	1.4×10^6	1.2×10^5	289 - ∞	2.2 - ∞	0.4 - ∞
D90A	1.0×10^6	1.7×10^5	∞	∞	∞

In summary, the role of residue r_1 (Figure 32) as a GSH and enzyme activator for Grx catalysis in the GSSCys assay could be confirmed using *Pf*Grx from the non-related apicomplexan *P. falciparum*. The determined kinetic constants of *Pf*Grx$^{C32S/C88S/K26A}$ revealed extreme similarities to the homologous mutant *Sc*Grx7^{K105A} in the GSSCys assay and support a conserved catalytic mechanism. The same is true for the role of residue r_6 with highly similar results for *Pf*Grx$^{C32S/C88S/D90A}$ compared to the homologous mutant *Sc*Grx7^{E170A}. Both mutants decelerated the reaction with GSSCys as a substrate in the GSSCys assay but not with GSH. In summary, also the role of residue r_6 (Figure 32) as a scaffold site in the GSSCys assay could be confirmed using *Pf*Grx.

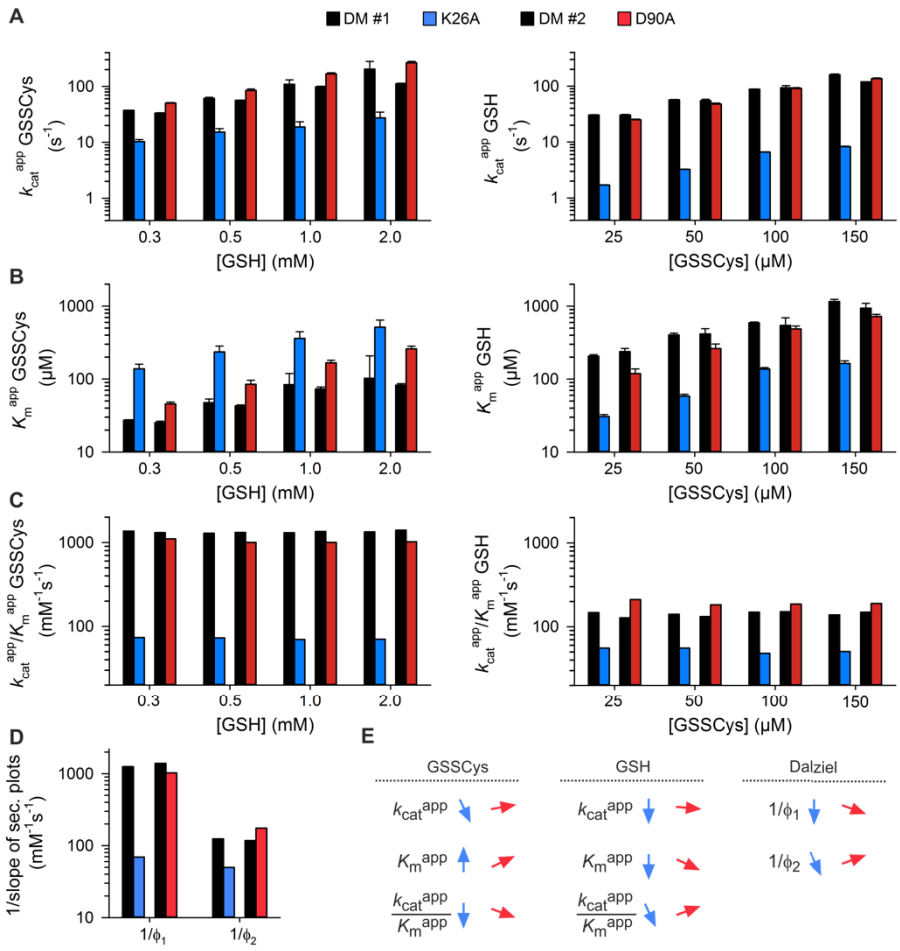

Figure 34 | Relevance of Lys26 and Asp90 of *Pf*Grx in the GSSCys assay. A: Selected k_{cat}^{app} values of the *Pf*Grx mutants for GSSCys and GSH obtained from Supplementary figure 1. B: Selected K_m^{app} values for the *Pf*Grx mutants for GSSCys and GSH obtained from Supplementary figure 1. C: The catalytic efficiencies for GSSCys and GSH were calculated from panels A and B. D: The reciprocal Dalziel coefficients were obtained from the slopes of the secondary plots in Supplementary figure 2. E: Summary of the kinetic parameters from panels A, B and C. DM: *Pf*Grx$^{C32S/C88S}$; K26A: *Pf*Grx$^{C32S/C88S/K26A}$; D90A: *Pf*Grx$^{C32S/C88S/D90A}$. Adapted from Begas *et al.* 2017 [116].

3.2.4 Kinetics of *Pf*Grx mutants in the HEDS assay confirm a conserved mechanism

It was tested if the generalized catalytic mechanism is also observed in the HEDS assay. The primary analyses of the *Pf*Grx mutants in the HEDS assay are shown in Supplementary figure 3, the apparent rate constants are listed in Supplementary table 2 and secondary plots are shown in Supplementary figure 4. Statistical analyses can be found in Supplementary table 8 B. As observed for the *Sc*Grx7 mutants analyzed in the HEDS assay, all *Pf*Grx mutants showed a sequential kinetic pattern in the Lineweaver-Burk plots with a common x axis interception. Replacement of Lys26 to alanine resulted in a decrease of the k_{cat}^{app} for both substrates of 89-96%, whereas the K_m^{app} for GSH stayed rather constant and the K_m^{app} for HEDS increased to 203-270% resulting in a decrease of the apparent catalytic efficiencies k_{cat}^{app}/K_m^{app} by 91-96% for both substrates.

The effect of the replacement of Asp90 to an alanine were not as drastic as for *Pf*Grx$^{C32S/C88S/K26A}$ in accordance with the previous results for the corresponding *Sc*Grx7 mutant. For both substrates, the k_{cat}^{app} dropped to 53-99% with mostly increased K_m^{app} values resulting in catalytic efficiencies that were reduced to 41-72% (Figure 35, panel C). The variation in the K_m^{app} values were mostly not statistically significant and the changes in the catalytic efficiencies were therefore mainly influenced by a change of the k_{cat}^{app} values.

Again, secondary plots were generated to gain further insights on the catalytic mechanisms of the analyzed mutants. The true k_{cat} value obtained from the secondary plots seemed to decrease for *Pf*Grx$^{C32S/C88S/K26A}$ with intercepts close to the origin. Both reciprocal Dalziel coefficients $1/\phi_1$ and $1/\phi_2$ were drastically decreased. The effects on the reciprocal Dalziel coefficient $1/\phi_1$ were more than one order of magnitude, whereas the reciprocal Dalziel coefficient $1/\phi_2$ dropped to a value of round 37% of the *Pf*Grx$^{C32S/C88S}$ (DM) value. The effects of a replacement of Asp90 to an alanine on the reciprocal Dalziel coefficients was less pronounced. The mutation mainly influenced the reciprocal Dalziel coefficient $1/\phi_1$ that was decreased to 37% of the DM value.

Again, the effects of both mutations on the kinetic parameters were highly similar to the effects observed before with the homologous *Sc*Grx7 mutant in the HEDS assay pointing to a conserved catalytic mechanism with a separated glutathione activator and glutathione scaffold site. In summary, the role of r_1 as a glutathione activator residue and r_6 as a glutathione scaffold site residue could be confirmed using *Pf*Grx as a non-related model enzyme also for the HEDS assays.

Table 15 | Kinetic constants for *Pf*Grx mutants in the HEDS assay. Estimated true kinetic constants k_{cat}, K_m and Dalziel coefficients of *Pf*Grx$^{C32S/C88S}$ and the mutants K26A and D90A in the HEDS assay. [a]Estimated k_{cat} values and Dalziel coefficients were obtained from Supplementary figure 4. [b]Estimated K_m values were obtained from supplementary figure 3 and 4. DM: *Pf*Grx$^{C32S/C88S}$; K26A: *Pf*Grx$^{C32S/C88S/K26A}$; D90A: *Pf*Grx$^{C32S/C88S/D90A}$. The data was already published in Begas *et al.* 2017 [116].

***Pf*Grx**	$1/\Phi_1$ [a] ($M^{-1}s^{-1}$)	$1/\Phi_2$ [a] ($M^{-1}s^{-1}$)	k_{cat} [a] (s-1)	$K_{m\ (GSH)}$ [b] (mM)	$K_{m\ (HEDS)}$ [b] (mM)
DM	2.2×10^5	8.3×10^4	∞	∞	∞
K26A	1.4×10^4	3.1×10^4	22 - ∞	2.5 - ∞	2.1 - ∞
DM	2.7×10^5	7.1×10^4	∞	∞	∞
D90A	1.0×10^5	5.3×10^4	∞	∞	∞

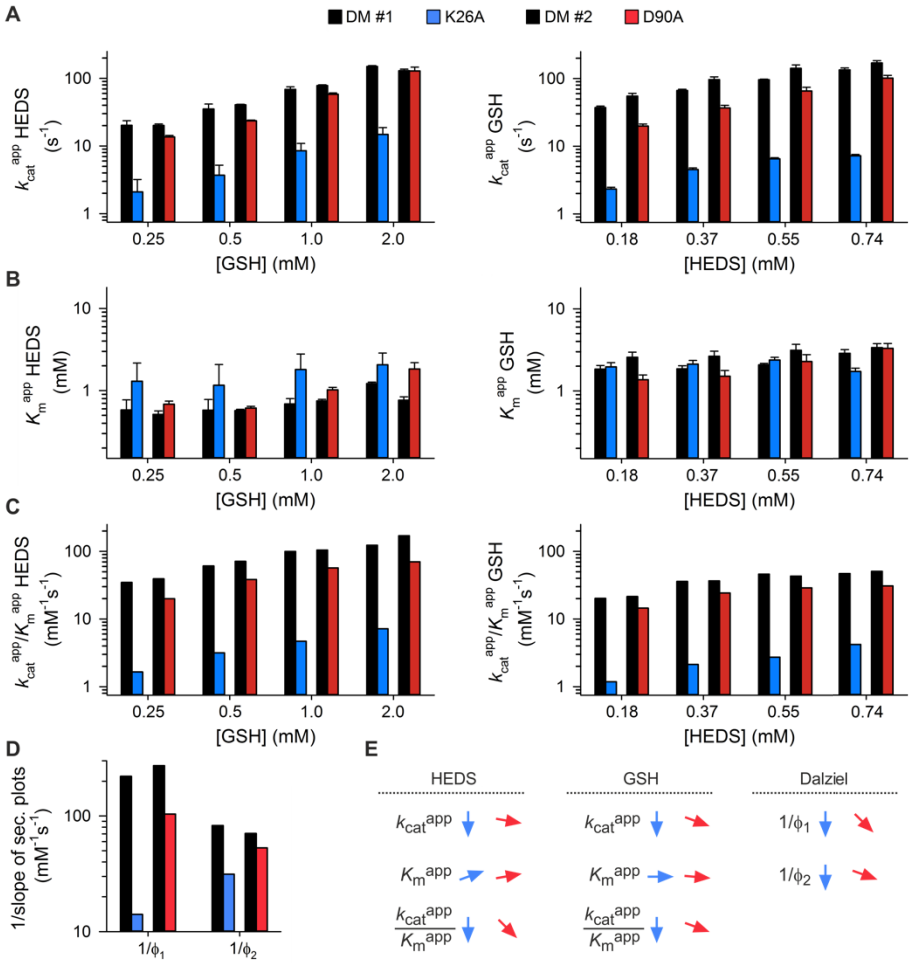

Figure 35 | Relevance of Lys26 and Asp90 of *Pf*Grx in the HEDS assay. A: Selected k_{cat}^{app} values of the *Pf*Grx mutants for HEDS and GSH obtained from Supplementary figure 3. B: Selected K_m^{app} values for the *Pf*Grx mutants for HEDS and GSH obtained from Supplementary figure 3. C: The catalytic efficiencies for HEDS and GSH were calculated from panels A and B. D: The reciprocal Dalziel coefficients were obtained from the slopes of the secondary plots in Supplementary figure 4. E: Summary of the kinetic parameters from panels A, B and C. DM: *Pf*Grx$^{C32S/C88S}$; K26A: *Pf*Grx$^{C32S/C88S/K26A}$; D90A: *Pf*Grx$^{C32S/C88S/D90A}$. Adapted from Begas *et al.* 2017 [116].

3.2.5 Kinetics of further potential activator site mutants of *Sc*Grx7

Additional residues of *Sc*Grx7 that could form an interaction site for GSH were analyzed in steady-state kinetic assays. Different mutants of the residues Asp144 and Glu147 in helix 3, residue Arg153 and the conserved Tyr110 were generated and analyzed regarding their kinetic parameters in standard enzymatic assays for a better understanding of the structure-function relationship of Grx and to further decipher the glutathione interaction site.

3.2.5.1 Kinetics of ScGrx7^{Y110X} mutants in the GSSCys assay

First, different *Sc*Grx7^{Y110X} mutants were analyzed in the GSSCys assay to elucidate the role of the hydroxyl group of this residue which is absent in enzymatically inactive Grx (Figure 32). The primary analyses of *Sc*Grx7^{Y110X} in the GSSCys assay according to Michaelis-Menten and Lineweaver-Burk are shown in Supplementary figure 5, the apparent rate constants are listed in Supplementary table 3 and secondary plots are shown in Supplementary figure 6. Statistical analyses can be found in Supplementary table 8 C.

The mutation of Tyr110 to a phenylalanine, histidine or alanine did not alter the general ping-pong kinetics visualized by the parallel lines in the Lineweaver-Burk plots. *Sc*Grx7^{Y110A} revealed the most drastic effects with k_{cat}^{app} values that were reduced for both substrates to 12-20% of the wild-type values. The effects of *Sc*Grx7^{Y110A} on the K_m^{app} values were mostly not significantly for both substrates whereas the effects on the k_{cat}^{app} values were significantly altered. The catalytic efficiency k_{cat}^{app}/K_m^{app} for *Sc*Grx7^{Y110A} was therefore mainly influenced by the changes of the k_{cat}^{app} values and showed a decrease to 18-23% of the wild-type value for GSH as a substrate and 9-15% of the wild-type value for GSSCys.

*Sc*Grx7^{Y110F} only showed minor effects on the apparent catalytic parameters. The k_{cat}^{app} and K_m^{app} values for GSH were mostly not significantly altered whereas the k_{cat}^{app} value for GSSCys was mainly significantly increased with unchanged K_m^{app} values for GSSCys resulting in a slightly improved catalytic efficiency k_{cat}^{app}/K_m^{app} (GSSCys) with 110-126% of the wild-type values. Please note that most of the changes of the apparent catalytic parameters for GSSCys for *Sc*Grx7^{Y110F} were not statistically significant but nevertheless consistent for different substrate concentrations.

For *Sc*Grx7^{Y110H} only the catalytic efficiency k_{cat}^{app}/K_m^{app} for GSSCys was drastically reduced to 29-33% of the wild-type value mainly because of significantly decreased k_{cat}^{app} and increased K_m^{app} values for GSSCys. The catalytic efficiency k_{cat}^{app}/K_m^{app} of *Sc*Grx7^{Y110H} for GSH was effected to a much lesser extent because both the k_{cat}^{app} and the K_m^{app} for GSH were

significantly reduced to a value of 24-43% of *Sc*Grx7^{wt} resulting in an unchanged catalytic efficiency for GSH.

Again, secondary plots should further elucidate the catalytic mechanisms of the different *Sc*Grx7^{Y110X} mutants and were generated as described above. Estimated true kinetic parameters and the reciprocal Dalziel coefficients for *Sc*Grx7^{Y110X} obtained from the GSSCys assay are listed in Table 16. The true k_{cat} and K_m value obtained from the secondary plots seemed to increase for both substrates of *Sc*Grx7^{Y110F}. For the other two mutants *Sc*Grx7^{Y110H} and *Sc*Grx7^{Y110A}, the k_{cat} values for both substrates decreased with more drastic effects for *Sc*Grx7^{Y110A}. The K_m for GSH was also reduced whereas the K_m for GSSCys was slightly increased for *Sc*Grx7^{Y110H} and *Sc*Grx7^{Y110A}. An effect on the reciprocal Dalziel coefficient $1/\phi_1$ was mainly shown by *Sc*Grx7^{Y110A} with a decrease by approximately factor 10. The reciprocal Dalziel coefficient $1/\phi_1$ for *Sc*Grx7^{Y110F} was slightly increased and decreased by 75% for *Sc*Grx7^{Y110H}. Only *Sc*Grx7^{Y110A} showed an effect on the reciprocal Dalziel coefficient $1/\phi_2$, which was reduced almost by factor 5. The reciprocal Dalziel coefficient $1/\phi_2$ for the other mutants was not altered in the GSSCys assay compared to *Sc*Grx7^{wt}.

In summary, the experimental data of different *Sc*Grx7^{Y110X} mutants in the GSSCys assay revealed that the hydroxyl group of this residue is probably not taking part in the glutathione activator site as it was expected before. Potential catalytic mechanisms that could explain the results are discussed in section 4.

Table 16 | Kinetic constants for *Sc*Grx7^{Y110X} mutants in the GSSCys assay. Estimated true kinetic constants k_{cat}, K_m and Dalziel coefficients of *Sc*Grx7^{wt} and the mutants Y110F, Y110H and Y110A in the GSSCys assay. [a]Estimated k_{cat} values and Dalziel coefficients were obtained from Supplementary figure 6. WT: *Sc*Grx7 wild-type; Y110F: *Sc*Grx7^{Y110F}; Y110H: *Sc*Grx7^{Y110H}; Y110A: *Sc*Grx7^{Y110A}. This data was in parts (WT and Y110A) already published in Begas *et al.* 2017 [116].

GSSCys assay						
***Sc*Grx7**	$1/\Phi_1$ [a] ($M^{-1}s^{-1}$)	$1/\Phi_2$ [a] ($M^{-1}s^{-1}$)	$k_{cat\ (GSH)}$ [a] (s^{-1})	$k_{cat\ (GSSCys)}$ [a] (s^{-1})	$K_{m\ (GSH)}$ [a] (µM)	$K_{m\ (GSSCys)}$ [a] (µM)
WT	7.2×10^5	2.2×10^5	219	380	762	292
Y110F	7.7×10^5	2.5×10^5	346	554	1067	784
Y110H	1.8×10^5	2.2×10^5	154	74	422	375
Y110A	9.2×10^4	4.7×10^4	36	35	426	332

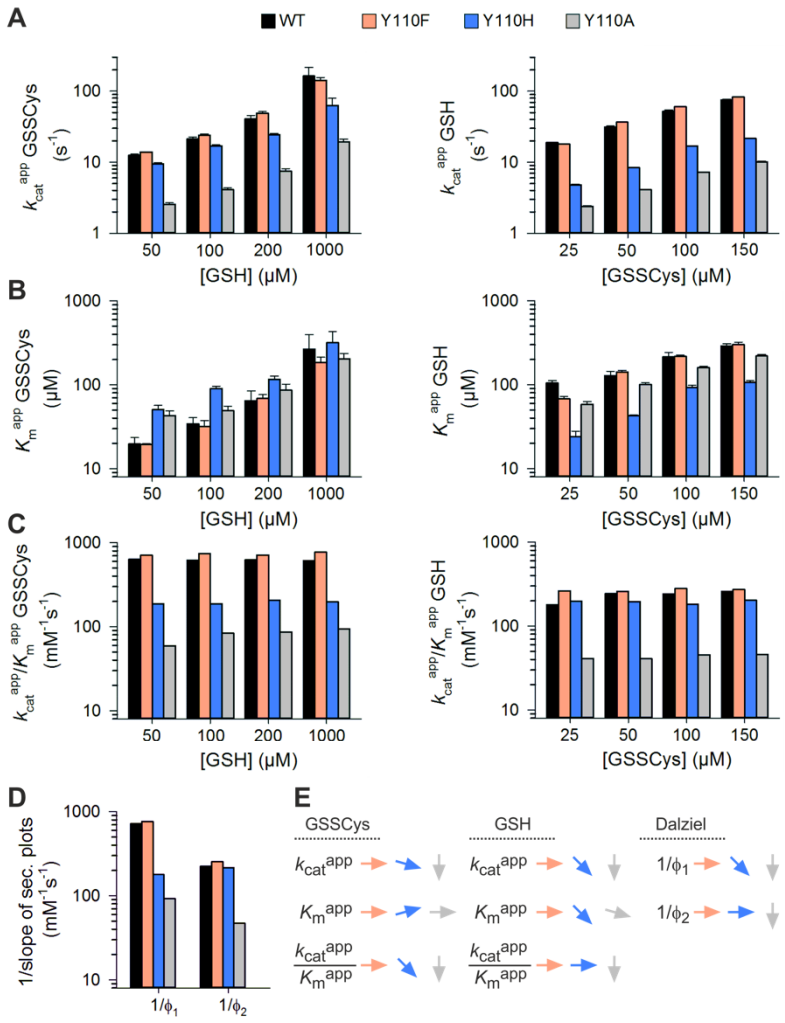

Figure 36 | The hydroxyl group of Tyr110 in *Sc*Grx7 does not act as a specific activator site in the GSSCys assay. A: Selected k_{cat}^{app} values of *Sc*Grx7^{Y110X} for GSSCys and GSH obtained from Supplementary figure 5. B: Selected K_m^{app} values for *Sc*Grx7^{Y110X} for GSSCys and GSH obtained from Supplementary figure 5. C: The catalytic efficiencies for GSSCys and GSH were calculated from panels A and B. D: The reciprocal Dalziel coefficients were obtained from the slopes of the secondary plots in Supplementary figure 6. E: Summary of the kinetic parameters from panels A, B and C. WT: *Sc*Grx7 wild-type; Y110F: *Sc*Grx7^{Y110F}; Y110H: *Sc*Grx7^{Y110H}; Y110A: *Sc*Grx7^{Y110A}. This data was in parts (WT and Y110A) already published in Begas *et al.* 2017 [116].

3.2.5.2 Kinetics of ScGrx7^{Y110X} mutants in the HEDS assay

The different *Sc*Grx7^{Y110X} mutants were also analyzed in a HEDS assay to further elucidate the catalytic mechanism. The analyses of these mutants in the HEDS assay according to Michaelis-Menten and Lineweaver-Burk are shown in Supplementary figure 7, the apparent rate constants are listed in Supplementary table 4 and secondary plots are shown in Supplementary figure 8. Statistical analyses can be found in Supplementary table 8 D.

As observed for *Sc*Grx7^{wt} and previously analyzed mutants in the HEDS assay, the *Sc*Grx7^{Y110X} mutants all showed a sequential kinetic pattern in the Lineweaver-Burk plots with a common x axis interception. *Sc*Grx7^{Y110A} showed the most drastic effects on the apparent catalytic

values for both substrates. The k_{cat}^{app} of *Sc*Grx7^{Y110A} for both substrates decreased statistically significant to 3-8% of the wild-type values, whereas the K_m^{app} values for both substrates were not significantly altered. The strongly reduced k_{cat}^{app} in combination with a constant K_m^{app} resulted in a drastically decreased catalytic efficiency k_{cat}^{app}/K_m^{app} of *Sc*Grx7^{Y110A} for both substrates to 4-7% of the wild-type values (Figure 37, panel C).

The *Sc*Grx7^{Y110H} mutant also showed strong effects on the apparent catalytic values but to a lesser extent than the *Sc*Grx7^{Y110A} mutant. Here, again the K_m^{app} values for both substrates were not significantly changed compared to *Sc*Grx7^{wt}, whereas the k_{cat}^{app} values for both substrates were significantly reduced. The k_{cat}^{app} value for GSH decreased by 78-85% and the k_{cat}^{app} value for HEDS by 70-78% for *Sc*Grx7^{Y110H}. These changes resulted in a decrease of the catalytic efficiency for both substrates to 12-15% of the value obtained for *Sc*Grx7^{wt}.

The *Sc*Grx7^{Y110F} mutant showed the least drastic effects on the catalytic efficiencies. The K_m^{app} for GSH and for HEDS were mainly not significantly altered. The k_{cat}^{app} for HEDS was mainly not significantly altered, whereas the k_{cat}^{app} for GSH was mostly significantly reduced. The combination of these effects led to catalytic efficiencies for *Sc*Grx7^{Y110F} with k_{cat}^{app}/K_m^{app} (GSH) of 58-72% of the wild-type enzyme and k_{cat}^{app}/K_m^{app} (HEDS) of 44-47%.

Again, secondary plots should further help to elucidate the catalytic mechanism of the analyzed mutants. The true k_{cat} values from the secondary plots can be found in Table 17 and seemed to increase for both substrates for *Sc*Grx7^{Y110F}. However, for the other two mutants *Sc*Grx7^{Y110H} and *Sc*Grx7^{Y110A}, the estimated true k_{cat} values both seemed to decrease. The true K_m values seemed to be rather constant for the different mutants compared to *Sc*Grx7^{wt}. Both reciprocal Dalziel coefficients $1/\phi_1$ and $1/\phi_2$ decreased for all of the mutants. Only minor effects were observed for *Sc*Grx7^{Y110F}, intermediate effects for *Sc*Grx7^{Y110H} with a decrease of up to one order of magnitude and even more drastic effects for *Sc*Grx7^{Y110A} with a decrease of almost two orders of magnitude.

As observed before in the GSSCys assay, kinetic constants of the different *Sc*Grx7^{Y110X} mutants in the HEDS assay show that the hydroxyl group of this residue is probably not taking part in the glutathione activator site as it was expected before because the hydroxyl group is absent in enzymatically inactive Grx. Potential catalytic mechanisms that could explain the role of this residue are discussed in section 4.

Table 17 | Kinetic constants for *Sc*Grx7^{Y110X} mutants in the HEDS assay. Estimated true kinetic constants k_{cat}, K_m and Dalziel coefficients of *Sc*Grx7^{wt} and the mutants Y110F, Y110H and Y110A in the HEDS assay. [a]Estimated k_{cat} values and Dalziel coefficients were obtained from Supplementary figure 8a. [b]Estimated K_m values were averaged from Supplementary figure 7. WT: *Sc*Grx7 wild-type; Y110F: *Sc*Grx7^{Y110F}; Y110H: *Sc*Grx7^{Y110H}; Y110A: *Sc*Grx7^{Y110A}. This data was in parts (WT and Y110A) already published in Begas *et al.* 2017 [116].

	HEDS assay					
***Sc*Grx7**	$1/\Phi_1$ [a] ($M^{-1}s^{-1}$)	$1/\Phi_2$ [a] ($M^{-1}s^{-1}$)	$k_{cat\ (GSH)}$ [a] (s^{-1})	$k_{cat\ (HEDS)}$ [a] (s^{-1})	$K_{m\ (GSH)}$ [b] (mM)	$K_{m\ (HEDS)}$ [b] (mM)
WT	2.4×10^5	1.5×10^5	136	185	1.3 ± 0.8	1.3 ± 0.3
Y110F	1.2×10^5	1.2×10^5	275	485	2.1 ± 0.9	1.5 ± 0.2
Y110H	2.9×10^4	3.7×10^4	92	43	1.8 ± 0.3	1.7 ± 0.2
Y110A	9.5×10^3	4.6×10^3	15	30	0.7 ± 0.2	1.4 ± 0.3

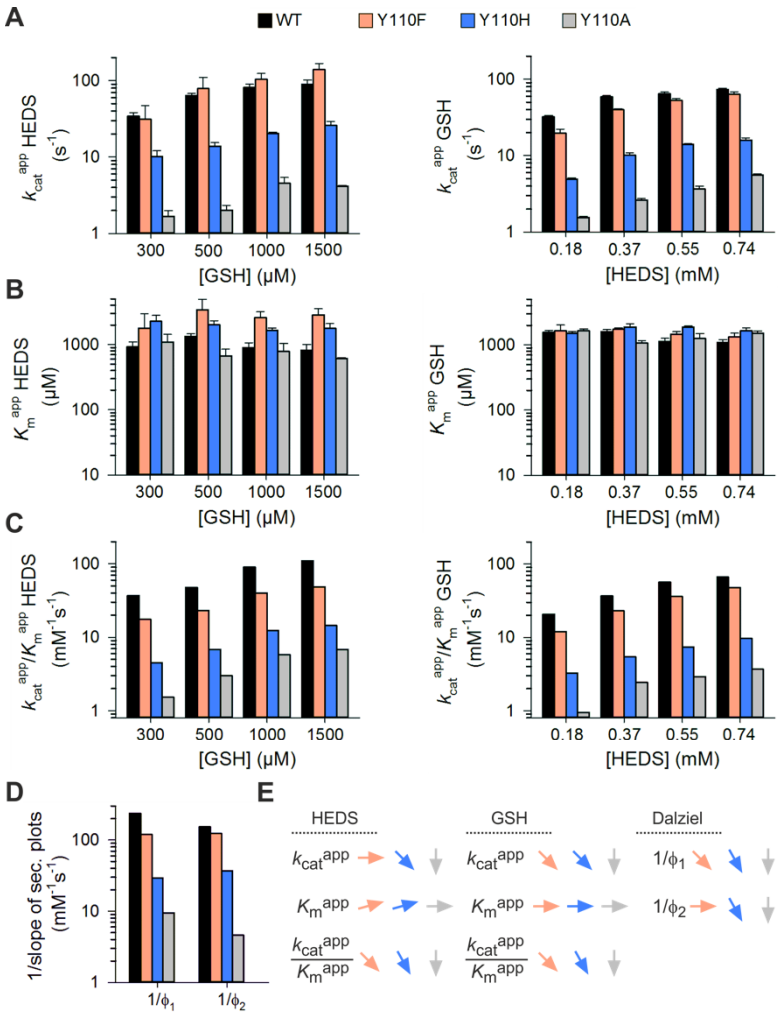

Figure 37 | Replacement of Tyr110 in *Sc*Grx7 slows down the turnover of both substrates in the HEDS assay. A: Selected k_{cat}^{app} values of the *Sc*Grx7 Y110X mutants for HEDS and GSH obtained from Supplementary figure 7. B: Selected K_m^{app} values for the *Sc*Grx7 mutants for HEDS and GSH obtained from Supplementary figure 7. C: The catalytic efficiencies for HEDS and GSH were calculated from panels A and B. D: The reciprocal Dalziel coefficients were obtained from the slopes of the secondary plots in Supplementary figure 8. E: Summary of the kinetic parameters from panels A, B and C. WT: *Sc*Grx7 wild-type; Y110F: *Sc*Grx7^{Y110F}; Y110H: *Sc*Grx7^{Y110H}; Y110A: *Sc*Grx7^{Y110A}. This data was in parts (WT and Y110A) already published in Begas *et al.* 2017 [116].

3.2.5.3 Kinetics of ScGrx7^{D144X} mutants in the GSSCys assay

An aspartate at position 144 in helix 3 of *Sc*Grx7 was analyzed as a further potential GSH activator site because it sticks out on the enzyme surface. The replacement of Asp144 by an alanine or a lysine as charge inversion mutation were analyzed in a GSSCys assay. For the sake of convenience, the primary plots are shown in Supplementary figure 9, the apparent rate constants are listed in Supplementary table 5 and secondary plots are shown in Supplementary figure 10. Statistical analyses can be found in Supplementary table 8 E.

Again, the general ping-pong kinetics were not altered by the mutations. In general, the effects of the mutated Asp144 was much more subtle than for the *Pf*Grx$^{C32S/C88S/K26A}$ or *Sc*Grx7^{Y110X} mutants. The k_{cat}^{app} (GSH) for *Sc*Grx7^{D144A} was slightly, but significantly decreased, whereas the K_m^{app} (GSH) was not significantly altered. This led to a catalytic efficiency k_{cat}^{app}/K_m^{app} (GSH) for *Sc*Grx7^{D144A} that was reduced to 77-89% compared to the control values. The changes for the apparent catalytic values of *Sc*Grx7^{D144A} for GSSCys were mainly not statistically significant, but for all concentrations of GSH a reduced catalytic efficiency k_{cat}^{app}/K_m^{app} (GSSCys) was observed.

For the charge inversion mutant *Sc*Grx7^{D144K}, the observed effects were more significant. The k_{cat}^{app} (GSH) was reduced by 14-33% with K_m^{app} (GSH) of 37-56% of the control value. This led to an increased catalytic efficiency k_{cat}^{app}/K_m^{app} (GSH) for *Sc*Grx7^{D144K} to 151-202%. The k_{cat}^{app} (GSSCys) and K_m^{app} (GSSCys) for *Sc*Grx7^{D144K} were significantly increased, leading to a decreased catalytic efficiency k_{cat}^{app}/K_m^{app} (GSSCys) for *Sc*Grx7^{D144K} to 66-75% of the wild-type value.

Again, secondary plots were generated to gain further insights into the catalytic mechanism of the analyzed residue. Estimated true kinetic parameters and the reciprocal Dalziel coefficients for the *Sc*Grx7^{D144X} mutants of *Sc*Grx7 in the GSSCys assay are listed in Table 18. The effects on the estimated true kinetic constants were in general very subtle. The most interesting result was the increase of the reciprocal Dalziel coefficient $1/\phi_2$ for *Sc*Grx7^{D144K} by almost factor 2. The replacement of Asp144 in helix 3 with a positively charged amino acid therefore seems to accelerate the reductive half-reaction.

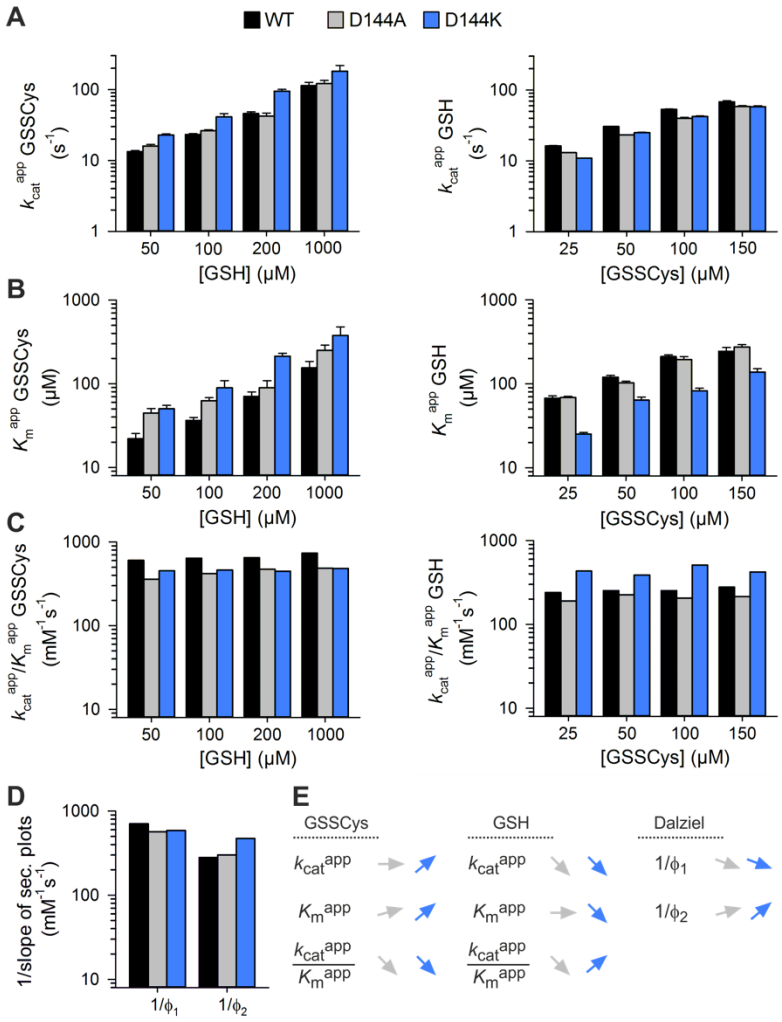

Figure 38 | The replacement of D144 in *Sc*Grx7 with a positively charged amino acid accelerates the reductive half-reaction. A: Selected k_{cat}^{app} values of *Sc*Grx7^{D144X} for GSSCys and GSH obtained from Supplementary figure 9. B: Selected K_m^{app} values for *Sc*Grx7^{D144X} for GSSCys and GSH obtained from Supplementary figure 9. C: The catalytic efficiencies for GSSCys and GSH were calculated from panels A and B. D: The reciprocal Dalziel coefficients were obtained from the slopes of the secondary plots in Supplementary figure 10. E: Summary of the kinetic parameters from panels A, B and C. WT: *Sc*Grx7 wild-type; D144A: *Sc*Grx7^{D144A}; D144K: *Sc*Grx7^{D144K}.

3.2.5.4 Kinetics of ScGrx7^{E147X} mutants in the GSSCys assay

As another residue of helix 3 that could form a potential GSH activator site, Glu147 was selected because of geometric reasons. Again, the residue was replaced by an alanine or a charge inversion mutation (*Sc*Grx7^{E147K}) and the different mutants were analyzed in a GSSCys assay with *Sc*Grx7^{wt} as a control. The primary analyses are summarized in Supplementary figure 11, the apparent rate constants are listed in Supplementary table 6, the secondary analyses can be found in Supplementary figure 12 and statistical analyses are shown in Supplementary table 8 F.

As observed before, mutation of *Sc*Grx7^{E147} did not alter the ping-pong kinetics. In general, the effects observed for the *Sc*Grx7^{E147X} mutants were highly similar to the other investigated helix

3 residue Asp144. The k_{cat}^{app} (GSH) for *Sc*Grx7^{E147A} was only slightly, but mainly significantly decreased, whereas the K_m^{app} (GSH) was in most of the cases not significantly altered. This led to an altered catalytic efficiency k_{cat}^{app}/K_m^{app} (GSH) for the *Sc*Grx7^{E147A} that was reduced to 86-91% of the control values. The changes for the apparent catalytic values of *Sc*Grx7^{E147A} for GSSCys were not statistically significant.

For the charge inversion mutant *Sc*Grx7^{E147K}, the observed effects were more pronounced. The k_{cat}^{app} (GSH) for this mutant was increased to 105-122% with K_m^{app} (GSH) of 58-73% of the control value. This led to an increased catalytic efficiency k_{cat}^{app}/K_m^{app} (GSH) for *Sc*Grx7^{E147K} to 156-195%. The k_{cat}^{app} (GSSCys) and K_m^{app} (GSSCys) for *Sc*Grx7^{E147K} were significantly increased, leading to a mainly unchanged catalytic efficiency k_{cat}^{app}/K_m^{app} (GSSCys) for *Sc*Grx7^{E147K} with 87-103% of *Sc*Grx7^{wt}.

Again, secondary plots were generated to gain further insights into the catalytic mechanism of the analyzed residue. Estimated true kinetic parameters and the reciprocal Dalziel coefficients for the Glu147 mutants of *Sc*Grx7 in the GSSCys assay are listed in table 18. The effects on the estimated true kinetic constants were in general very subtle. As observed before for the other investigated helix 3 residue Asp144, the reciprocal Dalziel coefficient $1/\phi_2$ for the charge inversion mutant *Sc*Grx7^{E147K} was increased by more than factor 2.

In summary, the effects of the two analyzed mutants of helix 3 both showed that a positively charged amino acid in helix 3 seems to accelerate the reductive half-reaction. Moreover, the positively charged amino acids in the mutants presumably influence the glutathione activator site.

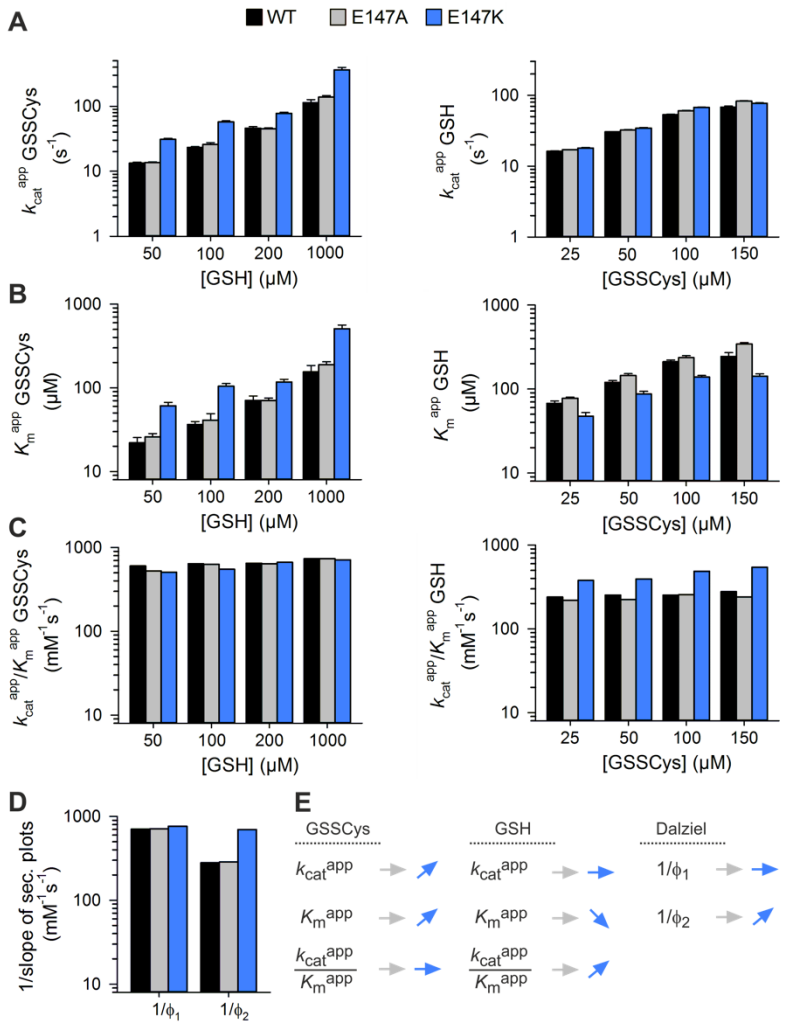

Figure 39 | The replacement of E147 in *Sc*Grx7 with a positively charged amino acid accelerates the reductive half-reaction. A: Selected k_{cat}^{app} values of *Sc*Grx7^{E147X} for GSSCys and GSH obtained from Supplementary figure 11. B: Selected K_m^{app} values for *Sc*Grx7^{E147X} for GSSCys and GSH obtained from Supplementary figure 11. C: The catalytic efficiencies for GSSCys and GSH were calculated from panels A and B. D: The reciprocal Dalziel coefficients were obtained from the slopes of the secondary plots in Supplementary figure 12. E: Summary of the kinetic parameters from panels A, B and C. WT: *Sc*Grx7 wild-type; E147A: *Sc*Grx7^{E147A}; E147K: *Sc*Grx7^{E147K}.

3.2.5.5 Kinetics of ScGrx7^{R153X} mutants in the GSSCys assay

Residue Arg153 of *Sc*Grx7 was analyzed in a GSSCys assay as a potential GSH activator site because it was previously proposed to be involved in the glutathione binding by Mesecke *et al.* [112]. The residue was replaced by an alanine or a charge inversion mutation (*Sc*Grx7^{R153E}). The primary analyses can be found in Supplementary figure 13, the apparent rate constants are listed in Supplementary table 7, the secondary analyses are summarized in Supplementary figure 14 and statistical analyses are shown in Supplementary table 8 G.

As for all other analyzed mutants of *Sc*Grx7, the ping-pong kinetics were not changed. The k_{cat}^{app} and K_m^{app} for GSH of *Sc*Grx7^{R153A} was significantly decreased to values of 41-52% of *Sc*Grx7^{wt}. This resulted in a catalytic efficiency k_{cat}^{app}/K_m^{app} (GSH) that was not altered much

with values of 84-96% of the wild-type enzyme. However, the catalytic efficiency k_{cat}^{app}/K_m^{app} for GSSCys was reduced to 35-43%, determined by mainly unchanged k_{cat}^{app} (GSH) values in combination with significantly increased K_m^{app} (GSH) values.

For the charge inversion mutant *Sc*Grx7^{R153E}, the observed effects were in general more pronounced. The k_{cat}^{app} (GSH) for this mutant was significantly decreased to 22-25% and the K_m^{app} (GSH) was 40-53% of *Sc*Grx7^{wt}. This led to a decreased catalytic efficiency k_{cat}^{app}/K_m^{app} (GSH) for *Sc*Grx7^{R153E} to 47-53%. The k_{cat}^{app} (GSSCys) for *Sc*Grx7^{R153E} was significantly decreased to values of 43-61% of the control and the K_m^{app} (GSSCys) values were significantly increased to 192-290%, leading to a reduced catalytic efficiency k_{cat}^{app}/K_m^{app} (GSSCys) for *Sc*Grx7^{R153E} with 20-23% of *Sc*Grx7^{wt}.

As a next step, secondary plots were generated to further elucidate the catalytic mechanism of the analyzed residue. Estimated true kinetic parameters and the reciprocal Dalziel coefficients for *Sc*Grx7^{R153X} in the GSSCys assay are listed in table 18. The mutation of Arg153 to alanine resulted in a decrease of the reciprocal Dalziel coefficient $1/\phi_1$ by more than factor 2. Even stronger effects were observed for the charge inversion mutant *Sc*Grx7^{R153E} with a reciprocal Dalziel coefficient $1/\phi_1$ that was decreased by around factor 5. The reciprocal Dalziel coefficient $1/\phi_2$ was not altered for *Sc*Grx7^{R153A}, but reduced by 50% for *Sc*Grx7^{R153E}.

Taken together, residue Arg153 seems to play a role mainly for the oxidative half-reaction in the GSSCys assay in accordance with the glutathione scaffold model.

Table 18 | Kinetic constants for *Sc*Grx7 Asp144, Glu147 and Arg153 mutants in the GSSCys assay. Estimated true kinetic constants k_{cat}, K_m and Dalziel coefficients of *Sc*Grx7^{wt} and the mutants D144A, D144K, E147A, E147K, R153A and R153E in the GSSCys assay. [a]Estimated $k_{cat,}$ K_m values and Dalziel coefficients were obtained from Supplementary figure 10a (D144X), Supplementary figure 12a (E147X) and Supplementary figure 14a (R153X). WT: *Sc*Grx7 wild-type; D144A: *Sc*Grx7^{D144A}; D144K: *Sc*Grx7^{D144K}; E147A: *Sc*Grx7^{E147A}; E147K: *Sc*Grx7^{E147K}; R153A: *Sc*Grx7^{R153A}; R153E: *Sc*Grx7^{R153E}.

	GSSCys assay					
***Sc*Grx7**	$1/\Phi_1$ [a] ($M^{-1}s^{-1}$)	$1/\Phi_2$ [a] ($M^{-1}s^{-1}$)	$k_{cat\ (GSH)}$ [a] (s^{-1})	$k_{cat\ (GSSCys)}$ [a] (s^{-1})	$K_{m\ (GSH)}$ [a] (µM)	$K_{m\ (GSSCys)}$ [a] (µM)
WT	7.1×10^5	2.8×10^5	206	213	744	257
D144A	5.7×10^5	3.0×10^5	151	161	488	250
D144K	5.9×10^5	4.7×10^5	161	591	590	760
E147A	7.1×10^5	2.9×10^5	370	259	926	314
E147K	7.6×10^5	7.0×10^5	332	263	300	280
R153A	2.8×10^5	2.7×10^5	168	125	293	404
R153E	1.4×10^5	1.4×10^5	113	72	807	491

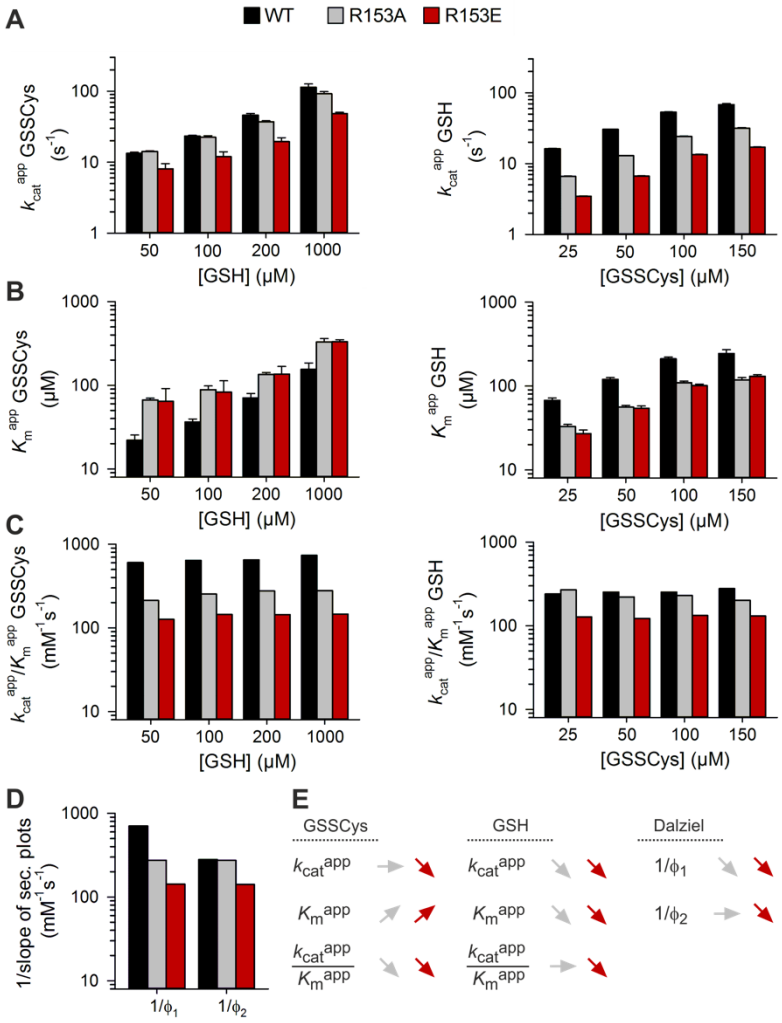

Figure 40 | Arg153 in *Sc*Grx7 is mainly important for the oxidative half reaction in the GSSCys assay. A: Selected k_{cat}^{app} values of *Sc*Grx7^{R153X} for GSSCys and GSH obtained from Supplementary figure 13. B: Selected K_m^{app} values for *Sc*Grx7^{R153X} for GSSCys and GSH obtained from Supplementary figure 13. C: The catalytic efficiencies for GSSCys and GSH were calculated from panels A and B. D: The reciprocal Dalziel coefficients were obtained from the slopes of the secondary plots in Supplementary figure 14. E: Summary of the kinetic parameters from panels A, B and C. WT: *Sc*Grx7 wild-type; R153A: *Sc*Grx7^{R153A}; R153E: *Sc*Grx7^{R153E}.

3.2.6 Influence of selected point mutations of *Sc*Grx7 on the pK_a value

Different residues of *Sc*Grx7 should be analyzed regarding their influence on the thiol pK_a value of the active site cysteine. The two residues Lys105 and Glu170 were analyzed acting as a glutathione activator and glutathione scaffold, respectively [116]. As another mutant *Sc*Grx7^{Y110A} was analyzed because this mutant also showed a strong effect in the GSSCys assay that might be influenced by an altered pK_a value. Additionally to the alanine mutants of these residues, *Sc*Grx7^{K105E} was analyzed as a control, because this mutation showed the most drastic effect of all the analyzed mutants in previous kinetic analyses [116].

The results are shown in Figure 41. The analysis revealed a pK_a value for *Sc*Grx7^{wt} of 4.34 ± 0.10. This value was not significantly altered for *Sc*Grx7^{Y110A} (4.50 ± 0.03), *Sc*Grx7^{K105A} (4.45 ±

0.02) and *Sc*Grx7^{E170A} (4.35 ± 0.13). Only the pK_a value of *Sc*Grx7^{K105E} was significantly increased compared to *Sc*Grx7^{wt} and all other analyzed mutants to a value of 4.97 ± 0.08**.** Of note, samples with iodoacetamide (IAM) were in general apparently more stable at lower pH values resulting in remaining activities > 100%. Taken together, point mutations of *Sc*Grx7 only had a minor influence on the pK_a value of the active site cysteine.

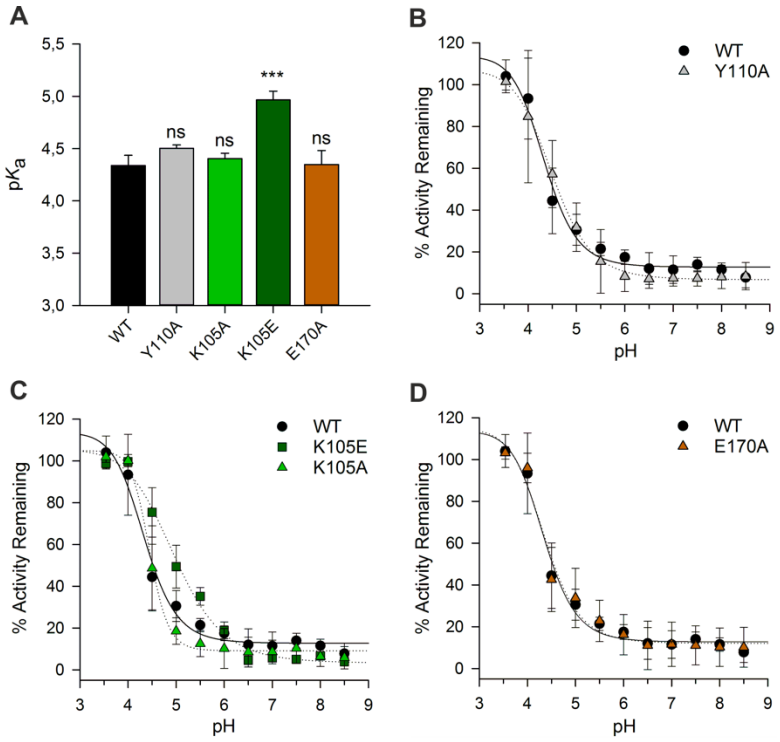

Figure 41 | Point mutations of *Sc*Grx7 only have a minor influence on the pK_a value of the active site cysteine. Freshly reduced *Sc*Grx7 (black circles) and selected mutants (colored circles) were incubated for 180 seconds with 150 µM iodoacetamide (IAM) at 23°C in a three-buffer system with different pH values varying from 3.5 to 8.5. The residual enzyme activity was measured in a standard HEDS assay and normalized against a control incubated without IAM. Symbols represent the mean ± SD of three independent determinations of *Sc*Grx7 activity. The sigmoidal curve fit (Hill, 4 parameter) for *Sc*Grx7 and mutants are represented as full and dashed lines, respectively. A: Only the pK_a value for the *Sc*Grx7^{K105E} mutant is statistically different from all other mutants and *Sc*Grx7^{wt}. There is no statistically significant difference between the other mutants and wild-type enzyme. B: The pK_a value of *Sc*Grx7^{wt} and *Sc*Grx7^{Y110A} is 4.34 ± 0.10 and 4.50 ± 0.03, respectively. C: The pK_a value of *Sc*Grx7^{K105A} and *Sc*Grx7^{K105E} is 4.45 ± 0.02 and 4.97 ± 0.08, respectively. D: The pK_a value of *Sc*Grx7^{E170A} is 4.35 ± 0.13. Samples with IAM were apparently more stable at lower pH values resulting in remaining activities > 100%. P-values from one way ANOVA analysis followed by a Holm-Sidak test were calculated in SigmaPlot 13 (P > 0.05: ns; P ≤ 0.001: ***).

4 Discussion

4.1 Mitochondrial protein import into the IMS of *Leishmania tarentolae*

4.1.1 A potential replacement for Mia40 in protists remains to be elucidated

The major objective of this thesis was the identification of a Mia40 adapter replacement for the mitochondrial protein import into the IMS of the kinetoplastid parasite *L. tarentolae*. The model organism might be representative also for other eukaryotes without an identified Mia40 homolog. Unraveling the mechanism of mitochondrial protein import into the IMS of early eukaryotes is a hot topic in the field because of its potential to find new targets for drug design. Furthermore, it could help to gain more insights into the evolution of eukaryotes. The two known components of mitochondrial protein import into the IMS of *L. infantum* (*Li*Erv and *Li*sTim1) seem to be essential for parasite survival [157]. Erv from the closely related parasite *T. brucei* was also shown to be essential by RNAi studies [37, 155, 158]. Therefore, the missing link – the putative Mia40 adapter replacement – is likely to be essential as well and may be a promising target for drug development. An appropriate drug would interfere only with the parasite specific Mia40 adapter replacement, but not with the MIA pathway of the host cell.

In this work, different strategies for endogenous chemical trapping of a mixed disulfide intermediate between *Lt*Erv and the unknown protein were applied using various alkylating, reducing and oxidizing compounds. None of these experiments revealed mixed disulfides in western blot analyses (Figure 13 and Figure 14). Moreover, trapping attempts with an upregulated cysteine mutant of *Lt*Erv with the aim to stabilize a mixed disulfide between *Lt*Erv and the unknown Mia40 replacement did not lead to the identification of an interacting protein (Figure 20). Even with highly enriched *Lt*Erv protein levels after denaturing (Figure 24) or native pull-down experiments (Figure 23), no mixed disulfide intermediate was detectable. Hence, *Lt*Erv could not be enriched as a trapped intermediate with the unknown interaction partner under the conditions being tested and no further analysis by mass spectrometry was possible. These results do not support the direct Erv-substrate interaction model that was previously proposed [155, 159].

Trapping attempts with the model substrate *Lt*sTim1 showed several disulfide-bridged intermediates that could potentially reflect heterodimers between *Lt*sTim1 and Mia40 adapter replacement candidates (Figure 16 and Figure 21). However, an enrichment of these intermediates by affinity chromatography was not possible because of systematic problems with western blot analyses of *Lt*sTim1. The protein is known to be highly hydrophobic [160] and tends to form oligomers that are visible as strong signals between the separating and stacking gel of the SDS-PAGE gel in western blot analyses. These oligomers could not be eliminated using various protocols (Figure 15).

Taken together, neither trapping attempts with *Lt*sTim1 as a model substrate for the oxidative folding pathway in the IMS, nor with *Lt*Erv led to the identification of a stable disulfide-bonded interaction partner. The correct localization of the bait proteins to the mitochondria of *L. tarentolae* were confirmed (Figure 22). Hence, the results cannot be explained by mislocalized bait proteins. However, a non-covalent or transient interaction with a Mia40 adapter replacement cannot be excluded. All experiments were based on the assumption that the interaction between *Lt*Erv or *Lt*sTim1 and the unknown adapter replacement is linked via disulfide bonds. Hence, non-covalent interactions would not be detectable with the approaches used in this work. Transient interactions are also difficult to enrich and detect. It is known that *Sc*Mia40 forms intermolecular disulfide species with its substrate that are stable for several seconds to minutes [159, 161]. This behavior is rather unusual compared to other oxidoreductases such as members of the protein disulfide isomerase (PDI) that catalyze very fast oxidative protein folding in the endoplasmatic reticulum [162]. It is possible that the Mia40 adapter replacement in kinetoplastida is also a highly specific and efficient enzyme and would hence be missed in the analyses because of very transient interactions.

BioID is a method that might overcome these problems because also very transient interactions can potentially be detected as the biotinylated interacting proteins accumulate over time [84]. Moreover, the interaction partner does not necessarily have to be linked via disulfide bonds. However, in this work, no Mia40 adapter replacement could be detected by the help of BioID. The failure was probably due to technical problems because even the bait protein itself did not show biotinylation. However, a biotinylated protein as a positive control was not included in the western blot analyses. Hence, it is possible that the streptavidin-HRP did not work for *L. tarentolae*. Such a control needs to be included in

the future. An alternative method to BioID is APEX that was already successfully used for mitochondrial proteins in the IMS with faster biotinylation rates than BioID [83, 163] and could be used for further studies. However, these methods are not specific and usually result in long lists of potential interacting proteins.

An interaction partner may also have been missed in this work if early eukaryotes do not possess a Mia40 homolog and rather have an Erv-only-system that directly catalyze the oxidation of the substrates as proposed by Peleh *et al.* [159]. The authors could show that in plants Mia40 is not essential and substrate oxidation can occur in a Mia40-independent manner. From this result, they propose an evolutionary scenario starting with an Erv1-like oxidase and hypothesize that a similar situation might still be found in some protists (starting from eukaryote B and taking route 4 in the evolutionary model in Figure 42). Might *Lt*Erv with its additional kinetoplastida-specific second (KISS) domain functionally replace Mia40 in kinetoplastida? This would imply an alternative pathway in apicomplexan parasites because they do not possess a KISS domain. Even if *Lt*Erv would operate alone with a simplified oxidative folding machinery as proposed by Haindrich *et al.* [155] and Peleh *et al.* [159], a direct interaction between *Lt*Erv and the substrate *Lt*sTim1 should be detectable with appropriate experimental methods. In this case, *Lt*Erv should be able to directly oxidize substrates of the oxidative folding pathway. This direct interaction was not observed in this work. According to the hypothesis of a simplified oxidative folding machinery, *Lt*Erv should also be able to complement the function of *Sc*Mia40 in yeast due to the evolutionary conservation of the import signals of IMS proteins in different eukaryotic supergroups [24]. There is no evidence for such a simplified oxidative folding machinery because neither *Lt*Erv nor *Pf*Erv were able to complement the loss of *Sc*Mia40 in yeast [157]. Moreover, oxidative folding assays with *Tb*Erv *in vitro* were not successful [37]. Taken together, these results rather point to the existence of an adapter replacement for Mia40 in kinetoplastida (protein Z in the evolutionary scenario proposed before by Eckers *et al.* 2012 [24], see Figure 42) that still remains elusive.

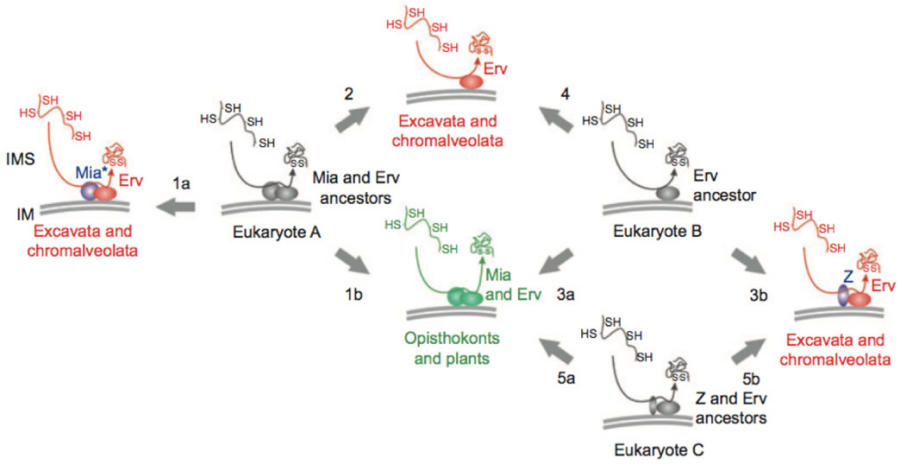

Figure 42 | Evolution of mitochondrial protein import into the intermembrane space. In general, there are three possibilities existing for the evolution of mitochondrial protein import into the intermembrane space of Excavata and Chromalveolata. Primitive eukaryotes either had a Mia40 and Erv ancestor (eukaryote A), only an Erv ancestor (eukaryote B) or an Erv ancestor as well as an unknown additional protein Z (eukaryote C). The current knowledge points to an evolutionary scenario starting from eukaryote B or C and producing protists containing Erv and protein Z. The evolutionary model was taken from Eckers *et al.* 2012 [24].

What can be done to overcome the systematic problems with *Lt*sTim1 to further analyze the reaction from the substrate side? *Lt*sTim1 is only one model substrate of the oxidative folding pathway in the IMS and alternative substrates may be tested that are potentially less hydrophobic. The recently published list of putative substrates of the oxidative folding pathway of the IMS by Peikert *et al.* in *T. brucei* [158] was therefore used to select alternative substrates that could serve as bait proteins for further investigations (Figure 43). What characterizes a protein from this list as a suited model substrate for further analyses? First, proteins were selected according to their mass that should be around 20 kDa to be different enough from *Lt*Erv around 35 kDa and not as small as the model substrate *Lt*sTim1. Second, the list was checked for the sequence coverage and proteins with a value below 20% were subsequently excluded. Third, the proteins were selected according to the number and motifs of their cysteines. Proteins with too many cysteines were excluded because of a too complicated subsequent workflow for generating different trapping mutants analogous to this work. The conservation of the proteins in apicomplexan parasites and opisthokonts was also considered because this list could also contain the potential Mia40 adapter replacement, which is presumably conserved in apicomplexan parasites but not in opisthokonts (or if it can also be found in opisthokonts, it will probably not be essential). In total, four substrates were selected as potential bait proteins, including Tb927.9.7980/substrate 1 and Tb927.10.15790/substrate 3 with classical twin Cx_9C-motifs,

as well as two proteins with less characteristic motifs (Tb927.10.4280/substrate 2 and Tb927.11.13510/substrate 4). Three of them also fulfill the last criterion (Tb927.9.7980, Tb927.10.4280 and Tb927.11.13510). The corresponding proteins from *L. tarentolae* were recently cloned by Mirko Höhn and Sandra Specht. Cysteine mutants for the stabilization of mixed disulfide intermediates were generated with substrate 2 and 4 according to the workflow with *Lt*sTim1 shown in this work. The proteins have already been expressed in *L. tarentolae* by Sandra Specht and are going to be further characterized by another student in the lab analogous to the experiments with *Lt*Erv and *Lt*sTim1 described in this thesis.

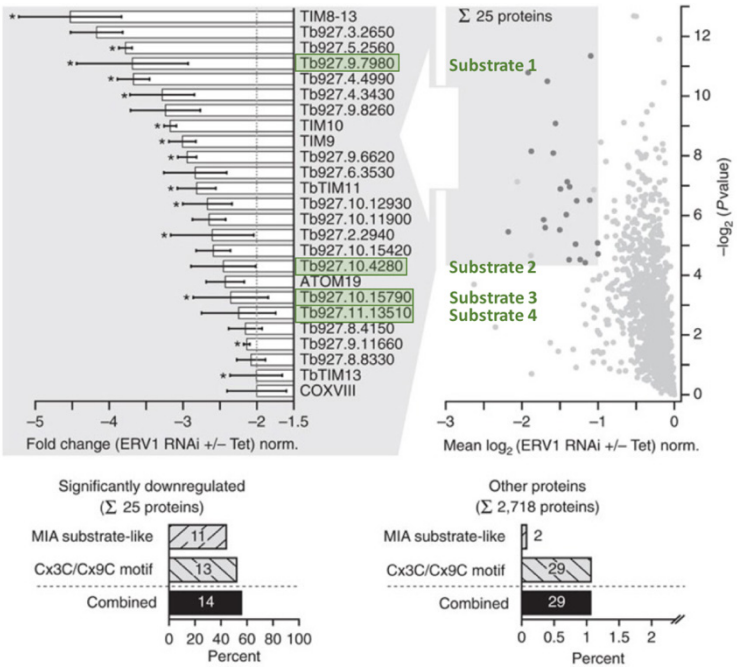

Figure 43 | Selection of new substrates of the oxidative folding pathway. Putative substrates of the oxidative protein folding pathway of the IMS were recently identified by Peikert *et al.* by comparing induced versus uninduced *TBERV* knockdown cultures [158]. Four new substrates for analysis in *L. tarentolae* were selected based on the published list with 25 downregulated proteins. Adapted from Peikert *et al.* 2017 [158].

A rather unexpected result was observed when the correct localization of the bait proteins was analyzed (Figure 22). The two mutated *Lt*sTim1 isoforms containing only one cysteine seem to correctly localize to the mitochondria of *L. tarentolae*. This behavior is not self-explanatory because these proteins cannot form internal disulfide bonds anymore, which are usually a prerequisite for trapping of the substrates in the IMS according to the folding trap mechanism [164, 165]. What could explain the correct import of mutated *Lt*sTim1 with only one cysteine residue left? In yeast, a cysteine-free mutant of the Mia40 substrate Atp23 was shown to be efficiently imported into isolated mitochondria [166]. The import required Mia40, but not the formation of mixed disulfide bonds with the adapter. Moreover, in the list of putative substrates of the oxidative protein folding pathway of the

IMS published by Peikert *et al.*, there are several proteins without the classical twin Cx_3C or Cx_9C motif, one protein with only one cysteine and another one without cysteines [158]. However, these proteins are presumably imported in an Erv-dependent manner because they are significantly downregulated after *TBERV* knockdown. This points to the presence of an altered pathway that is dependent on Mia40 or the unknown adapter replacement but does not necessarily rely on the formation of mixed disulfide intermediates. Another possible explanation for the behavior of the single-cysteine mutants of *Lt*sTim1 might be that they accumulate in inclusion bodies because of the strong upregulation and are only solubilized and transferred to the supernatant with high digitonin concentrations.

Initially, it was planned to perform pull-down experiments for the identification of a potential Mia40 adapter replacement coupled with a SILAC approach. An advantage of this method is that it can discriminate between unspecific hits and actual interaction partners as explained in the introduction. Several cultivation media combined with different supplements were tested in order to identify a defined medium for cultivation of *L. tarentolae* as a prerequisite for a SILAC approach. Even in an extensive search with 216 different compositions no completely defined medium could be determined for the use in a SILAC experiment. Moreover, a defined medium that was published for the use in *L. infantum* was not suited for the cultivation of the close relative *L. tarentolae* [71, 72]. The needs of these parasites seem to be very specific and to differ even among closely related strains. Thus, much more experiments would be needed to determine a defined medium for the cultivation of *L. tarentolae*. Instead, the new substrates may be analyzed with label-free mass spectrometry as a cheaper alternative for SILAC [73].

4.1.2 Redox state of *Lt*Erv

The native redox state of *Lt*Erv as an important component of the mitochondrial protein import machinery into the IMS was unknown so far. Therefore, a redox mobility shift assay was used to elucidate the redox state and to gain further insights into the altered import machinery of kinetoplastida (Figure 28). *Lt*Erv seems to be mainly oxidized under physiological conditions. The structural disulfide bonds in *Lt*Erv are stable against treatment with TCEP as a reductant at low temperature, and even at high temperature the reduction was not complete. Recently, a study was published investigating the redox state of the mammalian Mia40 homolog CHCHD4 [167]. Erdogan *et al.* could show that under

basal conditions, the protein is predominantly oxidized. Oxidative protein folding is impaired when the redox state of Mia40 is shifted to a more reduced state. Therefore, the redox state of Mia40/CHCHD4 is mainly controlled by Erv and the glutathione content of the IMS [168]. This is either induced by Erv depletion or glutaredoxin overexpression [168, 169]. We could previously show in collaboration with Kai Hell's group that an impaired protein import mediated by different chimeras of Erv can be presumably explained by the altered ratio between reduced and oxidized *Sc*Mia40 [157]. Moreover, a reduced Erv may impair the import of IMS substrates because it can only recover Mia40 efficiently, when Erv is mainly present in an oxidized state. This might also be the case in kinetoplastida if there is a Mia40 adapter replacement or if Erv directly oxidizes the substrates.

The mobility shift assay that I established in our lab for the determination of the redox state of *Lt*Erv might be used in the future for the investigation of other redox regulated proteins or to further analyze different mutants of *Lt*Erv in order to gain more insights into the structure-function relationships of this protein.

4.1.3 Recombinant expression and identification of interaction partners of *Pf*Erv

As explained in the introduction, *L. tarentolae* can be used as an expression system for the recombinant production of biologically active and natively processed proteins [60]. Therefore, *L. tarentolae* was used in this work to obtain recombinant *P. falciparum* Erv, which could not be purified from *E. coli* [38]. The successful production of *Pf*Erv in *L. tarentolae* was confirmed using a specific antibody (Figure 29). However, different native purification trials failed and no further characterization of *Pf*Erv was possible (Figure 30). A possible reason for this outcome may be the formation of insoluble aggregates of *Pf*Erv because of a strong upregulation. A potential strategy to overcome this problem might be the use of the inducible *L. tarentolae* Lexsy system that is currently being established in our lab [170]. Nevertheless, the *L. tarentolae* strain with upregulated *Pf*Erv protein levels may be useful for further investigations. For example, it might be tested, if the protein is transported into the IMS of *L. tarentolae* mitochondria. This may help to further elucidate the oxidative folding pathway for mitochondrial protein import into the IMS of different protists.

As the identification of a Mia40 adapter replacement in *L. tarentolae* did not succeed, it was also investigated if disulfide-bonded intermediates of *Pf*Erv can be observed in *P.*

falciparum. Western blot analyses revealed three additional bands to the one corresponding to the monomeric isoform of *Pf*Erv after NEM treatment under non-reducing conditions (Figure 31). The two upper bands may reflect mixed disulfide intermediates between *Pf*Erv and a potential interaction partner. However, the band observed at 34 kDa might also reflect dimeric *Pf*Erv. The band at around 26 kDa may indicate an interaction with a protein with a mass of around 9 kDa, which is a typical size for small Tim proteins as substrates of the oxidative folding pathway [17]. There was also one band detectable below the monomeric isoform of *Pf*Erv, which could be a degradation product or unspecific interaction of the antibody. However, this band was only observed for the sample treated with NEM under non-reducing conditions. Hence, most likely intramolecular disulfide bonds of *Pf*Erv were stabilized by alkylation with NEM and represent this band. In order to perform pull-down analyses with *Pf*Erv and further characterize the potential interaction partners, *Pf*Erv could be endogenously tagged using the CRISPR/Cas9 technology for future analyses.

4.1.3 Conclusion 1: Investigation of oxidative protein folding in protist mitochondria

Taken together, a potential replacement for Mia40 in parasitic protists remains to be identified and the oxidative folding machinery in the IMS of kinetoplastida and apicomplexa could not be unraveled during this PhD project. However, various protocols including trapping of potential mixed disulfide-bonded interaction partners, native and denaturing pull-downs and redox mobility shift assays were established in this work. These techniques might in the future be helpful to find a Mia40 adapter replacement (or to show that a comparable replacement does not exist) and to further elucidate the oxidative protein folding machinery. First results with *Pf*Erv already showed mixed disulfide-bonded interactions and can be characterized in future by endogenous tagging using the CRISPR/Cas9 technology. Moreover, initial results with the four newly designed cysteine-containing substrates of the oxidative protein folding pathway of the IMS were quite promising and could lead to a rather fast breakthrough in another PhD project.

As the results of the first project on oxidative protein folding in protist mitochondria were not conclusive, a backup project was started after about 1.5 years. The second, unrelated project on the elucidation of the catalytic mechanism of glutaredoxins led to numerous results, which are discussed in the following sections.

4.2 Glutaredoxins

4.2.1 Kinetics of *Pf*Grx mutants confirm a conserved catalysis mechanism

How exactly is the substrate preference for one of the two substrates of glutaredoxins determined by different enzyme residues? It was shown that the preference of glutaredoxins for GSSR and GSH depends on the γ-glutamyl moiety of glutathione [171-173]. However, the conventional model of Grx catalysis does not explain the exact binding of the different substrates. Therefore, I further investigated the interaction of specific enzyme areas with the substrates and the general mechanisms of Grx catalysis in the second project of my thesis [106, 116].

First, the applicability of the mechanistic model proposing two distinct glutathione interaction sites in *Sc*Grx7 was tested using the non-related enzyme *Pf*Grx. The mainly conserved residue Lys26 of *Pf*Grx was analyzed in analogy to *Sc*Grx7^{K105} (Figure 32). Kinetic parameters determined by GSSCys and HEDS assays were highly similar to the respective mutant *Sc*Grx7^{K105A} analyzed by Patricia Begas during her MD thesis [116]. The *Pf*Grx$^{C32S/C88S/K26A}$ mutant revealed a decelerated oxidative and reductive half-reaction in both assays, which is in accordance with the glutathione activator model as shown before for the *Sc*Grx7^{K105X} mutants [116].

Analyses of the analogous residue in human Grx revealed a decrease of the apparent V_{max} for *Hs*Grx^{K19L} and *Hs*Grx^{K19Q} by 70-80% compared to the control. Jao *et al.* assumed an impaired interaction of GSH and the glutathionylated mutant enzyme being responsible for the decrease of V_{max} [174]. These observations are in agreement with our data determined for residue 1 in Figure 32 from *Sc*Grx7 and *Pf*Grx [116].

Residue Asp90 of *Pf*Grx mostly affected the interaction with the first substrate during the oxidative half-reaction while the reductive half-reaction with GSH remained rate-limiting as observed for the control. The impaired oxidative half-reaction is in accordance with the results obtained from analysis of the homologous *Sc*Grx7 residue and the proposed glutathione-scaffold model [116]. Again, the determined kinetic parameters were highly similar. For a detailed discussion of the results mainly obtained from *Sc*Grx7 mutants, especially regarding the size and charge dependent effects, please also note the publication by Begas *et al.* 2017 [116].

Which is the rate-limiting step for glutaredoxin catalysis? *Pf*Grx$^{C32S/C88S}$ shows typical ping-pong kinetics with the substrates GSSCys and GSH as previously observed for *Sc*Grx7 [116]. Moreover, the enzyme tends to have infinite true k_{cat} and K_m values, which is in accordance with results obtained from analyses of human dithiol Grx or poplar GrxS12 [122, 175]. The rate constants for *Pf*Grx$^{C32S/C88S}$ and the mutants were in the range of 10^4-10^6 $M^{-1}s^{-1}$ and indicate a short-lived enzyme-substrate interaction with a rate-limiting re-orientation of the substrate. The reductive half-reaction with GSH is rate-limiting with a rate constant of 1.2×10^5 $M^{-1}s^{-1}$ and 10 times slower than the oxidation by GSSCys with a rate constant of 1.3×10^6 $M^{-1}s^{-1}$. However, when Lys26 was replaced by an alanine residue, the ratio between the rate constants for the oxidative and reductive half-reaction decreased and both reaction revealed similar rate constants. The stronger deceleration of the oxidative half-reaction supports the dual activator function for Lys26 of *Pf*Grx as also observed for *Sc*Grx7^{K105} [116]. The obtained rate constants are in accordance with analyses of mammalian glutaredoxins and poplar GrxS12 that revealed rate constants between 2.5×10^4 and 2×10^6 $M^{-1}s^{-1}$. These results also support the hypothesis of the reductive half-reaction as the rate-limiting step [150, 156, 174, 175]. The different rate constants for the oxidative and reductive half-reaction may be explained by different transition states for both substrates. The formation of the transition state between GSSCys and the reduced enzyme seems to be more efficient than the formation of the transition state between GSH and the glutathionylated enzyme. A possible explanation therefore could be a reorientation of Lys26 towards GS^-. This reorientation may result in a destabilization of the active site thiolate as the leaving group. The modeling of transition states will help to prove the proposed mechanism and will be done in collaboration with Holger Gohlke to gain further insights into the exact structure-function relationship of glutaredoxins.

In summary, I confirmed two distinct substrate interaction sites (r_1 with Lys26 of *Pf*Grx; r_6 with Asp90 of *Pf*Grx, Figure 32) and a conserved mechanism for glutaredoxin catalysis investigating the non-related enzyme *Pf*Grx. The kinetic parameters of mutant *Sc*Grx7 [116] and the respective *Pf*Grx mutants were highly similar. Therefore, the results obtained for the *Pf*Grx mutants support a general applicability of our mechanistic model with a glutathione-scaffold site interacting with GSSR and a glutathione activator site interacting with GSH [116]. Moreover, the results show that *Pf*Grx is an excellent model enzyme to study glutaredoxin catalysis.

In general, our study helps to understand the differences between enzymatically active and inactive glutaredoxins. Furthermore, this knowledge might be used for the generation of glutaredoxin-coupled fluorescent redox sensors or specific transition-state inhibitors [116]. Two distinct residues of two non-related Grx were assigned as part of the glutathione activator and glutathione scaffold site. Nevertheless, the prediction of the complete glutathione activator site without transition-state analogous is difficult because of instable GSH interactions [122]. Therefore, additional residues that could take part in the glutathione activator site were experimentally investigated in this work.

4.2.2 Further mapping of the activator site of *Sc*Grx7

A structure-based assignment of the glutathione activator site is difficult because of the labile GSH interaction [116]. However, in Begas *et al.* 2017, we proposed several possible residues [116]. These candidates are described in section 3 and were analyzed as potential activator site residues in this work.

The dimension of the kinetic parameters obtained from analyses of *Sc*Grx7 in this work is in accordance with our previous results [116]. Nevertheless, for a reliable comparison between the parameters of different mutants, *Sc*Grx7^{wt} was measured in parallel.

In this work, I showed that the hydroxyl group of Tyr110 in *Sc*Grx7 most probably does not contribute to the glutathione activator site. The effect of *Sc*Grx7^{Y110A} on the oxidative and reductive half-reaction in the GSSCys and HEDS assay can be explained by geometric influences due to the reduced size of this residue. This effect might point to a dual function of this residue for the interaction with both substrates. Another explanation could be, that the decreased oxidative half-reaction indirectly affects the reductive half-reaction with GSH because of a potential “sandwich-like” arrangement of the two different substrate interaction sites. This would imply that the effects also of other mutations on the oxidative half-reaction cannot be strictly separated from the reductive half-reaction. The behavior could in general also be explained by an influence on the reactivity of the active site cysteine. However, the pK_a value of this mutant is not significantly altered compared to the control (see next section) and therefore the first explanation is more likely. The reductive half-reaction is not rate-limiting for *Sc*Grx7^{Y110H} in the GSSCys assay as well as in the HEDS assay in contrast to the control. Both reactions show approximately the same reaction rate. In the HEDS assay, all *Sc*Grx7^{Y110X} mutants showed an influence on the oxidative and

reductive half-reaction in contrast to the GSSCys assay, in which only the *Sc*Grx7^{Y110A} mutant affected the reductive half-reaction with GSH. Comparing the results of the HEDS assay of the *Sc*Grx7^{Lys105} mutants and *Sc*Grx7^{Y110X} mutants, parameters are quite similar and could also point to a contribution of Tyr110 to the activator site. Again, this indicates the existence of two distinct glutathione interaction sites. As already discussed in Begas *et al*., the reciprocal Dalziel coefficient 2 most likely reflects the GSH-dependent reduction of a mixed disulfide intermediate between the glutaredoxin and β-ME [116].

Why is Tyr110 of *Sc*Grx7 not replaced by a phenylalanine in nature? *Sc*Grx7^{Y110F} revealed increased catalytic efficiencies compared to *Sc*Grx7^{wt} in the GSSCys assay. The monothiol glutaredoxins *At*GrxS15, *Sc*Grx3-5, *Hs*Grx5 and *Ec*Grx4 are inactive in standard enzymatic assays and have a phenylalanine at the same position (Figure 32) [106, 109, 116, 176]. Thus, a replacement at this position by phenylalanine does not necessarily lead to a higher enzymatic activity. Regulation of the enzyme by posttranslational modifications such as phosphorylation could play a role for the different preferences in various glutaredoxins. Sequence analysis of all three human Grx by Gallogly *et al.* revealed several putative phosphorylation sites with a probability score ≥ 0.6. However, these phosphorylation sites were not experimentally validated yet [122]. The probability score for the phosphorylation of Tyr110 was determined using the NetPhos 3.1 server [177] and revealed a much lower value of 0.513, which shows that a phosphorylation of this residue is not very likely. To the best of my knowledge, the only evidence for a phosphorylation of a glutaredoxin was published by Peggion *et al.* showing the phosphorylation of *Sc*Grx4 by the kinase Bud32p [178]. Taken together, it seems rather unlikely that a potential phosphorylation is the reason for a tyrosine (potentially leading to a reduced activity) instead of a phenylalanine at position 110 in *Sc*Grx7. A potential reason for a tyrosine at position 110 in *Sc*Grx7 could be the possible formation of hydrogen bonds between the hydroxyl group of the Tyr110 and a substrate or another protein.

Taken together, the hydroxyl group of Tyr110 in *Sc*Grx7 is most probably not part of the glutathione activator site but, nevertheless, the residue seems to be important for catalysis.

Mutants of the two potential activator site residues in helix 3, Asp144 and Glu147, showed very similar effects in the GSSCys assay. In both cases, the replacement of the residues with a positively charged amino acid accelerated the reductive half-reaction with GSH. This

suggests that a positively charged amino acid in helix 3 is beneficial for the recruitment of GS^-. In this case, the reductive half-reaction is not longer rate-limiting and both reactions have similar rate-constants. The "gain-of-function" mutants *Sc*Grx7^{D144K} and *Sc*Grx7^{E147K} indeed seem to affect the glutathione activator site. This may presumably be explained by an altered electrostatic complementarity of the mutated helix 3 of *Sc*Grx7 and the second substrate GSH. The electrostatic complementarity was shown to play an important role for the substrate specificity [179]

The homologous residue of *Sc*Grx7, Glu147, is replaced by a positively charged lysine in the catalytically active glutaredoxins *Sc*Grx6 and *Pf*Grx. However, a replacement of the homologs of Asp144 of *Sc*Grx7 is not always beneficial. In nature, this residue is replaced by a positively charged amino acid in several glutaredoxins that are inactive in standard kinetic assays or only show a low activity such as *Sc*Grx8 (Figure 32) [113, 180]. Taken together, the two analyzed residues in helix 3, previously proposed as potential activator site residues, are not part of the glutathione activator site but have a negative effect on the reductive half-reaction because of their acidic side chains. A replacement of these residues by an amino acid with a positively charged side chain leads to a gain of function and these mutants indeed seem to contribute to the glutathione activator site.

Mutations of Arg153 in *Sc*Grx7 mainly effected the oxidative half-reaction with GSSCys. However, the charge inversion mutation also decreased the reductive half-reaction with GSH. Thus, the charge but not the size of this residue seems to have an influence on the recruitment of GS^-. Tang *et al.* analyzed two residues in *Sc*Grx8 (Asn80 and Leu81) that are next to the homolog of *Sc*Grx7^{R153} in the loop of Grx (corresponding to Thr154 and Val155) [180]. They could show that these two residues contribute to the low activity of *Sc*Grx8 in the HEDS assay. However, residue 153 in *Sc*Grx7 that was analyzed in this work, is not replaced in *Sc*Grx8 (Arg79) and therefore does not explain the difference between active and inactive Grx. Further experiments might address the question, whether Thr154 and Val155 are part of the glutathione activator site. Taken together, residue 153 in *Sc*Grx7 does not seem to act as a specific activator site residue but seems to contribute to the scaffold site.

Modeling of transition states will be done in collaboration with Holger Gohlke and together with analyses by roGFP (redox-sensitive GFP) assays of the different mutants shown in this

work in collaboration with Bruce Morgan, this may help to understand the role of these and other mutants in more detail.

4.2.3 Mutations of *Sc*Grx7 only have a minor influence on the thiol pK_a value

The interaction of Grx with its second substrate GSH during the reductive half-reaction is the most important step for catalysis according to the glutathione activator model [113]. The reductive half-reaction is critical and often rate-limiting presumably because of GS^- nucleophile formation and for the stability of the thiolate leaving group [107, 113, 116, 180]. Therefore, a low pK_a value could accelerate the reaction or *vice versa*. In this work, I investigated how the different enzymatic activities of selected *Sc*Grx7 mutants correlate with the pK_a value of their active site cysteine.

The determination of the effects of selected point mutants of *Sc*Grx7 on the thiol pK_a value of the active site cysteine revealed only a minor influence (Figure 41). *Sc*Grx7^{wt} showed a pK_a value of 4.34 ± 0.1, which is in accordance with other studies showing that the thiol group of the active site cysteine in various Grx-isoforms is quite acidic with pK_a values between 3.2 and 5.5 [107, 108, 127, 149, 150, 175]. An exception is *Sc*Grx8 with a pK_a value of 7.1 ± 0.1 as reported by Tang *et al.* corresponding to the low enzymatic activity of this enzyme [180]. Often, a high pK_a value of the active site cysteine comes along with absent or reduced enzymatic activities because of the altered stability of the leaving group [106-108]. However, the pK_a value does not always correlate with the activity as shown by a comparison of *Sc*Grx1 and *Sc*Grx2 revealing similar pK_a values of the active site cysteine but differences in the activity [127]. Jao *et al.* analyzed the influence of residue 1 (Lys19; homologous to Lys105 of *Sc*Grx7) on the thiol pK_a value of the active site cysteine in human Grx [174]. The predicted increase of the pK_a value for enzymes carrying mutations of this residue, determined by modeling of the NMR structure, could not be experimentally confirmed and therefore does not fully account for the differences in the enzymatic activity.

A similar result was also observed in this work. Most of the analyzed mutants did not show a significantly altered pK_a value despite reduced enzymatic activities in the GSSCys and HEDS assay. The different enzymatic activities of the alanine mutants of the confirmed glutathione activator site in *Sc*Grx7^{K105A}, the scaffold site in *Sc*Grx7^{E170A} and *Sc*Grx7^{Y110A} did not correlate with the pK_a value of the active site cysteine. Only the pK_a value of the active

site cysteine in *Sc*Grx7^{K105E}, which also revealed the most drastically reduced enzymatic activity in previous studies [116], was significantly increased from 4.34 to 4.97.

Taken together, the contribution of both factors – GS^- nucleophile formation and the stability of the leaving group – have different influences on the enzyme activity. In the case of *Sc*Grx7^{K105A}, the GS^- nucleophile formation might be the crucial factor.

4.2.4 Conclusion 2: Elucidation of the catalytic mechanism of glutaredoxins

Taken together, the existence of two distinct glutathione interaction sites in glutaredoxins as it was shown before by Begas *et al.* could be confirmed using *Pf*Grx as a model enzyme from the non-related parasite *P. falciparum* [116]. Moreover, four additional residues that were suggested to also contribute to the glutathione activator site were analyzed in this work. However, for these residues a role as glutathione activators could not be confirmed although all residues seem to affect substrate interactions. In contrast, Arg153 of *Sc*Grx7 seem to contribute to the glutathione scaffold site. In addition, I could show that the two charge inversion mutants of the helix 3 residues Asp144 and Glu147 in *Sc*Grx7 enhanced the interaction with the second substrate GSH. Hence, helix 3 of these "gain-of-function" mutants indeed seems to affect the glutathione activator site. Furthermore, the influence of the pK_a value of the active site cysteine was determined for different mutants of *Sc*Grx7 that previously showed a decreased activity in standard enzymatic assays. Here, it was shown that the introduced mutations influenced the pK_a value of *Sc*Grx7 only to a minor degree.

5 Literature

[1] Chacinska, A., C.M. Koehler, D. Milenkovic, T. Lithgow, and N. Pfanner, *Importing mitochondrial proteins: machineries and mechanisms.* Cell, 2009. **138**(4): p. 628-44.

[2] Muhlenhoff, U. and R. Lill, *Biogenesis of iron-sulfur proteins in eukaryotes: a novel task of mitochondria that is inherited from bacteria.* Biochim Biophys Acta, 2000. **1459**(2-3): p. 370-82.

[3] Archibald, J.M., *Endosymbiosis and Eukaryotic Cell Evolution.* Curr Biol, 2015. **25**(19): p. R911-21.

[4] Sickmann, A., J. Reinders, Y. Wagner, C. Joppich, R. Zahedi, H.E. Meyer, B. Schonfisch, I. Perschil, A. Chacinska, B. Guiard, P. Rehling, N. Pfanner, and C. Meisinger, *The proteome of Saccharomyces cerevisiae mitochondria.* Proc Natl Acad Sci U S A, 2003. **100**(23): p. 13207-12.

[5] Perocchi, F., L.J. Jensen, J. Gagneur, U. Ahting, C. von Mering, P. Bork, H. Prokisch, and L.M. Steinmetz, *Assessing systems properties of yeast mitochondria through an interaction map of the organelle.* PLoS Genet, 2006. **2**(10): p. e170.

[6] Gonczarowska-Jorge, H., R.P. Zahedi, and A. Sickmann, *The proteome of baker's yeast mitochondria.* Mitochondrion, 2017. **33**: p. 15-21.

[7] Pagliarini, D.J., S.E. Calvo, B. Chang, S.A. Sheth, S.B. Vafai, S.E. Ong, G.A. Walford, C. Sugiana, A. Boneh, W.K. Chen, D.E. Hill, M. Vidal, J.G. Evans, D.R. Thorburn, S.A. Carr, and V.K. Mootha, *A mitochondrial protein compendium elucidates complex I disease biology.* Cell, 2008. **134**(1): p. 112-23.

[8] Calvo, S.E. and V.K. Mootha, *The mitochondrial proteome and human disease.* Annu Rev Genomics Hum Genet, 2010. **11**: p. 25-44.

[9] Wiedemann, N. and N. Pfanner, *Mitochondrial Machineries for Protein Import and Assembly.* Annu Rev Biochem, 2017. **86**: p. 685-714.

[10] Neupert, W. and J.M. Herrmann, *Translocation of proteins into mitochondria.* Annu Rev Biochem, 2007. **76**: p. 723-49.

[11] Chacinska, A., M. Lind, A.E. Frazier, J. Dudek, C. Meisinger, A. Geissler, A. Sickmann, H.E. Meyer, K.N. Truscott, B. Guiard, N. Pfanner, and P. Rehling, *Mitochondrial presequence translocase: switching between TOM tethering and motor recruitment involves Tim21 and Tim17.* Cell, 2005. **120**(6): p. 817-29.

[12] Bauer, M.F., S. Hofmann, W. Neupert, and M. Brunner, *Protein translocation into mitochondria: the role of TIM complexes.* Trends Cell Biol, 2000. **10**(1): p. 25-31.

[13] Hawlitschek, G., H. Schneider, B. Schmidt, M. Tropschug, F.U. Hartl, and W. Neupert, *Mitochondrial protein import: identification of processing peptidase and of PEP, a processing enhancing protein.* Cell, 1988. **53**(5): p. 795-806.

[14] Sirrenberg, C., M.F. Bauer, B. Guiard, W. Neupert, and M. Brunner, *Import of carrier proteins into the mitochondrial inner membrane mediated by Tim22.* Nature, 1996. **384**(6609): p. 582-5.

[15] Koehler, C.M., E. Jarosch, K. Tokatlidis, K. Schmid, R.J. Schweyen, and G. Schatz, *Import of mitochondrial carriers mediated by essential proteins of the intermembrane space.* Science, 1998. **279**(5349): p. 369-73.

[16] Sirrenberg, C., M. Endres, H. Folsch, R.A. Stuart, W. Neupert, and M. Brunner, *Carrier protein import into mitochondria mediated by the intermembrane proteins Tim10/Mrs11 and Tim12/Mrs5.* Nature, 1998. **391**(6670): p. 912-5.

[17] Backes, S. and J.M. Herrmann, *Protein Translocation into the Intermembrane Space and Matrix of Mitochondria: Mechanisms and Driving Forces.* Front Mol Biosci, 2017. **4**: p. 83.

[18] Calvo, S.E., K.R. Clauser, and V.K. Mootha, *MitoCarta2.0: an updated inventory of mammalian mitochondrial proteins.* Nucleic Acids Res, 2016. **44**(D1): p. D1251-7.

[19] Morgenstern, M., S.B. Stiller, P. Lubbert, C.D. Peikert, S. Dannenmaier, F. Drepper, U. Weill, P. Hoss, R. Feuerstein, M. Gebert, M. Bohnert, M. van der Laan, M. Schuldiner, C. Schutze, S. Oeljeklaus, N. Pfanner, N. Wiedemann, and B. Warscheid, *Definition of a High-Confidence Mitochondrial Proteome at Quantitative Scale.* Cell Rep, 2017. **19**(13): p. 2836-2852.

[20] Herrmann, J.M. and K. Hell, *Chopped, trapped or tacked--protein translocation into the IMS of mitochondria.* Trends Biochem Sci, 2005. **30**(4): p. 205-11.

[21] Chacinska, A., S. Pfannschmidt, N. Wiedemann, V. Kozjak, L.K. Sanjuan Szklarz, A. Schulze-Specking, K.N. Truscott, B. Guiard, C. Meisinger, and N. Pfanner, *Essential role of Mia40 in import and assembly of mitochondrial intermembrane space proteins.* Embo J, 2004. **23**(19): p. 3735-46.

[22] Becker, T., F.N. Vogtle, D. Stojanovski, and C. Meisinger, *Sorting and assembly of mitochondrial outer membrane proteins.* Biochim Biophys Acta, 2008. **1777**(7-8): p. 557-63.

[23] Becker, T., S. Pfannschmidt, B. Guiard, D. Stojanovski, D. Milenkovic, S. Kutik, N. Pfanner, C. Meisinger, and N. Wiedemann, *Biogenesis of the mitochondrial TOM complex: Mim1 promotes insertion and assembly of signal-anchored receptors.* J Biol Chem, 2008. **283**(1): p. 120-7.

[24] Eckers, E., M. Cyrklaff, L. Simpson, and M. Deponte, *Mitochondrial protein import pathways are functionally conserved among eukaryotes despite compositional diversity of the import machineries.* Biol Chem, 2012. **393**(6): p. 513-24.

[25] Deponte, M. and K. Hell, *Disulphide bond formation in the intermembrane space of mitochondria.* J Biochem, 2009. **146**(5): p. 599-608.

[26] Mesecke, N., N. Terziyska, C. Kozany, F. Baumann, W. Neupert, K. Hell, and J.M. Herrmann, *A disulfide relay system in the intermembrane space of mitochondria that mediates protein import.* Cell, 2005. **121**(7): p. 1059-69.

[27] Naoe, M., Y. Ohwa, D. Ishikawa, C. Ohshima, S. Nishikawa, H. Yamamoto, and T. Endo, *Identification of Tim40 that mediates protein sorting to the mitochondrial intermembrane space.* J Biol Chem, 2004. **279**(46): p. 47815-21.

[28] Terziyska, N., T. Lutz, C. Kozany, D. Mokranjac, N. Mesecke, W. Neupert, J.M. Herrmann, and K. Hell, *Mia40, a novel factor for protein import into the intermembrane space of mitochondria is able to bind metal ions.* FEBS Lett, 2005. **579**(1): p. 179-84.

[29] Herrmann, J.M. and R. Kohl, *Catch me if you can! Oxidative protein trapping in the intermembrane space of mitochondria.* J Cell Biol, 2007. **176**(5): p. 559-63.

[30] Muller, J.M., D. Milenkovic, B. Guiard, N. Pfanner, and A. Chacinska, *Precursor oxidation by Mia40 and Erv1 promotes vectorial transport of proteins into the mitochondrial intermembrane space.* Mol Biol Cell, 2008. **19**(1): p. 226-36.

[31] Bihlmaier, K., N. Mesecke, N. Terziyska, M. Bien, K. Hell, and J.M. Herrmann, *The disulfide relay system of mitochondria is connected to the respiratory chain.* J Cell Biol, 2007. **179**(3): p. 389-95.

[32] Dabir, D.V., E.P. Leverich, S.K. Kim, F.D. Tsai, M. Hirasawa, D.B. Knaff, and C.M. Koehler, *A role for cytochrome c and cytochrome c peroxidase in electron shuttling from Erv1.* Embo J, 2007. **26**(23): p. 4801-11.

[33] Neal, S.E., D.V. Dabir, J. Wijaya, C. Boon, and C.M. Koehler, *Osm1 facilitates the transfer of electrons from Erv1 to fumarate in the redox-regulated import pathway in the mitochondrial intermembrane space.* Mol Biol Cell, 2017. **28**(21): p. 2773-2785.

[34] Adl, S.M., A.G. Simpson, M.A. Farmer, R.A. Andersen, O.R. Anderson, J.R. Barta, S.S. Bowser, G. Brugerolle, R.A. Fensome, S. Fredericq, T.Y. James, S. Karpov, P. Kugrens, J. Krug, C.E. Lane, L.A. Lewis, J. Lodge, D.H. Lynn, D.G. Mann, R.M. McCourt, L. Mendoza, O. Moestrup, S.E. Mozley-Standridge, T.A. Nerad, C.A. Shearer, A.V. Smirnov, F.W. Spiegel, and M.F. Taylor, *The new higher level classification of eukaryotes with emphasis on the taxonomy of protists.* J Eukaryot Microbiol, 2005. **52**(5): p. 399-451.

[35] Baldauf, S.L., *The deep roots of eukaryotes.* Science, 2003. **300**(5626): p. 1703-6.

[36] Steenkamp, E.T., J. Wright, and S.L. Baldauf, *The protistan origins of animals and fungi.* Mol Biol Evol, 2006. **23**(1): p. 93-106.

[37] Basu, S., J.C. Leonard, N. Desai, D.A. Mavridou, K.H. Tang, A.D. Goddard, M.L. Ginger, J. Lukes, and J.W. Allen, *Divergence of Erv1-associated mitochondrial import and export pathways in trypanosomes and anaerobic protists.* Eukaryot Cell, 2013. **12**(2): p. 343-55.

[38] Eckers, E., C. Petrungaro, D. Gross, J. Riemer, K. Hell, and M. Deponte, *Divergent molecular evolution of the mitochondrial sulfhydryl:cytochrome C oxidoreductase Erv in opisthokonts and parasitic protists.* J Biol Chem, 2013. **288**(4): p. 2676-88.

[39] Andrews, K.T., G. Fisher, and T.S. Skinner-Adams, *Drug repurposing and human parasitic protozoan diseases.* Int J Parasitol Drugs Drug Resist, 2014. **4**(2): p. 95-111.

[40] Lozano, R., M. Naghavi, K. Foreman, S. Lim, K. Shibuya, V. Aboyans, J. Abraham, T. Adair, R. Aggarwal, S.Y. Ahn, M. Alvarado, H.R. Anderson, L.M. Anderson, K.G. Andrews, C. Atkinson, L.M. Baddour, S. Barker-Collo, D.H. Bartels, M.L. Bell, E.J. Benjamin, D. Bennett, K. Bhalla, B. Bikbov, A. Bin Abdulhak, G. Birbeck, F. Blyth, I. Bolliger, S. Boufous, C. Bucello, M. Burch, P. Burney, J. Carapetis, H. Chen, D. Chou, S.S. Chugh, L.E. Coffeng, S.D. Colan, S. Colquhoun, K.E. Colson, J. Condon, M.D. Connor, L.T. Cooper, M. Corriere, M. Cortinovis, K.C. de Vaccaro, W. Couser, B.C. Cowie, M.H. Criqui, M. Cross, K.C. Dabhadkar, N. Dahodwala, D. De Leo, L. Degenhardt, A. Delossantos, J. Denenberg, D.C. Des Jarlais, S.D. Dharmaratne, E.R. Dorsey, T. Driscoll, H. Duber, B. Ebel, P.J. Erwin, P. Espindola, M. Ezzati, V. Feigin, A.D. Flaxman, M.H. Forouzanfar, F.G. Fowkes, R. Franklin, M. Fransen, M.K. Freeman, S.E. Gabriel, E. Gakidou, F. Gaspari, R.F. Gillum, D. Gonzalez-Medina, Y.A. Halasa, D. Haring, J.E. Harrison, R. Havmoeller, R.J. Hay, B. Hoen, P.J. Hotez, D. Hoy, K.H. Jacobsen, S.L. James, R. Jasrasaria, S. Jayaraman, N. Johns, G. Karthikeyan, N. Kassebaum, A. Keren, J.P. Khoo, L.M. Knowlton, O. Kobusingye, A. Koranteng, R. Krishnamurthi, M. Lipnick, S.E. Lipshultz, S.L. Ohno, J. Mabweijano, M.F. MacIntyre, L. Mallinger, L. March, G.B. Marks, R. Marks, A. Matsumori, R. Matzopoulos, B.M. Mayosi, J.H. McAnulty, M.M. McDermott, J. McGrath, G.A. Mensah, T.R. Merriman, C. Michaud, M. Miller, T.R. Miller, C. Mock, A.O. Mocumbi, A.A. Mokdad, A. Moran, K. Mulholland, M.N. Nair, L. Naldi, K.M. Narayan, K. Nasseri, P. Norman, M. O'Donnell, S.B. Omer, K. Ortblad, R. Osborne, D. Ozgediz, B. Pahari, J.D. Pandian, A.P. Rivero, R.P. Padilla, F. Perez-Ruiz, N. Perico, D. Phillips, K. Pierce, C.A. Pope, 3rd, E. Porrini, F. Pourmalek, M. Raju, D. Ranganathan, J.T. Rehm, D.B. Rein, G. Remuzzi, F.P. Rivara, T. Roberts, F.R. De Leon, L.C. Rosenfeld, L. Rushton, R.L. Sacco, J.A. Salomon, U. Sampson, E. Sanman, D.C. Schwebel, M. Segui-Gomez, D.S. Shepard, D. Singh, J. Singleton, K. Sliwa, E. Smith, A. Steer, J.A. Taylor, B. Thomas, I.M. Tleyjeh, J.A. Towbin, T. Truelsen, E.A. Undurraga, N. Venketasubramanian, L. Vijayakumar, T. Vos, G.R. Wagner, M. Wang, W. Wang, K. Watt, M.A. Weinstock, R. Weintraub, J.D. Wilkinson, A.D. Woolf, S. Wulf, P.H. Yeh, P. Yip, A. Zabetian, Z.J. Zheng, A.D. Lopez, C.J. Murray, M.A. AlMazroa and Z.A. Memish, *Global and regional mortality from 235 causes of death for 20 age groups in 1990 and 2010: a systematic analysis for the Global Burden of Disease Study 2010.* Lancet, 2012. **380**(9859): p. 2095-128.

[41] Murray, C.J., L.C. Rosenfeld, S.S. Lim, K.G. Andrews, K.J. Foreman, D. Haring, N. Fullman, M. Naghavi, R. Lozano, and A.D. Lopez, *Global malaria mortality between 1980 and 2010: a systematic analysis.* Lancet, 2012. **379**(9814): p. 413-31.

[42] WHO, *World Malaria Report*. 2016.

[43] Tuteja, R., *Malaria - an overview.* Febs j, 2007. **274**(18): p. 4670-9.

[44] Cowman, A.F., J. Healer, D. Marapana, and K. Marsh, *Malaria: Biology and Disease.* Cell, 2016. **167**(3): p. 610-624.

[45] Shapiro, T.A. and P.T. Englund, *The structure and replication of kinetoplast DNA.* Annu Rev Microbiol, 1995. **49**: p. 117-43.

[46] Lukes, J., D.L. Guilbride, J. Votypka, A. Zikova, R. Benne, and P.T. Englund, *Kinetoplast DNA network: evolution of an improbable structure.* Eukaryot Cell, 2002. **1**(4): p. 495-502.

[47] Cross, G.A., *Trypanosomes at the gates.* Science, 2005. **309**(5733): p. 355.

[48] Buscher, P., G. Cecchi, V. Jamonneau, and G. Priotto, *Human African trypanosomiasis.* Lancet, 2017. **390**(10110): p. 2397-2409.

[49] WHO. *Chagas disease*. 2018; Available from: http://www.who.int/chagas/en/.

[50] Alvar, J., S. Yactayo, and C. Bern, *Leishmaniasis and poverty.* Trends Parasitol, 2006. **22**(12): p. 552-7.
[51] WHO. *Leishmaniasis*. 2018; Available from: http://www.who.int/leishmaniasis/en/.
[52] Basile, G. and M. Peticca, *Recombinant protein expression in Leishmania tarentolae.* Mol Biotechnol, 2009. **43**(3): p. 273-8.
[53] Pineda, T., Y. Valencia, M.F. Florez, S.A. Pulido, I.D. Velez, and S.M. Robledo, *A non-commercial approach for the generation of transgenic Leishmania tarentolae and its application in antileishmanial drug discovery.* Parasitology, 2016: p. 1-10.
[54] Benne, R., *RNA editing in mitochondria of Leishmania tarentolae and Crithidia fasciculata.* Semin Cell Biol, 1993. **4**(4): p. 241-9.
[55] Landweber, L.F. and W. Gilbert, *RNA editing as a source of genetic variation.* Nature, 1993. **363**(6425): p. 179-82.
[56] Simpson, L., G.C. Frech, and D.A. Maslov, *RNA editing in trypanosomatid mitochondria.* Methods Enzymol, 1996. **264**: p. 99-121.
[57] Knoop, V., *When you can't trust the DNA: RNA editing changes transcript sequences.* Cell Mol Life Sci, 2011. **68**(4): p. 567-86.
[58] Ferguson, M.A., *The structure, biosynthesis and functions of glycosylphosphatidylinositol anchors, and the contributions of trypanosome research.* J Cell Sci, 1999. **112 (Pt 17)**: p. 2799-809.
[59] Eckers, E. and M. Deponte, *No need for labels: the autofluorescence of Leishmania tarentolae mitochondria and the necessity of negative controls.* PLoS One, 2012. **7**(10): p. e47641.
[60] Breitling, R., S. Klingner, N. Callewaert, R. Pietrucha, A. Geyer, G. Ehrlich, R. Hartung, A. Muller, R. Contreras, S.M. Beverley, and K. Alexandrov, *Non-pathogenic trypanosomatid protozoa as a platform for protein research and production.* Protein Expr Purif, 2002. **25**(2): p. 209-18.
[61] Fischer, K., V.P. dos Reis, S. Finke, L. Sauerhering, E. Stroh, A. Karger, A. Maisner, M.H. Groschup, S. Diederich, and A. Balkema-Buschmann, *Expression, characterisation and antigenicity of a truncated Hendra virus attachment protein expressed in the protozoan host Leishmania tarentolae.* J Virol Methods, 2016. **228**: p. 48-54.
[62] Rooney, B., T. Piening, P. Buscher, S. Roge, and C.M. Smales, *Expression of Trypanosoma brucei gambiense Antigens in Leishmania tarentolae. Potential for Use in Rapid Serodiagnostic Tests (RDTs).* PLoS Negl Trop Dis, 2015. **9**(12): p. e0004271.
[63] Legastelois, I., S. Buffin, I. Peubez, C. Mignon, R. Sodoyer, and B. Werle, *Non-conventional expression systems for the production of vaccine proteins and immunotherapeutic molecules.* Hum Vaccin Immunother, 2017. **13**(4): p. 947-961.
[64] Niimi, T., *Recombinant protein production in the eukaryotic protozoan parasite Leishmania tarentolae: a review.* Methods Mol Biol, 2012. **824**: p. 307-15.
[65] Carneiro, D.G., T. Clarke, C.C. Davies, and D. Bailey, *Identifying novel protein interactions: Proteomic methods, optimisation approaches and data analysis pipelines.* Methods, 2016. **95**: p. 46-54.
[66] Jiang, H. and A.M. English, *Quantitative analysis of the yeast proteome by incorporation of isotopically labeled leucine.* J Proteome Res, 2002. **1**(4): p. 345-50.
[67] Ong, S.E., B. Blagoev, I. Kratchmarova, D.B. Kristensen, H. Steen, A. Pandey, and M. Mann, *Stable isotope labeling by amino acids in cell culture, SILAC, as a simple and accurate approach to expression proteomics.* Mol Cell Proteomics, 2002. **1**(5): p. 376-86.
[68] Zhu, H., S. Pan, S. Gu, E.M. Bradbury, and X. Chen, *Amino acid residue specific stable isotope labeling for quantitative proteomics.* Rapid Commun Mass Spectrom, 2002. **16**(22): p. 2115-23.
[69] Ong, S.E., *The expanding field of SILAC.* Anal Bioanal Chem, 2012. **404**(4): p. 967-76.
[70] Kani, K., *Quantitative Proteomics Using SILAC.* Methods Mol Biol, 2017. **1550**: p. 171-184.

[71] Brotherton, M.C., S. Bourassa, P. Leprohon, D. Legare, G.G. Poirier, A. Droit, and M. Ouellette, *Proteomic and genomic analyses of antimony resistant Leishmania infantum mutant.* PLoS One, 2013. **8**(11): p. e81899.

[72] Brotherton, M.C., S. Bourassa, D. Legare, G.G. Poirier, A. Droit, and M. Ouellette, *Quantitative proteomic analysis of amphotericin B resistance in Leishmania infantum.* Int J Parasitol Drugs Drug Resist, 2014. **4**(2): p. 126-32.

[73] Patel, V.J., K. Thalassinos, S.E. Slade, J.B. Connolly, A. Crombie, J.C. Murrell, and J.H. Scrivens, *A comparison of labeling and label-free mass spectrometry-based proteomics approaches.* J Proteome Res, 2009. **8**(7): p. 3752-9.

[74] Roux, K.J., D.I. Kim, M. Raida, and B. Burke, *A promiscuous biotin ligase fusion protein identifies proximal and interacting proteins in mammalian cells.* J Cell Biol, 2012. **196**(6): p. 801-10.

[75] Morriswood, B., K. Havlicek, L. Demmel, S. Yavuz, M. Sealey-Cardona, K. Vidilaseris, D. Anrather, J. Kostan, K. Djinovic-Carugo, K.J. Roux, and G. Warren, *Novel bilobe components in Trypanosoma brucei identified using proximity-dependent biotinylation.* Eukaryot Cell, 2013. **12**(2): p. 356-67.

[76] McAllaster, M.R., K.N. Ikeda, A. Lozano-Nunez, D. Anrather, V. Unterwurzacher, T. Gossenreiter, J.A. Perry, R. Crickley, C.J. Mercadante, S. Vaughan, and C.L. de Graffenried, *Proteomic identification of novel cytoskeletal proteins associated with TbPLK, an essential regulator of cell morphogenesis in Trypanosoma brucei.* Mol Biol Cell, 2015. **26**(17): p. 3013-29.

[77] Chen, A.L., E.W. Kim, J.Y. Toh, A.A. Vashisht, A.Q. Rashoff, C. Van, A.S. Huang, A.S. Moon, H.N. Bell, L.A. Bentolila, J.A. Wohlschlegel, and P.J. Bradley, *Novel components of the Toxoplasma inner membrane complex revealed by BioID.* MBio, 2015. **6**(1): p. e02357-14.

[78] Kehrer, J., F. Frischknecht, and G.R. Mair, *Proteomic Analysis of the Plasmodium berghei Gametocyte Egressome and Vesicular bioID of Osmiophilic Body Proteins Identifies Merozoite TRAP-like Protein (MTRAP) as an Essential Factor for Parasite Transmission.* Mol Cell Proteomics, 2016. **15**(9): p. 2852-62.

[79] Schnider, C.B., D. Bausch-Fluck, F. Bruhlmann, V.T. Heussler, and P.C. Burda, *BioID Reveals Novel Proteins of the Plasmodium Parasitophorous Vacuole Membrane.* mSphere, 2018. **3**(1).

[80] Khosh-Naucke, M., J. Becker, P. Mesen-Ramirez, P. Kiani, J. Birnbaum, U. Frohlke, E. Jonscher, H. Schluter, and T. Spielmann, *Identification of novel parasitophorous vacuole proteins in P. falciparum parasites using BioID.* Int J Med Microbiol, 2017.

[81] Wei, Y., R.N. Vellanki, E. Coyaud, V. Ignatchenko, L. Li, J.R. Krieger, P. Taylor, J. Tong, N.A. Pham, G. Liu, B. Raught, B.G. Wouters, T. Kislinger, M.S. Tsao, and M.F. Moran, *CHCHD2 Is Coamplified with EGFR in NSCLC and Regulates Mitochondrial Function and Cell Migration.* Mol Cancer Res, 2015. **13**(7): p. 1119-29.

[82] Bhaduri, A., A. Ungewickell, L.D. Boxer, V. Lopez-Pajares, B.J. Zarnegar, and P.A. Khavari, *Network Analysis Identifies Mitochondrial Regulation of Epidermal Differentiation by MPZL3 and FDXR.* Dev Cell, 2015. **35**(4): p. 444-57.

[83] Kim, D.I. and K.J. Roux, *Filling the Void: Proximity-Based Labeling of Proteins in Living Cells.* Trends Cell Biol, 2016. **26**(11): p. 804-817.

[84] Roux, K.J., D.I. Kim, B. Burke, and D.G. May, *BioID: A Screen for Protein-Protein Interactions.* Curr Protoc Protein Sci, 2018. **91**: p. 19.23.1-19.23.15.

[85] Firat-Karalar, E.N. and T. Stearns, *Probing mammalian centrosome structure using BioID proximity-dependent biotinylation.* Methods Cell Biol, 2015. **129**: p. 153-70.

[86] Kim, D.I., K.C. Birendra, W. Zhu, K. Motamedchaboki, V. Doye, and K.J. Roux, *Probing nuclear pore complex architecture with proximity-dependent biotinylation.* Proc Natl Acad Sci U S A, 2014. **111**(24): p. E2453-61.

[87] Hung, V., N.D. Udeshi, S.S. Lam, K.H. Loh, K.J. Cox, K. Pedram, S.A. Carr, and A.Y. Ting, *Spatially resolved proteomic mapping in living cells with the engineered peroxidase APEX2.* Nat Protoc, 2016. **11**(3): p. 456-75.

[88] Deponte, M., *The Incomplete Glutathione Puzzle: Just Guessing at Numbers and Figures?* Antioxid Redox Signal, 2017. **27**(15): p. 1130-1161.
[89] Herrero, E. and M.A. de la Torre-Ruiz, *Monothiol glutaredoxins: a common domain for multiple functions.* Cell Mol Life Sci, 2007. **64**(12): p. 1518-30.
[90] Outten, C.E. and A.N. Albetel, *Iron sensing and regulation in Saccharomyces cerevisiae: Ironing out the mechanistic details.* Curr Opin Microbiol, 2013. **16**(6): p. 662-8.
[91] Couturier, J., J. Przybyla-Toscano, T. Roret, C. Didierjean, and N. Rouhier, *The roles of glutaredoxins ligating Fe-S clusters: Sensing, transfer or repair functions?* Biochim Biophys Acta, 2015. **1853**(6): p. 1513-27.
[92] Holmgren, A., *Thioredoxin and glutaredoxin systems.* J Biol Chem, 1989. **264**(24): p. 13963-6.
[93] Elledge, S.J., Z. Zhou, and J.B. Allen, *Ribonucleotide reductase: regulation, regulation, regulation.* Trends Biochem Sci, 1992. **17**(3): p. 119-23.
[94] Holmgren, A., *Hydrogen donor system for Escherichia coli ribonucleoside-diphosphate reductase dependent upon glutathione.* Proc Natl Acad Sci U S A, 1976. **73**(7): p. 2275-9.
[95] Holmgren, A., *Glutathione-dependent synthesis of deoxyribonucleotides. Purification and characterization of glutaredoxin from Escherichia coli.* J Biol Chem, 1979. **254**(9): p. 3664-71.
[96] Gon, S., M.J. Faulkner, and J. Beckwith, *In vivo requirement for glutaredoxins and thioredoxins in the reduction of the ribonucleotide reductases of Escherichia coli.* Antioxid Redox Signal, 2006. **8**(5-6): p. 735-42.
[97] Zahedi Avval, F. and A. Holmgren, *Molecular mechanisms of thioredoxin and glutaredoxin as hydrogen donors for Mammalian s phase ribonucleotide reductase.* J Biol Chem, 2009. **284**(13): p. 8233-40.
[98] Song, J.J. and Y.J. Lee, *Differential role of glutaredoxin and thioredoxin in metabolic oxidative stress-induced activation of apoptosis signal-regulating kinase 1.* Biochem J, 2003. **373**(Pt 3): p. 845-53.
[99] Sun, J., X. Wei, Y. Lu, M. Cui, F. Li, J. Lu, Y. Liu, and X. Zhang, *Glutaredoxin 1 (GRX1) inhibits oxidative stress and apoptosis of chondrocytes by regulating CREB/HO-1 in osteoarthritis.* Mol Immunol, 2017. **90**: p. 211-218.
[100] Li, Y., M. Ren, X. Wang, X. Cui, H. Zhao, C. Zhao, J. Zhou, Y. Guo, Y. Hu, C. Yan, B. Berk, and J. Wang, *Glutaredoxin 1 mediates the protective effect of steady laminar flow on endothelial cells against oxidative stress-induced apoptosis via inhibiting Bim.* Sci Rep, 2017. **7**(1): p. 15539.
[101] Zhu, Y.Y., Z.J. Wang, N. Ma, and J.W. Zhou, *[Proliferation and apoptosis of lung cancer cells regulated by gultaredoxin 3].* Zhonghua Zhong Liu Za Zhi, 2018. **40**(5): p. 325-329.
[102] Mieyal, J.J., M.M. Gallogly, S. Qanungo, E.A. Sabens, and M.D. Shelton, *Molecular mechanisms and clinical implications of reversible protein S-glutathionylation.* Antioxid Redox Signal, 2008. **10**(11): p. 1941-88.
[103] Gorelenkova Miller, O. and J.J. Mieyal, *Critical Roles of Glutaredoxin in Brain Cells-Implications for Parkinson's Disease.* Antioxid Redox Signal, 2018.
[104] Lillig, C.H., C. Berndt, and A. Holmgren, *Glutaredoxin systems.* Biochim Biophys Acta, 2008. **1780**(11): p. 1304-17.
[105] Martin, J.L., *Thioredoxin--a fold for all reasons.* Structure, 1995. **3**(3): p. 245-50.
[106] Deponte, M., *Glutathione catalysis and the reaction mechanisms of glutathione-dependent enzymes.* Biochim Biophys Acta, 2013. **1830**(5): p. 3217-66.
[107] Tamarit, J., G. Belli, E. Cabiscol, E. Herrero, and J. Ros, *Biochemical characterization of yeast mitochondrial Grx5 monothiol glutaredoxin.* J Biol Chem, 2003. **278**(28): p. 25745-51.
[108] Deponte, M., K. Becker, and S. Rahlfs, *Plasmodium falciparum glutaredoxin-like proteins.* Biol Chem, 2005. **386**(1): p. 33-40.
[109] Fernandes, A.P., M. Fladvad, C. Berndt, C. Andresen, C.H. Lillig, P. Neubauer, M. Sunnerhagen, A. Holmgren, and A. Vlamis-Gardikas, *A novel monothiol glutaredoxin (Grx4)*

from Escherichia coli can serve as a substrate for thioredoxin reductase. J Biol Chem, 2005. **280**(26): p. 24544-52.

[110] Filser, M., M.A. Comini, M.M. Molina-Navarro, N. Dirdjaja, E. Herrero, and R.L. Krauth-Siegel, *Cloning, functional analysis, and mitochondrial localization of Trypanosoma brucei monothiol glutaredoxin-1.* Biol Chem, 2008. **389**(1): p. 21-32.

[111] Zaffagnini, M., L. Michelet, V. Massot, P. Trost, and S.D. Lemaire, *Biochemical characterization of glutaredoxins from Chlamydomonas reinhardtii reveals the unique properties of a chloroplastic CGFS-type glutaredoxin.* J Biol Chem, 2008. **283**(14): p. 8868-76.

[112] Mesecke, N., S. Mittler, E. Eckers, J.M. Herrmann, and M. Deponte, *Two novel monothiol glutaredoxins from Saccharomyces cerevisiae provide further insight into iron-sulfur cluster binding, oligomerization, and enzymatic activity of glutaredoxins.* Biochemistry, 2008. **47**(5): p. 1452-63.

[113] Eckers, E., M. Bien, V. Stroobant, J.M. Herrmann, and M. Deponte, *Biochemical characterization of dithiol glutaredoxin 8 from Saccharomyces cerevisiae: the catalytic redox mechanism redux.* Biochemistry, 2009. **48**(6): p. 1410-23.

[114] Mesecke, N., A. Spang, M. Deponte, and J.M. Herrmann, *A novel group of glutaredoxins in the cis-Golgi critical for oxidative stress resistance.* Mol Biol Cell, 2008. **19**(6): p. 2673-80.

[115] Izquierdo, A., C. Casas, U. Muhlenhoff, C.H. Lillig, and E. Herrero, *Saccharomyces cerevisiae Grx6 and Grx7 are monothiol glutaredoxins associated with the early secretory pathway.* Eukaryot Cell, 2008. **7**(8): p. 1415-26.

[116] Begas, P., L. Liedgens, A. Moseler, A.J. Meyer, and M. Deponte, *Glutaredoxin catalysis requires two distinct glutathione interaction sites.* Nat Commun, 2017. **8**: p. 14835.

[117] Bushweller, J.H., M. Billeter, A. Holmgren, and K. Wuthrich, *The nuclear magnetic resonance solution structure of the mixed disulfide between Escherichia coli glutaredoxin(C14S) and glutathione.* J Mol Biol, 1994. **235**(5): p. 1585-97.

[118] Bushweller, J.H., F. Aslund, K. Wuthrich, and A. Holmgren, *Structural and functional characterization of the mutant Escherichia coli glutaredoxin (C14----S) and its mixed disulfide with glutathione.* Biochemistry, 1992. **31**(38): p. 9288-93.

[119] Holmgren, A. and F. Aslund, *Glutaredoxin.* Methods Enzymol, 1995. **252**: p. 283-92.

[120] Holmgren, A., *Glutathione-dependent synthesis of deoxyribonucleotides. Characterization of the enzymatic mechanism of Escherichia coli glutaredoxin.* J Biol Chem, 1979. **254**(9): p. 3672-8.

[121] Yang, Y.F. and W.W. Wells, *Catalytic mechanism of thioltransferase.* J Biol Chem, 1991. **266**(19): p. 12766-71.

[122] Gallogly, M.M., D.W. Starke, and J.J. Mieyal, *Mechanistic and kinetic details of catalysis of thiol-disulfide exchange by glutaredoxins and potential mechanisms of regulation.* Antioxid Redox Signal, 2009. **11**(5): p. 1059-81.

[123] Begas, P., V. Staudacher, and M. Deponte, *Systematic re-evaluation of the bis(2-hydroxyethyl) disulfide (HEDS) assay reveals an alternative mechanism and activity of glutaredoxins.* Chemical Science, 2015. **6**(7): p. 3788-3796.

[124] Nagai, S. and S. Black, *A thiol-disulfide transhydrogenase from yeast.* J Biol Chem, 1968. **243**(8): p. 1942-7.

[125] Rahlfs, S., M. Fischer, and K. Becker, *Plasmodium falciparum possesses a classical glutaredoxin and a second, glutaredoxin-like protein with a PICOT homology domain.* J Biol Chem, 2001. **276**(40): p. 37133-40.

[126] Ceylan, S., V. Seidel, N. Ziebart, C. Berndt, N. Dirdjaja, and R.L. Krauth-Siegel, *The dithiol glutaredoxins of african trypanosomes have distinct roles and are closely linked to the unique trypanothione metabolism.* J Biol Chem, 2010. **285**(45): p. 35224-37.

[127] Discola, K.F., M.A. de Oliveira, J.R. Rosa Cussiol, G. Monteiro, J.A. Barcena, P. Porras, C.A. Padilla, B.G. Guimaraes, and L.E. Netto, *Structural aspects of the distinct biochemical properties of glutaredoxin 1 and glutaredoxin 2 from Saccharomyces cerevisiae.* J Mol Biol, 2009. **385**(3): p. 889-901.

[128] Luikenhuis, S., G. Perrone, I.W. Dawes, and C.M. Grant, *The yeast Saccharomyces cerevisiae contains two glutaredoxin genes that are required for protection against reactive oxygen species.* Mol Biol Cell, 1998. **9**(5): p. 1081-91.

[129] Herrero, E., J. Ros, J. Tamarit, and G. Belli, *Glutaredoxins in fungi.* Photosynth Res, 2006. **89**(2-3): p. 127-40.

[130] Li, W.F., J. Yu, X.X. Ma, Y.B. Teng, M. Luo, Y.J. Tang, and C.Z. Zhou, *Structural basis for the different activities of yeast Grx1 and Grx2.* Biochim Biophys Acta, 2010. **1804**(7): p. 1542-7.

[131] Pedrajas, J.R., P. Porras, E. Martinez-Galisteo, C.A. Padilla, A. Miranda-Vizuete, and J.A. Barcena, *Two isoforms of Saccharomyces cerevisiae glutaredoxin 2 are expressed in vivo and localize to different subcellular compartments.* Biochem J, 2002. **364**(Pt 3): p. 617-23.

[132] Muhlenhoff, U., S. Molik, J.R. Godoy, M.A. Uzarska, N. Richter, A. Seubert, Y. Zhang, J. Stubbe, F. Pierrel, E. Herrero, C.H. Lillig, and R. Lill, *Cytosolic monothiol glutaredoxins function in intracellular iron sensing and trafficking via their bound iron-sulfur cluster.* Cell Metab, 2010. **12**(4): p. 373-85.

[133] Rodriguez-Manzaneque, M.T., J. Tamarit, G. Belli, J. Ros, and E. Herrero, *Grx5 is a mitochondrial glutaredoxin required for the activity of iron/sulfur enzymes.* Mol Biol Cell, 2002. **13**(4): p. 1109-21.

[134] Rodriguez-Manzaneque, M.T., J. Ros, E. Cabiscol, A. Sorribas, and E. Herrero, *Grx5 glutaredoxin plays a central role in protection against protein oxidative damage in Saccharomyces cerevisiae.* Mol Cell Biol, 1999. **19**(12): p. 8180-90.

[135] Luo, M., Y.L. Jiang, X.X. Ma, Y.J. Tang, Y.X. He, J. Yu, R.G. Zhang, Y. Chen, and C.Z. Zhou, *Structural and biochemical characterization of yeast monothiol glutaredoxin Grx6.* J Mol Biol, 2010. **398**(4): p. 614-22.

[136] Jortzik, E. and K. Becker, *Thioredoxin and glutathione systems in Plasmodium falciparum.* Int J Med Microbiol, 2012. **302**(4-5): p. 187-94.

[137] Kehr, S., N. Sturm, S. Rahlfs, J.M. Przyborski, and K. Becker, *Compartmentation of redox metabolism in malaria parasites.* PLoS Pathog, 2010. **6**(12): p. e1001242.

[138] Djuika, C.F., S. Fiedler, M. Schnolzer, C. Sanchez, M. Lanzer, and M. Deponte, *Plasmodium falciparum antioxidant protein as a model enzyme for a special class of glutaredoxin/glutathione-dependent peroxiredoxins.* Biochim Biophys Acta, 2013. **1830**(8): p. 4073-90.

[139] Yogavel, M., T. Tripathi, A. Gupta, M.M. Banday, S. Rahlfs, K. Becker, H. Belrhali, and A. Sharma, *Atomic resolution crystal structure of glutaredoxin 1 from Plasmodium falciparum and comparison with other glutaredoxins.* Acta Crystallogr D Biol Crystallogr, 2014. **70**(Pt 1): p. 91-100.

[140] Sturm, N., E. Jortzik, B.M. Mailu, S. Koncarevic, M. Deponte, K. Forchhammer, S. Rahlfs, and K. Becker, *Identification of proteins targeted by the thioredoxin superfamily in Plasmodium falciparum.* PLoS Pathog, 2009. **5**(4): p. e1000383.

[141] Raymond, F., S. Boisvert, G. Roy, J.F. Ritt, D. Legare, A. Isnard, M. Stanke, M. Olivier, M.J. Tremblay, B. Papadopoulou, M. Ouellette, and J. Corbeil, *Genome sequencing of the lizard parasite Leishmania tarentolae reveals loss of genes associated to the intracellular stage of human pathogenic species.* Nucleic Acids Res, 2012. **40**(3): p. 1131-47.

[142] Urscher, M., S.S. More, R. Alisch, R. Vince, and M. Deponte, *Tight-binding inhibitors efficiently inactivate both reaction centers of monomeric Plasmodium falciparum glyoxalase 1.* FEBS J, 2012. **279**(14): p. 2568-78.

[143] LeBowitz, J.H., C.M. Coburn, D. McMahon-Pratt, and S.M. Beverley, *Development of a stable Leishmania expression vector and application to the study of parasite surface antigen genes.* Proc Natl Acad Sci U S A, 1990. **87**(24): p. 9736-40.

[144] Birnboim, H.C. and J. Doly, *A rapid alkaline extraction procedure for screening recombinant plasmid DNA.* Nucleic Acids Res, 1979. **7**(6): p. 1513-23.

[145] Fic, E., S. Kedracka-Krok, U. Jankowska, A. Pirog, and M. Dziedzicka-Wasylewska, *Comparison of protein precipitation methods for various rat brain structures prior to proteomic analysis.* Electrophoresis, 2010. **31**(21): p. 3573-9.

[146] Trager, W. and J.B. Jensen, *Human malaria parasites in continuous culture.* Science, 1976. **193**(4254): p. 673-5.
[147] Bradford, M.M., *A rapid and sensitive method for the quantitation of microgram quantities of protein utilizing the principle of protein-dye binding.* Anal Biochem, 1976. **72**: p. 248-54.
[148] Laemmli, U.K., *Cleavage of structural proteins during the assembly of the head of bacteriophage T4.* Nature, 1970. **227**(5259): p. 680-5.
[149] Mieyal, J.J., D.W. Starke, S.A. Gravina, and B.A. Hocevar, *Thioltransferase in human red blood cells: kinetics and equilibrium.* Biochemistry, 1991. **30**(36): p. 8883-91.
[150] Gallogly, M.M., D.W. Starke, A.K. Leonberg, S.M. Ospina, and J.J. Mieyal, *Kinetic and mechanistic characterization and versatile catalytic properties of mammalian glutaredoxin 2: implications for intracellular roles.* Biochemistry, 2008. **47**(42): p. 11144-57.
[151] Ellis, K.J. and J.F. Morrison, *Buffers of constant ionic strength for studying pH-dependent processes.* Methods Enzymol, 1982. **87**: p. 405-26.
[152] Ulrich, K., C. Finkenzeller, S. Merker, F. Rojas, K. Matthews, T. Ruppert, and R.L. Krauth-Siegel, *Stress-Induced Protein S-Glutathionylation and S-Trypanothionylation in African Trypanosomes-A Quantitative Redox Proteome and Thiol Analysis.* Antioxid Redox Signal, 2017. **27**(9): p. 517-533.
[153] Hansen, R.E., D. Roth, and J.R. Winther, *Quantifying the global cellular thiol-disulfide status.* Proc Natl Acad Sci U S A, 2009. **106**(2): p. 422-7.
[154] Schagger, H., *Tricine-SDS-PAGE.* Nat Protoc, 2006. **1**(1): p. 16-22.
[155] Haindrich, A.C., M. Boudova, M. Vancova, P.P. Diaz, E. Horakova, and J. Lukes, *The intermembrane space protein Erv1 of Trypanosoma brucei is essential for mitochondrial Fe-S cluster assembly and operates alone.* Mol Biochem Parasitol, 2017. **214**: p. 47-51.
[156] Srinivasan, U., P.A. Mieyal, and J.J. Mieyal, *pH profiles indicative of rate-limiting nucleophilic displacement in thioltransferase catalysis.* Biochemistry, 1997. **36**(11): p. 3199-206.
[157] Specht, S., L. Liedgens, M. Duarte, A. Stiegler, U. Wirth, M. Eberhardt, A. Tomas, K. Hell, and M. Deponte, *A single-cysteine mutant and chimeras of essential Leishmania Erv can complement the loss of Erv1 but not of Mia40 in yeast.* Redox Biol, 2018. **15**: p. 363-374.
[158] Peikert, C.D., J. Mani, M. Morgenstern, S. Kaser, B. Knapp, C. Wenger, A. Harsman, S. Oeljeklaus, A. Schneider, and B. Warscheid, *Charting organellar importomes by quantitative mass spectrometry.* Nat Commun, 2017. **8**: p. 15272.
[159] Peleh, V., F. Zannini, S. Backes, N. Rouhier, and J.M. Herrmann, *Erv1 of Arabidopsis thaliana can directly oxidize mitochondrial intermembrane space proteins in the absence of redox-active Mia40.* BMC Biol, 2017. **15**(1): p. 106.
[160] Ceh-Pavia, E., M.P. Spiller, and H. Lu, *Folding and biogenesis of mitochondrial small Tim proteins.* Int J Mol Sci, 2013. **14**(8): p. 16685-705.
[161] Koch, J.R. and F.X. Schmid, *Mia40 targets cysteines in a hydrophobic environment to direct oxidative protein folding in the mitochondria.* Nat Commun, 2014. **5**: p. 3041.
[162] Koch, J.R. and F.X. Schmid, *Mia40 is optimized for function in mitochondrial oxidative protein folding and import.* ACS Chem Biol, 2014. **9**(9): p. 2049-57.
[163] Lee, S.Y., M.G. Kang, J.S. Park, G. Lee, A.Y. Ting, and H.W. Rhee, *APEX Fingerprinting Reveals the Subcellular Localization of Proteins of Interest.* Cell Rep, 2016. **15**(8): p. 1837-47.
[164] Allen, S., H. Lu, D. Thornton, and K. Tokatlidis, *Juxtaposition of the two distal CX3C motifs via intrachain disulfide bonding is essential for the folding of Tim10.* J Biol Chem, 2003. **278**(40): p. 38505-13.
[165] Lutz, T., W. Neupert, and J.M. Herrmann, *Import of small Tim proteins into the mitochondrial intermembrane space.* Embo J, 2003. **22**(17): p. 4400-8.
[166] Weckbecker, D., S. Longen, J. Riemer, and J.M. Herrmann, *Atp23 biogenesis reveals a chaperone-like folding activity of Mia40 in the IMS of mitochondria.* Embo J, 2012. **31**(22): p. 4348-58.
[167] Erdogan, A.J., M. Ali, M. Habich, S.L. Salscheider, L. Schu, C. Petrungaro, L.W. Thomas, M. Ashcroft, L.I. Leichert, L.P. Roma, and J. Riemer, *The mitochondrial oxidoreductase CHCHD4 is present in a semi-oxidized state in vivo.* Redox Biol, 2018. **17**: p. 200-206.

[168] Kojer, K., M. Bien, H. Gangel, B. Morgan, T.P. Dick, and J. Riemer, *Glutathione redox potential in the mitochondrial intermembrane space is linked to the cytosol and impacts the Mia40 redox state.* Embo J, 2012. **31**(14): p. 3169-82.

[169] Kojer, K., V. Peleh, G. Calabrese, J.M. Herrmann, and J. Riemer, *Kinetic control by limiting glutaredoxin amounts enables thiol oxidation in the reducing mitochondrial intermembrane space.* Mol Biol Cell, 2015. **26**(2): p. 195-204.

[170] Kushnir, S., K. Gase, R. Breitling, and K. Alexandrov, *Development of an inducible protein expression system based on the protozoan host Leishmania tarentolae.* Protein Expr Purif, 2005. **42**(1): p. 37-46.

[171] Rabenstein, D.L. and K.K. Millis, *Nuclear magnetic resonance study of the thioltransferase-catalyzed glutathione/glutathione disulfide interchange reaction.* Biochim Biophys Acta, 1995. **1249**(1): p. 29-36.

[172] Peltoniemi, M.J., A.R. Karala, J.K. Jurvansuu, V.L. Kinnula, and L.W. Ruddock, *Insights into deglutathionylation reactions. Different intermediates in the glutaredoxin and protein disulfide isomerase catalyzed reactions are defined by the gamma-linkage present in glutathione.* J Biol Chem, 2006. **281**(44): p. 33107-14.

[173] Elgan, T.H. and K.D. Berndt, *Quantifying Escherichia coli glutaredoxin-3 substrate specificity using ligand-induced stability.* J Biol Chem, 2008. **283**(47): p. 32839-47.

[174] Jao, S.C., S.M. English Ospina, A.J. Berdis, D.W. Starke, C.B. Post, and J.J. Mieyal, *Computational and mutational analysis of human glutaredoxin (thioltransferase): probing the molecular basis of the low pKa of cysteine 22 and its role in catalysis.* Biochemistry, 2006. **45**(15): p. 4785-96.

[175] Zaffagnini, M., M. Bedhomme, C.H. Marchand, J.R. Couturier, X.H. Gao, N. Rouhier, P. Trost, and S.P. Lemaire, *Glutaredoxin s12: unique properties for redox signaling.* Antioxid Redox Signal, 2012. **16**(1): p. 17-32.

[176] Moseler, A., I. Aller, S. Wagner, T. Nietzel, J. Przybyla-Toscano, U. Muhlenhoff, R. Lill, C. Berndt, N. Rouhier, M. Schwarzlander, and A.J. Meyer, *The mitochondrial monothiol glutaredoxin S15 is essential for iron-sulfur protein maturation in Arabidopsis thaliana.* Proc Natl Acad Sci U S A, 2015. **112**(44): p. 13735-40.

[177] Blom, N., S. Gammeltoft, and S. Brunak, *Sequence and structure-based prediction of eukaryotic protein phosphorylation sites.* J Mol Biol, 1999. **294**(5): p. 1351-62.

[178] Peggion, C., R. Lopreiato, E. Casanova, M. Ruzzene, S. Facchin, L.A. Pinna, G. Carignani, and G. Sartori, *Phosphorylation of the Saccharomyces cerevisiae Grx4p glutaredoxin by the Bud32p kinase unveils a novel signaling pathway involving Sch9p, a yeast member of the Akt / PKB subfamily.* Febs j, 2008. **275**(23): p. 5919-33.

[179] Berndt, C., J.D. Schwenn, and C.H. Lillig, *The specificity of thioredoxins and glutaredoxins is determined by electrostatic and geometric complementarity.* Chem Sci, 2015. **6**(12): p. 7049-7058.

[180] Tang, Y., J. Zhang, J. Yu, L. Xu, J. Wu, C.Z. Zhou, and Y. Shi, *Structure-guided activity enhancement and catalytic mechanism of yeast grx8.* Biochemistry, 2014. **53**(13): p. 2185-96.

6 Supplementary Data

6.1 Kinetics of *Pf*Grx mutants in the GSSCys assay

6.1.1 Steady-state kinetics of *Pf*Grx mutants in the GSSCys assay

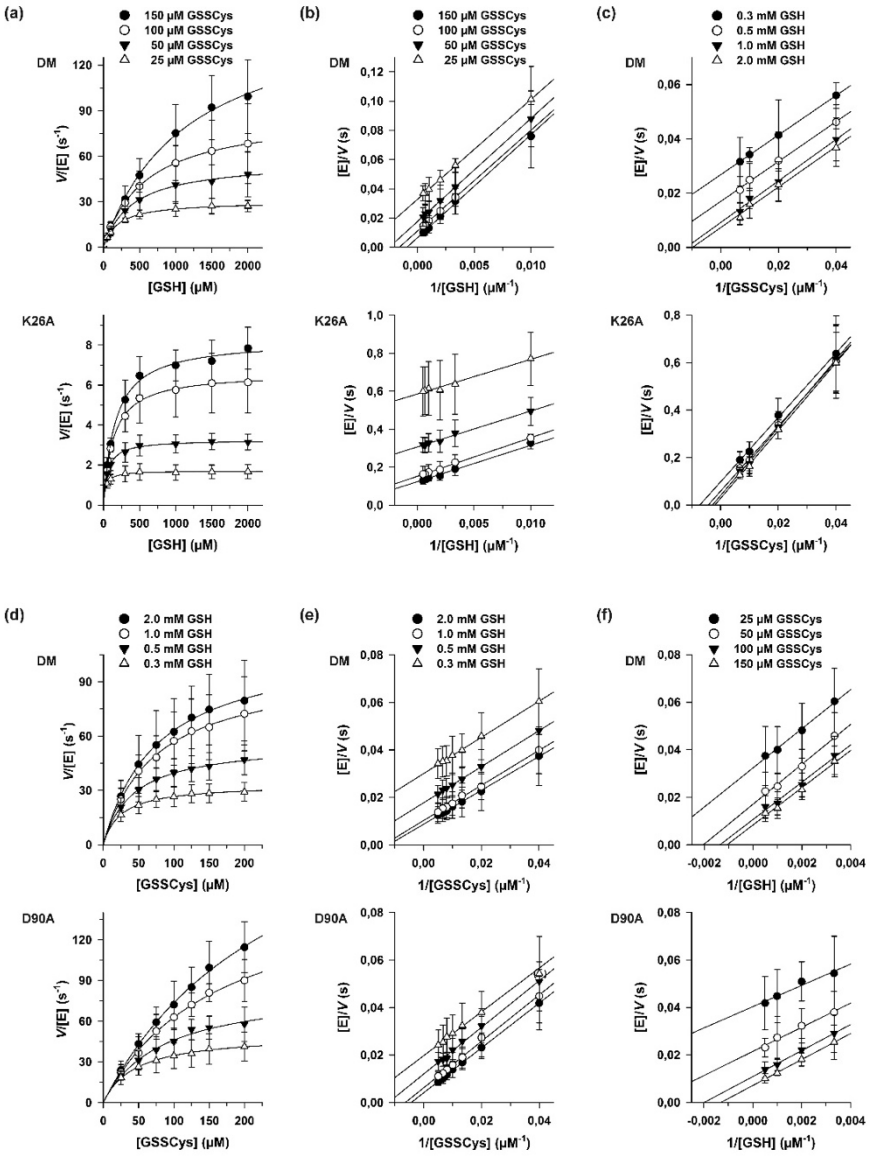

Supplementary figure 1 | Steady-state kinetics of *Pf*Grx mutants in the GSSCys assay. (a) Michaelis-Menten plots showing the GSH-dependent reaction velocity at different fixed GSSCys-concentrations. (b) Lineweaver-Burk plots of the data shown in (a) reveal ping-pong kinetics. (c) Lineweaver-Burk plots showing the GSSCys-dependent reaction velocity at four selected fixed GSH concentrations. (d) Michaelis-Menten plots showing the GSSCys-dependent reaction velocity at different fixed GSH-concentrations. (e) Lineweaver-Burk plots of the data shown in (d) reveal ping-pong kinetics. (f) Lineweaver-Burk plots showing the GSH-dependent reaction velocity at four selected fixed GSSCys-concentrations. All data points represent the mean ± standard deviation from at least three independent experiments. DM: *Pf*Grx$^{C32S/C88S}$; K26A: *Pf*Grx$^{C32S/C88S/K26A}$; D90A: *Pf*Grx$^{C32S/C88S/D90A}$. The figure was taken from Begas *et al.* 2017 [116].

6.1.2 Apparent rate constants of *Pf*Grx mutants in the GSSCys assay

Supplementary table 1 | Apparent rate constants of *Pf*Grx mutants in the GSSCys assay. Selected k_{cat}^{app} and K_m^{app} values of the GSSCys assays with the *Pf*Grx mutants obtained from supplementary figure 1. [a]Mean±SD from Michaelis-Menten plots of supplementary figure 1 of at least three independent protein purifications. Percentages are relative to *Pf*Grx$^{C32S/C88S}$. DM: *Pf*Grx$^{C32S/C88S}$; K26A: *Pf*Grx$^{C32S/C88S/K26A}$; D90A: *Pf*Grx$^{C32S/C88S/D90A}$. This data was already published in Begas *et al.* 2017 [116].

***Pf*Grx**	**[GSSCys]** (µM)	$k_{cat}^{app}{}_{(GSH)}$ [a] (s^{-1})		$K_m^{app}{}_{(GSH)}$ [a] (µM)		$k_{cat}^{app}/K_m^{app}{}_{(GSH)}$ ($mM^{-1}s^{-1}$)	
DM	25	30.4 ± 0.4	100 %	206 ± 10	100 %	147	100 %
K26A	25	1.7 ± 0.1	6 %	31.2 ± 2.0	15 %	55	37 %
D90A	25	25.1 ± 0.7	83 %	119 ± 19	58 %	211	144 %
DM	50	56.8 ± 1.1	100 %	403 ± 25	100 %	141	100 %
K26A	50	3.3 ± 0.1	6 %	61.6 ± 3.6	15 %	53	38 %
D90A	50	47.8 ± 2.0	84 %	262 ± 41	65 %	182	129 %
DM	100	88.3 ± 0.9	100 %	591 ± 17	100 %	149	100 %
K26A	100	6.6 ± 0.1	7 %	134 ± 6.9	23 %	49	33 %
D90A	100	90.9 ± 3.2	103 %	488 ± 47	83 %	186	125 %
DM	150	160 ± 5.6	100 %	1157 ± 84	100 %	138	100 %
K26A	150	8.1 ± 0.2	5 %	156 ± 14	13 %	52	38 %
D90A	150	136 ± 4.0	85 %	723 ± 51	62 %	189	137 %

***Pf*Grx**	**[GSH]** (µM)	$k_{cat}^{app}{}_{(GSSCys)}$ [a] (s^{-1})		$K_m^{app}{}_{(GSSCys)}$ [a] (µM)		$k_{cat}^{app}/K_m^{app}{}_{(GSSCys)}$ ($mM^{-1}s^{-1}$)	
DM	300	33.3 ± 0.4	100 %	25.3 ± 1.2	100 %	1399	100 %
K26A	300	10.3 ± 0.9	31 %	139 ± 21	549 %	74	5 %
D90A	300	50.4 ± 1.0	151 %	45.6 ± 2.8	180 %	1105	79 %
DM	500	56.4 ± 0.6	100 %	42.8 ± 1.4	100 %	1351	100 %
K26A	500	17.2 ± 2.4	30 %	235 ± 48	549 %	73	5 %
D90A	500	84.9 ± 5.1	151 %	84.6 ± 12	198 %	1003	74 %
DM	1000	98.2 ± 2.5	100 %	73.1 ± 4.7	100 %	1316	100 %
K26A	1000	25.2 ± 4.5	26 %	361 ± 86	494 %	70	5 %
D90A	1000	168 ± 7.9	171 %	167 ± 14	228 %	1004	76 %
DM	2000	112 ± 2.4	100 %	82.9 ± 4.0	100 %	1311	100 %
K26A	2000	36.1 ± 7.4	32 %	516 ± 130	622 %	70	5 %
D90A	2000	265 ± 15	237 %	260 ± 22	314 %	1019	78 %

6.1.3 Secondary plots for the *Pf*Grx mutants in the GSSCys assay

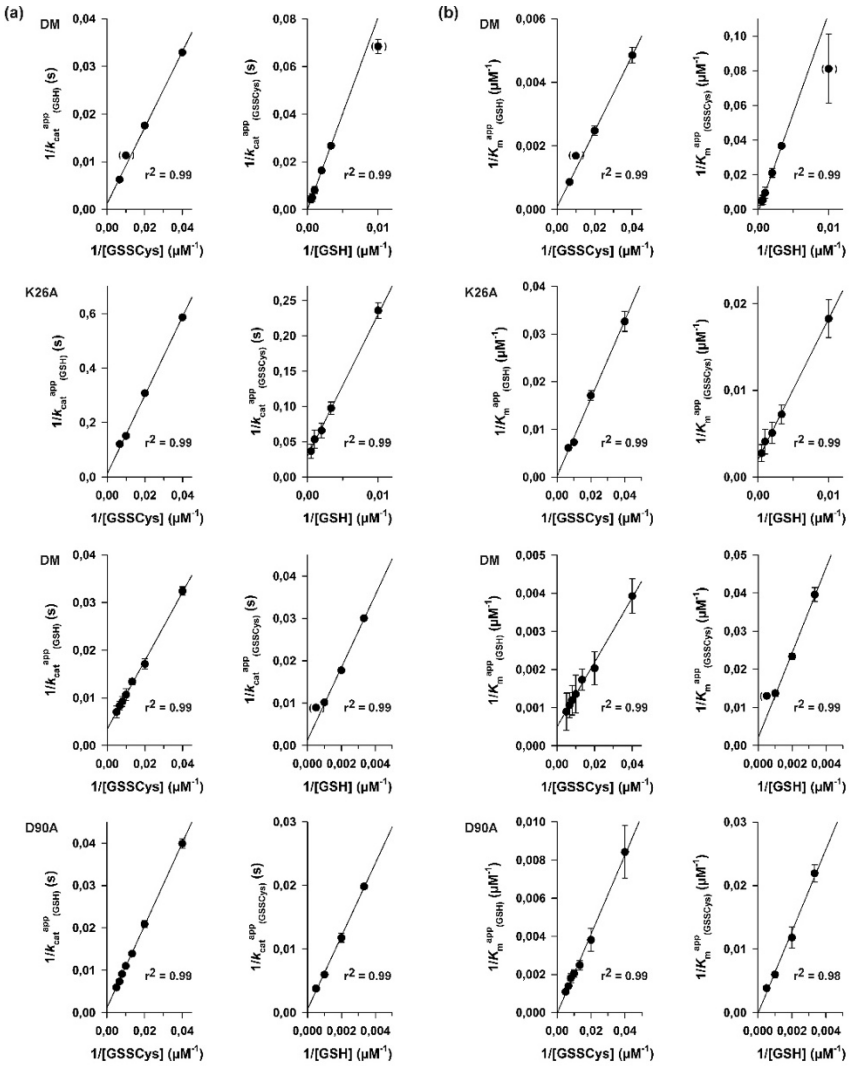

Supplementary figure 2 | Secondary plots for the *Pf*Grx mutants obtained from the GSSCys assay. Values for K_m^{app} and k_{cat}^{app} were obtained from the Michaelis-Menten plots in supplementary figure 1. (a) Secondary plots of the k_{cat}^{app} values at different concentrations of GSSCys (left side) and GSH (right side). (b) Secondary plots of the K_m^{app} values at different concentrations of GSSCys (left side) and GSH (right side). Outliers based on the r^2 values (in brackets) were omitted from the linear regression analysis. All data points represent the mean ± standard deviation from at least three independent experiments. DM: *Pf*Grx$^{C32S/C88S}$; K26A: *Pf*Grx$^{C32S/C88S/K26A}$; D90A: *Pf*Grx$^{C32S/C88S/D90A}$. The figure was taken from Begas *et al.* 2017 [116].

6.2 Kinetics of *Pf*Grx mutants in the HEDS assay

6.2.1 Steady-state kinetics of *Pf*Grx mutants in the HEDS assay

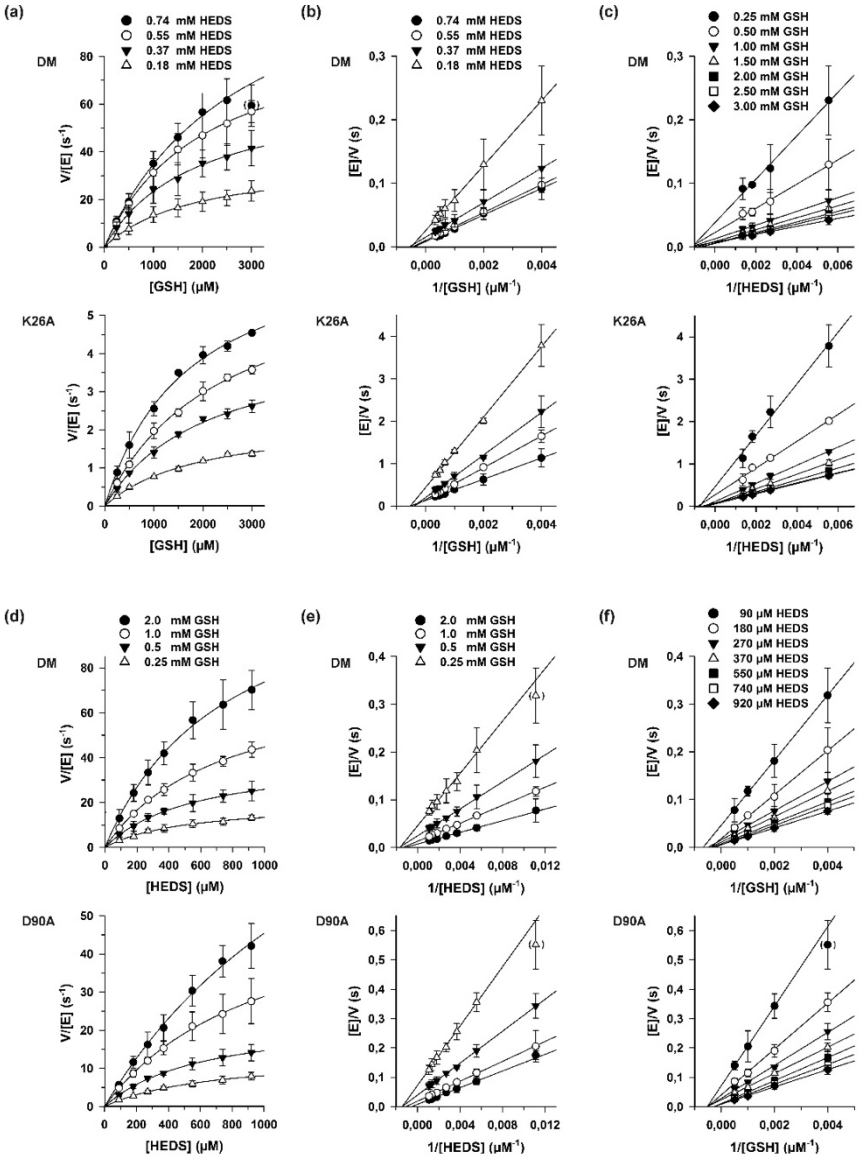

Supplementary figure 3 | Steady-state kinetics of *Pf*Grx mutants in the HEDS assay. (a) Michaelis-Menten plots showing the GSH-dependent reaction velocity at different fixed HEDS-concentrations. (b) Lineweaver-Burk plots of the data shown in (a) reveal sequential kinetic patterns. (c) Lineweaver-Burk plots showing the HEDS-dependent reaction velocity at seven fixed GSH concentrations. (d) Michaelis-Menten plots showing the HEDS-dependent reaction velocity at different fixed GSH-concentrations. (e) Lineweaver-Burk plots of the data shown in (d) reveal sequential kinetic patterns. (f) Lineweaver-Burk plots showing the GSH-dependent reaction velocity at seven fixed HEDS-concentrations. All data points represent the mean ± standard deviation from at least three independent experiments. DM: *Pf*Grx$^{C32S/C88S}$; K26A: *Pf*Grx$^{C32S/C88S/K26A}$; D90A: *Pf*Grx$^{C32S/C88S/D90A}$. The figure was taken from Begas *et al.* 2017 [116].

6.2.2 Apparent rate constants of *Pf*Grx mutants in the HEDS assay

Supplementary table 2 | Apparent rate constants of *Pf*Grx mutants in the HEDS assay. Selected k_{cat}^{app} and K_m^{app} values of the HEDS assays with the *Pf*Grx mutants obtained from supplementary figure 3. [a]Mean±SD from Michaelis-Menten plots of supplementary figure 3 of at least three independent protein purifications. Percentages are relative to *Pf*Grx$^{C32S/C88S}$. DM: *Pf*Grx$^{C32S/C88S}$; K26A: *Pf*Grx$^{C32S/C88S/K26A}$; D90A: *Pf*Grx$^{C32S/C88S/D90A}$. This data was already published in Begas *et al.* 2017 [116].

***Pf*Grx**	**[HEDS]** (mM)	$k_{cat}^{app}{}_{(GSH)}$ [a] (s^{-1})		$K_m^{app}{}_{(GSH)}$ [a] (mM)		$k_{cat}^{app}/K_m^{app}{}_{(GSH)}$ ($mM^{-1}s^{-1}$)	
DM	0.18	37.1 ± 2.0	100 %	1.84 ± 0.20	100 %	20.2	100 %
K26A	0.18	2.3 ± 0.1	6 %	1.96 ± 0.24	107%	1.2	6 %
D90A	0.18	19.8 ± 1.5	53 %	1.37 ± 0.19	74 %	14.5	72 %
DM	0.37	66.7 ± 3.0	100 %	1.86 ± 0.17	100 %	35.9	100 %
K26A	0.37	4.5 ± 0.3	7 %	2.12 ± 0.23	114 %	2.1	6 %
D90A	0.37	36.7 ± 3.5	55 %	1.51 ± 0.26	81 %	24.3	68 %
DM	0.55	96.0 ± 2.1	100 %	2.08 ± 0.09	100 %	46.2	100 %
K26A	0.55	6.5 ± 0.3	7 %	2.38 ± 0.19	114 %	2.7	6 %
D90A	0.55	65.6 ± 8.8	68 %	2.27 ± 0.49	109 %	28.8	62 %
DM	0.74	134 ± 9.1	100 %	2.86 ± 0.31	100 %	46.9	100 %
K26A	0.74	7.2 ± 0.3	5 %	1.72 ± 0.17	60 %	4.2	9 %
D90A	0.74	101 ± 10	75 %	3.29 ± 0.48	115 %	30.8	66 %

***Pf*Grx**	**[GSH]** (mM)	$k_{cat}^{app}{}_{(HEDS)}$ [a] (s^{-1})		$K_m^{app}{}_{(HEDS)}$ [a] (mM)		$k_{cat}^{app}/K_m^{app}{}_{(HEDS)}$ ($mM^{-1}s^{-1}$)	
DM	0.25	20.1 ± 1.0	100 %	0.51 ± 0.05	100 %	39.3	100 %
K26A	0.25	2.1 ± 1.1	11 %	1.30 ± 0.86	253 %	1.7	4 %
D90A	0.25	13.6 ± 0.7	68 %	0.68 ± 0.06	133 %	20.0	51 %
DM	0.5	40.6 ± 0.7	100 %	0.57 ± 0.02	100 %	71.2	100 %
K26A	0.5	3.7 ± 1.5	9 %	1.16 ± 0.91	203 %	3.2	4 %
D90A	0.5	23.6 ± 0.6	58 %	0.61 ± 0.03	108 %	38.4	54 %
DM	1.0	78.2 ± 2.0	100 %	0.75 ± 0.03	100 %	105	100 %
K26A	1.0	8.5 ± 2.4	11 %	1.80 ± 0.98	241 %	4.7	4 %
D90A	1.0	58.3 ± 2.6	75 %	1.02 ± 0.07	137 %	57.1	55 %
DM	2.0	130 ± 7.4	100 %	0.76 ± 0.08	100 %	170	100 %
K26A	2.0	14.8 ± 3.9	11 %	2.06 ± 0.80	270 %	7.2	4 %
D90A	2.0	129 ± 18	99 %	1.83 ± 0.35	241 %	70.2	41 %

6.2.3 Secondary plots for the *Pf*Grx mutants in the HEDS assay

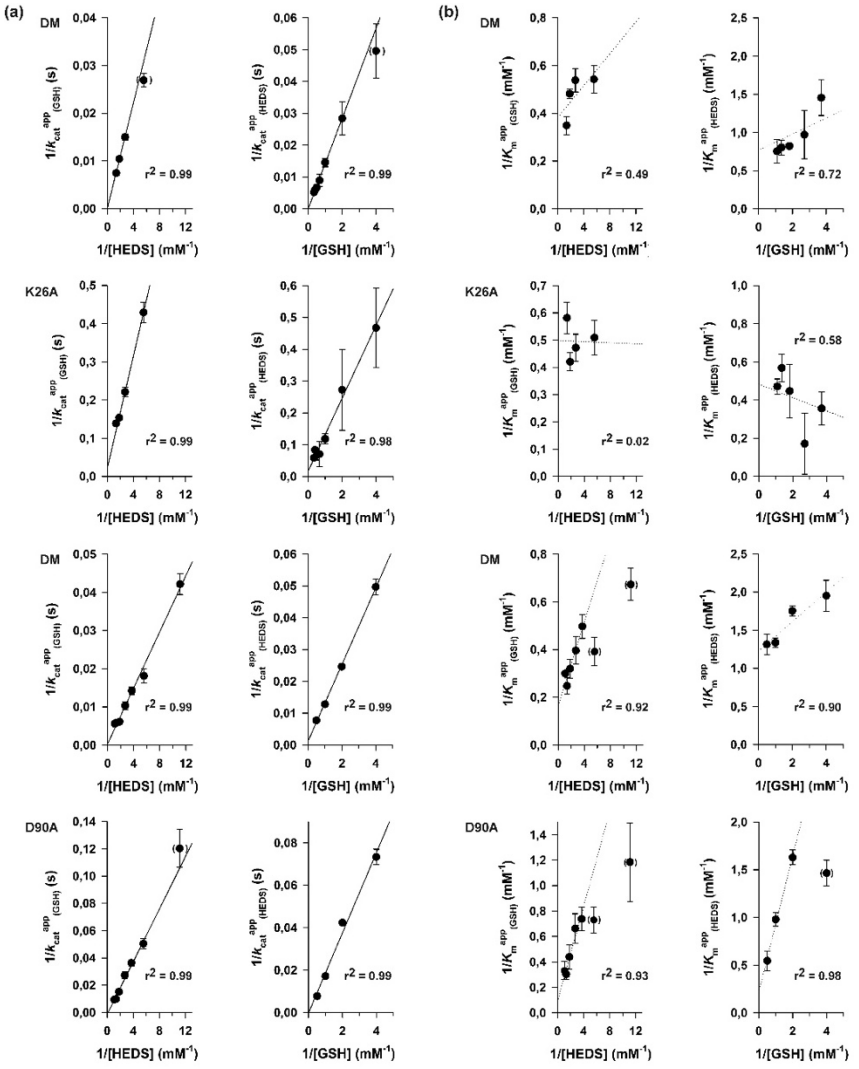

Supplementary figure 4 | Secondary plots for the *Pf*Grx mutants obtained from the HEDS assay. Values for K_m^{app} and k_{cat}^{app} were obtained from the Michaelis-Menten plots in supplementary figure 3. (a) Secondary plots of the k_{cat}^{app} values at different concentrations of HEDS (left side) and GSH (right side). (b) Secondary plots of the K_m^{app} values at different concentrations of HEDS (left side) and GSH (right side). Outliers at the lowest substrate concentration based on the r^2 values (in brackets) were omitted from the linear regression analysis. All data points represent the mean ± standard deviation from at least three independent experiments. DM: *Pf*Grx$^{C32S/C88S}$; K26A: *Pf*Grx$^{C32S/C88S/K26A}$; D90A: *Pf*Grx$^{C32S/C88S/D90A}$. The figure was taken from Begas *et al.* 2017 [116].

6.3 Kinetics of *Sc*Grx7^{Y110X} mutants in the GSSCys assay

6.3.1 Steady-state kinetics of *Sc*Grx7^{Y110X} mutants in the GSSCys assay

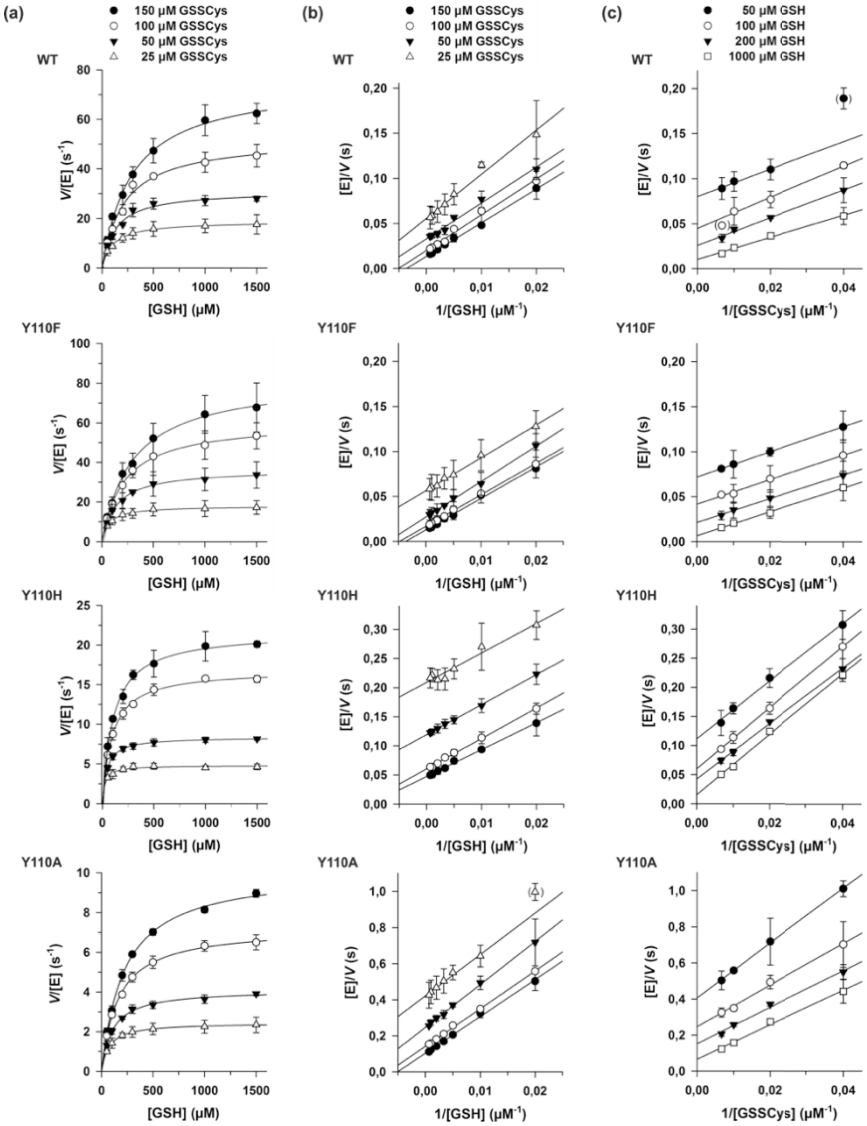

Supplementary figure 5 | Steady-state kinetics of *Sc*Grx7^{Y110X} mutants in the GSSCys assay. (a) Michaelis-Menten plots showing the GSH-dependent reaction velocity at different fixed GSSCys-concentrations. (b) Lineweaver-Burk plots of the data shown in (a) reveal ping-pong kinetic patterns. (c) Lineweaver-Burk plots showing the GSSCys-dependent reaction velocity at different fixed GSH concentrations. All data points represent the mean ± standard deviation from three independent experiments. WT: *Sc*Grx7 wild-type; Y110F: *Sc*Grx7^{Y110F}; Y110H: *Sc*Grx7^{Y110H}; Y110A: *Sc*Grx7^{Y110A}.

6.3.2 Apparent rate constants of *Sc*Grx7^{Y110X} mutants in the GSSCys assay

Supplementary table 3 | Apparent rate constants of *Sc*Grx7^{Y110X} mutants in the GSSCys assay. Selected k_{cat}^{app} and K_m^{app} values of the GSSCys assays with the *Sc*Grx7^{wt} enzyme and Y110X mutants obtained from supplementary figure 5. [a]Mean±SD from Michaelis-Menten plots of supplementary figure 5 of three independent protein purifications. Percentages are relative to *Sc*Grx7^{wt}. WT: *Sc*Grx7 wild-type; Y110F: *Sc*Grx7^{Y110F}; Y110H: *Sc*Grx7^{Y110H}; Y110A: *Sc*Grx7^{Y110A}.

*Sc*Grx7	[GSSCys] (µM)	$k_{cat}^{app}{}_{(GSH)}$ [a] (s^{-1})		$K_m^{app}{}_{(GSH)}$ [a] (µM)		$k_{cat}^{app}/K_m^{app}{}_{(GSH)}$ ($mM^{-1}s^{-1}$)	
WT	25	18.8 ± 0.3	100 %	104 ± 7.6	100 %	180	100 %
Y110F	25	17.9 ± 0.2	95 %	68.1 ± 4.2	65 %	264	147 %
Y110H	25	4.8 ± 0.1	26 %	24.8 ± 3.8	24 %	198	110 %
Y110A	25	2.4 ± 0.0	13 %	58.2 ± 4.5	56 %	41	23 %
WT	50	31.1 ± 1.1	100 %	128 ± 16.8	100 %	243	100 %
Y110F	50	36.6 ± 0.5	118 %	141 ± 7.7	110 %	259	107 %
Y110H	50	8.4 ± 0.0	27 %	42.8 ± 0.9	33 %	196	81 %
Y110A	50	4.1 ± 0.1	13 %	100 ± 5.7	78 %	41	17 %
WT	100	52.3 ± 2.2	100 %	215 ± 28.5	100 %	243	100 %
Y110F	100	60.7 ± 1.0	116 %	216 ± 10.8	101 %	280	115 %
Y110H	100	16.9 ± 5.0	32 %	93.0 ± 5.0	43 %	181	74 %
Y110A	100	7.2 ± 0.1	14 %	159 ± 7.1	74 %	46	19 %
WT	150	75.2 ± 1.6	100 %	291 ± 17.6	100 %	258	100 %
Y110F	150	82.5 ± 2.0	110 %	302 ± 20.1	104 %	273	106 %
Y110H	150	21.6 ± 0.3	29 %	105 ± 6.4	36 %	204	79 %
Y110A	150	10.1 ± 0.1	13 %	219 ± 9.6	75 %	46	18 %

*Sc*Grx7	[GSH] (µM)	$k_{cat}^{app}{}_{(GSSCys)}$ [a] (s^{-1})		$K_m^{app}{}_{(GSSCys)}$ [a] (µM)		$k_{cat}^{app}/K_m^{app}{}_{(GSSCys)}$ ($mM^{-1}s^{-1}$)	
WT	50	12.6 ± 0.5	100 %	19.7 ± 3.8	100 %	639	100 %
Y110F	50	13.9 ± 0.03	110 %	19.6 ± 0.2	99 %	712	111 %
Y110H	50	9.4 ± 0.5	75 %	50.4 ± 6.4	256 %	187	29 %
Y110A	50	2.5 ± 0.1	20 %	42.8 ± 6.5	217 %	60	9 %
WT	100	21.2 ± 1.5	100 %	34.2 ± 6.4	100 %	621	100 %
Y110F	100	23.9 ± 1.2	113 %	32.0 ± 5.2	94 %	746	120 %
Y110H	100	17.0 ± 0.6	80 %	90.3 ± 6.1	264 %	188	30 %
Y110A	100	4.1 ± 0.2	19 %	48.9 ± 6.7	143 %	84	14 %
WT	200	40.4 ± 5.2	100 %	64.7 ± 19.7	100 %	624	100 %
Y110F	200	49.1 ± 2.4	122 %	68.6 ± 7.6	106 %	716	115 %
Y110H	200	24.2 ± 1.1	60 %	116 ± 10.3	180 %	207	33 %
Y110A	200	7.5 ± 0.7	19 %	85.9 ± 15.9	133 %	87	14 %
WT	1000	163 ± 54.8	100 %	266 ± 129	100 %	612	100 %
Y110F	1000	142 ± 13.7	87 %	184 ± 28.3	69 %	771	126 %
Y110H	1000	63.1 ± 16.3	39 %	319 ± 113	120 %	198	32 %
Y110A	1000	19.2 ± 1.9	12 %	204 ± 30.7	77 %	94	15 %

6.3.3 Secondary plots for the *Sc*Grx7^{Y110X} mutants in the GSSCys assay

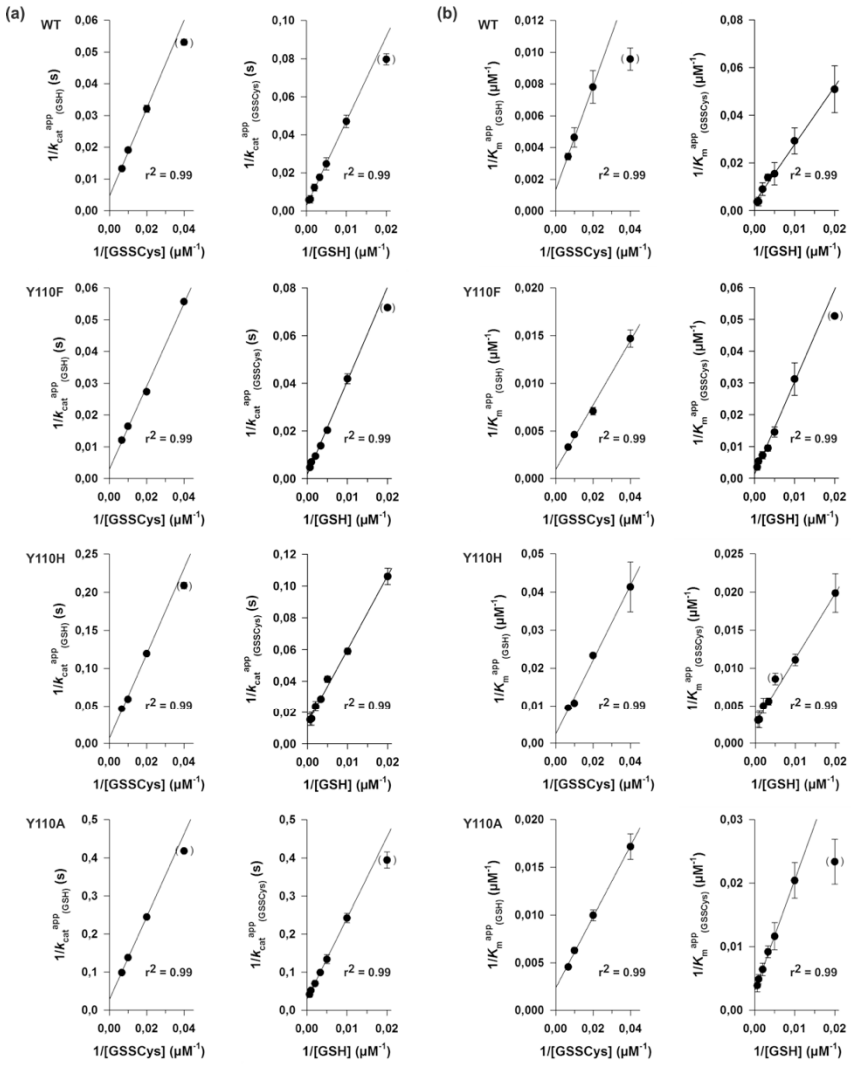

Supplementary figure 6 | Secondary plots for the *Sc*Grx7^{Y110X} mutants obtained from the GSSCys assay. Values for K_m^{app} and k_{cat}^{app} were obtained from the Michaelis-Menten plots in supplementary figure 5. (a) Secondary plots of the k_{cat}^{app} values at different concentrations of GSSCys (left side) and GSH (right side). (b) Secondary plots of the K_m^{app} values at different concentrations of GSSCys (left side) and GSH (right side). Outliers based on the r^2 values (in brackets) were omitted from the linear regression analysis. All data points represent the mean ± standard deviation from three independent experiments. WT: *Sc*Grx7 wild-type; Y110F: *Sc*Grx7^{Y110F}; Y110H: *Sc*Grx7^{Y110H}; Y110A: *Sc*Grx7^{Y110A}.

6.4 Kinetics of *Sc*Grx7^{Y110X} mutants in the HEDS assay

6.4.1 Steady-state kinetics of *Sc*Grx7^{Y110X} mutants in the HEDS assay

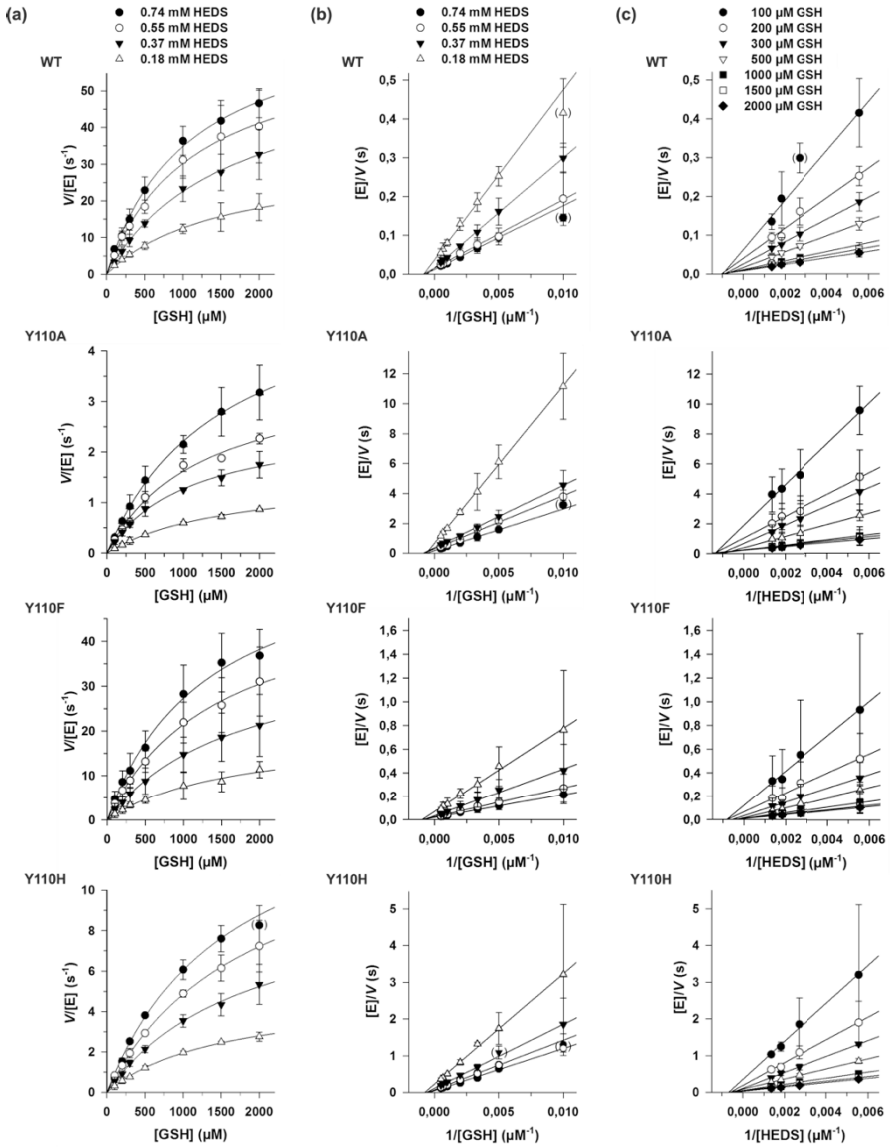

Supplementary figure 7 | Steady-state kinetics of *Sc*Grx7^{Y110X} mutants in the HEDS assay. (a) Michaelis-Menten plots showing the GSH-dependent reaction velocity at different fixed HEDS-concentrations. (b) Lineweaver-Burk plots of the data shown in (a) reveal ping-pong kinetic patterns. (c) Lineweaver-Burk plots showing the HEDS-dependent reaction velocity at different fixed GSH concentrations. All data points represent the mean ± standard deviation from three independent experiments. WT: *Sc*Grx7 wild-type; Y110F: *Sc*Grx7^{Y110F}; Y110H: *Sc*Grx7^{Y110H}; Y110A: *Sc*Grx7^{Y110A}.

6.4.2 Apparent rate constants of *Sc*Grx7^{Y110X} mutants in the HEDS assay

Supplementary table 4 | Apparent rate constants of *Sc*Grx7^{Y110X} mutants in the HEDS assay. Selected k_{cat}^{app} and K_m^{app} values of the HEDS assays with the *Sc*Grx7^{wt} enzyme and Y110X mutants obtained from supplementary figure 7. [a]Mean±SD from Michaelis-Menten plots of supplementary figure 7 of three independent protein purifications. Percentages are relative to *Sc*Grx7^{wt}. WT: *Sc*Grx7 wild-type; Y110F: *Sc*Grx7^{Y110F}; Y110H: *Sc*Grx7^{Y110H}; Y110A: *Sc*Grx7^{Y110A}.

*Sc*Grx7	[HEDS] (mM)	$k_{cat}^{app}{}_{(GSH)}$ [a] (s^{-1})		$K_m^{app}{}_{(GSH)}$ [a] (mM)		$k_{cat}^{app}/K_m^{app}{}_{(GSH)}$ ($mM^{-1}s^{-1}$)	
WT	0.18	32.1 ± 1.4	100 %	1.55 ± 0.12	100 %	20.7	100 %
Y110F	0.18	19.7 ± 2.5	61 %	1.64 ± 0.38	106 %	12.0	58 %
Y110H	0.18	4.9 ± 0.2	15 %	1.52 ± 0.10	98 %	3.2	15 %
Y110A	0.18	1.6 ± 0.1	5 %	1.64 ± 0.12	106 %	0.9	4 %
WT	0.37	58.6 ± 2.4	100 %	1.60 ± 0.12	100 %	36.7	100 %
Y110F	0.37	39.9 ± 1.0	68 %	1.73 ± 0.08	108 %	23.0	63 %
Y110H	0.37	10.2 ± 0.7	17 %	1.89 ± 0.23	118 %	5.4	15 %
Y110A	0.37	2.6 ± 0.1	4 %	1.07 ± 0.09	67 %	2.5	7 %
WT	0.55	64.6 ± 3.4	100 %	1.14 ± 0.12	100 %	56.6	100 %
Y110F	0.55	52.7 ± 2.8	82 %	1.46 ± 0.14	128 %	36.1	64 %
Y110H	0.55	14.0 ± 0.3	22 %	1.89 ± 0.06	166 %	7.4	13 %
Y110A	0.55	3.6 ± 0.4	6 %	1.25 ± 0.24	110 %	2.9	5 %
WT	0.74	72.9 ± 3.4	100 %	1.10 ± 0.10	100 %	66.5	100 %
Y110F	0.74	63.4 ± 4.9	87 %	1.32 ± 0.19	120 %	48.0	72 %
Y110H	0.74	16.0 ± 1.1	22 %	1.64 ± 0.18	149 %	9.7	15 %
Y110A	0.74	5.6 ± 0.2	8 %	1.52 ± 0.12	138 %	3.7	6 %

*Sc*Grx7	[GSH] (mM)	$k_{cat}^{app}{}_{(HEDS)}$ [a] (s^{-1})		$K_m^{app}{}_{(HEDS)}$ [a] (mM)		$k_{cat}^{app}/K_m^{app}{}_{(HEDS)}$ ($mM^{-1}s^{-1}$)	
WT	0.3	34.1 ± 4.1	100 %	0.92 ± 0.18	100 %	36.9	100 %
Y110F	0.3	31.2 ± 15.8	91 %	1.78 ± 1.20	193 %	17.5	47 %
Y110H	0.3	10.2 ± 1.9	30 %	2.27 ± 0.53	245 %	4.5	12 %
Y110A	0.3	1.7 ± 0.3	5 %	1.10 ± 0.33	120 %	1.5	4 %
WT	0.5	63.9 ± 4.1	100 %	1.33 ± 0.12	100 %	47.8	100 %
Y110F	0.5	78.5 ± 31	123 %	3.40 ± 1.58	256 %	23.1	48 %
Y110H	0.5	13.8 ± 1.6	22 %	2.02 ± 0.30	152 %	6.9	14 %
Y110A	0.5	2.0 ± 0.3	3 %	0.67 ± 0.18	50 %	3.0	6 %
WT	1.0	81.1 ± 8.9	100 %	0.90 ± 0.16	100 %	90.1	100 %
Y110F	1.0	104.4 ± 19.4	129 %	2.59 ± 0.59	288 %	40.2	45 %
Y110H	1.0	20.4 ± 0.8	25 %	1.65 ± 0.15	183 %	12.3	14 %
Y110A	1.0	4.5 ± 0.9	6 %	0.79 ± 0.26	88 %	5.8	6 %
WT	1.5	90.0 ± 12.5	100 %	0.82 ± 0.19	100 %	110	100 %
Y110F	1.5	138.9 ± 28.9	154 %	2.85 ± 0.71	348 %	48.8	44 %
Y110H	1.5	25.8 ± 3.6	29 %	1.77 ± 0.32	216 %	14.6	13 %
Y110A	1.5	4.2 ± 0.1	5 %	0.61 ± 0.02	74 %	6.8	6 %

6.4.3 Secondary plots for the *Sc*Grx7^{Y110X} mutants in the HEDS assay

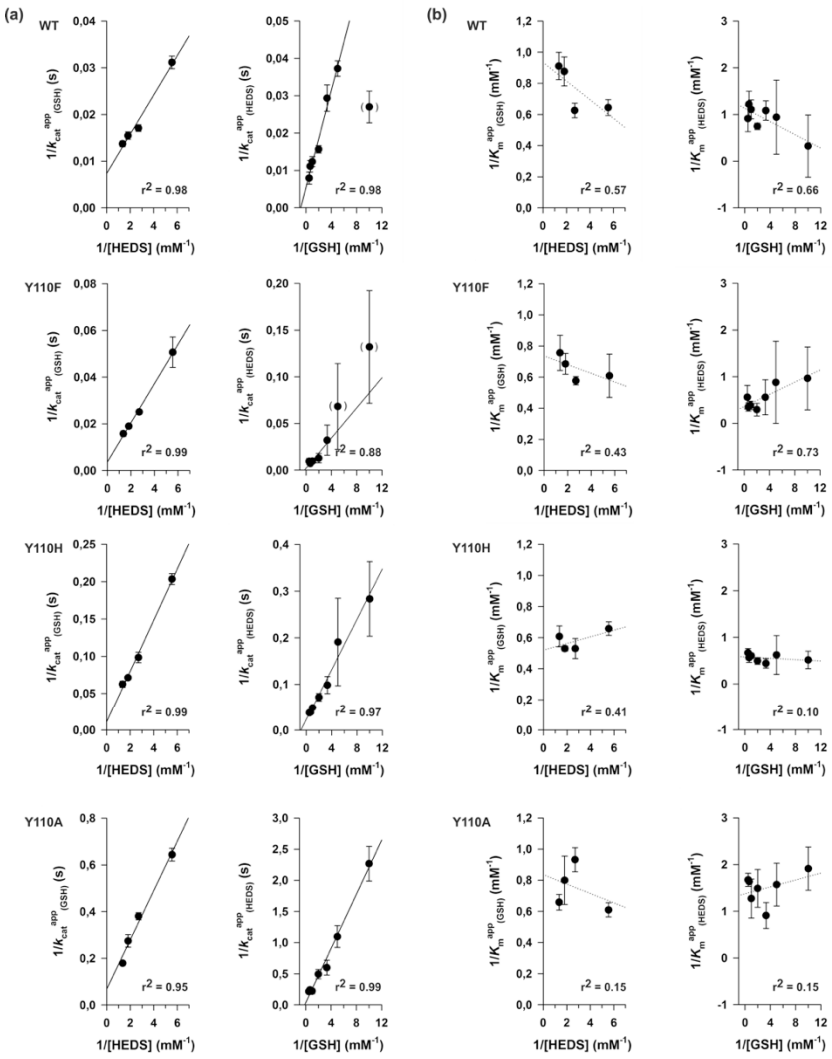

Supplementary figure 8 | Secondary plots for the *Sc*Grx7^{Y110X} mutants obtained from the HEDS assay. Values for K_m^{app} and k_{cat}^{app} were obtained from the Michaelis-Menten plots in supplementary figure 7. (a) Secondary plots of the k_{cat}^{app} values at different concentrations of HEDS (left side) and GSH (right side). (b) Secondary plots of the K_m^{app} values at different concentrations of HEDS (left side) and GSH (right side). Outliers based on the r^2 values (in brackets) were omitted from the linear regression analysis. All data points represent the mean ± standard deviation from three independent experiments. WT: *Sc*Grx7 wild-type; Y110F: *Sc*Grx7^{Y110F}; Y110H: *Sc*Grx7^{Y110H}; Y110A: *Sc*Grx7^{Y110A}.

6.5 Kinetics of *Sc*Grx7^{D144X} mutants in the GSSCys assay

6.5.1 Steady-state kinetics of *Sc*Grx7^{D144X} mutants in the GSSCys assay

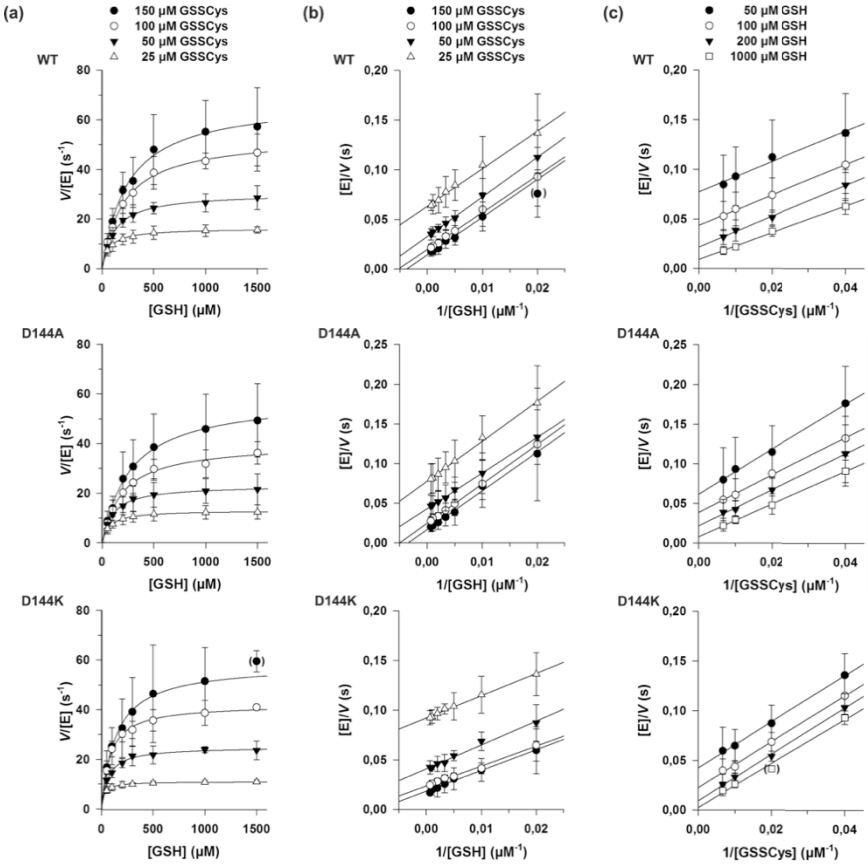

Supplementary figure 9 | Steady-state kinetics of *Sc*Grx7^{D144X} mutants in the GSSCys assay. (a) Michaelis-Menten plots showing the GSH-dependent reaction velocity at different fixed GSSCys-concentrations. (b) Lineweaver-Burk plots of the data shown in (a) reveal ping-pong kinetic patterns. (c) Lineweaver-Burk plots showing the GSSCys-dependent reaction velocity at different fixed GSH concentrations. All data points represent the mean ± standard deviation from three independent experiments. WT: *Sc*Grx7 wild-type; D144A: *Sc*Grx7^{D144A}; D144K: *Sc*Grx7^{D144K}.

6.5.2 Apparent rate constants of *Sc*Grx7^{D144X} mutants in the GSSCys assay

Supplementary table 5 | Apparent rate constants of *Sc*Grx7^{D144X} mutants in the GSSCys assay. Selected k_{cat}^{app} and K_m^{app} values of the GSSCys assays with the *Sc*Grx7^{wt} enzyme and D144X mutants obtained from supplementary figure 9. [a]Mean±SD from Michaelis-Menten plots of supplementary figure 9 of three independent protein purifications. Percentages are relative to *Sc*Grx7^{wt}. WT: *Sc*Grx7 wild-type; D144A: *Sc*Grx7^{D144A}; D144K: *Sc*Grx7^{D144K}.

***Sc*Grx7**	**[GSSCys]** (µM)	$k_{cat}^{app}{}_{(GSH)}$ [a] (s^{-1})		$K_m^{app}{}_{(GSH)}$ [a] (µM)		$k_{cat}^{app}/K_m^{app}{}_{(GSH)}$ ($mM^{-1}s^{-1}$)	
WT	25	16.2 ± 0.2	100 %	67.5 ± 4.4	100 %	240	100 %
D144A	25	13.0 ± 0.1	80 %	68.6 ± 2.6	102 %	190	79 %
D144K	25	10.9 ± 0.1	67 %	25.2 ± 1.2	37 %	433	180 %
WT	50	30.4 ± 0.4	100 %	120 ± 5.6	100 %	253	100 %
D144A	50	23.1 ± 0.2	76 %	103 ± 4.2	86 %	225	89 %
D144K	50	24.9 ± 0.4	82 %	64.0 ± 5.6	53 %	389	154 %
WT	100	53.3 ± 0.9	100 %	211 ± 11.1	100 %	253	100 %
D144A	100	40.0 ± 1.0	75 %	194 ± 16.4	92 %	214	85 %
D144K	100	42.2 ± 0.7	79 %	82.6 ± 6.2	38 %	511	202 %
WT	150	68.0 ± 2.4	100 %	244 ± 27.1	100 %	279	100 %
D144A	150	58.7 ± 1.3	86 %	275 ± 18.1	113 %	214	77 %
D144K	150	58.2 ± 1.7	86 %	138 ± 13.1	56 %	422	151 %

***Sc*Grx7**	**[GSH]** (µM)	$k_{cat}^{app}{}_{(GSSCys)}$ [a] (s^{-1})		$K_m^{app}{}_{(GSSCys)}$ [a] (µM)		$k_{cat}^{app}/K_m^{app}{}_{(GSSCys)}$ ($mM^{-1}s^{-1}$)	
WT	50	13.3 ± 0.5	100 %	22.1 ± 3.3	100 %	603	100 %
D144A	50	16.0 ± 0.8	120 %	44.4 ± 6.0	201 %	360	60 %
D144K	50	22.7 ± 0.8	171 %	50.2 ± 4.9	227 %	453	75 %
WT	100	23.2 ± 0.7	100 %	36.4 ± 3.1	100 %	639	100 %
D144A	100	26.2 ± 0.9	112 %	62.7 ± 5.3	172 %	418	65 %
D144K	100	41.3 ± 4.4	178 %	89.2 ± 19.5	245 %	463	72 %
WT	200	45.8 ± 2.6	100 %	70.7 ± 9.0	100 %	648	100 %
D144A	200	42.3 ± 4.4	92 %	89.3 ± 19.1	126 %	473	73 %
D144K	200	95.2 ± 5.3	208 %	213 ± 18.1	301 %	446	69 %
WT	1000	114 ± 13.0	100 %	155 ± 29.9	100 %	735	100 %
D144A	1000	122 ± 12.5	107 %	252 ± 37.3	163 %	485	66 %
D144K	1000	182 ± 37.1	160 %	377 ± 103	243 %	483	66 %

6.5.3 Secondary plots for the *Sc*Grx7^{D144X} mutants in the GSSCys assay

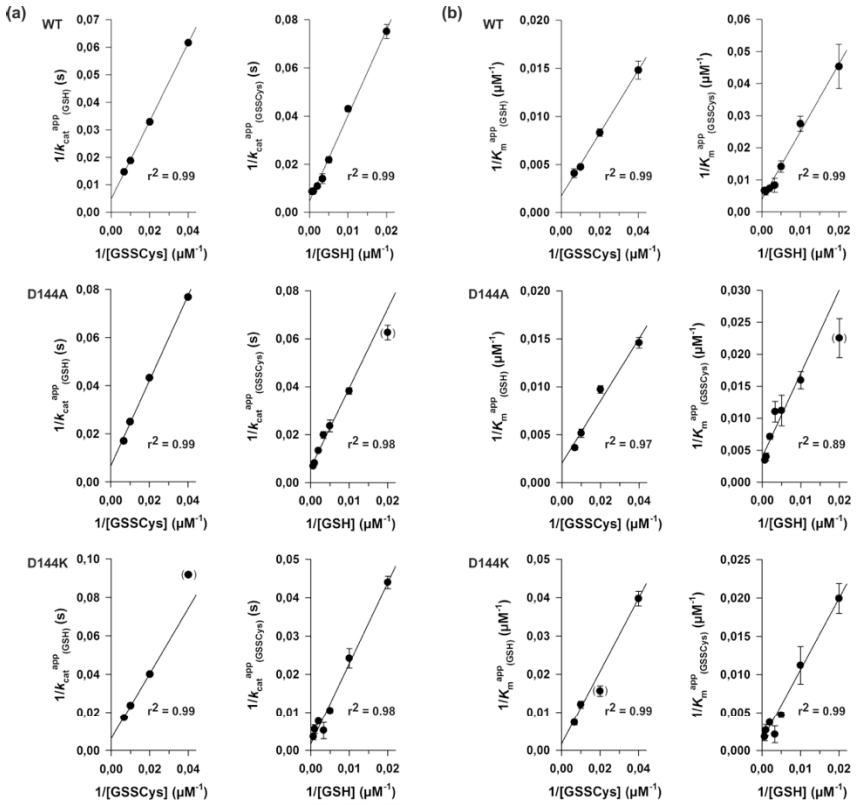

Supplementary figure 10 | Secondary plots for the *Sc*Grx7^{D144X} mutants obtained from the GSSCys assay. Values for K_m^{app} and k_{cat}^{app} were obtained from the Michaelis-Menten plots in supplementary figure 9. (a) Secondary plots of the k_{cat}^{app} values at different concentrations of GSSCys (left side) and GSH (right side). (b) Secondary plots of the K_m^{app} values at different concentrations of GSSCys (left side) and GSH (right side). Outliers based on the r^2 values (in brackets) were omitted from the linear regression analysis. All data points represent the mean ± standard deviation from three independent experiments. WT: *Sc*Grx7 wild-type; D144A: *Sc*Grx7^{D144A}; D144K: *Sc*Grx7^{D144K}.

6.6 Kinetics of *Sc*Grx7^{E147X} mutants in the GSSCys assay

6.6.1 Steady-state kinetics of *Sc*Grx7^{E147X} mutants in the GSSCys assay

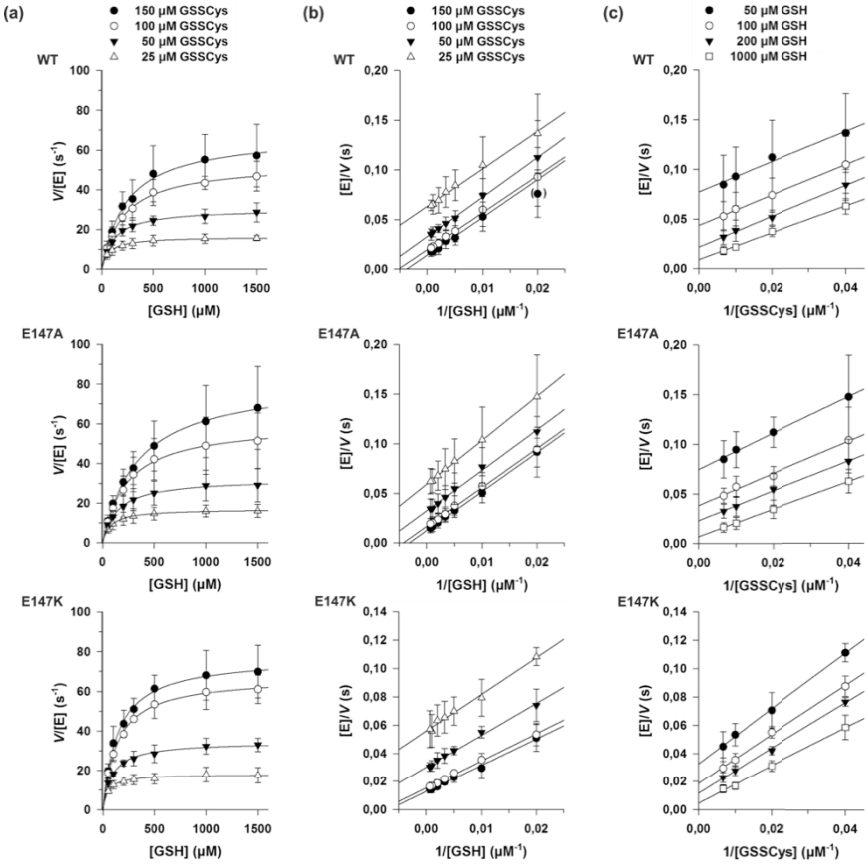

Supplementary figure 11 | Steady-state kinetics of *Sc*Grx7^{E147X} mutants in the GSSCys assay. (a) Michaelis-Menten plots showing the GSH-dependent reaction velocity at different fixed GSSCys-concentrations. (b) Lineweaver-Burk plots of the data shown in (a) reveal ping-pong kinetic patterns. (c) Lineweaver-Burk plots showing the GSSCys-dependent reaction velocity at different fixed GSH concentrations. All data points represent the mean ± standard deviation from three independent experiments. WT: *Sc*Grx7 wild-type; E147A: *Sc*Grx7^{E147A}; E147K: *Sc*Grx7^{E147K}.

6.6.2 Apparent rate constants of *Sc*Grx7^{E147X} mutants in the GSSCys assay

Supplementary table 6 | Apparent rate constants of *Sc*Grx7^{E147X} mutants in the GSSCys assay. Selected k_{cat}^{app} and K_m^{app} values of the GSSCys assays with the *Sc*Grx7^{wt} enzyme and E147X mutants obtained from supplementary figure 11. [a]Mean±SD from Michaelis-Menten plots of supplementary figure 11 of three independent protein purifications. Percentages are relative to *Sc*Grx7^{wt}. WT: *Sc*Grx7 wild-type; E147A: *Sc*Grx7^{E147A}; E147K: *Sc*Grx7^{E147K}.

***Sc*Grx7**	**[GSSCys]** (µM)	$k_{cat}^{app}{}_{(GSH)}$ [a] (s^{-1})		$K_m^{app}{}_{(GSH)}$ [a] (µM)		$k_{cat}^{app}/K_m^{app}{}_{(GSH)}$ ($mM^{-1}s^{-1}$)	
WT	25	16.2 ± 0.2	100 %	67.5 ± 4.4	100 %	240	100 %
E147A	25	17.0 ± 0.1	105 %	77.6 ± 2.3	115 %	219	91 %
E147K	25	18.0 ± 0.3	111 %	47.4 ± 4.9	70 %	379	158 %
WT	50	30.4 ± 0.4	100 %	120 ± 5.6	100 %	253	100 %
E147A	50	32.3 ± 0.5	106 %	145 ± 0.5	121 %	223	88 %
E147K	50	34.4 ± 0.6	113 %	87.2 ± 6.5	73 %	395	156 %
WT	100	53.3 ± 0.9	100 %	211 ± 11.1	100 %	253	100 %
E147A	100	60.4 ± 1.0	113 %	237 ± 12.4	112 %	255	101 %
E147K	100	67.3 ± 0.8	126 %	139 ± 6.3	66 %	486	192 %
WT	150	68.0 ± 2.4	100 %	244 ± 27.1	100 %	279	100 %
E147A	150	82.9 ± 1.3	122 %	344 ± 14.0	141 %	241	86 %
E147K	150	77.2 ± 1.4	114 %	142 ± 9.2	58 %	543	195 %

***Sc*Grx7**	**[GSH]** (µM)	$k_{cat}^{app}{}_{(GSSCys)}$ [a] (s^{-1})		$K_m^{app}{}_{(GSSCys)}$ [a] (µM)		$k_{cat}^{app}/K_m^{app}{}_{(GSSCys)}$ ($mM^{-1}s^{-1}$)	
WT	50	13.3 ± 0.5	100 %	22.1 ± 3.3	100 %	603	100 %
E147A	50	13.6 ± 0.4	102 %	25.8 ± 2.5	117 %	526	87 %
E147K	50	30.9 ± 1.3	232 %	60.9 ± 6.0	276 %	508	84 %
WT	100	23.2 ± 0.7	100 %	36.4 ± 3.1	100 %	639	100 %
E147A	100	25.8 ± 1.8	111 %	41.1 ± 8.0	113 %	629	98 %
E147K	100	57.5 ± 2.2	248 %	104 ± 7.9	287 %	550	86 %
WT	200	45.8 ± 2.6	100 %	70.7 ± 9.0	100 %	648	100 %
E147A	200	45.0 ± 1.4	98 %	70.4 ± 4.9	100 %	640	99 %
E147K	200	77.9 ± 3.3	170 %	117 ± 9.2	165 %	665	103 %
WT	1000	114 ± 13.0	100 %	155 ± 29.9	100 %	735	100 %
E147A	1000	139 ± 7.3	122 %	189 ± 15.6	122 %	737	100 %
E147K	1000	363 ± 33.2	318 %	509 ± 54.2	328 %	714	97 %

6.6.3 Secondary plots for the *Sc*Grx7^{E147X} mutants in the GSSCys assay

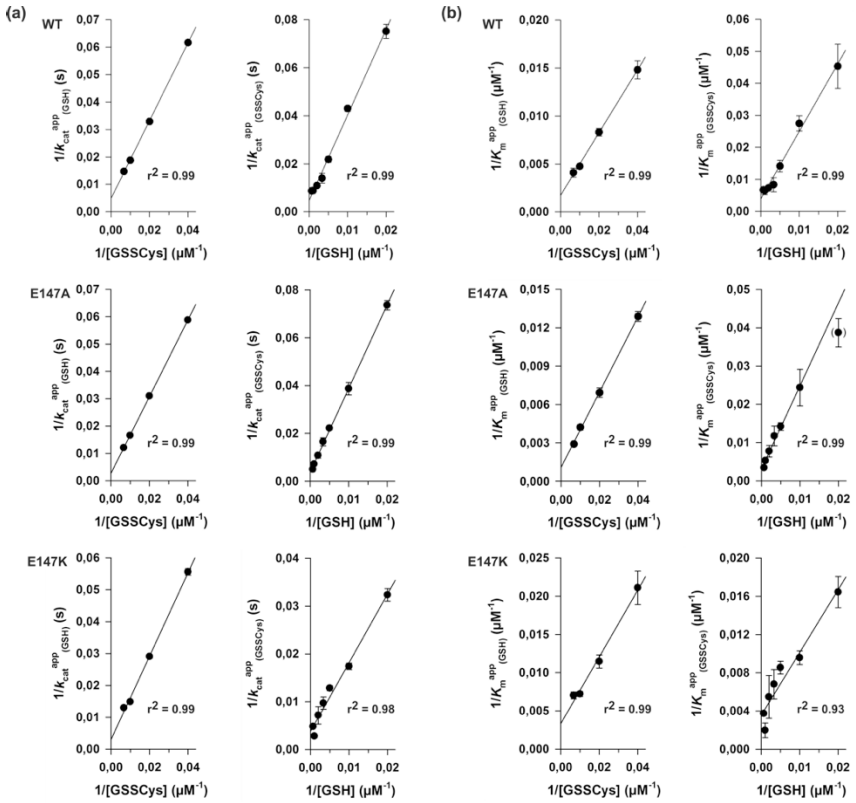

Supplementary figure 12 | Secondary plots for the *Sc*Grx7^{E147X} mutants obtained from the GSSCys assay. Values for K_m^{app} and k_{cat}^{app} were obtained from the Michaelis-Menten plots in supplementary figure 11. (a) Secondary plots of the k_{cat}^{app} values at different concentrations of GSSCys (left side) and GSH (right side). (b) Secondary plots of the K_m^{app} values at different concentrations of GSSCys (left side) and GSH (right side). Outliers based on the r^2 values (in brackets) were omitted from the linear regression analysis. All data points represent the mean ± standard deviation from three independent experiments. WT: *Sc*Grx7 wild-type; E147A: *Sc*Grx7^{E147A}; E147K: *Sc*Grx7^{E147K}.

6.7 Kinetics of *Sc*Grx7^{R153X} mutants in the GSSCys assay

6.7.1 Steady-state kinetics of *Sc*Grx7^{R153X} mutants in the GSSCys assay

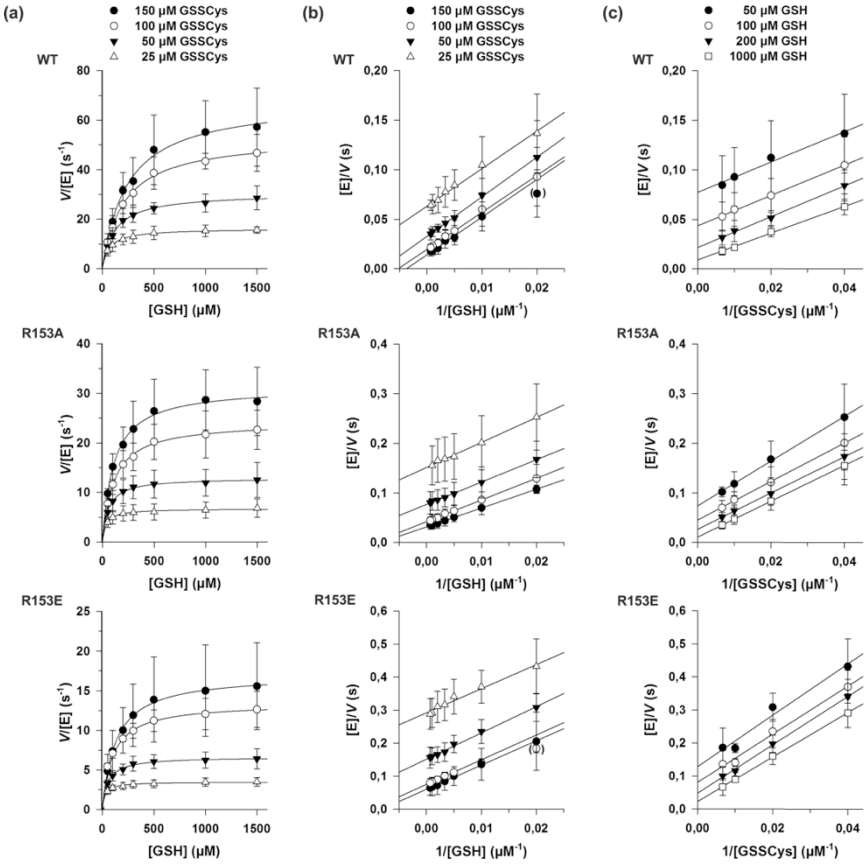

Supplementary figure 13 | Steady-state kinetics of *Sc*Grx7^{R153X} mutants in the GSSCys assay. (a) Michaelis-Menten plots showing the GSH-dependent reaction velocity at different fixed GSSCys-concentrations. (b) Lineweaver-Burk plots of the data shown in (a) reveal ping-pong kinetic patterns. (c) Lineweaver-Burk plots showing the GSSCys-dependent reaction velocity at different fixed GSH concentrations. All data points represent the mean ± standard deviation from three independent experiments. WT: *Sc*Grx7 wild-type; R153A: *Sc*Grx7^{R153A}; R153E: *Sc*Grx7^{R153E}.

6.7.2 Apparent rate constants of *Sc*Grx7^{R153X} mutants in the GSSCys assay

Supplementary table 7 | Apparent rate constants of *Sc*Grx7^{R153X} mutants in the GSSCys assay. Selected k_{cat}^{app} and K_m^{app} values of the GSSCys assays with the *Sc*Grx7^{wt} enzyme and R153X mutants obtained from supplementary figure 13. [a]Mean±SD from Michaelis-Menten plots of supplementary figure 13 of three independent protein purifications. Percentages are relative to *Sc*Grx7^{wt}. WT: *Sc*Grx7 wild-type; R153A: *Sc*Grx7^{R153A}; R153E: *Sc*Grx7^{R153E}.

***Sc*Grx7**	**[GSSCys]** (µM)	$k_{cat}^{app}{}_{(GSH)}$ [a] (s^{-1})		$K_m^{app}{}_{(GSH)}$ [a] (µM)		$k_{cat}^{app}/K_m^{app}{}_{(GSH)}$ ($mM^{-1}s^{-1}$)	
WT	25	16.2 ± 0.2	100 %	67.5 ± 4.4	100 %	240	100 %
R153A	25	6.6 ± 0.1	41 %	32.8 ± 2.0	49 %	201	84 %
R153E	25	3.5 ± 0.0	22 %	27.1 ± 2.8	40 %	128	53 %
WT	50	30.4 ± 0.4	100 %	120 ± 5.6	100 %	253	100 %
R153A	50	12.9 ± 0.1	42 %	56.2 ± 2.7	47 %	230	91 %
R153E	50	6.6 ± 0.1	22 %	54.3 ± 3.4	45 %	122	48 %
WT	100	53.3 ± 0.9	100 %	211 ± 11.1	100 %	253	100 %
R153A	100	24.2 ± 0.3	45 %	110 ± 4.8	52 %	221	87 %
R153E	100	13.4 ± 0.1	25 %	101 ± 4.3	48 %	133	53 %
WT	150	68.0 ± 2.4	100 %	244 ± 27.1	100 %	279	100 %
R153A	150	31.6 ± 0.6	46 %	118 ± 8.0	48 %	268	96 %
R153E	150	17.0 ± 0.2	25 %	130 ± 6.2	53 %	131	47 %

***Sc*Grx7**	**[GSH]** (µM)	$k_{cat}^{app}{}_{(GSSCys)}$ [a] (s^{-1})		$K_m^{app}{}_{(GSSCys)}$ [a] (µM)		$k_{cat}^{app}/K_m^{app}{}_{(GSSCys)}$ ($mM^{-1}s^{-1}$)	
WT	50	13.3 ± 0.5	100 %	22.1 ± 3.3	100 %	603	100 %
R153A	50	14.1 ± 0.3	106 %	66.5 ± 3.5	306 %	212	35 %
R153E	50	8.1 ± 1.5	61 %	64.1 ± 27.3	290 %	126	21 %
WT	100	23.2 ± 0.7	100 %	36.4 ± 3.1	100 %	639	100 %
R153A	100	22.5 ± 1.2	97 %	88.5 ± 9.5	243 %	254	40 %
R153E	100	11.9 ± 2.0	51 %	82.7 ± 30.3	227 %	144	23 %
WT	200	45.8 ± 2.6	100 %	70.7 ± 9.0	100 %	648	100 %
R153A	200	37.1 ± 1.2	81 %	135 ± 7.6	191 %	276	43 %
R153E	200	19.5 ± 2.6	43 %	136 ± 32.2	192 %	144	22 %
WT	1000	114 ± 13.0	100 %	155 ± 29.9	100 %	735	100 %
R153A	1000	79.0 ± 5.8	69 %	270 ± 28.2	174 %	293	40 %
R153E	1000	52.2 ± 4.1	46 %	332 ± 19.0	214 %	145	20 %

6.7.3 Secondary plots for the *Sc*Grx^{7R153X} mutants in the GSSCys assay

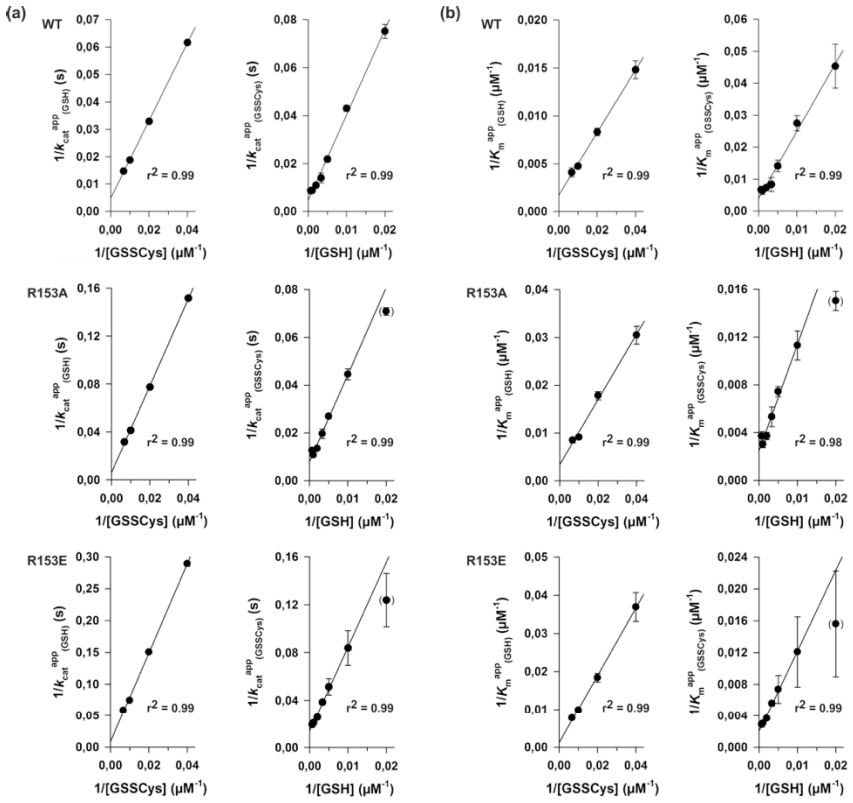

Supplementary figure 14 | Secondary plots for the *Sc*Grx7^{R153X} mutants obtained from the GSSCys assay. Values for K_m^{app} and k_{cat}^{app} were obtained from the Michaelis-Menten plots in supplementary figure 13. (a) Secondary plots of the k_{cat}^{app} values at different concentrations of GSSCys (left side) and GSH (right side). (b) Secondary plots of the K_m^{app} values at different concentrations of GSSCys (left side) and GSH (right side). Outliers based on the r^2 values (in brackets) were omitted from the linear regression analysis. All data points represent the mean ± standard deviation from three independent experiments. WT: *Sc*Grx7 wild-type; R153A: *Sc*Grx7^{R153A}; R153E: *Sc*Grx7^{R153E}.

6.8 Statistical analyses of kinetic data

Supplementary table 8 | Statistical analyses of kinetic data. Statistical analysis of k_{cat}^{app} and K_m^{app} values from the indicated measurements of *Pf*Grx and *Sc*Grx7 mutants. P-values from one way ANOVA analysis followed by a Holm-Sidak test were calculated in SigmaPlot 13 (P > 0.05: ns; P ≤ 0.05: *; P ≤ 0.01: **, P ≤ 0.001: ***).

A) GSSCys assay *Pf*Grx (Fig. 34, Supplementary Fig. 1 and Supplementary Table 1)

A1.1) $k_{cat}^{app}{}_{(GSSCys)}$ @ 300 µM GSH

Comparison		P-value	
DM	→ K26A	<0.001	***
DM	→ D90A	<0.001	***
K26A	→ D90A	<0.001	***

A1.2) $k_{cat}^{app}{}_{(GSSCys)}$ @ 500 µM GSH

Comparison		P-value	
DM	→ K26A	<0.001	***
DM	→ D90A	<0.001	***
K26A	→ D90A	<0.001	***

A1.3) $k_{cat}^{app}{}_{(GSSCys)}$ @ 1000 µM GSH

Comparison		P-value	
DM	→ K26A	<0.001	***
DM	→ D90A	<0.001	***
K26A	→ D90A	<0.001	***

A1.4) $k_{cat}^{app}{}_{(GSSCys)}$ @ 2000 µM GSH

Comparison		P-value	
DM	→ K26A	<0.001	***
DM	→ D90A	<0.001	***
K26A	→ D90A	<0.001	***

A2.1) $k_{cat}^{app}{}_{(GSH)}$ @ 25 µM GSSCys

Comparison		P-value	
DM	→ K26A	<0.001	***
DM	→ D90A	<0.001	***
K26A	→ D90A	<0.001	***

A2.2) $k_{cat}^{app}{}_{(GSH)}$ @ 50 µM GSSCys

Comparison		P-value	
DM	→ K26A	<0.001	***
DM	→ D90A	0.002	**
K26A	→ D90A	<0.001	***

A2.3) $k_{cat}^{app}{}_{(GSH)}$ @ 100 µM GSSCys

Comparison		P-value	
DM	→ K26A	<0.001	***
DM	→ D90A	0.247	ns
K26A	→ D90A	<0.001	***

A2.4) $k_{cat}^{app}{}_{(GSH)}$ @ 150 µM GSSCys

Comparison		P-value	
DM	→ K26A	<0.001	***
DM	→ D90A	0.354	ns
K26A	→ D90A	<0.001	***

A3.1) $K_m^{app}{}_{(GSSCys)}$ @ 300 µM GSH

Comparison		P-value	
DM	→ K26A	<0.001	***
DM	→ D90A	<0.001	***
K26A	→ D90A	0.002	**

A3.2) $K_m^{app}{}_{(GSSCys)}$ @ 500 µM GSH

Comparison		P-value	
DM	→ K26A	0.002	**
DM	→ D90A	0.004	**
K26A	→ D90A	0.006	**

A3.3) $K_m^{app}{}_{(GSSCys)}$ @ 1000 µM GSH

Comparison		P-value	
DM	→ K26A	0.004	**
DM	→ D90A	<0.001	***
K26A	→ D90A	0.018	*

A3.4) $K_m^{app}{}_{(GSSCys)}$ @ 2000 µM GSH

Comparison		P-value	
DM	→ K26A	0.006	**
DM	→ D90A	<0.001	***
K26A	→ D90A	0.028	*

A4.1) $K_m^{app}{}_{(GSH)}$ @ 25 µM GSSCys

Comparison		P-value	
DM	→ K26A	<0.001	***
DM	→ D90A	0.002	**
K26A	→ D90A	0.001	***

A4.2) $K_m^{app}{}_{(GSH)}$ @ 50 µM GSSCys

Comparison		P-value	
DM	→ K26A	<0.001	***
DM	→ D90A	0.007	**
K26A	→ D90A	0.001	***

A4.3) $K_m^{app}{}_{(GSH)}$ @ 100 µM GSSCys

Comparison		P-value	
DM	→ K26A	<0.001	***
DM	→ D90A	0.232	ns
K26A	→ D90A	<0.001	***

A4.4) $K_m^{app}{}_{(GSH)}$ @ 150 µM GSSCys

Comparison		P-value	
DM	→ K26A	<0.001	***
DM	→ D90A	0.002	**
K26A	→ D90A	<0.001	***

B) HEDS assay *Pf*Grx (Fig. 35, Supplementary Fig. 3 and Supplementary Table 2)

B1.1) $k_{cat}^{app}{}_{(HEDS)}$ @ 250 µM GSH

Comparison		P-value	
DM	→ K26A	<0.001	***
DM	→ D90A	<0.001	***
K26A	→ D90A	<0.001	***

B1.2) $k_{cat}^{app}{}_{(HEDS)}$ @ 500 µM GSH

Comparison		P-value	
DM	→ K26A	<0.001	***
DM	→ D90A	<0.001	***
K26A	→ D90A	<0.001	***

B1.3) $k_{cat}^{app}{}_{(HEDS)}$ @ 1000 µM GSH

Comparison		P-value	
DM	→ K26A	<0.001	***
DM	→ D90A	<0.001	***
K26A	→ D90A	<0.001	***

B1.4) $k_{cat}^{app}{}_{(HEDS)}$ @ 2000 µM GSH

Comparison		P-value	
DM	→ K26A	<0.001	***
DM	→ D90A	0.933	ns
K26A	→ D90A	<0.001	***

B2.1) $k_{cat}^{app}{}_{(GSH)}$ @ 0.18 mM HEDS

Comparison		P-value	
DM	→ K26A	<0.001	***
DM	→ D90A	<0.001	***
K26A	→ D90A	<0.001	***

B2.2) $k_{cat}^{app}{}_{(GSH)}$ @ 0.37 mM HEDS

Comparison		P-value	
DM	→ K26A	<0.001	***
DM	→ D90A	<0.001	***
K26A	→ D90A	<0.001	***

B2.3) $k_{cat}^{app}{}_{(GSH)}$ @ 0.55 mM HEDS

Comparison		P-value	
DM	→ K26A	<0.001	***
DM	→ D90A	0.004	**
K26A	→ D90A	<0.001	***

B2.4) $k_{cat}^{app}{}_{(GSH)}$ @ 0.74 mM HEDS

Comparison		P-value	
DM	→ K26A	<0.001	***
DM	→ D90A	0.013	*
K26A	→ D90A	<0.001	***

B3.1) $K_m^{app}{}_{(HEDS)}$ @ 250 µM GSH

Comparison		P-value	
DM	→ K26A	0.187	ns
DM	→ D90A	0.020	*
K26A	→ D90A	0.281	ns

B3.2) $K_m^{app}{}_{(HEDS)}$ @ 500 µM GSH

Comparison		P-value	
DM	→ K26A	0.324	ns
DM	→ D90A	0.127	ns
K26A	→ D90A	0.354	ns

B3.3) $K_m^{app}{}_{(HEDS)}$ @ 1000 µM GSH

Comparison		P-value	
DM	→ K26A	0.137	ns
DM	→ D90A	0.004	**
K26A	→ D90A	0.241	ns

B3.4) $K_m^{app}{}_{(HEDS)}$ @ 2000 µM GSH

Comparison		P-value	
DM	→ K26A	0.049	*
DM	→ D90A	0.007	**
K26A	→ D90A	0.672	ns

B4.1) $K_m^{app}{}_{(GSH)}$ @ 0.18 mM HEDS

Comparison		P-value	
DM	→ K26A	0.542	ns
DM	→ D90A	0.042	*
K26A	→ D90A	0.029	*

B4.2) $K_m^{app}{}_{(GSH)}$ @ 0.37 mM HEDS

Comparison		P-value	
DM	→ K26A	0.190	ns
DM	→ D90A	0.015	*
K26A	→ D90A	0.038	*

B4.3) $K_m^{app}{}_{(GSH)}$ @ 0.55 mM HEDS

Comparison		P-value	
DM	→ K26A	0.069	ns
DM	→ D90A	0.118	ns
K26A	→ D90A	0.735	ns

B4.4) $K_m^{app}{}_{(GSH)}$ @ 0.74 mM HEDS

Comparison		P-value	
DM	→ K26A	0.005	**
DM	→ D90A	0.262	ns
K26A	→ D90A	0.006	**

C) GSSCys assay *Sc*Grx7^{Y110X} (Fig. 36, Supplementary Fig. 5 and Supplementary Table 3)

C1.1) $k_{cat}^{app}{}_{(GSSCys)}$ @ 50 µM GSH

Comparison		P-value	
WT	→ Y110F	0.019	*
WT	→ Y110H	<0.001	***
WT	→ Y110A	<0.001	***
Y110F	→ Y110H	<0.001	***
Y110F	→ Y110A	<0.001	***
Y110H	→ Y110A	<0.001	***

C1.2) $k_{cat}^{app}{}_{(GSSCys)}$ @ 100 µM GSH

Comparison		P-value	
WT	→ Y110F	0.101	ns
WT	→ Y110H	0.033	*
WT	→ Y110A	<0.001	***
Y110F	→ Y110H	0.004	**
Y110F	→ Y110A	<0.001	***
Y110H	→ Y110A	<0.001	***

C1.3) $k_{cat}^{app}{}_{(GSSCys)}$ @ 200 µM GSH

Comparison		P-value	
WT	→ Y110F	0.070	ns
WT	→ Y110H	0.009	*
WT	→ Y110A	<0.001	***
Y110F	→ Y110H	0.001	***
Y110F	→ Y110A	<0.001	***
Y110H	→ Y110A	0.012	*

C1.4) $k_{cat}^{app}{}_{(GSSCys)}$ @ 1000 µM GSH

Comparison		P-value	
WT	→ Y110F	0.413	ns
WT	→ Y110H	0.013	*
WT	→ Y110A	0.002	**
Y110F	→ Y110H	0.032	*
Y110F	→ Y110A	0.004	**
Y110H	→ Y110A	0.199	ns

C2.1) $k_{cat}^{app}{}_{(GSH)}$ @ 25 µM GSSCys

Comparison		P-value	
WT	→ Y110F	0.017	*
WT	→ Y110H	<0.001	***
WT	→ Y110A	<0.001	***
Y110F	→ Y110H	<0.001	***
Y110F	→ Y110A	<0.001	***
Y110H	→ Y110A	<0.001	***

C2.2) $k_{cat}^{app}{}_{(GSH)}$ @ 50 µM GSSCys

Comparison		P-value	
WT	→ Y110F	<0.001	***
WT	→ Y110H	<0.001	***
WT	→ Y110A	<0.001	***
Y110F	→ Y110H	<0.001	***
Y110F	→ Y110A	<0.001	***
Y110H	→ Y110A	0.001	***

C2.3) $k_{cat}^{app}{}_{(GSH)}$ @ 100 µM GSSCys

Comparison		P-value	
WT	→ Y110F	0.001	***
WT	→ Y110H	<0.001	***
WT	→ Y110A	<0.001	***
Y110F	→ Y110H	<0.001	***
Y110F	→ Y110A	<0.001	***
Y110H	→ Y110A	0.001	***

C2.4) $k_{cat}^{app}{}_{(GSH)}$ @ 150 µM GSSCys

Comparison		P-value	
WT	→ Y110F	<0.001	***
WT	→ Y110H	<0.001	***
WT	→ Y110A	<0.001	***
Y110F	→ Y110H	<0.001	***
Y110F	→ Y110A	0.004	**
Y110H	→ Y110A	<0.001	***

C3.1) $K_m^{app}{}_{(GSSCys)}$ @ 50 µM GSH

Comparison		P-value	
WT	→ Y110F	0.991	ns
WT	→ Y110H	0.011	*
WT	→ Y110A	0.032	*
Y110F	→ Y110H	0.013	*
Y110F	→ Y110A	0.041	*
Y110H	→ Y110A	0.520	ns

C3.2) $K_m^{app}{}_{(GSSCys)}$ @ 100 µM GSH

Comparison		P-value	
WT	→ Y110F	0.807	ns
WT	→ Y110H	<0.001	***
WT	→ Y110A	0.237	ns
Y110F	→ Y110H	<0.001	***
Y110F	→ Y110A	0.236	ns
Y110H	→ Y110A	0.006	**

C3.3) $K_m^{app}{}_{(GSSCys)}$ @ 200 µM GSH

Comparison		P-value	
WT	→ Y110F	0.747	ns
WT	→ Y110H	0.012	*
WT	→ Y110A	0.283	ns
Y110F	→ Y110H	0.016	*
Y110F	→ Y110A	0.317	ns
Y110H	→ Y110A	0.111	ns

C3.4) $K_m^{app}{}_{(GSSCys)}$ @ 1000 µM GSH

Comparison		P-value	
WT	→ Y110F	0.114	ns
WT	→ Y110H	0.672	ns
WT	→ Y110A	0.214	ns
Y110F	→ Y110H	0.310	ns
Y110F	→ Y110A	0.667	ns
Y110H	→ Y110A	0.379	ns

C4.1) $K_m^{app}{}_{(GSH)}$ @ 25 µM GSSCys

Comparison		P-value	
WT	→ Y110F	0.004	**
WT	→ Y110H	<0.001	***
WT	→ Y110A	0.001	***
Y110F	→ Y110H	0.001	***
Y110F	→ Y110A	0.223	ns
Y110H	→ Y110A	0.004	**

C4.2) $K_m^{app}{}_{(GSH)}$ @ 50 µM GSSCys

Comparison		P-value	
WT	→ Y110F	0.355	ns
WT	→ Y110H	0.001	***
WT	→ Y110A	0.151	ns
Y110F	→ Y110H	<0.001	***
Y110F	→ Y110A	0.051	ns
Y110H	→ Y110A	0.012	*

C4.3) $K_m^{app}{}_{(GSH)}$ @ 100 µM GSSCys

Comparison		P-value	
WT	→ Y110F	0.949	ns
WT	→ Y110H	0.003	**
WT	→ Y110A	0.072	ns
Y110F	→ Y110H	0.003	**
Y110F	→ Y110A	0.096	ns
Y110H	→ Y110A	0.071	ns

C4.4) $K_m^{app}{}_{(GSH)}$ @ 150 µM GSSCys

Comparison		P-value	
WT	→ Y110F	0.608	ns
WT	→ Y110H	<0.001	***
WT	→ Y110A	0.017	*
Y110F	→ Y110H	<0.001	***
Y110F	→ Y110A	0.012	*
Y110H	→ Y110A	0.002	**

D) HEDS assay *Sc*Grx7^{Y110X} (Fig. 37, Supplementary Fig. 7 and Supplementary Table 4)

D1.1) $k_{cat}^{app}{}_{(HEDS)}$ @ 300 µM GSH

Comparison		P-value	
WT	→ Y110F	0.596	ns
WT	→ Y110H	0.007	**
WT	→ Y110A	0.001	***
Y110F	→ Y110H	0.011	*
Y110F	→ Y110A	0.002	**
Y110H	→ Y110A	0.262	ns

D1.2) $k_{cat}^{app}{}_{(HEDS)}$ @ 500 µM GSH

Comparison		P-value	
WT	→ Y110F	0.223	ns
WT	→ Y110H	<0.001	***
WT	→ Y110A	<0.001	***
Y110F	→ Y110H	<0.001	***
Y110F	→ Y110A	<0.001	***
Y110H	→ Y110A	0.196	ns

D1.3) $k_{cat}^{app}{}_{(HEDS)}$ @ 1000 µM GSH

Comparison		P-value	
WT	→ Y110F	0.298	ns
WT	→ Y110H	0.011	*
WT	→ Y110A	0.004	**
Y110F	→ Y110H	0.003	**
Y110F	→ Y110A	0.001	***
Y110H	→ Y110A	0.325	ns

D1.4) $k_{cat}^{app}{}_{(HEDS)}$ @ 1500 µM GSH

Comparison		P-value	
WT	→ Y110F	0,033	*
WT	→ Y110H	0,012	*
WT	→ Y110A	0.003	**
Y110F	→ Y110H	<0.001	***
Y110F	→ Y110A	<0.001	***
Y110H	→ Y110A	0.218	ns

D2.1) $k_{cat}^{app}{}_{(GSH)}$ @ 0.18 mM HEDS

Comparison		P-value	
WT	→ Y110F	<0.001	***
WT	→ Y110H	<0.001	***
WT	→ Y110A	<0.001	***
Y110F	→ Y110H	<0.001	***
Y110F	→ Y110A	<0.001	***
Y110H	→ Y110A	0.139	ns

D2.2) $k_{cat}^{app}{}_{(GSH)}$ @ 0.37 mM HEDS

Comparison		P-value	
WT	→ Y110F	<0.001	***
WT	→ Y110H	<0.001	***
WT	→ Y110A	<0.001	***
Y110F	→ Y110H	<0.001	***
Y110F	→ Y110A	<0.001	***
Y110H	→ Y110A	0.005	**

D2.3) $k_{cat}^{app}{}_{(GSH)}$ @ 0.55 mM HEDS

Comparison		P-value	
WT	→ Y110F	0.010	**
WT	→ Y110H	<0.001	***
WT	→ Y110A	<0.001	***
Y110F	→ Y110H	<0.001	***
Y110F	→ Y110A	<0.001	***
Y110H	→ Y110A	0.010	**

D2.4) $k_{cat}^{app}{}_{(GSH)}$ @ 0.74 mM HEDS

Comparison		P-value	
WT	→ Y110F	0.057	ns
WT	→ Y110H	<0.001	***
WT	→ Y110A	<0.001	***
Y110F	→ Y110H	<0.001	***
Y110F	→ Y110A	<0.001	***
Y110H	→ Y110A	0.081	ns

D3.1) $K_m^{app}{}_{(HEDS)}$ @ 300 µM GSH

Comparison			P-value	
WT	→	Y110F	0.511	ns
WT	→	Y110H	0.511	ns
WT	→	Y110A	0.511	ns
Y110F	→	Y110H	0.511	ns
Y110F	→	Y110A	0.511	ns
Y110H	→	Y110A	0.511	ns

D3.2) $K_m^{app}{}_{(HEDS)}$ @ 500 µM GSH

Comparison			P-value	
WT	→	Y110F	0.182	ns
WT	→	Y110H	0.182	ns
WT	→	Y110A	0.182	ns
Y110F	→	Y110H	0.182	ns
Y110F	→	Y110A	0.182	ns
Y110H	→	Y110A	0.182	ns

D3.3) $K_m^{app}{}_{(HEDS)}$ @ 1000 µM GSH

Comparison			P-value	
WT	→	Y110F	0.039	*
WT	→	Y110H	0.289	ns
WT	→	Y110A	0.816	ns
Y110F	→	Y110H	0.305	ns
Y110F	→	Y110A	0.033	*
Y110H	→	Y110A	0.293	ns

D3.4) $K_m^{app}{}_{(HEDS)}$ @ 1500 µM GSH

Comparison			P-value	
WT	→	Y110F	0.037	*
WT	→	Y110H	0.250	ns
WT	→	Y110A	0.723	ns
Y110F	→	Y110H	0.261	ns
Y110F	→	Y110A	0.026	*
Y110H	→	Y110A	0.272	ns

D4.1) $K_m^{app}{}_{(GSH)}$ @ 0.18 mM HEDS

Comparison			P-value	
WT	→	Y110F	0.966	ns
WT	→	Y110H	0.966	ns
WT	→	Y110A	0.966	ns
Y110F	→	Y110H	0.966	ns
Y110F	→	Y110A	0.966	ns
Y110H	→	Y110A	0.966	ns

D4.2) $K_m^{app}{}_{(GSH)}$ @ 0.37 mM HEDS

Comparison			P-value	
WT	→	Y110F	0.884	ns
WT	→	Y110H	0.525	ns
WT	→	Y110A	0.159	ns
Y110F	→	Y110H	0.470	ns
Y110F	→	Y110A	0.156	ns
Y110H	→	Y110A	0.022	*

D4.3) $K_m^{app}{}_{(GSH)}$ @ 0.55 mM HEDS

Comparison			P-value	
WT	→	Y110F	0.443	ns
WT	→	Y110H	0.057	ns
WT	→	Y110A	0.621	ns
Y110F	→	Y110H	0.277	ns
Y110F	→	Y110A	0.594	ns
Y110H	→	Y110A	0.084	ns

D4.4) $K_m^{app}{}_{(GSH)}$ @ 0.74 mM HEDS

Comparison			P-value	
WT	→	Y110F	0.146	ns
WT	→	Y110H	0.146	ns
WT	→	Y110A	0.146	ns
Y110F	→	Y110H	0.146	ns
Y110F	→	Y110A	0.146	ns
Y110H	→	Y110A	0.146	ns

E) GSSCys assay *Sc*Grx7^{D144X} (Fig. 38, Supplementary Fig. 9 and Supplementary Table 5)

E1.1) $k_{cat}^{app}{}_{(GSSCys)}$ @ 50 µM GSH

Comparison		P-value	
WT	→ D144A	0.040	*
WT	→ D144K	<0.001	***
D144A	→ D144K	0.001	***

E1.2) $k_{cat}^{app}{}_{(GSSCys)}$ @ 100 µM GSH

Comparison		P-value	
WT	→ D144A	0.453	ns
WT	→ D144K	0.008	**
D144A	→ D144K	0.013	*

E1.3) $k_{cat}^{app}{}_{(GSSCys)}$ @ 200 µM GSH

Comparison		P-value	
WT	→ D144A	0.576	ns
WT	→ D144K	<0.001	***
D144A	→ D144K	<0.001	***

E1.4) $k_{cat}^{app}{}_{(GSSCys)}$ @ 1000 µM GSH

Comparison		P-value	
WT	→ D144A	0.682	ns
WT	→ D144K	0.038	*
D144A	→ D144K	0.043	*

E3.1) $K_m^{app}{}_{(GSSCys)}$ @ 50 µM GSH

Comparison		P-value	
WT	→ D144A	0.035	*
WT	→ D144K	0.020	*
D144A	→ D144K	0.437	ns

E3.2) $K_m^{app}{}_{(GSSCys)}$ @ 100 µM GSH

Comparison		P-value	
WT	→ D144A	0.034	*
WT	→ D144K	0.005	**
D144A	→ D144K	0.066	ns

E3.3) $K_m^{app}{}_{(GSSCys)}$ @ 200 µM GSH

Comparison		P-value	
WT	→ D144A	0.443	ns
WT	→ D144K	0.002	**
D144A	→ D144K	0.003	**

E3.4) $K_m^{app}{}_{(GSSCys)}$ @ 1000 µM GSH

Comparison		P-value	
WT	→ D144A	0.119	ns
WT	→ D144K	0.018	*
D144A	→ D144K	0.112	ns

E2.1) $k_{cat}^{app}{}_{(GSH)}$ @ 25 µM GSSCys

Comparison		P-value	
WT	→ D144A	<0.001	***
WT	→ D144K	<0.001	***
D144A	→ D144K	<0.001	***

E2.2) $k_{cat}^{app}{}_{(GSH)}$ @ 50 µM GSSCys

Comparison		P-value	
WT	→ D144A	<0.001	***
WT	→ D144K	<0.001	***
D144A	→ D144K	0.012	*

E2.3) $k_{cat}^{app}{}_{(GSH)}$ @ 100 µM GSSCys

Comparison		P-value	
WT	→ D144A	<0.001	***
WT	→ D144K	<0.001	***
D144A	→ D144K	0.131	ns

E2.4) $k_{cat}^{app}{}_{(GSH)}$ @ 150 µM GSSCys

Comparison		P-value	
WT	→ D144A	0.027	*
WT	→ D144K	0.032	*
D144A	→ D144K	0.855	ns

E4.1) $K_m^{app}{}_{(GSH)}$ @ 25 µM GSSCys

Comparison		P-value	
WT	→ D144A	0.813	ns
WT	→ D144K	<0.001	***
D144A	→ D144K	<0.001	***

E4.2) $K_m^{app}{}_{(GSH)}$ @ 50 µM GSSCys

Comparison		P-value	
WT	→ D144A	0.056	ns
WT	→ D144K	<0.001	***
D144A	→ D144K	0.004	**

E4.3) $K_m^{app}{}_{(GSH)}$ @ 100 µM GSSCys

Comparison		P-value	
WT	→ D144A	0.366	ns
WT	→ D144K	<0.001	***
D144A	→ D144K	0.001	***

E4.4) $K_m^{app}{}_{(GSH)}$ @ 150 µM GSSCys

Comparison		P-value	
WT	→ D144A	0.325	ns
WT	→ D144K	0.020	*
D144A	→ D144K	0.009	**

F) GSSCys assay *Sc*Grx7^{E147X} (Fig. 39, Supplementary Fig. 11 and Supplementary Table 6)

F1.1) $k_{cat}^{app}{}_{(GSSCys)}$ @ 50 µM GSH

Comparison		P-value	
WT	→ E147A	0.999	ns
WT	→ E147K	<0.001	***
E147A	→ E147K	<0.001	***

F1.2) $k_{cat}^{app}{}_{(GSSCys)}$ @ 100 µM GSH

Comparison		P-value	
WT	→ E147A	0.317	ns
WT	→ E147K	<0.001	***
E147A	→ E147K	<0.001	***

F1.3) $k_{cat}^{app}{}_{(GSSCys)}$ @ 200 µM GSH

Comparison		P-value	
WT	→ E147A	0.840	ns
WT	→ E147K	<0.001	***
E147A	→ E147K	<0.001	***

F1.4) $k_{cat}^{app}{}_{(GSSCys)}$ @ 1000 µM GSH

Comparison		P-value	
WT	→ E147A	0.427	ns
WT	→ E147K	<0.001	***
E147A	→ E147K	<0.001	***

F2.1) $k_{cat}^{app}{}_{(GSH)}$ @ 25 µM GSSCys

Comparison		P-value	
WT	→ E147A	0.054	ns
WT	→ E147K	0.006	**
E147A	→ E147K	0.058	ns

F2.2) $k_{cat}^{app}{}_{(GSH)}$ @ 50 µM GSSCys

Comparison		P-value	
WT	→ E147A	0.037	*
WT	→ E147K	0.004	**
E147A	→ E147K	0.042	*

F2.3) $k_{cat}^{app}{}_{(GSH)}$ @ 100 µM GSSCys

Comparison		P-value	
WT	→ E147A	0.003	**
WT	→ E147K	<0.001	***
E147A	→ E147K	0.002	**

F2.4) $k_{cat}^{app}{}_{(GSH)}$ @ 150 µM GSSCys

Comparison		P-value	
WT	→ E147A	0.003	**
WT	→ E147K	0.021	*
E147A	→ E147K	0.063	ns

F3.1) $K_m^{app}{}_{(GSSCys)}$ @ 50 µM GSH

Comparison		P-value	
WT	→ E147A	0.550	ns
WT	→ E147K	0.002	**
E147A	→ E147K	0.002	**

F3.2) $K_m^{app}{}_{(GSSCys)}$ @ 100 µM GSH

Comparison		P-value	
WT	→ E147A	0.641	ns
WT	→ E147K	0.001	***
E147A	→ E147K	0.001	***

F3.3) $K_m^{app}{}_{(GSSCys)}$ @ 200 µM GSH

Comparison		P-value	
WT	→ E147A	0.984	ns
WT	→ E147K	0.012	*
E147A	→ E147K	0.018	*

F3.4) $K_m^{app}{}_{(GSSCys)}$ @ 1000 µM GSH

Comparison		P-value	
WT	→ E147A	0.539	ns
WT	→ E147K	0.002	**
E147A	→ E147K	0.001	***

F4.1) $K_m^{app}{}_{(GSH)}$ @ 25 µM GSSCys

Comparison		P-value	
WT	→ E147A	0.125	ns
WT	→ E147K	0.025	*
E147A	→ E147K	0.005	**

F4.2) $K_m^{app}{}_{(GSH)}$ @ 50 µM GSSCys

Comparison		P-value	
WT	→ E147A	0.042	*
WT	→ E147K	0.025	*
E147A	→ E147K	0.003	**

F4.3) $K_m^{app}{}_{(GSH)}$ @ 100 µM GSSCys

Comparison		P-value	
WT	→ E147A	0.122	ns
WT	→ E147K	0.005	**
E147A	→ E147K	0.002	**

F4.4) $K_m^{app}{}_{(GSH)}$ @ 150 µM GSSCys

Comparison		P-value	
WT	→ E147A	0.008	**
WT	→ E147K	0.016	*
E147A	→ E147K	<0.001	***

G) GSSCys assay *Sc*Grx7^{R153X} (Fig. 40, Supplementary Fig. 13 and Supplementary Table 7)

G1.1) $k_{cat}^{app}{}_{(GSSCys)}$ @ 50 µM GSH

Comparison		P-value	
WT	→ R153A	0.549	ns
WT	→ R153E	0.013	*
R153A	→ R153E	0.010	**

G1.2) $k_{cat}^{app}{}_{(GSSCys)}$ @ 100 µM GSH

Comparison		P-value	
WT	→ R153A	0.710	ns
WT	→ R153E	0.004	**
R153A	→ R153E	0.004	**

G1.3) $k_{cat}^{app}{}_{(GSSCys)}$ @ 200 µM GSH

Comparison		P-value	
WT	→ R153A	0.033	*
WT	→ R153E	<0.001	***
R153A	→ R153E	0.003	**

G1.4) $k_{cat}^{app}{}_{(GSSCys)}$ @ 1000 µM GSH

Comparison		P-value	
WT	→ R153A	0.125	ns
WT	→ R153E	0.005	**
R153A	→ R153E	0.021	*

G3.1) $K_m^{app}{}_{(GSSCys)}$ @ 50 µM GSH

Comparison		P-value	
WT	→ R153A	0.043	*
WT	→ R153E	0.036	*
R153A	→ R153E	0.857	ns

G3.2) $K_m^{app}{}_{(GSSCys)}$ @ 100 µM GSH

Comparison		P-value	
WT	→ R153A	0.039	*
WT	→ R153E	0.043	*
R153A	→ R153E	0.713	ns

G3.3) $K_m^{app}{}_{(GSSCys)}$ @ 200 µM GSH

Comparison		P-value	
WT	→ R153A	0.015	*
WT	→ R153E	0.021	*
R153A	→ R153E	0.950	ns

G3.4) $K_m^{app}{}_{(GSSCys)}$ @ 1000 µM GSH

Comparison		P-value	
WT	→ R153A	0.008	**
WT	→ R153E	0.011	*
R153A	→ R153E	0.970	ns

G2.1) $k_{cat}^{app}{}_{(GSH)}$ @ 25 µM GSSCys

Comparison		P-value	
WT	→ R153A	<0.001	***
WT	→ R153E	<0.001	***
R153A	→ R153E	<0.001	***

G2.2) $k_{cat}^{app}{}_{(GSH)}$ @ 50 µM GSSCys

Comparison		P-value	
WT	→ R153A	<0.001	***
WT	→ R153E	<0.001	***
R153A	→ R153E	<0.001	***

G2.3) $k_{cat}^{app}{}_{(GSH)}$ @ 100 µM GSSCys

Comparison		P-value	
WT	→ R153A	<0.001	***
WT	→ R153E	<0.001	***
R153A	→ R153E	<0.001	***

G2.4) $k_{cat}^{app}{}_{(GSH)}$ @ 150 µM GSSCys

Comparison		P-value	
WT	→ R153A	<0.001	***
WT	→ R153E	<0.001	***
R153A	→ R153E	<0.001	***

G4.1) $K_m^{app}{}_{(GSH)}$ @ 25 µM GSSCys

Comparison		P-value	
WT	→ R153A	<0.001	***
WT	→ R153E	<0.001	***
R153A	→ R153E	0.255	ns

G4.2) $K_m^{app}{}_{(GSH)}$ @ 50 µM GSSCys

Comparison		P-value	
WT	→ R153A	<0.001	***
WT	→ R153E	<0.001	***
R153A	→ R153E	0.760	ns

G4.3) $K_m^{app}{}_{(GSH)}$ @ 100 µM GSSCys

Comparison		P-value	
WT	→ R153A	<0.001	***
WT	→ R153E	<0.001	***
R153A	→ R153E	0.454	ns

G4.4) $K_m^{app}{}_{(GSH)}$ @ 150 µM GSSCys

Comparison		P-value	
WT	→ R153A	0.005	**
WT	→ R153E	0.006	**
R153A	→ R153E	0.611	ns